Universität Zürich
Physik-Institut

www.physik.unizh.ch

Wissenschaftlicher Jahresbericht

April 2005 - März 2006

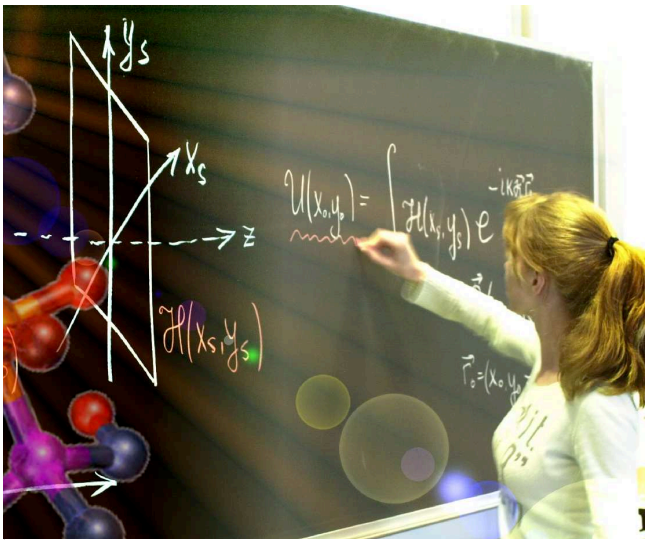

Winterthurerstrasse 190, CH-8057 Zürich/Schweiz

Universität Zürich
Physik-Institut
www.physik.unizh.ch

Wissenschaftlicher Jahresbericht

April 2005 - März 2006

Winterthurerstrasse 190, CH-8057 Zürich/Schweiz

The picture on the front shows Tatiana Latychevskaia of the **Physics of Biological Systems** group (Sec. 12) explaining the principles of hologram reconstruction. On the back of the cover a new type of noble ion source is shown developed by the group.

Sekretariat	044 635 5721	secret@physik.unizh.ch
Prof. C. Amsler	044 635 5784 022 767 2914	amsler@cern.ch
Prof. H.-W. Fink	044 635 5801	hwfink@physik.unizh.ch
Prof. H. Keller	044 635 5748	keller@physik.unizh.ch
Prof. J. Osterwalder	044 635 5827	osterwal@physik.unizh.ch
Prof. A. Schilling	044 635 5791	schilling@physik.unizh.ch
Prof. U.D. Straumann	044 635 5768	strauman@physik.unizh.ch
Prof. P. Truöl	044 635 5777	truoel@physik.unizh.ch

The annual reports are available on the internet: http://www.physik.unizh.ch/reports.html.

Begleitwort

Mit seinen sieben Forschungsgruppen deckt das Physik-Institut ein breites, national und international vernetztes Spektrum experimenteller Forschung ab, das von den Eigenschaften biologischer Makromoleküle bis zu jenen der elementaren Bestandteile des Universums in seiner Frühphase reicht. In den beiden etwa gleich starken Hauptbereichen, Physik der kondensierten Materie und Physik fundamentaler Systeme, finden sich Gruppen in der Bio-, der Oberflächen-, der Festkörper- und der Elementarteilchenphysik.

Die Forschungsgruppen am Physik-Institut sind vom Nationalfonds durch 21 Forschungsprojekte und von Beiträgen aus der K. Alex Müller Stiftung, der Gebert-Rüf Stiftung, sowie durch diverse andere Drittmittelbeiträge unterstützt worden. Das Physik-Institut ist unter anderem an dem Nationalen Forschungskompetenzzentrum (NCCR) MaNEP (**Materials with novel electronic properties**) beteiligt und gehört zu den Mitgründern des Swiss Institute of Particle Physics (CHIPP). Als erste Forschungsgruppe der Universität hat die **Oberflächenphysik** erfolgreich ein dreijähriges EU Projekt auf dem Gebiet der Nanowissenschaften (**Nanomesh - Boron Nitride Nanomesh as a Scaffold for Nanocatalysts, Nanomagnets and Functional Surfaces**) mit insgesamt acht Partnerinstitutionen iniziiert, welches von ihr auch koordiniert wird. Prof. Fink leitet das EU Projekt **Obtaining atomically resolved structural information on individual bio-molecules using electron holography** mit fünf Partnerinstitutionen und die Gruppe **Supraleitung und Magnetismus** ist Partner im dreijährigen EU Projekt **Controlling mesoscopic phase separation**, welches von der Technischen Universität Athen geleitet wird und zwölf Partnerinstitutionen umfasst.

Einige wichtige Entwicklungen bei den Projekten der **Teilchenphysik** seien hier kurz erwähnt: Am CERN wurden die Vorbereitungen für das CMS Experiment am Large Hadron Collider fortgesetzt. Die Amsler Gruppe entwickelt den Silizium-Pixeldetektor nahe dem Wechselwirkungspunkt und bereitet die Auswerteprogramme für das Experiment vor, das Ende 2007 in Betrieb genommen wird. Ebenfalls am CERN arbeitet diese Gruppe an einem Projekt, das mit Flüssigargon nach der dunklen Materie im Universum suchen wird. Sie beteiligt sich ferner am CERN - DIRAC Experiment und entwickelt einen Aerogeldetektor, mit dem K-π Atome nachgewiesen und studiert werden können. Die am Elektron (Positron) - Proton Speicherring HERA am DESY in Hamburg arbeitende H1-Kollaboration hat 2005/6 u.a. den vom geladenen Anteil der elektroschwachen Wechselwirkung gesteuerten Prozess eP $\rightarrow \nu$X bei den höchsten Energien (320 GeV) erstmals in Abhängigkeit des Polarisationsgrads für Elektronen und Positronen untersucht. Der gemessene Wirkungsquerschnitt bestätigt die Vorhersagen des Standardmodells und schliesst Beiträge anomaler Händigkeit aus.

Im Forschungsbereich **Physik der kondensierten Materie** sind unter anderem folgende Fortschritte erzielt worden: In einem gemeinsamen Projekt zwischen der **Low-Energy Muon** Gruppe des PSI und der Gruppe **Supraleitung und Magnetismus** konnte erstmals das Magnetfeldprofil (Meissner-Ochsenfeld-Effekt) in einem dünnen Film eines Kuprat-Supraleiters mit Hilfe von niederenergetischen Myonen direkt ausgemessen werden. Die Gruppe **Oberflächenphysik** zeigte das Prinzip einer neuartigen Quelle für niederenergetische spinpolarisierte Elektronen mit einer Pulsdauer von wenigen Picosekunden. In Zusammenarbeit mit dem Biochemischen Institut ist es der Gruppe **Physik Biologischer Systeme** gelungen Viren mit Mikrostrukturen zu verbinden. Dadurch ist es möglich geworden Elektronen-Hologramme einzelner Viren aufzunehmen und zu rekonstruieren.

Am Physik-Institut haben im Berichtsjahr zwei bedeutende internationale Konferenzen stattgefunden:

Vom 3. bis 7. Oktober 2005 fand an unserem Institut ein **Workshop on tracking in high multiplicity environments** (TIME 05) statt. Rund 50 internationale Experten in Spurdetektoren und Analyseprogrammen aus laufenden und geplanten Experimenten der Hochenergiephysik diskutierten vor allem Fragen, die bei hohen Teilchenraten auftreten. Die Teilnehmer pflegten einen intensiven Gedankenaustausch in operationellen und systemtechnischen Aspekten, Rekonstruktionsalgorithmen, Strahlungsschäden und Detektortechnologien.

Die Entdeckung der Hochtemperatur-Supraleitung durch J. Georg Bednorz und K. Alex Müller am IBM Forschungslaboratorium in Rüschlikon löste 1986 weltweit eine beispiellose Euphorie in der Fachwelt aus. Zu Ehren der beiden Nobelpreisträger, denen vor 20 Jahren diese bahnbrechende Entdeckung gelang, wurde am Physik-Institut vom 27. bis 29. März 2006 ein Internationales Symposium durchgeführt. Rund 30 renommierte nationale und internationale Referentinnen und Referenten haben über aktuelle Entwicklungn der Hochtemperatur-Supraleitung (Gittereffekte, Polaronbildung, Phasenseparation) berichtet. Am Symposium haben zahlreiche namhafte Ehrengäste und Teilnehmer aus aller Welt teilgenommen. Diese Veranstaltung hat bei den Beteiligten und in den Medien grosse Resonanz gefunden.

Die Forschungsprojekte des Physik-Instuts findet man auf den Websites der Forschungsdatenbank der Universität Zürich [1]. Der wissenschaftliche Jahresbericht des Physik-Instituts wurde wie schon in den letzten Jahren in englischer Sprache abgefasst, um unsere Forschungstätigkeit einem internationalen Publikum besser zugänglich zu machen. Der vollständige Jahresbericht wie auch die Jahresberichte früherer Jahre können auf der Website des Physik-Instituts (http://www. physik.unizh.ch/reports.html) eingesehen werden. Eine allgemein verständliche Zusammenfassung (auf Deutsch) der laufenden Forschungsprojekte folgt auf den nächsten Seiten.

Zürich, im Mai

Prof. Dr. Hugo Keller

[1] http://www.research-projects.unizh.ch/math/unit71600/index.htm

Persönliches

Rücktritte

PD Prof. Dr. Peter Fritz Meier

Nach fast 30 Jahren erfolgreicher Tätigkeit am Physik-Institut ist unser geschätzter Kollege PD Prof. Dr. Peter F. Meier im April 2005 in den Ruhestand getreten. Nach seinem Physik-Studium und seinem Doktorat (1968) am Institut für theoretische Physik an unserer Universität erweiterte er seine Kenntnisse in Festkörperphysik als Postdoktorand an der Universität Nijmegen (NL) und am IBM Forschungslaboratorium in Rüschlikon. Es folgten zwei Jahre als wissenschaftlicher Mitarbeiter in der Theoriegruppe am SIN (Swiss Institue for Nuclear Research) und Habilitation an der Universität Zürich. 1977 wurde Peter Meier als Oberassistent in die Gruppe von Prof. Walter Kündig aufgenommen und 1981 erfolgte die Ernennung zum Titularprofessor. Seit 1992 hat Peter Meier als wissenschaftlicher Abteilungsleiter seine eigene, sehr erfolgreiche Forschungsgruppe geleitet. Sein wissenschaftliches Interesse im Bereich der theoretischen Festkörperphysik und der **computational solid state physics** ist sehr vielfältig. Auf veschiedenenen Gebieten hat er wesentliche Beiträge geliefert und dabei immer den Dialog mit den Experimentatoren gesucht. Einige Beiträge seien hier kurz erwähnt: In seinen frühen Arbeiten interpretierte er μSR Daten von magnetischen Systemen und Halbleitern mit Hilfe von numerischen Methoden. Mit Dichtefunktionalrechnungen und der approximativen Lösung des Hubbard Hamiltonoperators wurden statische und dynamische Eigenschaften der Myonen, vor allem in Halbleitern, bestimmt. Weiter spielte die Interpretation von NMR-, NQR- und Knightshift-Messungen eine immer grössere Rolle, vor allem als diese Messmethoden auch auf die Hochtemperatur-Supraleiter ausgedehnt wurden. In Zusammenarbeit mit den Experminentalphysik-Gruppen (Profs. E. Brun und F. Waldner) hat er sich auch mit Problemen der Chaosforschung befasst. In einem interdisziplinären Projekt mit Medizinern der Universität Zürich hat er mit seiner Gruppe physikalische Methoden entwickelt, um Gehirnstrommessungen zu analysieren und interpretieren. Neben diesen Forschungsaufgaben in der Grundlagenforschung gab Peter Meier seine fundamentalen Kentnisse in Festkörpertheorie und spezieller Informatik für Naturwissenschafter in Vorlesungen den Studierenden weiter. Nicht wenige von ihnen haben als Diplomand und/oder Doktorand in seiner Forschungsgruppe abgeschlossen. Nebenbei gelang es ihm, als begeisteter Anhänger des FC Aarau, in einem rechtsmedizinischen Streitfall durch Studien der Physik des Fussballs zu zeigen, dass ein sehr schneller Fussball bei einem unverhoften Aufprall auf das Gesicht die Augen eines Spielers durch die Beschleunigung des Kopfes nicht nachhaltig schädigen kann. Peter Meier hat seine Forschungsgruppe **Computer Assistierte**

Physik mit grossem Engagement geleitet. Dank seiner fundierten und breiten Fachkenntnis und seinem offenen und väterlichen Charakter ist es ihm gelungen das Vertrauen seiner Studierenden, Mitarbeiterinnen und Mitarbeiter zu gewinnen und sie für die Physik zu begeistern. Seine freundliche, zuvorkommende und diplomatische Art und seine ausgesprochene Teamfähigkeit werden am Institut sehr geschätzt. Wir danken Peter Meier für sein enormes Engagement am Physik-Institut und wünschen ihm alles Gute in seinem Ruhestand.

PD Prof. Dr. Hendrik Pruys

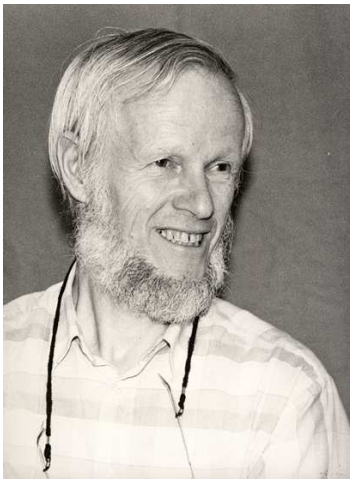

Am 1. September 2005 ist unser langjähriger Kollege PD Prof. Dr. Hendrik Pruys in den Ruhestand getreten. Henk studierte Physik an der Universität Utrecht. Nach einer Tätigkeit als Reaktorphysiker am EIR fing er 1975 eine Dissertation bei Prof. R. Engfer am Institut an über Pion- und Myon- induzierte Kernreaktionen. Ab 1978 war er Oberassistent am Institut, wo er 1993 habilitierte und 2000 zum Titularprofessor ernannt wurde. Er hat während seiner Karriere wesentlich zu Experimenten über seltene Elementarteilchenprozesse am PSI beigetragen, und neulich zum ATHENA Antiwasserstoffprojekt am CERN. Seine Lehrfähigkeiten und Vorlesungen wurden von unseren Studierenden sehr geschätzt. Wir danken Henk für seinen grossen Einsatz in Lehre und Forschung und wünschen ihm viel Musse beim Ausüben seiner geliebten Hobbies (Weinbau und Schachspielen).

Wir gedenken

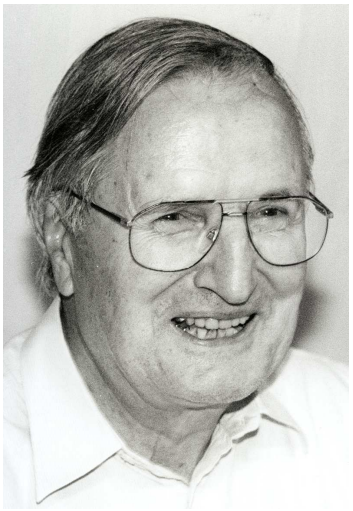

Prof. Dr. Walter Kündig

4. April 1932 bis 25. Mai 2005

Am 25. Mai 2005 ist Walter Kündig unerwartet in seinem 74. Altersjahr an einem akuten Herzversagen verstorben. Er wurde am 4. April 1932 in Zürich geboren und ist in Pfäffikon ZH aufgewachsen, wo er Primar- und Sekundarschule durchlief. Nach dem Besuch der Oberrealschule in Winterthur, studierte er an der ETH Zürich (Abteilung X) Physik und Chemie, wo er unter der Leitung von Prof. Paul Scherrer als Naturwissenschafter diplomierte und mit einer Arbeit "Einfluss des Paramagnetismus auf die Richtungskorrelation" promovierte. Zeit seines Lebens war Paul Scherrer für Walter Kündig das grosse wissenschaftliche und didaktische Vorbild und dieser hat Kündig's erfolgreiche Forschungs- und Lehrtätigkeit wesentlich mitgeprägt. Immer wieder hat Walter Kündig Geschichten und Anekdoten aus seiner "Scherrer-Zeit" erzählt, die er als Assistent und insbesondere als Scherrer's Vorlesungsassistent erlebt hatte. Nach seiner Promotion hat Walter Kündig im Jahre 1960 eine Postdoktorandenstelle an der Purdue University (U.S.A.) angenommen, wo er seine bahnbrechenden Experimente zum transversalen Doppler-Effekt (Zwillingsparadox-Experiment) durchführte. Nach seinem Umzug im Jahre 1962 an die University of California in Los Angeles (UCLA), war er dort zuerst als wissenschaftlicher Mitarbeiter und von 1964 bis 1969 als Assistenzprofessor tätig. Seine Forschungstätigkeit war damals für einen jungen Forscher bereits sehr vielfältig (Mössbauer-Spektroskopie, Superparamagnetismus, Auger-Effekt, Oberflächenphysik, Magnetismus). Es war kein geringerer als Prof. K. Alex Müller (Physik-Nobelpreisträger 1987), der sich für Walter Kündig beim damaligen Institutsdirektor Prof. Hans Staub eingesetzt hatte, um den erfolgreichen jungen Experimentalphysiker als Assistenzprofessor im Jahre 1969 ans Physik-Institut der Universität Zürich zu berufen. Im Sommer 1973 folgte die Wahl zum Extraordinarius, sechs Jahre später diejenige zum Ordinarius. Auch als ihn nach seinem Rücktritt im Sommer 1999 krankheitsbedingte Beschwerden plagten, nahm Walter Kündig rege an den Veranstaltungen des Physik-Instituts teil und verfolgte weiter seine hohen wissenschaftlichen Ziele.

Walter Kündig war mit Herz und Seele ein Experimentalphysiker. Neben seiner Familie, die ihm sehr viel bedeutete und in deren Umfeld er immer wieder neue Kraft schöpfen konnte, war die Experimentalphysik seine grosse Leidenschaft. Er war ein ideenreicher und ebenso vielseitiger wie mutiger Wissenschafter, der mit seiner Begeisterungsfähigkeit seine jüngeren Mitarbeiter anspornte und mit ihnen auch die schwierigsten Forschungsprojekte zum Erfolg führte. Er hatte die besondere Gabe das wesentliche Experiment zur richtigen Zeit zu realisieren. Es ging ihm immer darum, fundamentale Fragen der Physik vom Experiment her zu ergründen. Dabei ist er mit seinen anspruchsvollen Forschungsvorhaben immer wieder an die Grenze des Machbaren vorgestossen.

Während seiner dreissigjährigen Tätigkeit am Physik-Institut widmete sich Walter Kündig bevorzugt fundamentalen Fragen der Festkörper- und der Teilchenphysik. Neben wegweisenden Arbeiten zur nuklearen Festkörperphysik (Anwendung der Mössbauer-Spektroskopie und der Myon-Spin-Rotation) widmete er sich in den letzten Jahren vor allem zwei fundamentalen Experimenten, der präzisen Messung der Neutrinomasse und der genauen Bestimmung der Gravitationskonstanten. Beide Experimente haben in der Fachwelt grosses Aufsehen erregt und massgeblich zur internationalen Anerkennung des Physik-Instituts beigetragen. Das Gravitations-Experiment hat ihn bis zu seinem Tod beschäftigt.

Zusammen mit Prof. K. Alex Müller war er eine der treibenden Kräfte in der Realisation einer Synchrotronstrahlungsquelle (Swiss Light Source) am Paul Scherrer Institut in Villigen AG. Er hatte früh erkannt, dass ein Synchrotron dieser Art für den Forschungsplatz Schweiz von nationaler Bedeutung ist. Heute wird dieses Instrument in den verschiedensten Gebieten der Naturwissenschaften, der Medizin und der Technik erfolgreich eingesetzt.

Als hervorragender akademischer Lehrer vermochte er die Studierenden in seinen Vorlesungen über Experimentalphysik, die von einem "Feuerwerk" von originellen Demonstrationsexperimenten umrahmt waren, für die Physik zu begeistern. Auch als Präsident der Schweizerischen Physikalischen Gesellschaft hat er sich für sein Fachgebiet eingesetzt. Es war ihm ein wichtiges Anliegen, neue Erkenntnisse aus der Grundlagenforschung durch allgemein verständliche Vorträge und Artikel einer breiteren Öffentlichkeit zugänglich zu machen.

Mit Walter Kündig verliert das Physik-Institut, die Universität Zürich, die nationale und internationale Physikergemeinschaft einen herausragenden Forscher und Lehrer, der als origineller und kreativer Experimentalist immer wieder neue Wege beschritten hat, mit dem Ziel fundamentale physikalische Zusammenhänge in der Natur zu ergründen. Aus seiner Schule sind zahlreiche erfolgreiche Wissenschaftlerinnen und Wissenschaftler hervorgegangen, einige davon in akademischen Positionen in der ganzen Welt. Durch seine vielfältige und einzigartige wissenschaftliche Hinterlassenschaft wie durch seinen offenen, liebenswürdigen Charakter wird er vielen in lebendiger Erinnerung bleiben.

Mitarbeiter

Wissenschaftliches Personal

Enver	Alagöz	CMS
Milan	Allan	Oberflächenphysik
Yves	Allkofer	Dirac
Prof. Claude	Amsler	Dark Matter, Dirac, CMS
Holger	Bartolf	PTM
Dr. Jan	Becker	H1
Dr. Roland	Bernet	LHCb
Dr. Ralf Patrick	Bernhard	DØ, LHCb
Vittorio	Boccone	Dark Matter
Louis	Brandenberger	Oberflächenphysik
Thomas	Brugger	Oberflächenphysik
Dr. Vincenzo	Chiochia	CMS
Claudio	Cirelli	Oberflächenphysik
Martina	Corso	Oberflächenphysik
Raffaele	Dell'Amore	PTM
Andrei	Dolocan	Oberflächenphysik
Dr. Andreas	Engel	PTM
Conrad	Escher	Bio-Physik
Dr. Dmitry	Eshchenko	Supraleitung & Magnetismus
Dr. Peter	Fierlinger	UCN
Prof. Hans-Werner	Fink	Bio-Physik
Dr. Carine	Galli Marxer	Oberflächenphysik
Dr. Johannes	Gassner	LHCb
Prof. Thomas	Greber	Oberflächenphysik
Dr. Matthias	Hengsberger	Oberflächenphysik
Stefan	Heule	UCN
Sosuke	Horikawa	Dirac
Christoph	Hörmann	CMS
Dr. Ian	Johnson	Dark Matter
Prof. Hugo	Keller	Supraleitung & Magnetismus
Dr. Rustem	Khasanov	Supraleitung & Magnetismus
Martin	Klöckner	Oberflächenphysik
Andreas	Knecht	UCN
Stefan	Kohout	Supraleitung & Magnetismus
Dr. Michael	Krüger	Bio-Physik
Fabio	La Mattina	Supraleitung & Magnetismus
Dr. Igor	Landau	Supraleitung & Magnetismus
Dr. Tatiana	Latychevskaia	Bio-Physik
Dr. Frank	Lehner	DØ, LHCb
Dominik	Leuenberger	Oberflächenphysik
Linus	Lindfeld	H1
Dr. Jorge	Lobo-Checa	Oberflächenphysik
Alexander	Maisuradze	Supraleitung & Magnetismus
Dr. Mihael	Mali	Supraleitung & Magnetismus

Wissenschaftliches Personal (cont)

Martin	Morscher	Oberflächenphysik
Prof. K. Alex	Müller	Supraleitung & Magnetismus
Dr. Katharina	Müller	H1
Dr. Matthew	Needham	LHCb
Krzysztof	Nowak	H1
Dr. Hiroshi	Okamoto	Bio-Physik
Dr. Taichi	Okuda	Oberflächenphysik
Prof. Jürg	Osterwalder	Oberflächenphysik
Taofiq	Paraiso	Supraleitung & Magnetismus
Dr. Kirill	Prokofiev	CMS
Prof. Henk	Pruys	CMS, Dirac
Dr. Christian	Regenfus	CMS, Dark Matter, Dirac
Markus	Regli	LHCb
Mark	Reibelt	PTM
Dr. Peter	Robmann	CMS, H1, $\pi \to e\nu$
Dr. Josef	Roos	Supraleitung & Magnetismus
Rosmarie	Rössel	Studienberatung
Dr. Tariel	Sakhelashvili	LHCb, $\pi \to e\nu$
Christophe	Salzmann	DØ
Dr. Andries	van der Schaaf	$\pi \to e\nu$
Simon	Scheu	$\pi \to e\nu$
Prof. Andreas	Schilling	PTM
Dr. Richard	Schillinger	Oberflächenphysik
Dr. Stefan	Schmitt	H1
Carsten	Schmitz	H1
Prof. Toni	Schneider	Supraleitung & Magnetismus
Dr. Alexander	Shengelaya	Supraleitung & Magnetismus
Stefan	Siegrist	PTM
Dr. Thomas	Speer	CMS
Dr. Olaf	Steinkamp	LHCb
Gregory	Stevens	Bio-Physik
Simon	Strässle	Supraleitung & Magnetismus
Prof. Ulrich	Straumann	H1, LHCb, $\pi \to e\nu$, UCN
Dr. Anna	Tamai	Oberflächenphysik
Dr. Jeroen	van Tilburg	LHCb
Prof. Peter	Truöl	H1, $\pi \to e\nu$
Dr. Achim	Vollhardt	LHCb
Dimitro	Volyanskyy	LHCb
Andreas	Wenger	DØ, LHCb
Stephen	Weyeneth	Supraleitung & Magnetismus
Lotte	Wilke	CMS
Dr. Stefania	Xella Hansen	H1
Dr. Bingzhang	Xue	Oberflächenphysik

Technisches und administratives Personal

Cornel	Andreoli	Bio-Physik
Eva	Baby	Sekretariat
Kurt	Bösiger	Werkstatt
Tiziano	Crudeli	Dokumentation
Walter	Fässler	Dokumentation, Elektronik
Omid	Fardin	Werkstatt
Ruth	Halter	Sekretariat
Martin	Klöckner	Oberflächenphysik
Bruno	Lussi	Werkstatt
Reto	Meier	Werkstatt
Hanspeter	Meyer	Elektronik
Lucien	Pauli	Vorlesungsbetrieb
Rolf	Reichen	Werkstatt
Jacky	Rochet	CMS, Dark Matter, Dirac
Monika	Röllin	Sekretariat
Marcel	Schaffner	Werkstatt
Jacqueline	Schenk	Sekretariat
Silvio	Scherr	Werkstatt
Jürg	Seiler	Vorlesungsbetrieb
Peter	Soland	Elektronik
Stefan	Steiner	CAD, CMS, LHCb
Karoly	Szeker	Elektronik
Peter	Treier	Werkstatt
Ursula	Wolf	Sekretariat

Contents

Physics of Fundamental Interactions and Particles 1

1 Towards a Dark Matter Experiment 1

1.1 Introduction . . . 1

1.2 The liquid argon detector . . . 1

1.3 Light collection . . . 3

2 Ultracold Neutrons 7

2.1 Wall-loss and depolarization of stored UCN . . . 7

2.2 Production of Diamond-like carbon coatings . . . 7

3 Precision Measurements in Rare Pion Decays 9

3.1 The $\pi^+ \to e^+\nu_e\gamma$ decay . . . 9

3.2 A precision determination of the $\pi^+ \to e^+\nu$ branching ratio . . . 11

4 Search for $K\pi$-Atoms 14

4.1 The $K\pi$ scattering length . . . 14

4.2 The DIRAC II experiment . . . 16

4.3 The aerogel counters . . . 17

5 Particle Physics at DESY/HERA (H1) 21

5.1 Electron-proton collisions at a centre of mass energy of 320 GeV - summary . . . 21

5.2 Inner multiwire chamber and vertex trigger . . . 21

5.3 Analysis activities . . . 22

6 The DØ Experiment: Search for Rare B_s^0 Decays 33

7 High-precision CP-violation Physics at LHCb 36

7.1 LHCb experiment . . . 36

7.2 Silicon tracker . . . 37

7.3 Trigger tracker . . . 38

7.4 Silicon sensors . . . 41
7.5 Readout system . . . 41
7.6 Detector simulation and reconstruction software . . . 42
7.7 Physics studies . . . 43
7.8 Summary and outlook . . . 43

8 Particle Physics with CMS 45

8.1 B - physics with CMS . . . 45
8.2 Silicon pixel sensors . . . 47
8.3 Readout electronics . . . 51
8.4 Mechanical support structure . . . 51

Condensed Matter Physics 54

9 Superconductivity and Magnetism 54

9.1 Studies of isotope effects in novel superconductors . . . 54
9.2 Studies of pressure effects in novel superconductors . . . 56
9.3 Spectroscopic studies of novel superconductors . . . 57
9.4 Electric field effects in perovskites . . . 62
9.5 New developments in instrumentation . . . 64

10 Phase Transitions, New Materials and Superconducting Photon Detectors 65

10.1 Physics of superconducting thin-film nanostructures . . . 65
10.2 Search for resonance phenomena in $\mathrm{TlCuCl_3}$ . . . 67
10.3 Vortex phases in type-II superconductors . . . 69
10.4 Synthesis and characterization of $\mathrm{LaBaNiO_{4-\delta}}$ . . . 70

11 Surface Physics 71

11.1 Spin polarization and exchange splitting of the surface states on Ni(111) . . . 73
11.2 Boron nitride nanomeshes on different substrates . . . 74
11.3 *h*-BN and boron nanowires on Mo(110) . . . 76
11.4 Stability of the *h*–BN nanomesh on Rh(111) in aqueous environment . . . 77
11.5 Two-photon photoemission from the *h*-BN nanomesh . . . 78

11.6 A source of spin-polarized electrons: *h*-BN/Ni(111) 80
11.7 Corannulene adsorption on h-BN/Ni(110) 81
11.8 LUMO photoemission lineshape in low-dimensional C_{60} arrays 82
11.9 Identifying enantiomers with core level photoelectron spectroscopy: the amino acid cysteine on Au(17 11 9)^S 84
11.10 Time-resolved low-energy electron diffraction 85

12 Physics of Biological Systems **88**
12.1 Structure of individual biological molecules 88
12.2 The SIBMAR project 91
12.3 The cryogenic LEEPS project 91
12.4 Numerical hologram reconstruction 93
12.5 Studies on the Conduction Mechanism in a Solid Electrolyte 94
12.6 Teaching 98

Infrastructure and Publications **99**

13 Mechanical Workshop **99**

14 Electronics Workshop **102**

15 Publications **104**
15.1 Research group of Prof. C. Amsler 104
15.2 Research group of Prof. H.-W. Fink 108
15.3 Research group of Prof. H. Keller 109
15.4 Research group of Prof. J. Osterwalder 112
15.5 Research group of Prof. A. Schilling 116
15.6 Research group of Prof. U. Straumann 117
15.7 H1 Publications 123
15.8 Research group of Prof. P. Truöl 125

1 Towards a Dark Matter Experiment

C. Amsler, V. Boccone, A. Büchler[2], A. Knecht[2], C. Regenfus, and J. Rochet

In collaboration with:
CIEMAT, ETHZ, Soltan Institute (Warsaw), Universities of Granada and Sheffield

(ArDM Collaboration)

1.1 Introduction

The search for dark matter is one of the most pressing activities in particle physics. Dark matter is probably made of Weakly Interacting Massive Particles (WIMP) which are stable particles trapped in the gravitational fields of galaxies. The favored candidate for WIMPs is the lightest supersymmetric (SUSY) particle, the neutralino with a mass of at least 40 GeV, according to LEP searches. The direct detection of WIMPs involves scattering on target nuclei with recoil energies in the range 1 - 100 keV. The cross-sections are tiny but rate predictions are model dependent, and therefore uncertain by several orders of magnitude. They depend e.g. on the nuclear target (atomic number, spin, form factors) and the type of detector used (energy threshold, resolution, signal discrimination). The search for WIMPS is hence experiment driven. The experimental upper limit for the cross-section of WIMPS with nucleons is about 10^{-6} pb.

Noble liquid detectors such as xenon or argon could act as target for WIMP detection. They have high scintillation and ionization yields because of their relatively low ionization potentials. Ionisation electrons *and* scintillation light may be detected (1). Argon is less sensitive to the threshold of the nuclear recoil energy than xenon, because of form factors, and is also much cheaper. Also, recoil energy spectra in xenon and argon are quite different (Fig. 1.1). These liquids are therefore complementary in providing a crosscheck once a WIMP signal has been found.

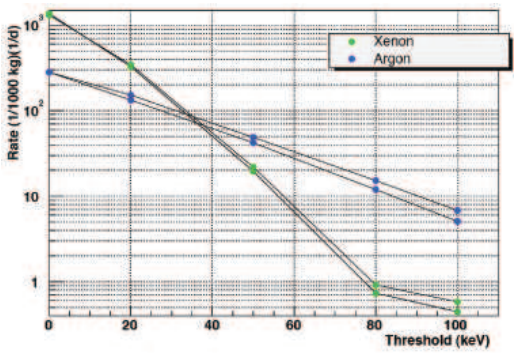

Figure 1.1:
Expected daily WIMP detection rate for a 1 ton detector as a function of threshold for xenon and argon, assuming a mass of 100 GeV and a cross section of 10^{-6} pb. The steeper curve is for xenon.

1.2 The liquid argon detector

We describe here R &D developments for an experiment that could possibly reach a cross-section of 10^{-10} pb. The detector (Fig. 1.2) would contain 1 ton of liquid argon. It exploits the ratio of scintillation to ionisation in argon and the scintillation time discrimination between nuclear and electron recoils. With a nuclear recoil energy threshold of say 30 keV, a WIMP-nucleon cross-section of 10^{-6} pb would yield 100 events per day per ton. Therefore, a 1 ton

[2]Diploma student

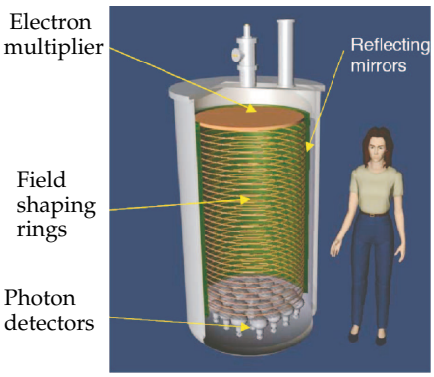

Figure 1.2: Artist's view of the 1 ton ArDM liquid argon detector to search for WIMPS.

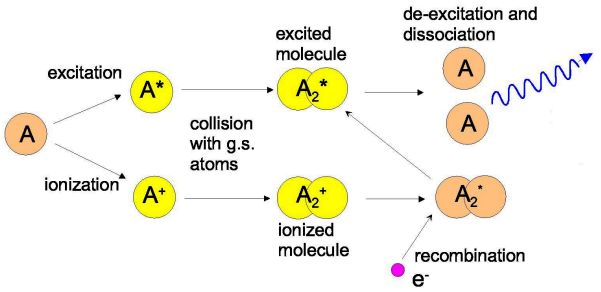

Figure 1.3: The two mechanisms leading to the emission of 128 nm photons are excitation $Ar^* + Ar \rightarrow Ar_2^* \rightarrow Ar + Ar + \gamma$ and ionisation $Ar^+ + Ar \rightarrow Ar_2^+ + e^- \rightarrow Ar_2^* \rightarrow Ar + Ar + \gamma$. The energy required to generate a photon is 68 eV.

argon detector could improve significantly on the upper limits, provided that the threshold of 30 keV and sufficient background rejection can be achieved. A drawback of natural argon liquefied from the atmosphere is namely the radioactive β-emitter ^{39}Ar. Its activity in atmospheric argon has been measured to be about 1 Bq/kg (2). It therefore induces a background rate of about 1 kHz in a 1 ton detector. The first milestone in the design of an experiment is therefore the optimization of the light detection from nuclear recoils and and the rejection of the γ and β background. Figure 1.3 shows the two mechanisms leading to the emission of 128 nm light in argon.

The concept of WIMP detection in argon is shown in Fig. 1.4. Primary scintillation light from argon and secondary charge signals are read independently. Following an ionizing event, ionization charges drift towards the top of the detector where they are extracted from the liquid to the gas phase. An electron multiplier system then amplifies the electrons to produce a detectable signal. The ratio of the scintillation to the ionization yields is extremely high for WIMP events, due to quenching. Very high drift fields up to 5 kV/cm must be reached to detect an ionization signal from highly quenched nuclear recoils.

Because background discrimination requires a high ratio of scintillation to ionization yields, the VUV scintillation light needs to be detected efficiently. This is the main task and responsibility of the Zurich group. We are also investigating alternative schemes to photomultipliers, such as wavelength shifters read out by avalanche photodiodes (APD).

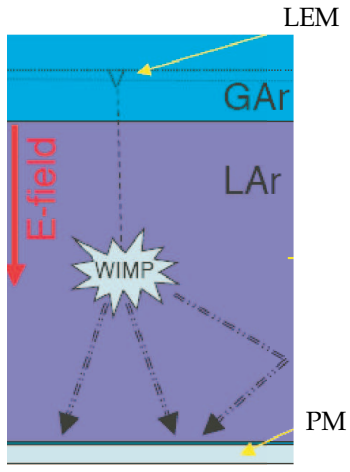

Figure 1.4: Principle of WIMP detection in liquid argon (LAR). WIMPs lead to a high ratio of primary scintillation light detected by the photomultipliers (PM) to charge collected by the electron multiplier (LEM) in gaseous argon (GAR).

1.3 Light collection

Monte Carlo simulations suggest that a light collection efficiency of at least 5% for 128 nm photons will be required to suppress the background from ^{39}Ar β-decay. However, VUV photons are absorbed by most materials, with few exceptions such as MgF_2 and LiF. A large area coverage using phototubes with MgF_2 windows is excluded for cost reasons. Also, the operation of phototubes at cryogenic temperatures requires photocathodes with a metallic underlayer to prevent electrical charge-up.

However, 128 nm light can be reflected or wavelength shifted. We have therefore investigated aluminized mylar foils with MgF_2 coating and Tetratex (porous teflon) foils as specular or diffuse VUV-mirrors (3). The reflecting material is mounted on a rotating frame in the test box immersed in clean gaseous argon at NTP (Fig. 1.5). The gas atoms are excited by α- particles yielding 68 eV/ emitted photon and leading to tracks of typically 5 cm length. An APD is used as the trigger. Direct and reflected photons are measured by another large area APD (15 mm in diameter) with a wide spectral range. The reflection coefficient is derived from the measurement by Monte Carlo simulation of the acceptance, as a function of mirror angle φ. These results are shown in Fig. 1.6, superimposed to measurements from literature. For Al + MgF_2 we obtain a reflectivity of 91.5% and for Tetratex 95%. The high reflectivity of Tetratex is probably due to the fluorescence of teflon in the yellow region.

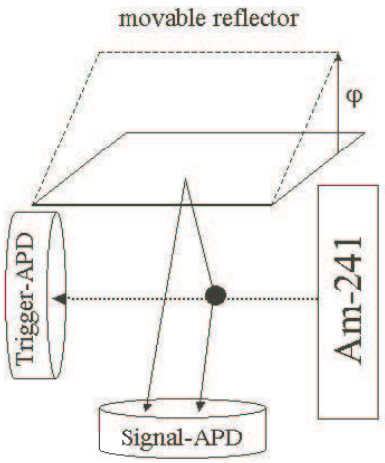

Figure 1.5: Setup used to measure the reflectivity of various coated mirrors.

Large area APDs (from Advanced Photonics) with very thin entrance windows read the 128 nm light. Their quantum efficiency is about 60% at 128 nm (6). However, their small active area require a method for light concentration. We have therefore investigated wavelength shifters bound to light guides with filling materials such as polystyrene (7). Preliminary

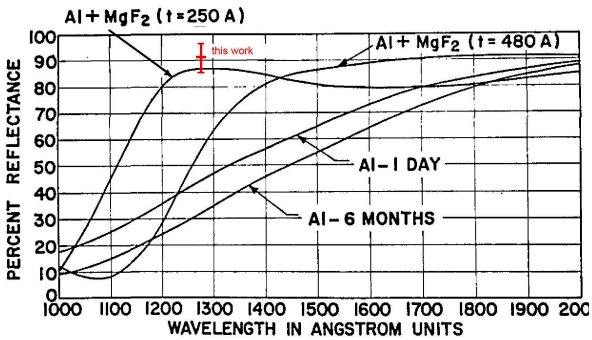

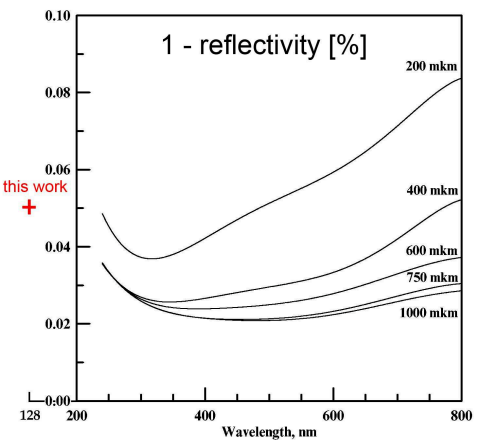

Figure 1.6: Reflectivity of Al + MgF_2 (above, from ref. [4]) and Tetratex (right, from ref. [5]), compared to our own measurements.

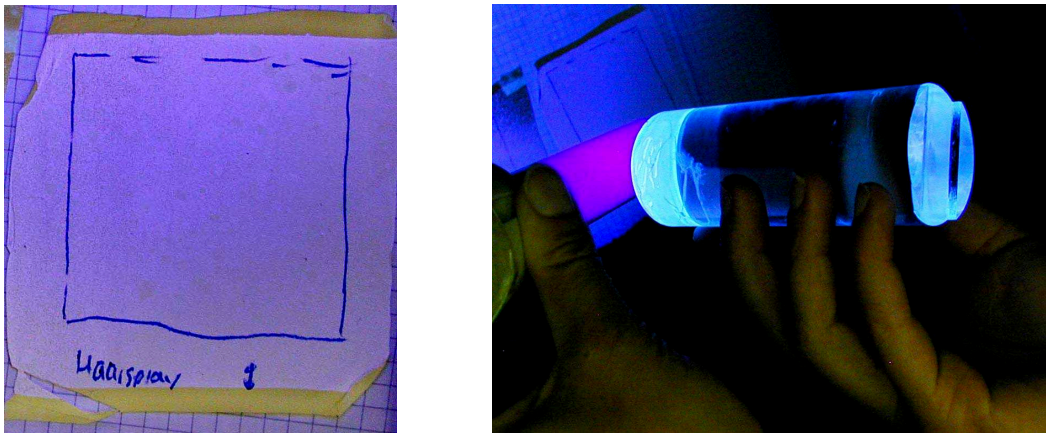

Figure 1.7: Reflection of UV light on teflon coated with TPB (left) and emitted light (right).

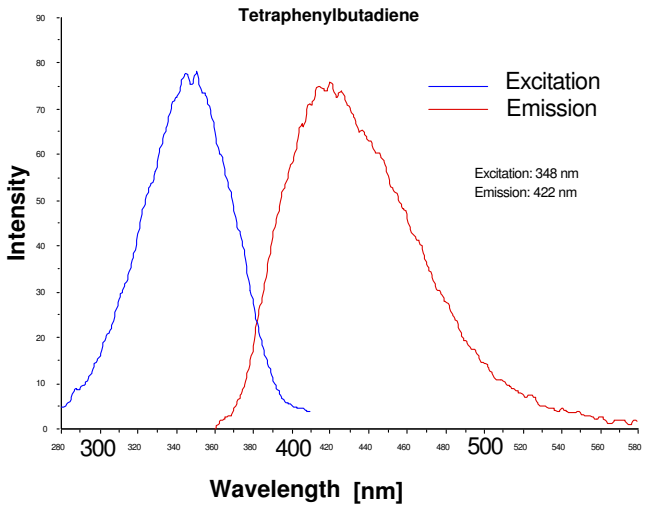

Figure 1.8: Absorption and emission spectra of TPB.

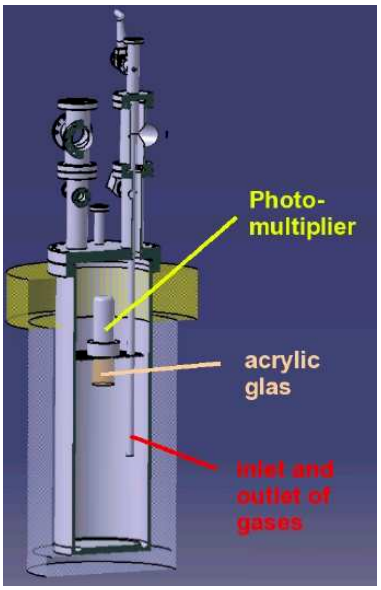

Figure 1.9: Vacuum chamber.

tests with Tetratex foils or acrylic glass coated with wavelength shifters give promising results. Figure 1.7 shows two samples illuminated with 250 nm UV light. The white-bluish centre of the Tetratex sample (left) was coated with tetraphenylbutadiene (TPB) dissolved in chloroform before being sprayed on the teflon tissue. The absorption maximum of TPB is around 340 nm, its emission maximum around 420 nm (Fig. 1.8). The yellow fluorescence of the uncoated teflon can be clearly seen around the borders. Figure 1.7 (right) shows a TPB/polystyrene mixture applied to one end of a plexiglas cylinder, which demonstrates trapping of the emitted light at 420 nm from TPB.

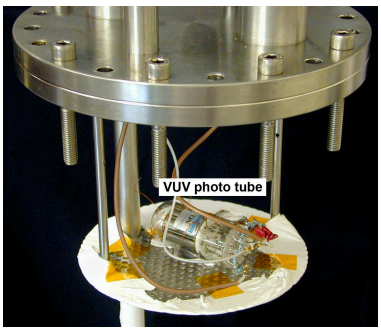

Figure 1.10: Vacuum chamber with VUV tube.

To test functionality and measure light yields, decay times, outgasing and other properties, we have built a 7 ℓ vacuum chamber which can be filled with gaseous or liquid argon (Fig. 1.9). The chamber will also be used to search for the ^{39}Ar signal. A gas purification system filters out residual water or oxygen traces, both being strong UV absorbers. The gas composition is monitored by a quadrupole mass spectrometer with high sensitivity (10^{-10}) connected through a dosing valve. Figure 1.10 shows the top flange holding a small VUV phototube (1 cm^2 Cs-Te photocathode) with MgF_2 window. This device has a narrow spectral response (115-320 nm) and a well known quantum efficency ($\sim$ 25%) and is therefore mainly used for calibration. Figure 1.11 shows a standard bialkali photomultiplier (2", 300-600 nm) mounted on the flange for the first spectroscopical measurements.

Figure 1.12 shows an intensity spectrum from 5.3 MeV α's emitted by a ^{210}Po source in argon gas at NTP. With a total coverage of the inner wall with TPB coated Tetratex we could obtain 885 photoelectrons (p.e.), corresponding to a detection efficiency of roughly 1%, which is already encouraging for a large detector. This setup should be able to detect the ^{39}Ar decays with a mean energy deposit of 218 keV (corresponding to 30 p.e.).

However, as Fig. 1.13 shows, the number of photoelectrons depends crucially on the purity of argon. The data sample at a partial air pressure of 2 $\times$ 10^{-6} mbar was selected to analyze the time evolution of the light output in gaseous argon. The signal amplitude is shown as a function of time in Fig. 1.14. One clearly observes two components which correspond to the decay of the singlet and triplet molecular states. The data were fitted by two exponential functions convoluted with a Gaussian to describe the time resolution. The fast component has a mean life of 15.7 $\pm$ 4.0 ns, the slow component a mean life of 3.12 $\pm$ 0.08 μs. The latter agrees with the published value 3.2 $\pm$ 0.3 μs (9).

Figure 1.11: Bialkali tube with reflector.

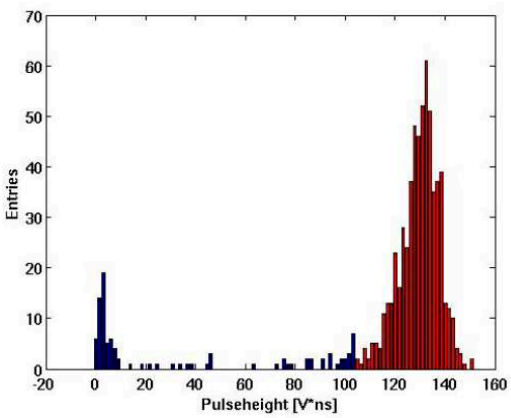

Figure 1.12: Intensity distribution of the 128 nm light measured in gaseous argon.

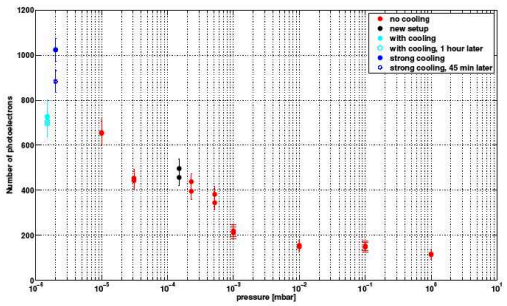

Figure 1.13: Number of photoelectrons as a function of residual partial air pressure measured for different experimental conditions (from ref. [8]).

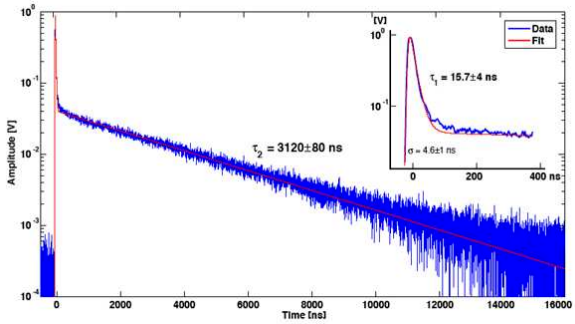

Figure 1.14:
Intensity as a function of time showing the fast and slow components of scintillating argon (from ref. [8]).

These developments will be pursued in 2006 with liquid argon. We will then investigate the performance of APDs using focussing Winston cones. Assuming that enough light can be detected we will then formally propose a dark matter experiment e.g. in the underground Canfranc Laboratory in Spain. We have already expressed our interests to the corresponding Scientific Committee.

[1] ÊP. Cennini *et al.*, Nucl. Instr. Methods in Phys. Research **A 432** (1999) 240.
[2] P. Benetti *et al.* (WARP Collaboration), preprint astro-ph/0603131 (2006).
[3] A. Knecht, Diploma Thesis, ETHZ, 2005.
[4] L. Canfield *et al.*, Applied Optics **5** (1966) 45.
[5] A. Buzykaev *et al.*, Nucl. Instr. Methods in Phys. Research **A 379** (1996) 453.
[6] R. Chandrasekharan, M. Messina, and A. Rubbia, Nucl. Instr. Methods in Phys. Research **A 546** (2005) 426.
[7] G. Eigen, E. Lorenz, Nucl. Instr. Methods **166** (1979) 165.
[8] A. Büchler, Bachelor Thesis, Universität Zürich, 2006.
[9] J.W. Keto *et al.*, Phys. Rev. Lett. **33** (1974) 1365.

2 Ultracold Neutrons

P. Fierlinger, S. Heule, A. Knecht, U. Straumann

in collaboration with: ETHZ; Fraunhofer IWS, Dresden; ILL, Grenoble; Jagellonian University, Cracow; JINR, Dubna; LPC, Caen; LPSC, Grenoble; PSI, Villigen; Université de Fribourg

At the Paul Scherrer Institute (PSI), a new high-intensity source for ultracold neutrons (UCN) is currently under construction, to which we presently contribute. It will provide the opportunity to search for the electric dipole moment of the neutron (nEDM, see (1; 2)) with one to two orders of magnitude better sensitivity. At this level, e.g., supersymmetric theories predict a finite nEDM, and its observation would correspond to the discovery of new physics.

2.1 Wall-loss and depolarization of stored UCN

Ultracold neutrons (3; 4) have a kinetic energy which is below the Fermi potential of some materials (e.g. Beryllium 258 neV) and thus are totally reflected by walls covered with such material. This UCN energy corresponds to a temperature of 3 mK, a velocity of 6.8 m/s and a wavelength of about 50 nm. However, Beryllium is highly toxic, and therefore efforts are made to replace it by a non-hazardous material like diamond-like Carbon (DLC), which belongs to the group of amorphous Carbon materials.

In addition to the Fermi potential, the wall-loss probability per wall collision and the depolarization probability are the important parameters for the performance of a material used for UCN storage. In 2004 in an experiment (5) at Grenoble we trapped polarized neutrons in 'bottles', coated with DLC and Beryllium. The resulting measurements of the two parameters were published in 2005 (6; 7) and showed that DLC foils can be used for UCN storage in a wide range of new experiments, as well as for the UCN source at PSI. In addition the first time loss coefficient and depolarisation were measured simultaneously, thus correlations between these two parameters could be studied more reliably

2.2 Production of Diamond-like carbon coatings

In the past year, we developed and optimized a characterization procedure that allows quality control of self-produced DLC samples (8). The procedure consists mainly of two different methods, Raman spectroscopy and X-ray photoelectron spectroscopy (XPS). With this procedure we could characterize samples that were produced in an existing coating facility at PSI, based on the pulsed Laser deposition (PLD) method. There, pyrolytic graphite is ablated by a pulsed UV-Laser and can form a thin layer of DLC on various kind of substrates as stainless steel, Aluminium, Silicon, etc. The advantage of the PLD method is, that it can be performed under (ultra-)high vacuum conditions. This minimizes the incorporation of other elements, especially strong neutron absorbers and up-scatterers, like Boron or Hydrogen. However, the Fermi potential of these first coatings (Laser wavelengths 266 nm and 248 nm) was slightly below that of Beryllium, but was approximately on the same level as the DLC measured in our experiment (7) mentioned above. Figure 2.1 shows the XPS spectrum of a DLC film deposited at 266 nm on Silicon.

An XPS spectrum of a DLC coating can be deconvolved into two peaks corresponding to

the sp^2 (graphite bonds) and sp^3 (diamond bonds) fraction. With increasing experience in producing DLC films by PLD, we could increase the sp^3 fraction to about 50% and consequently the Fermi potential to about 260 neV.

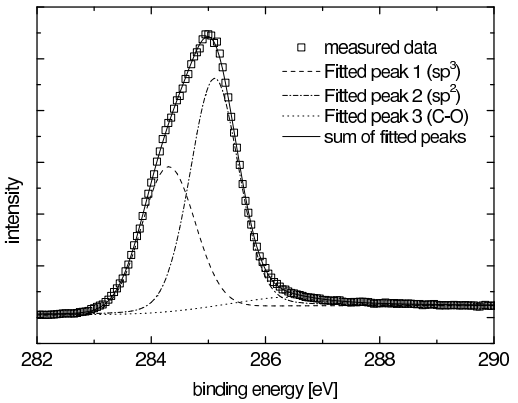

Figure 2.1: XPS spectrum of DLC coating grown on Silicon by PLD with 266 nm wavelength. Measured data (squares) and the corresponding fit (lines) of three peaks are shown.

Finally we began with the construction of a new PLD setup for coating the inside of tubes with an inner diameter of 70-250 mm. Such tubes with a DLC coating can be used as UCN guides. The setup consists of an excimer Laser which is run at 193 nm wavelength and a vacuum chamber, in which the deposition takes place. The laser can reach up to 500 mJ per pulse and can be operated at repetition rates up to 50 Hz. A quartz lens focuses the laser beam onto the graphite target. The power density of the laser beam on the target is in the order of $5 \cdot 10^8$ to $1 \cdot 10^9$ W/cm^2. The substrate tube will be rotated around and translated along the target. The chamber is also equipped with an electrode that allows in-situ glow discharge cleaning of the substrate in order to optimize the adhesion of the DLC film and to minimize impurities in the coating. A more detailed description can be found in (9). In a first stage we will produce small test samples mounted in a few centimeters distance from the target in order to find optimal process parameters. For this purpose we only use the central part of the coating facility, which is a one meter long vacuum tube with 40 cm diameter. In a second step we will extend the vacuum tube to a full length of 2.5 m which gives us enough space for coating tubes with one meter length. First tests have shown that we can reach a pressure of about $2 \cdot 10^{-6}$ Pa without special cleaning and baking out the vacuum tube.
The DLC characterization and the PLD setup for tubes are the thesis subject of Stefan Heule.

[1] P. G. Harris et al., Phys. Rev. Lett. 82 (1999) 904.

[2] C.A. Baker et al., hep-ex/0602020.

[3] R. Golub, D. J. Richardson, S. K. Lamoreaux, Ultra-cold Neutrons, Adam Hilger, Bristol, Philadelphia and New York (1991).

[4] V. K. Ignatovich, The Physics of Ultracold Neutrons, Oxford University Press, USA.

[5] **A novel apparatus for the investigation of material properties for the storage of ultracold neutrons**, T. Brys et al., Nucl. Instr. Meth. A 550 (2005) 637.

[6] **Losses and Depolarization of Stored Ultra-cold Neutrons on Diamond-like Carbon**, P. Fierlinger, Doctoral Thesis, University of Zurich (2005).

[7] **First storage of ultracold neutrons using foils coated with diamond-like carbon**, F. Atchison et al., Phys. Lett. B 625 (2005) 19.

[8] S. Heule et al., submitted to Diamond and Rel. Materials.

[9] **Diamond-like carbon for ultracold neutron applications**, S. Heule et al., Diamond and Rel. Materials, in press.

3 Precision Measurements in Rare Pion Decays

P. Robmann, T. Sakhelashvili, A. van der Schaaf, S. Scheu, U. Straumann and P. Truöl

in collaboration with:
CSRT, Faculty of Physics, Sofia, Bulgaria; Department of Physics, University of Virginia, Charlottesville, USA; Dept. of Physics and Astronomy, Arizona State University, Tempe, USA; Institute for Nuclear Studies, Swierk, Poland; Institute for High Energy Physics, Tbilisi, Georgia; JINR, Dubna, Russia; Paul Scherrer Institut, Villigen, Switzerland and Rudjer Bošković Intitute, Zagreb, Croatia

(PIBETA/PEN Collaboration)

The PIBETA Collaboration performs a research program on rare π and μ decays at PSI. Two decay modes are presently being studied:

- $\pi^+ \to e^+\nu_e\gamma$
  Data taken parasitically with the $\pi^+ \to \pi^0 e^+\nu_e$ experiment showed 20% deviations from the Standard Model prediction in the kinematic region of high E_γ and low E_{e^+}. To clarify the situation a dedicated experiment was performed in the year 2004 and first results became available last year. These new data showed no anomaly and allowed very significant improvements in the determination of the vector and axial-vector form factors F_V and F_A. Using the conserved-vector-current hypothesis (CVC) F_V is connected with the lifetime of neutral pions. The value of F_A is model-dependent.

- $\pi^+ \to e^+\nu_e$
  This decay mode offers the most sensitive test of lepton universality in charged-current interactions. During 2005 extensive beam studies were performed at PSI. A proposal by the PEN Collaboration to measure the branching ratio with a precision of $O(0.1\%)$ was accepted with high priority by the PSI Program Advisory Committee in February 2006.

3.1 The $\pi^+ \to e^+\nu_e\gamma$ decay

The $\pi^+ \to e^+\nu_e\gamma$ decay was recorded during $\pi^+ \to \pi^0 e^+\nu_e$ data taking (1). This was the first time that this decay mode was studied with a setup with almost complete geometric acceptance. Two decades ago we studied this decay (2) and its Dalitz correction $\pi^+ \to e^+\nu_e e^+e^-$ (3) and more recently the corresponding kaon modes $K^+ \to e^+\nu_e e^+e^-$, $K^+ \to \mu^+\nu_\mu e^+e^-$, and $K^+ \to e^+\nu_e \mu^+\mu^-$. These decays proceed via a combination of inner bremsstrahlung (IB) and two structure dependent (SD^+, SD^-) amplitudes. Whereas inner bremsstrahlung bears no information of interest the structure dependent contribution allows a determination of meson form factors which, in turn, are an important input into chiral perturbation theory. Figure 3.1 shows the relative contributions to the distribution of photon and electron energies.

In the first data taken with the PIBETA setup 20% deviations were observed in the kinematic region of high E_γ and low E_{e^+}. This kinematic region could not be studied in earlier measurements because of the high level of accidental coincidences with positrons from $\mu \to e\nu\overline{\nu}$

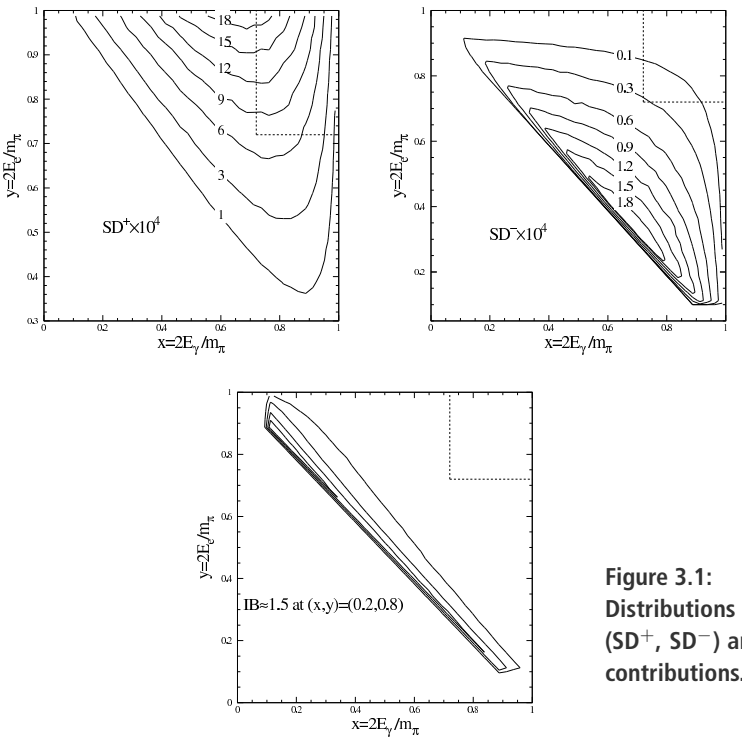

Figure 3.1:
Distributions of the structure dependent (SD^+, SD^-) and inner Bremsstrahlung (IB) contributions.

decay. To clarify the situation a dedicated measurement (4) was performed at reduced beam intensity for which we contributed an improved active target. Thanks to the improved conditions almost background free data could be collected as is demonstrated in Fig. 3.2.

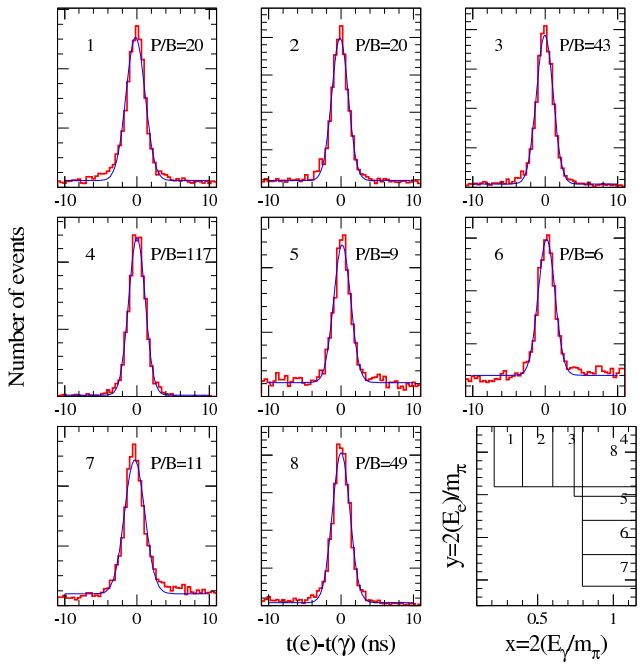

Figure 3.2:
Signal histograms for eight kinematic regions defined in the last panel.

The fit of the form factors to these data resulted in:

$$F_A = 0.0118 \pm 0.0003 \quad (3.1)$$

$$F_V = 0.0262 \pm 0.0015 \quad (3.2)$$

$$a = 0.241 \pm 0.093 \ , \quad (3.3)$$

where a describes the momentum dependence of the form factors which was never determined before. These results were obtained without any constraints or theoretical hypotheses. Earlier measurements usually resulted in a value for F_A/F_V only. This ratio is directly connected to the pion polarizability α_E defined by: $\vec{p} = \alpha_E \times \vec{E}$ ($\vec{p}$ pion electric dipole moment) through:

$$\alpha_E = \frac{2\alpha}{8\pi^3 m_\pi f_\pi^2} \times \frac{F_A}{F_V} = (2.81 \pm 0.07) \times 10^{-4} \text{ fm}^3 \ , \quad (3.4)$$

where the numerical value was determined using our new results.

As mentioned above F_A and F_V also give constraints on terms (l_9 and l_{10}) of the Lagrangian of Chiral Perturbation Theory:

$$l_9 + l_{10} = \frac{1}{32\pi^2}\frac{F_A}{F_V} = (1.42 \pm 0.04) \times 10^{-3} \ . \quad (3.5)$$

[1] **Precise measurement of the pion axial form factor in the $\pi^+ \to e^+\nu\gamma$ decay**, E. Frlež *et al.*, Phys.Rev.Lett.**93** (2004) 181804 [arXiv:hep-ex/0312029].

[2] A. Bay *et al.*, Phys.Lett.B 174, 445 (1986).

[3] S. Egli *et al.*, Phys.Lett.B 222, 533 (1989).

[4] **Study of the $\pi^+ \to e^+\nu\gamma$ anomaly**, PSI Proposal R-04-01.1, E. Frlež and D. Počanić spokesmen, January 2004.

3.2 A precision determination of the $\pi^+ \to e^+\nu$ branching ratio

As was discussed in last year's annual report the $\pi^+ \to e^+\nu$ / $\pi^+ \to \mu^+\nu$ branching ratio is the best test of μe universality, *i.e.* the equality of the couplings of $\mu\nu_\mu$ and $e\nu_e$ to the W boson. Two experiments (1; 2) contribute to the present world average (3) for the measured value:

$$R_{e/\mu}^{\text{exp}} = 1.230(4) \times 10^{-4} \quad (3.6)$$

During the years 1999/2001 the PIBETA experiment recorded a huge sample of $\pi^+ \to e^+\nu$ decays. Although the measurements were not optimized for this decay mode a clear $\pi^+ \to e^+\nu$ signal was observed with a total systematic error below $\approx 1\%$, i.e. within a factor 2-3 of the dedicated experiments. The main contribution to this uncertainty is in the determination of the number of stopped pions. The statistical uncertainty associated with the number of observed $\pi^+ \to e^+\nu$ events is totally negligible in this data set.

In February 2006 a proposal by the now-called PEN Collaboration (4) was accepted with high priority at PSI. It is planned to take first test data with the new setup in the year 2006 which will be followed by two years of real data taking. Our group took over the responsibility to develop an ultra-fast beam monitoring system based on 0.6 ns scintillator and microchannel photomultipliers. Waveform digitizers with ≈ 5 GHz sampling rates would be used with the aim of reaching a double pulse resolution $O(1\text{ ns})$ in the target detector. During a test period

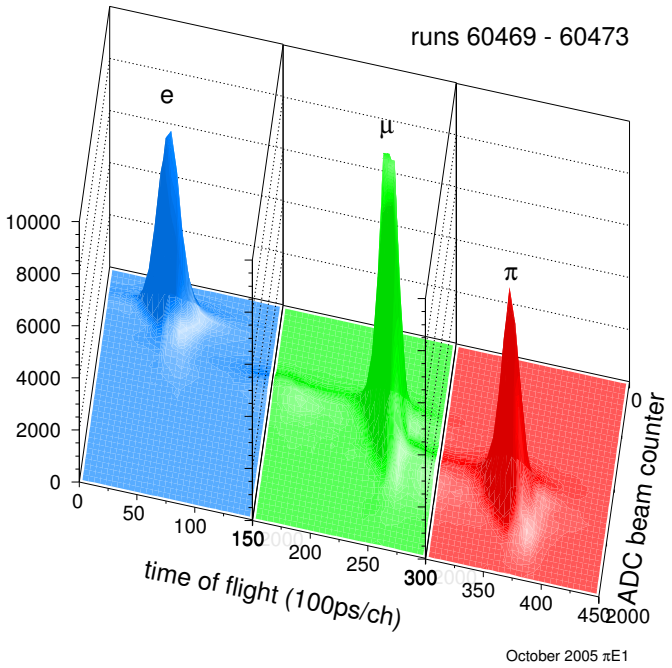

Figure 3.3: Distribution of flight time along the last ≈4 m of the πE1 beamline and energy loss in a moderator counter. Results from our 2005 tests at PSI. Pions, muons and electrons are clearly separated. This information will be crucial in estimating the contribution from pion decay in flight in the final data. The time of flight will also allow a precise determination of the pion momentum.

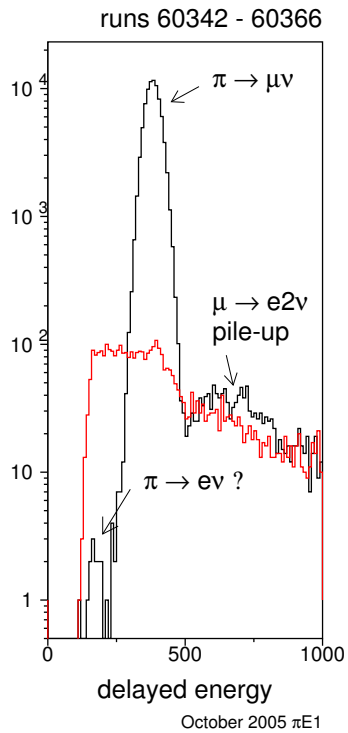

Figure 3.4: Secondary (black) and tertiary (red) target signals. The secondary signals are totally dominated by muons from pion decay at rest. The very low background left of the peak is close to the level expected from $\pi \to e\nu$.

of several weeks at PSI we learned, however, that these novel photo-detectors are very fast indeed but show a strong ringing after the signal. For this reason it was decided to use very fast (0.7 ns risetime) standard photomultipliers instead. During the tests at PSI we also tried to tune the beam to the lowest possible momentum (≈ 70 MeV/c as compared to ≈ 120 MeV/c for PIBETA running). At these lower momenta the range straggling is much reduced leading to a better definition of the pion stop distribution. At the other hand, because of the 26 ns pion lifetime the pion rate at the exit of the πE1 channel drops quickly towards lower momenta where the beam contains orders of magnitude more electrons and muons. This problem could be solved by inserting a thin degrader halfway the channel. After the degrader pions have lower momenta than the other particles which can be exploited to suppress electrons and muons. As can be seen from Fig. 3.3 the selected beam contains similar amounts of π, μ and e which can be easily distinguished on the basis of their velocity and dE/dx.

The $\pi \to e\nu$ decays are distinguished from $\pi \to \mu\nu$ decays followed by $\mu \to e\nu\overline{\nu}$ on the basis of the different positron energy distributions and the different decay time distributions. A major source of systematic errors is the uncertainty in the low-energy tail of the $\pi \to e\nu$ decay caused by shower leakage in the electromagnetic calorimeter and nuclear interactions producing neutrons. It is thus important to be able to measure a $\pi \to e\nu$ spectrum with as little $\pi \to \mu\nu$ contamination as possible. For this reason we checked during the tests at πE1 the

ability to distinguish $\pi \to e$ events from $\pi \to \mu \to e$ events on the basis of target signals alone. Here one exploits the fact that muons from pion decay at rest are mon-energetic, have a range of only 2 mm and deposit their full kinetic energy in the target. As is demonstrated in Fig.3.4 it is possible to distinguish the two components in the amplitude distribution for secondary particles observed in the target shortly after a pion stop.

[1] G. Czapek *et al.*, Phys.Rev.Lett.70, 17 (1993).

[2] D.I. Britton *et al.*, Phys.Rev.Lett.68 (1992) 3000, D.I. Britton *et al.*, Phys.Rev.D 49, 28 (1994).

[3] S. Eidelman *et al.*, (Particle Data Group), Phys.Lett.B 592, 1 (2004).

[4] **Precise Measurement of the $\pi^+ \to e^+\nu$ Branching ratio**,
D. Pocanic and A. van der Schaaf spokesmen, PSI Proposal R-05-01.1.

4 Search for $K\pi$-Atoms

Y. Allkofer, C. Amsler, S. Horikawa, I. Johnson[3], H. Pruys[4], C. Regenfus, and J. Rochet

In collaboration with:
Academy of Sciences of the Czech Republic, CERN, KEK (Tsukuba), Institute of Atomic Physics (Bucarest), JINR (Dubna), Laboratory Nazionali di Frascati, IHEP (Protvino), University of Basel, Bern, Ioannina, Kyoto, Lomonosov, Prague, Santiago, Trieste, Tokyo (Metropolitan) (DIRAC II Collaboration)

4.1 The $K\pi$ scattering length

The $K^-\pi^+$-atom is a hydrogen-like non-relativistic system of a K^- and a π^+ bound by the Coulomb force. Such atoms have not been observed so far, in contrast to $\pi^+\pi^-$ atoms which were observed and studied by the DIRAC Collaboration at CERN (1). For $K\pi$-atoms the binding energy of the 1s level is 2.9 keV and the Bohr radius 250 fm. The atom is unstable and decays into $\bar{K}^0\pi^0$ (Fig. 4.1). The atomic level is shifted by the overlap of the pion and kaon wave functions. The energy shift, determined by the scattering lengths a_1 and a_3 in the isospin 1/2 and 3/2 $K\pi$ states, respectively, is predicted to be about - 10 eV (i.e. towards stronger binding) (2). Up to a calculable small correction (2) the width Γ (or the lifetime τ) of the 1s level is related to the scattering lengths by the equation

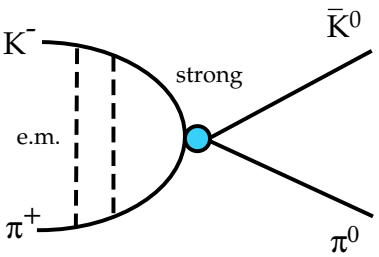

Figure 4.1:
$K^-\pi^+$ **- atoms decay into** $\bar{K}^0\pi^0$.

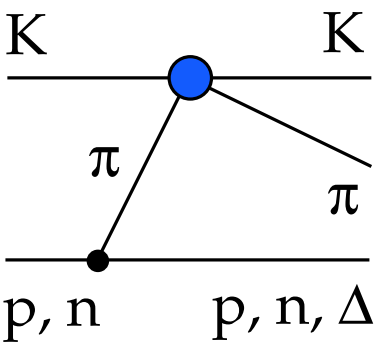

Figure 4.2: $K\pi$**-scattering in** Kp **- interactions.**

$$\Gamma = \frac{1}{\tau} = 8p^*\mu^2\alpha^3\left[\frac{a_1 - a_3}{3}\right]^2, \qquad (4.7)$$

where p^* = 11.5 MeV/c is the π^0 (or K^0) momentum in the rest frame of the atom, μ is the $K\pi$ reduced mass, and α the fine-structure constant.
Predictions for τ can, in principle, be derived from the $K\pi$ S - wave phase shifts obtained from $K\pi$ - scattering, e.g. by scattering kaons on nucleons (Fig. 4.2). We recall that the scattering lengths a_1 and a_3 are the *slopes* of the phase shifts $\delta_1(k)$ and $\delta_3(k)$ in the limit where the momentum k becomes vanishingly small. The scattering lengths a_1 and a_3 are poorly known. Figure 4.3 shows the S - wave $K\pi$ phase shifts from ref. (3). The δ_1 ($S_{1/2}$) - phase is poorly known below 1 GeV, showing a peculiar oscillation pattern. Above 1 GeV the S - wave interaction is dominated by the $K_0^*(1430)$ resonance. Figure 4.3 also shows the $P_{1/2}$ phase which is dominated by the $K^*(892)$ resonance. The interaction is attractive in the i = 1/2 and repulsive in the i = 3/2 state. The uncertainties in a_1 and a_3 are substantial: the extrapolation to zero energy from the various phase shift measurements disagree

[3] until October 2005
[4] until August 2005

by large factors: measurements of a_1 vary between 0.17 and 0.34 m_π^{-1}, those of a_3 between - 0.07 and - 0.14 m_π^{-1}. The scattering lengths were also computed from dispersion relations using scattering data, assuming analytical continuation, unitarity and crossing symmetry (4):

$$a_1 = 0.224 \pm 0.022\ \mathrm{m}_\pi^{-1} \text{ and}$$
$$a_3 = -0.0448 \pm 0.0077\ \mathrm{m}_\pi^{-1}. \quad (4.8)$$

However, there are inconsistencies below 1 GeV/c (4). Using eqs. (4.7) and (4.8) one finds a mean life $\tau \sim 3.7$ fs for the $K\pi$ atom, with a rather large uncertainty.
The scattering lengths are of great importance for chiral perturbation theories (ChPT). The mean life of $\pi^+\pi^-$-atoms, recently measured by the DIRAC Collaboration (1), is in excellent agreement with predictions from ChPT (5) and with direct measurements of the scattering length from the $K \to \pi^+\pi^- e\nu$ decay (6). In contrast, the $K\pi$ - scattering length probes ChPT extended to s-quarks, i.e. in the limit where the masses of the u-, d- and s-quarks vanish. Figure 4.4 shows the prediction for a_3 vs. a_1 from ChPT predictions (7), together with the dispersion calculation from ref. (4). They are not in good agreement and there is a strong correlation between a_3 and a_1. The blue band shows the sensitivity of a hypothetical 20% accurate measurement of the lifetime of $K\pi$-atoms. A 20% measurement error in the lifetime leads to a 10% error in $|a_1 - a_3|$.

A measurement of the scattering length also yields information on nearby broad resonances. As mentioned above, S - wave $K\pi$ scattering is dominated by the $K_0^*(1430)$ resonance. However, there is mounting evidence for a very broad resonance around 800 MeV, the $K_0^*(800)$ (or κ). For example, recent data in $J/\psi \to K^+K^-\pi^+\pi^-$ report the κ at a mass of $\sim$ 800 MeV with a width of $\sim$ 600 MeV (8). Establishing the κ is essential to understand the nature of scalar mesons. The ground state nonet could be made of the four-quark states and/or meson-meson resonances $a_0(980)$, $f_0(980)$, $f_0(600)$ (σ) and $K_0^*(800)$ (κ) (9). If the latter indeed exists as a very broad state, it will influence the value of a_1.

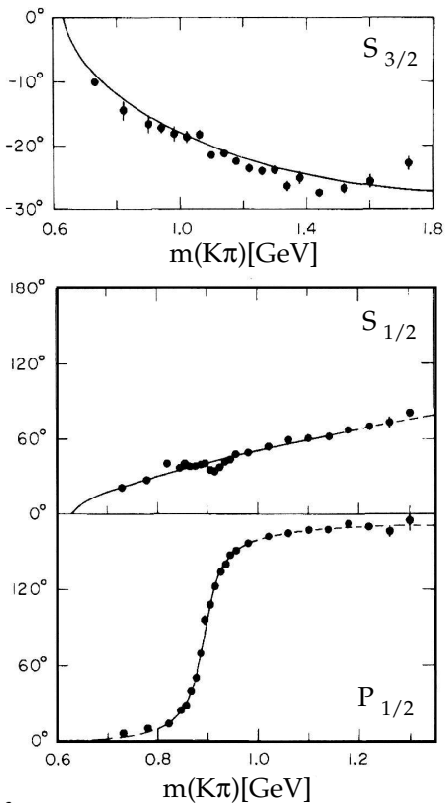

Figure 4.3: $K\pi$ phase shifts from ref. [3] showing the δ_3 ($S_{3/2}$), the δ_1 ($S_{1/2}$), and the $P_{1/2}$ phases as a function of $K\pi$ mass.

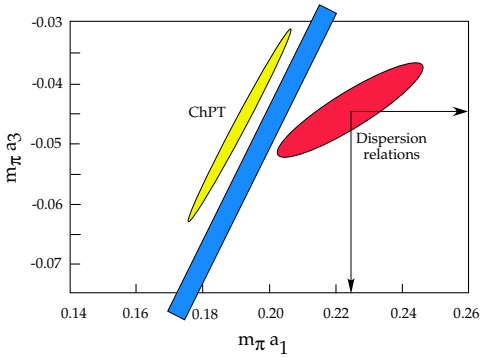

Figure 4.4: a_3 vs. a_1 from ChPT [7] and from dispersion relations [4]. The most recent measurements ($m_\pi a_1$ = 0.335 $\pm$ 0.006, $m_\pi a_3$ = - 0.14 $\pm$ 0.007, see ref. [3]) lie outside the range of this plot. The blue band shows the sensitivity of a 20% measurement of the mean life of $K\pi$-atoms.

4.2 The DIRAC II experiment

The Zurich group has joined the DIRAC experiment and will concentrate on the search and study of $K\pi$ - atoms. We will provide the aerogel Čerenkov counters for kaon detection and also the heavy gas system for the pion Čerenkov counters.

In the DIRAC apparatus kaons and pions are produced by the primary 24 GeV/c proton beam from the PS impinging on a 100 μm thick nickel foil (10). The emerging particles are analyzed in a double-arm magnetic spectrometer measuring the momentum vectors of two oppositely charged hadrons (Fig. 4.5). $K^-\pi^+$ - atoms, once produced, move forward and either annihilate into $\bar{K}^0\pi^0$ or ionize in the target. Since annihilation and ionization are competing processes, the mean life is obtained by measuring the breakup probability in the target, which can be calculated as a function of mean life. It is about 30 % in a 100 μm Ni target, assuming a mean life of 4.7 fs (11).

The breakup probability is given by the ratio of the number of dissociated pairs to the number of produced atoms. The dissociated kaon and pion emerge behind the target with a very small relative momentum $Q < 3$ MeV/c. One therefore expects an accumulation of events near $Q = 0$ which gives the number of dissociated pairs. Then one calculates the number of produced $K\pi$-atoms by measuring the number of unbound Coulomb pairs from the measured Q-distribution at large Q. The number of produced $K\pi$-atoms is obtained through a known relation between unbound and bound Coulomb pairs. This procedure has been applied to $\pi^+\pi^-$ atoms and details can be found in ref. (1).

The DIRAC apparatus (Fig. 4.5) has to be modified to discriminate between pions and kaons. Muons are identified by counters behind the concrete absorber. Electrons trigger the N_2 gas

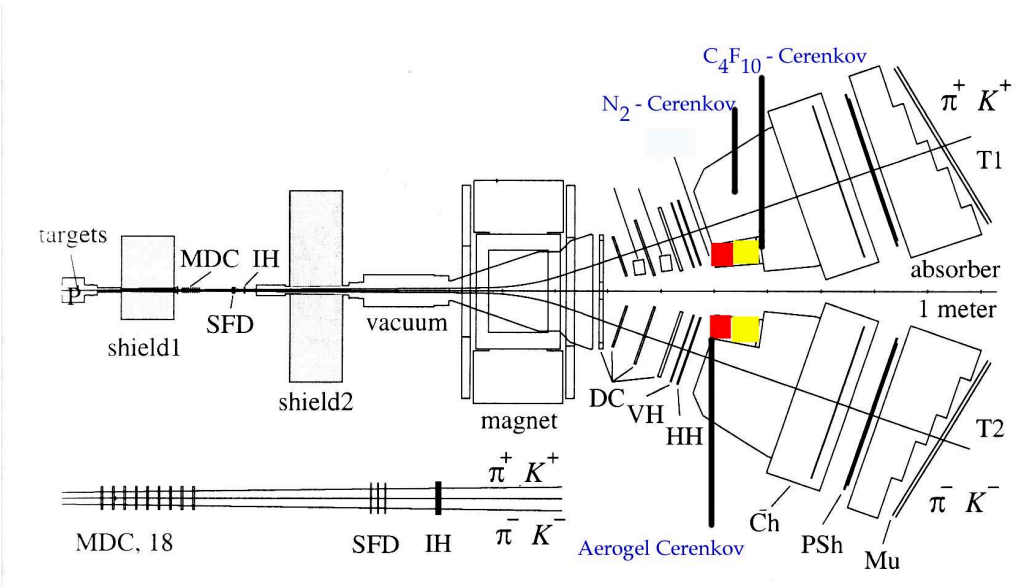

Figure 4.5: Sketch of the updated DIRAC spectrometer, showing the locations of the Čerenkov counters to identify electrons, pions and kaons. MDC = microdrift chambers, SFD = scintillating fibre detector, IH = ionization hodoscope, DC = drift chambers, VH, HH = scintillation hodoscopes, PSh = preshower, Mu = muon counters.

Čerenkov counter. The new C_4F_{10} gas Čerenkov counter identifies pions, while kaons are detected in the aerogel Čerenkov. Contaminating protons in the left arm are suppressed since they are below threshold for Čerenkov radiation. The right arm aerogel (for $K^-\pi^+$ -atoms) is not essential since the flux of antiprotons is much smaller than the flux of negative kaons.

4.3 The aerogel counters

Figure 4.6 shows the momentum distribution of kaons from $K\pi$-atoms at the entrance of the Čerenkov counters as a function of horizontal coordinate (in the plane of Fig. 4.5). This distribution was calculated using the known production cross sections at 24 GeV/c. Kaons from $K\pi$-atoms have momenta between 3.9 and 8.9 GeV/c. Figure 4.7 shows the vertical distribution which is not flat due to the slight upwards inclination of the spectrometers. For the emission of Čerenkov radiation the refractive index n has to be chosen so that $n > 1/\beta$ (where β is the velocity of the particle). Hence the quantity $n-1$ has to be small enough to avoid signals from fast protons ($\beta \simeq 1$), yet large enough to detect kaons. In the momentum range covered by the apparatus, n is required to be typically 1.010, which is larger than can be achieved with pressurized gas counters and smaller than for all known solid or liquid radiators, except aerogel. One concludes from Fig. 4.6 and 4.6 that the aerogel counter has to cover a surface of about 35 x 40 cm^2.

Aerogel is made of colloidal SiO_2 grains of size $\sim$ 2 nm and pores $\sim$ 50 nm. The index of refraction depends on density ρ ($n = 1 + 0.21\rho$ [g/cm^3]). For example, for the $n = 1.008$ aerogel needed here, the density is 0.039 g/cm^3. The light yield is proportional to the factor

$$f = 1 - \frac{1}{\beta^2 n^2} \qquad (4.9)$$

which decreases quickly when $n \simeq 1$. This fact is the main difficulty with thin Čerenkov counters. As we show below in Fig. 4.9, a good $K-p$ separation can be achieved with two indices of refraction, n = 1.008 and 1.015. The lowest index is needed to improve the separation in the region of high energy protons close to the primary beam line.

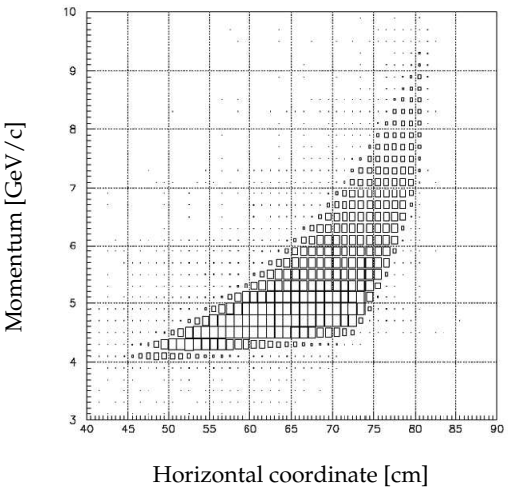

Figure 4.6: Momentum distribution of kaons from the breakup of $K\pi$-atoms. Small angles with respect to the primary proton beam are towards the right.

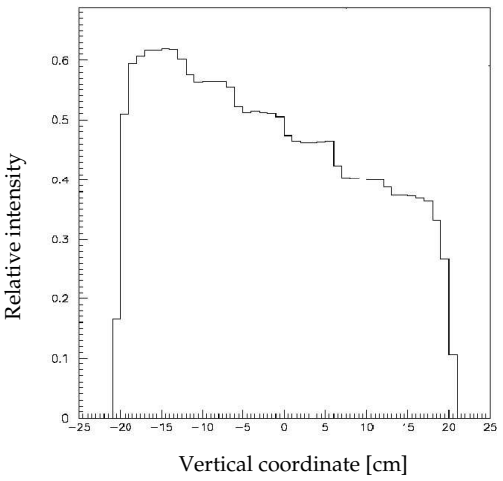

Figure 4.7: Vertical distribution.

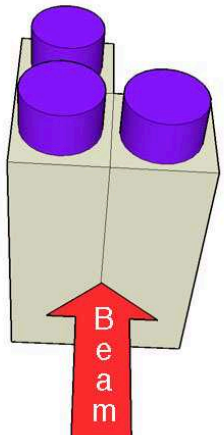

Figure 4.8: Three aerogel counters are needed to separate protons from kaons. The upstream pair has n = 1.015, the downstream counter n = 1.008. Small angles with respect to the primary proton beam are towards the left.

The 1.015 counter is segmented into two parts to reduce pileup. Figure 4.8 shows the conceptual design. Each counter is vertical (40 cm long) viewed by two photomultipliers, one at each end.

We have initiated an R&D program to measure the light yield of aerogel and to optimize the geometry. Most of the measurements were made with n = 1.05 aerogel which is easily available. We have measured the number of photoelectrons $N_{p.e.}$ for a thickness of 10 cm of aerogel and for a 10 cm long slab viewed by two photomultipliers (PM) with UV windows. The measurements were made with cosmic ray muons which have an average momentum of 700 MeV/c ($\bar{\beta}$ = 0.989) since test beams were not available at CERN in 2005. We have obtained about 3 photoelectrons / cm of aerogel (summing the signals from both tubes). Extrapolation from n = 1.05 to lower indices and β = 1 can then easily be made using eq. (4.9).

However, the absorption length increases rapidly from about 10 cm at 270 nm to 3 m at 350 nm (12). Therefore, 40 cm long aerogel counters are likely to be problematic. Figure 4.9 shows the expected average number of photoelectrons as a function of momentum for kaons and protons. The upper boundaries of the bands are for particles traversing the counter close to one of the PM, the lower boundary for those crossing the counter in the middle. The strong absorption can be compensated by increasing the thickness of aerogel in the middle of the counter (see Fig. 4.16 below), which is easily feasible since aerogel is delivered in 1cm thick tiles. Figure 4.10 shows a simulation of the signal attenuation.

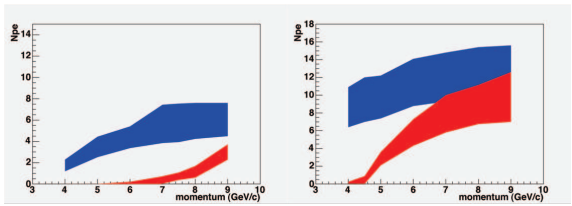

Figure 4.9: Average number of photoelectrons as a function of momentum for n = 1.008 (left) and 1.016 (right) for a thickness of 15 cm and a length of 40 cm.

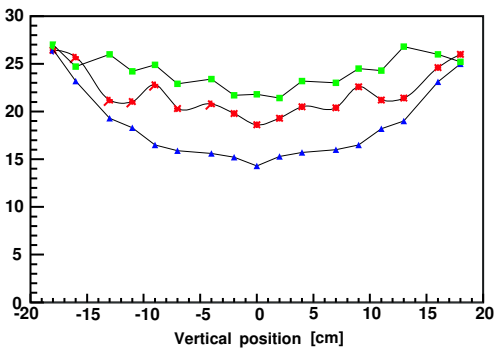

Figure 4.10: Signal amplitude as a function of the distance at which the particle crosses the aerogel counter (arbitrary scale). The photomultipliers are located at the edges ($\pm$ 20 cm). The blue (bottom) curve is for a counter with constant thickness, the red (middle) curve for 4 additional tiles and the green (top) curve for 6 additional tiles in the middle of the counter.

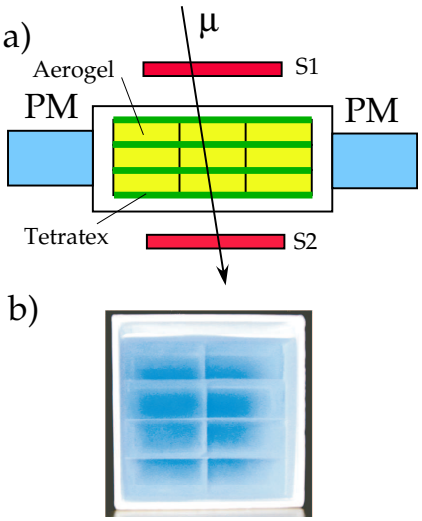

Figure 4.11: a) setup for light yield measurements,
b) photograph of the aerogel tiles.

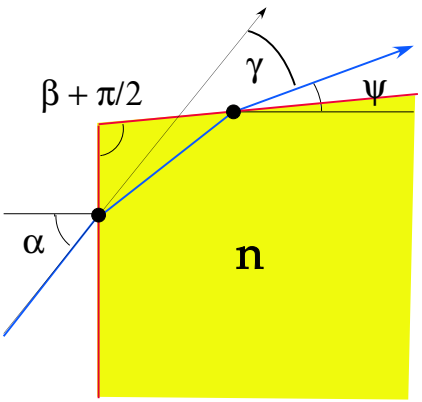

Figure 4.12: Principle of setup to measure the refractive index.

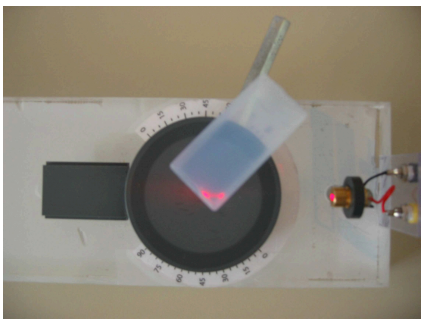

Figure 4.13:Photograph of the setup.

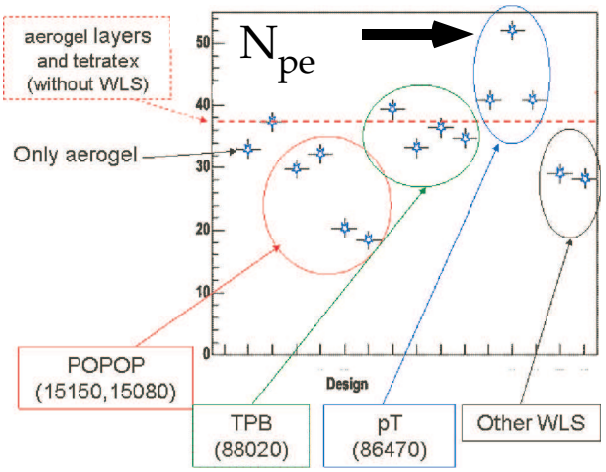

Figure 4.14:
Number of photoelectrons for a 10 cm thick, 10 cm long, n=1.05 aerogel counter, using cosmic muons, and for different geometries and WLS. The arrow shows the optimum design with p-terphenyl dissolved in chloroform.

We also tried a novel setup using wavelength shifters (WLS). Figure 4.11 shows the arrangement in our lab. The 2.5 cm thick aerogel tiles were sandwiched between reflective Tetratex foils which were sprayed with WLS. For example, p-terphenyl dissolved in chloroform shifts light from 270 to 340 nm, which reduces absorption and leads to some 5.5 p.e. /cm or 7 p.e. /cm for $\beta = 1$ (Fig. 4.14). Using this last figure one then expects about 3 (12) photoelectrons at 4.5 (8) GeV/c for 15 cm of 1.008 aerogel. These results are quite encouraging when compared to Fig. 4.9a, but they need to be checked with a prototype of the final length and depth.
We have also built a simple apparatus to measure the refractive index of aerogel using the refraction of a laser beam, following ref. (12). Figures 4.12 and 4.13 show a tile of aerogel illuminated by a laser beam incident under the angle α. One measures the displacement of the beam spot on a distant screen, i.e. the deflection γ of the beam which exits the aerogel:

$$\gamma = \alpha - \beta + \frac{\pi}{2} + \mathrm{asin}[\sin\alpha \sin\beta + n\sqrt{1 - \frac{\sin^2\alpha}{n^2}}\cos\beta]. \quad (4.10)$$

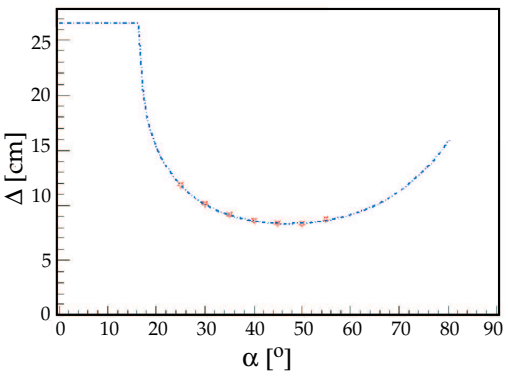

Figure 4.15:
Measurement of laser spot displacement as a function of incident angle, with fit following eq. (4.10).

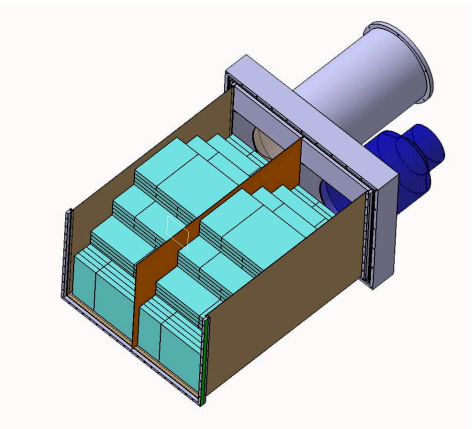

Figure 4.16:
Exploded view of the n = 1.015 aerogel counter showing the pyramidal design.

With at least two incident angles α one can eliminate β (expected to be around 0^0). Figure 4.15 shows the measurements for a piece of n = 1.05 aerogel, together with the fit leading to $n = 1.055 \pm$ 0.002.

Figure 4.16 shows the design of the n = 1.015 aerogel detector built in the workshop of the Physik - Institut. The 5" Photonis - Philips XP4570/B photomultipliers with UV windows will be used. The 14 ℓ of n = 1.008 aerogel has been produced by the Budker and Boreskov Institutes in Novosibirsk, the 24 ℓ of n = 1.015 by Panasonic. The construction and tests are being performed in early 2006 and the detectors will be installed in the summer of 2006, when DIRAC resumes data taking. DIRAC (PS212) has been approved by the CERN Research Board to run at least until 2008. Extrapolating from $\pi\pi$ data, we estimate that some 1000 $K\pi$-atoms should be observed by DIRAC during 2006 - 2008.

[1] B. Adeva *et al.* (DIRAC Collaboration), Phys. Lett. **B 619** (2005) 50.
[2] J. Schweizer, Eur. Phys. J **C 36** (2004) 483; Phys. Lett. **B 587** (2004) 33.
[3] P. Estabrooks *et al.*, Nucl. Phys. **B 133** (1978) 490.
[4] P. Büttiker, S. Descotes-Genon, B. Moussallam, Eur. Phys. J. **C 33** (2004) 409.
[5] G. Colangelo, J. Gasser and H. Leutwyler, Nucl. Phys. **B 603** (2001) 125 and references therein.
[6] S. Pislak *et al.*, Phys. Rev. **D 67** (2003) 072004.
[7] V. Bernard *et al.*, Nucl. Phys. **B 357** (1991) 129.
[8] M. Ablikim et *et al.* (BES Collaboration), Phys. Lett. **B 633** (2006) 681.
[9] For a review see C. Amsler and N. Törnqvist, Phys. Rep. **389** (2004) 61.
[10] B. Adeva *et al.*, Nucl. Instr. and Meth. in Phys. Research **A 515** (2003) 467.
[11] B. Adeva *et al.*, Add. to DIRAC proposal, CERN - SPSC - 2004 - 009.
[12] A. R. Buziatev *et al.*, Nucl. Instr. Meth. in Phys. Research **A 433** (1999) 396.

5 Particle Physics at DESY/HERA (H1)

J. Becker (until April 2005), L. Lindfeld, Katharina Müller, K. Nowak (since November 2005), P. Robmann, S. Schmitt (until May 2005), C. Schmitz, U. Straumann, P. Truöl, and Stefania Xella Hansen

in collaboration with:
N. Berger, M. Del Degan, C. Grab, G. Leibenguth, B. List, M. Sauter, A. Schöning, R. Weber and T. Zimmermann, Institut für Teilchenphysik der ETH, Zürich; S. Egli, R. Eichler, M. Hildebrandt, and R. Horisberger, Paul–Scherrer–Institut, Villigen, and 34 institutes outside Switzerland

(H1 - Collaboration)

5.1 Electron-proton collisions at a centre of mass energy of 320 GeV - summary

Between April 2003 and April 2006 the H1-collaboration has collected 260 pb^{-1} of data from collisions of 27.4 GeV electrons (192 pb^{-1}) and positrons (68 pb^{-1}) with 920 GeV protons with its detector at the HERA storage ring at DESY. Apart from the increased luminosity this post-upgrade HERA-II phase differs from the HERA-I phase (1993-2000) through the availability of both left- and right-handed longitudinally polarized electron and positron beams with polarisations of up to 40%. With this integrated luminosity we have now more than doubled the useful data from the HERA-I phase. That this still falls short of what is needed for searches aiming at beyond the Standard Model physics may be illustrated with the results of a multilepton analysis. Using all available data accumulated between 1994 and 2005 (275 pb^{-1}) multilepton (electron or muon) events at high transverse momenta were analysed. The yields of dilepton and trilepton events were found to be in generally good agreement with Standard Model (SM) predictions. Combining all channels, four events are observed with a scalar sum of lepton transverse momenta (ΣP_t) greater than 100 GeV/c, compared to a SM expectation of 1.1 ± 0.2. These four events are observed in e^+p collisions only where the SM expectation is of 0.6 ± 0.1 and only one of them in the $e\mu$ channel is from the HERA-II data (157 pb^{-1} in this analysis).

However for the vigorous program of both the H1- and the ZEUS-Collaboration dedicated to the exploration of proton structure and tests of quantum chromodynamics (QCD) predictions a wealth of data is available, is being analysed and leads to a continuous flow of publications. This program entails the precise determination of the neutral and charged electroweak current cross sections at high momentum transfer leading to parton density functions in pre-HERA inaccessible domains of Bjorken x and momentum transfer Q^2, diffractively produced final states, hidden and open charm and beauty production as well as the already mentioned searches for states outside the Standard Model.

5.2 Inner multiwire chamber and vertex trigger

The new five-layer inner multiwire proportional chamber with finer granularity and increased redundancy, equipped with new electronics and a new optical readout delivering signals for an improved z-vertex trigger, which was built by the Zurich group for the upgraded H1-detector, requires only maintenance now. It is an essential ingredient of most H1 trigger combinations, and hence its performance needs to be carefully and continuously moni-

tored by our group members. In November 2005 the opportunity of a HERA maintenance shutdown was used to access the chamber and replace a few broken electronics items, like power supply regulators and optical transmission units.

5.3 Analysis activities

The focus of the Zurich group has now shifted to data analysis. Our contributions deal with excited fermions, where a thesis of a Zürich graduate student has been concluded (1). A τ-lepton analysis has been finished and submitted to a journal (2) (see section 5.3.2 below). Search for lepton flavor violation and photons within jets are studied within the framework of two ongoing Zürich thesis projects. They are nearing conclusion and discussed in Sec. 5.3.3 and 5.3.4 below.

The analysis of HERA-I data in the H1 collaboration lead to 17 publications (2)-(18), of which five are still being reviewed or are in print. Additional, however preliminary results have been communicated to the summer 2005 high-energy physics conferences (19)-(31). These analyses deal in the worst case with about 15 pb^{-1} of data (6; 14) and in the best case with about 120 pb^{-1} of data (2; 10; 11; 18). The first publication from HERA-II running with polarized positrons has appeared in print (32) (27 pb^{-1} righthanded, 21 pb^{-1} lefthanded). An update of the high Q^2 charged and neutral current data taken with polarized electron and proton beams between 2003 and 2006 is given below in Sec. 5.3.1.

A large fraction of these publications deals with searches for states and interactions outside the Standard Model, either of general type (27; 28), or dedicated to specific objects such as excited fermions (1), gravitinos (4), magnetic monopoles (5), leptoquarks (10; 33; 34) and a doubly charged Higgs boson (18). The other two areas, where our group has been active in the past, charm and beauty production (3; 7; 8; 12; 15; 23; 24; 25; 26; 29) benefit strongly from the precise tracking information available from the silicon vertex detector, which was built almost exclusively by the Swiss groups within the H1-collaboration. The studies of the diffractive component of deep inelastic scattering have yielded only to two new results, an analysis of elastic $J\Psi$- and of high transverse momenta ρ-production (15; 17).

5.3.1 New results from measurements with polarized beams

Data taken with electrons and positrons of different longitudinal polarisation states in collision with unpolarised protons at HERA are used to measure the cross sections of the neutral and charged current processes, $e^{\pm}p \to e^{\pm}X$ and $e^{\pm}p \to \nu X$, respectively. The polarisation asymmetry is measured as a function of the four-momentum transfer Q^2, and compared with the Standard Model prediction. An improved determination of structure function xF_3 is obtained using the new neutral current data in combination with previously published unpolarised data from HERA-I. The HERA-II charged current total cross section analysis so far has been restricted to the kinematical domain $Q^2 > 400$ GeV^2 and inelasticity $y < 0.9$. Together with the corresponding cross section obtained from the previously published unpolarised data, the polarisation dependence of the charged current cross section is measured and found to be in agreement with the Standard Model prediction.

Figure 5.1 shows a distribution of the integrated luminosity versus the longitudinal beam polarisation for both directions of the handedness. Considerable variations of the degree of polarisation measured by the polarimeters between 20% and 40% have to be tolerated.

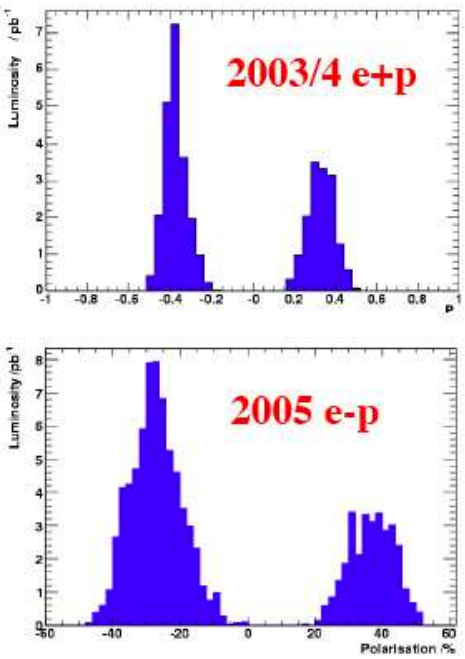

Figure 5.1: Distribution of the integrated luminosity versus polarisation during the two HERA-II running periods with electrons and electrons.

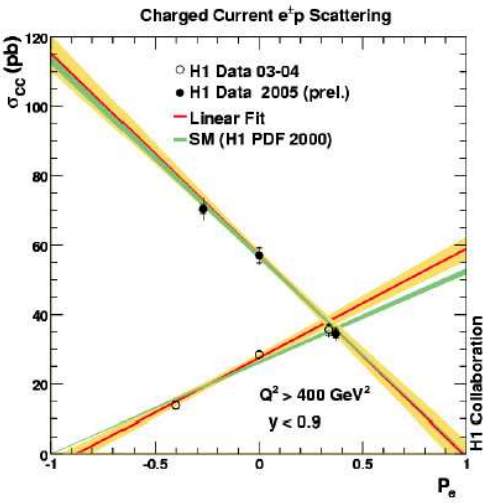

Figure 5.2: Charged current cross section versus polarisation. HERA-II positron (2003/4) and electron data (2005) for $Q^2 > 400$ GeV^2 and inelasticity $y < 0.9$ are combined with unpolarised lepton data from 1999/2000 (e^+) and 1998 (e^-). The solid lines represent the standard model predictions using particle density functions derived from H1 neutral current data.

One of the main physics topics with longitudinally polarized leptons at H1 is the direct search for right-handed charged currents using the relation

$$\sigma_{CC} = (1 \pm P) * \sigma_L + (1 \mp P) * \sigma_R \, .$$

The linear dependence on the polarisation is evident from the data shown in Fig. 5.2. The data shown include those published for e^+p (32), and a 2006 update of the preliminary data shown in summer 2005 (20). The data agree with standard model predictions and do not require right-handed charged currents. A linear fit to the new electron data points given below and displayed in Fig. 5.2 at large momentum transfer ($Q^2 > 400$ GeV$^2/c$) and inelasticity $y < 0.9$ yields a result consistent with the SM prediction $\sigma_{CC}(RH) = 0$ at $P_e = 1$:

P	σ_{CC} (pb)	$\mathcal{L}$ (pb^{-1})
-0.272±0.005	70.4± 1.2 (stat) ± 3.1 (syst)	70.7
+0.370±0.007	34.5± 1.4 (stat) ± 1.5 (syst)	29.7
0	57.0± 2.6 (stat) ± 2.4 (syst)	16.4
-1	-0.9± 2.9 (stat) ± 1.9 (syst)	

The polarisation uncertainty (± 5 %) introduces a systematic error of ± 2.9 pb in the result for $P_e = -1$.

For neutral currents the dependence of the cross section on the polarisation is less pronounced, since it enters through the vector (v_e) and axial vector (a_e) quark coupling constants in the electroweak interference between γ and Z-exchange. By measuring both electrons and positrons, polarised and unpolarised one can disentangle the individual quark

flavours:

$$\frac{d^2\sigma^{NC}}{dx\,dQ^2}(e^-_{L,R}) = \frac{2\pi\alpha^2}{xQ^4}\left[\left(1+(1-y)^2\right)F_2^{L,R} + \left(1-1(1-y)^2\right)xF_3^{L,R}\right]$$

$$F_2^{L,R} = \sum_q \left[x\,q(x,Q^2) + x\,\bar{q}(x,Q^2)\right]\cdot A_q^{L,R}$$

$$xF_3^{L,R} = \sum_q \left[x\,q(x,Q^2) - x\,\bar{q}(x,Q^2)\right]\cdot B_q^{L,R}$$

$$A_q^{L,R} = Q_q^2 + 2Q_eQ_q(v_e \pm a_e)v_q\chi_Z + (v_e \pm a_e)^2(v_q^2+a_q^2)(\chi_Z)^2$$

$$B_q^{L,R} = \pm 2Q_eQ_q(v_e \pm a_e)a_q\chi_Z \pm (v_e \pm a_e)^2 v_q a_q(\chi_Z)^2$$

$$\chi_Z = \frac{1}{4s_W^2c_W^2}\frac{Q^2}{Q^2+M_Z^2} \qquad (= 0.67\,\text{at}\,Q^2 = 10^4\,\text{GeV}^2)$$

This program however requires high Q^2 and high statistics, as evident from the above expressions and from the data displayed in Figures 5.3 and 5.4. The asymmetry RH/LH increases with Q^2 and reaches values of ± 20 % for $Q^2 \approx 10^4$ GeV^2 for $e^\pm p$ scattering. Only the e^-p data from 2005 are displayed in Fig. 5.3. To enhance the statistical significance of the observed asymmetry one may however combine electron and positron data and plot the ratio

$$R = \frac{\sigma_{NC}(e^+, P_e = +0.336) + \sigma_{NC}(e^-, P_e = -0.270)}{\sigma_{NC}(e^+, P_e = -0.402) + \sigma_{NC}(e^-, P_e = +0.370)}$$

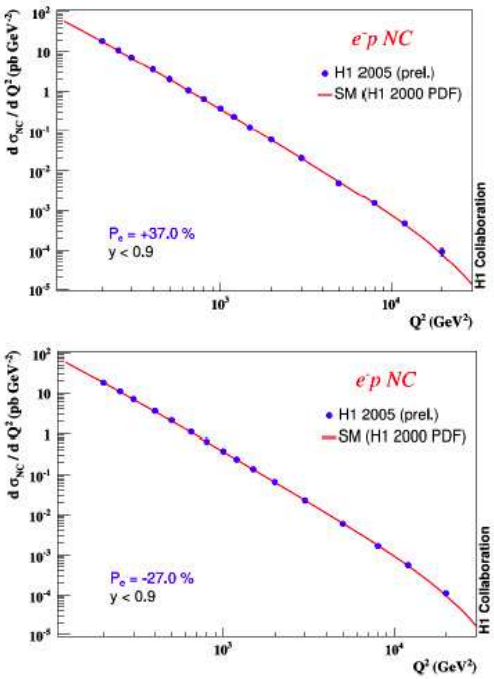

Figure 5.3: Neutral current cross section $d\sigma/dQ^2$ versus momentum transfer for left-handed and righthanded longitudinally polarized electrons.

This is shown in Fig. 5.4. It is apparent that the expectations derived from the particle density functions as extracted from H1 HERA-I data are in good agreement with the data.

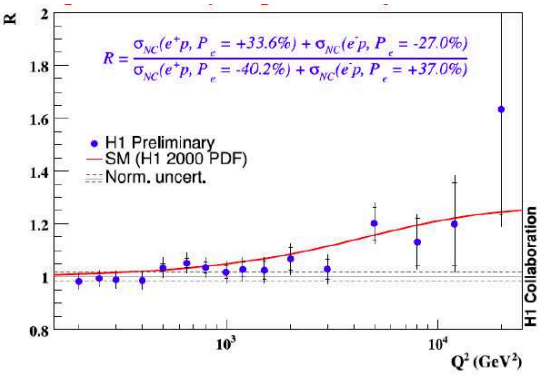

Figure 5.4: Combined neutral current cross section asymmetry from the 2003/2004 positron and the 2005 electron data.

5.3.2 Tau lepton production

Stefania Xella Hansen was involved strongly in an analysis of production of tau lepton pairs ($\tau^+\tau^-$) and a search for events with an isolated tau lepton accompanied by large missing transverse momentum ($\tau + P_t^{\rm miss}$).
In the Standard Model (SM), tau leptons are produced either in pairs or in association with a tau anti–neutrino, as expected from lepton flavour conservation. In electron/positron–proton collisions, pairs of tau leptons are produced via photon–photon interaction $\gamma\gamma \rightarrow \tau^+\tau^-$ (Fig. 5.5a) (35). Tau leptons and tau anti–neutrinos are produced in W boson decays, as illustrated in Fig. 5.5b (36). The signature of these events is a high transverse momentum (P_t) isolated tau lepton, large missing transverse momentum $P_t^{\rm miss}$ due to the undetected neutrinos, and a hadronic system X, typically of low P_t.
H1 is the first experiment at HERA to perform a measurement of $\tau^+\tau^-$ production. The search for $\tau + P_t^{\rm miss}$ events complements the previous H1 measurements of the production of events with an isolated electron or muon and large missing transverse momentum, which have revealed an excess over the SM expectation of events containing in addition a high P_t hadronic system (37; 38; 39).
The analysis is based on data from electron/positron–proton collisions at a centre–of–mass energy of 301 or 319 GeV, recorded by the H1 experiment at HERA in the period 1994–2000. The total integrated luminosity amounts to 106 pb^{-1} for the measurement of $\tau^+\tau^-$ production and 115 pb^{-1} for the search for $\tau + P_t^{\rm miss}$ events.

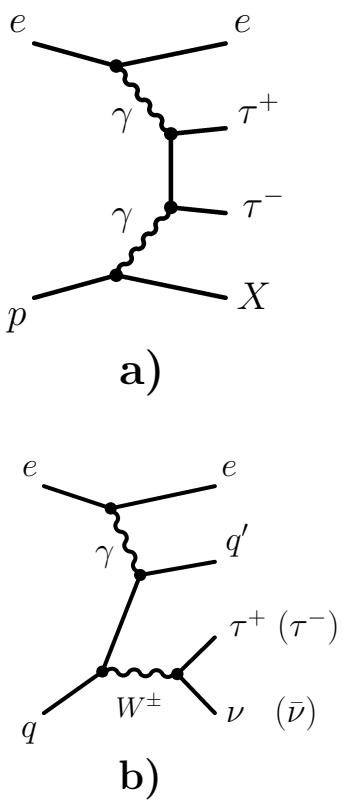

Figure 5.5: Diagrams of the main production mechanisms of tau leptons in electron–proton collisions: a) tau pair production via photon–photon collisions and b) single W boson production followed by the subsequent decay of the W into a tau lepton and a tau anti–neutrino.

Two different algorithms to identify hadronic tau decays have been developed for this analysis. The measurement of tau lepton pair production, in which the tau leptons generally have low momentum, requires an optimal background rejection. A Neural Network based identification algorithm is used for this. In contrast, the search for tau leptons produced in W decays at high P_t uses an algorithm that maximises the identification efficiency, since the signal cross section is low and the background is less severe. This algorithm uses the radial size and the charged track multiplicity of the tau jet as discriminators against quark/gluon jets.

The measured cross section for elastic tau pair production $ep \rightarrow ep\tau^+\tau^-$ is 13.6 ± 5.7 pb. The result is in agreement with the SM expectation of 11.2 ± 0.3 pb.

In the final event sample of the $\tau + P_t^{\rm miss}$ search, 6 events are observed in the data, compared to a total SM expectation of 9.9 $^{+2.5}_{-3.6}$ events, of which $0.89^{+0.15}_{-0.26}$ are expected from SM W production. In the region $P_t^X > 25$ GeV, where an excess of events containing isolated electrons or muons is observed (39), no event is found for a SM prediction of 0.39 ± 0.10, of which 0.20 ± 0.04 are expected from SM W production.

An upper limit at 95% confidence level is obtained for the production cross section of events containing an isolated tau lepton and large missing transverse momentum in the region $P_t^X > 25$ GeV/c, $\sigma(P_t^X > 25\ \mathrm{GeV/c}) < 0.31$ pb. The present measurement is compatible with the previous measurement of events with an electron or muon and $P_t^{\rm miss}$, as expected if lepton universality is assumed.

The analysis has been completed and the paper was submitted for publication recently (2).

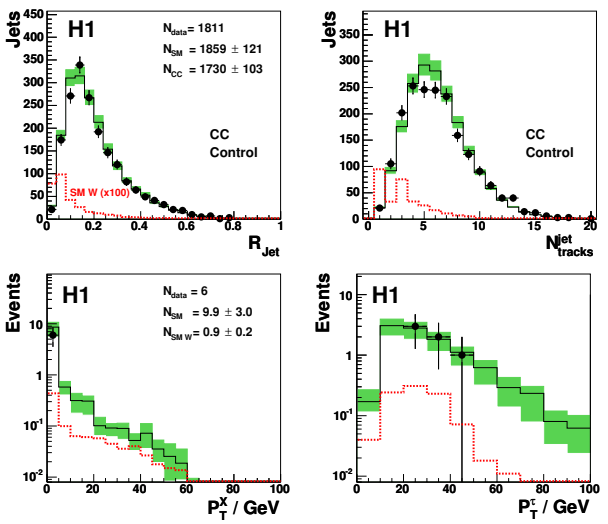

Figure 5.6:
Top: The radius of isolated jets R_{jet} and the number of charged particles N^{jet}_{tracks} in isolated jets in the main background (CC) to the $\tau + P_t^{\rm miss}$ search, at preselection level. Bottom: The hadronic transverse momentum P_t^X and the transverse momentum P_t^τ of the τ candidate in the final selection of $\tau + P_t^{\rm miss}$ events. In each figure the data (points) are compared to the SM expectation (solid histogram) shown with its uncertainty (shaded band). The signal contribution dominated by the SM W production is also shown (dashed histogram).

5.3.3 Search for lepton flavor violation

This analysis is the thesis project of Linus Lindfeld.

In ep collisions, a lepton flavor violating process (LFV) can induce the appearence of a muon or tau instead of the electron in the final state. A convenient concept to explain such exotic signatures is the exchange of a leptoquark. Leptoquarks appear naturally as color triplet scalar and vector bosons in many extensions of the standard model such as Grand Unified Theories (40), Supersymmetry (41), Compositeness (42) and Technicolor (43) allowing for LFV transitions like $e \to \mu$ and $e \to \tau$.

After presenting the preliminary H1 result of the search for LFV processes in e^+p-collisions at the summer conferences ICHEP'04 (Beijing) and TAU'04 (Nara), the analysis was extended in 2005 to cover also e^-p-collisions. Analysing additional $13.5\,\mathrm{pb}^{-1}$ of e^-p-data taken in 1998-1999 gives sensitivity to $F = 2$ leptoquarks, where the fermion number $F = |3B + L|$ is a combination of the baryon and lepton number of the initial particles. As in the previously analysed e^+p-data, no deviation from the Standard Model is found in the e^-p-data.

Extending the Buchmüller-Rückl-Wyler (BRW) effective model (44) to LFV processes, limits on the Yukawa coupling of all 14 leptoquark types to a muon or tau and a light quark are established. The statistical analysis is completely revised and performed in analogy to the latest

published H1 results of a search for leptoquark bosons (45). This statistical analysis follows a modified frequentist approach and combines different search channels including all systematic uncertainties with correlations. Within this new method, the search for LFV decays of leptoquarks into tau-quark pairs could be extended to processes with a subsequent muonic and electronic decay of the tau lepton. The analysis in the electronic tau decay channel follows a NC DIS selection with additional missing transverse momentum in the electron direction. The search in the muonic tau decay channel is performed in analogy to the search for LFV decays of leptoquarks into muon-quark pairs. The addition of the leptonic channels to the hadronic tau decays improve the tau selection efficiency significantly. Fig. 5.7 shows limits on the Yukawa coupling of scalar (left colum) and vector (right colum) F=2 leptoquarks to muon-quark pairs (top row) and F=0 leptoquarks tau-quark pairs (bottom row) as a representative example for the interpretation of the analysis. Furthermore, the extended BRW model is opened to arbitrary values of the lepton flavour violating branching ratio β_{LFV} with

$$\beta_{\mathrm{LFV}} = \frac{\lambda_{lq}^2}{\lambda_{lq}^2 + \lambda_{eq}^2}\ , \quad l = \mu, \tau\ . \tag{5.11}$$

In order to set most stringent limits in the λ_{eq}-λ_{lq}-plane, the published results from the search for first generation leptoquarks (45) are combined with the results of this analysis. The combined limits from the search for tau-quark pairs are illustrated in Fig.5.8. The not shown limits on leptoquarks decaying to muon-quark pairs are slightly more stringent and with similar features.

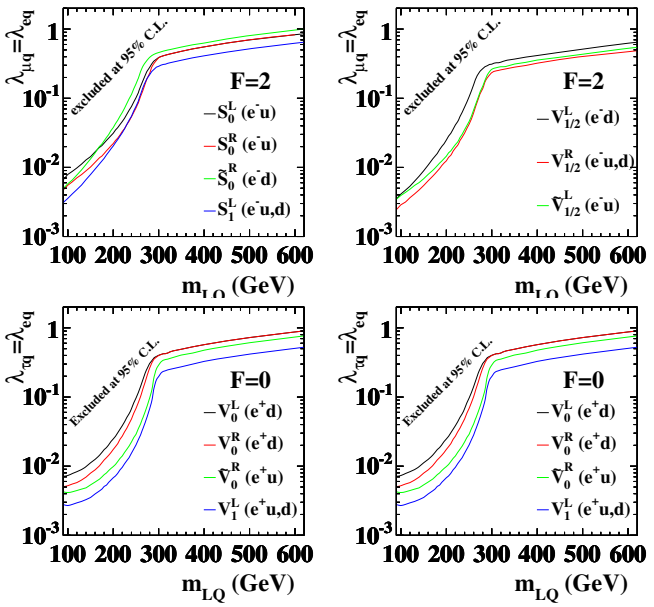

Figure 5.7:
Limits on the coupling constant strength $\lambda_{lq} = \lambda_{eq}$ at 95% C.L. as a function of the leptoquark mass for scalar and vector F=2 leptoquarks decaying to a muon-quark pair (top row) and F=0 leptoquarks decaying to a tau-quarks pair (bottom row).

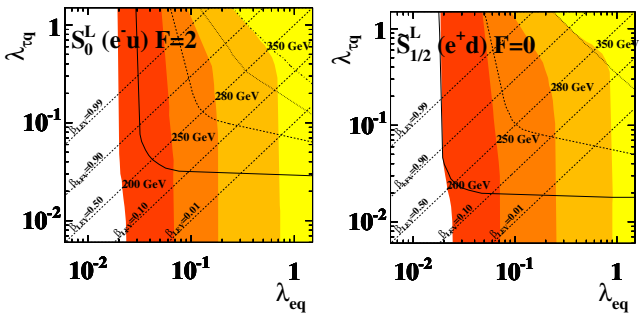

Figure 5.8: Four different masses limits at 95% C.L. on $\lambda_{\tau q}$ as a function of λ_{eq} in a model where the LFV branching ratio $BR = \lambda_{\tau q}^2/(\lambda_{\tau q}^2 + \lambda_{eq}^2)$ is not fixed (Left: F=2, Right: F=0).

It is planned to publish these results in summer 2006.

5.3.4 Inclusive prompt photon production

This analysis is the thesis project of Carsten Schmitz. A very close and fruitful cooperation with the members of the theory group at our University, T. Gehrmann, A. Gehrman-De Ridder and E. Poulsen made it possible to provide in parallel both a novel data analysis and a new theoretical calculation, based on carefully coordinated selection criterias.

Isolated photons with high transverse momentum in the final state are a direct probe of the dynamics of the hard subprocess, since they are directly observable without large corrections due to hadronisation and fragmentation. Previously ZEUS and H1 have measured the prompt photon cross section in photoproduction(46; 47). ZEUS has recently published an analysis of the prompt photon cross section for photon virtualities Q^2 larger than 35 GeV^2(48). The results are compared to the new leading order calculation of our theory colleagues (49; 50), $\mathcal{O}(\alpha^3)$, that offers first predictions for the inclusive prompt photon production in Deep Inelastic Scattering.

The events have been collected in the years 99/00 at a center of mass energy of 318 GeV, with a total integrated luminosity of 70.6 pb^{-1}. Events were selected with the electron reconstructed in the backward calorimeter (SpaCal(52)). Photons are identified in the liquid argon calorimeter (LAR)(53) by a compact electromagnetic cluster with no track pointing to it. The transverse energy is restricted to 3 GeV$< E_t^\gamma <$ 10 GeV in the pseudorapidity region $-1.2 < \eta_\gamma < 1.8$.

The main experimental difficulty is the separation of the photons from neutral mesons, mainly π^0 or η, since at high energies their decay photons are not resolved but reconstructed in one single electromagnetic cluster. These mesons are mainly produced in hadronic jets, therefore an isolation criterium is applied for the γ candidates. To ease the comparison with pQCD calculations we use an infrared-safe definition of the isolation requirement(54; 55): the energy fraction z of the photon energy to the energy of the jet which contains the photon (Photonjet) has to be larger than 0.9: $z = E^\gamma / E^{Photonjet} > 0.9$ After the selection cuts there is still a large fraction of background from neutral meson decays. Then the photon signal is extracted by a shower shape analysis which uses six discriminating shower shape functions in a likelihood analysis.

The data are corrected for detector effects by taking the average of the corrections of the PYTHIA 6.2(56) and the HERWIG 6.5(57) event generator. The background from neutral mesons was generated with the RAPGAP(58) generator. However, the background Monte Carlo was only used to control the sample, not for the extraction of the signal. This was done using single particles only.

In a first step events are selected with a good electron and a jet which contains a photon candidate as defined above. In a second step the prompt photon signal is extracted by a likelihood analysis of the shower shapes. The photon candidate clusters are analysed using six different shower shape variables to discriminate between the signal of a single photon and neutral mesons.

- Hot core fraction: fraction of energy deposited in four or eight - depending on the granularity of the calorimeter - contiguous cells including the cell with highest energy.
- Transverse radius of the cluster (transverse plane is perpendicular to the direction of the incoming particle).
- Energy fraction of the hottest cell.

- Energy fraction in the first layer.
- Kurtosis of the transverse energy distribution of the cluster cells.
- Transverse symmetry of the cluster: a photon is expected to have a symmetric cluster (S=1), whereas neutral mesons with more than one decay photon are of more asymmetric shape.

Figure 5.9 shows the six different shower shape variables together with the background from RAPGAP as well as photons radiated off the electron as predicted by RAPGAP and the signal prediction from PYTHIA (scaled by 2.3) for photons being radiated off the quark. Both contributions from RAPGAP are used unscaled. All variables are nicely described by the sum of the Monte Carlo predictions.

The estimators are combined in a likelihood analysis as well as a neural net and a range search analysis as a cross check. Monte Carlo studies showed that neutral mesons can be well separated from photons for transverse energies below 10 GeV. Only particles which decay very asymmetrically are misidentified as photons.

The probability densities that are used for the likelihood method are taken from the simulation of single particles. Only the contributing fraction of any neutral meson (π^0, η^0, η', K^0, ρ, ω, $K^\star$, K_L,K_s, n and $\bar{n}$) is taken from Monte Carlo simulation (RAPGAP). The likelihood functions are calculated separately for different bins in E_t and different wheels of the calorimeter(53) which correspond to different η_γ ranges. The contribution of photons and neutral mesons is then determined by independent fits to the data using likelihood distributions obtained from a set of single particle photons and background, respectively. The advantage of the use of single particles is that they can easily be produced in high statistics.

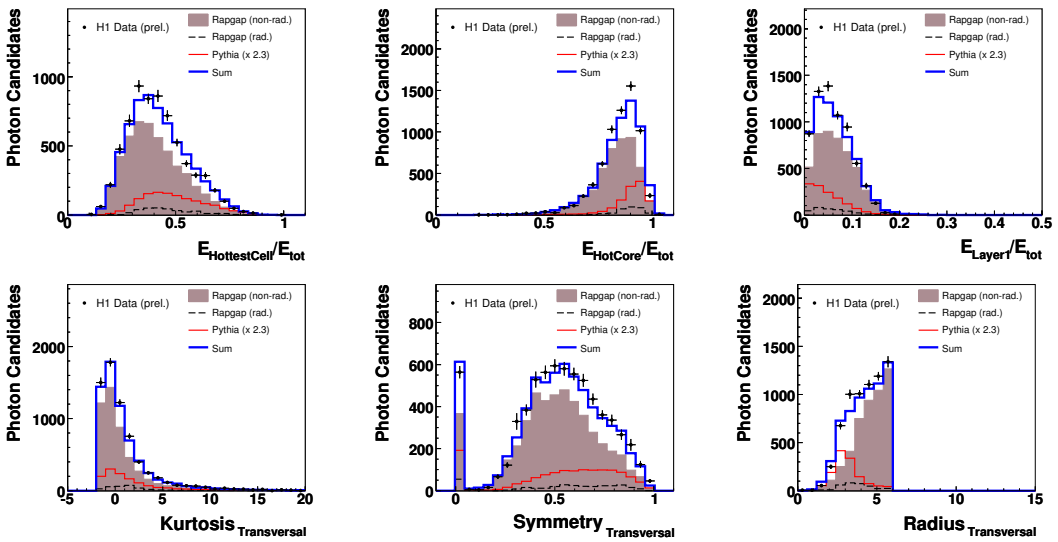

Figure 5.9: Shower shape variables used as input for the discrimination between the photon and neutral mesons: Transverse kurtosis, symmetry and radius and energy fractions of the hottest cell, the hot core and the first layer. The measured data points are shown together with the signal Monte Carlo from PYTHIA, scaled by a factor 2.3, photons radiated off the incoming or outgoing electron (rad) and background from neutral mesons (non-rad) as estimated by RAPGAP. The contributions from RAPGAP are used unscaled. The sum of the Monte Carlo prediction is indicated by the blue line.

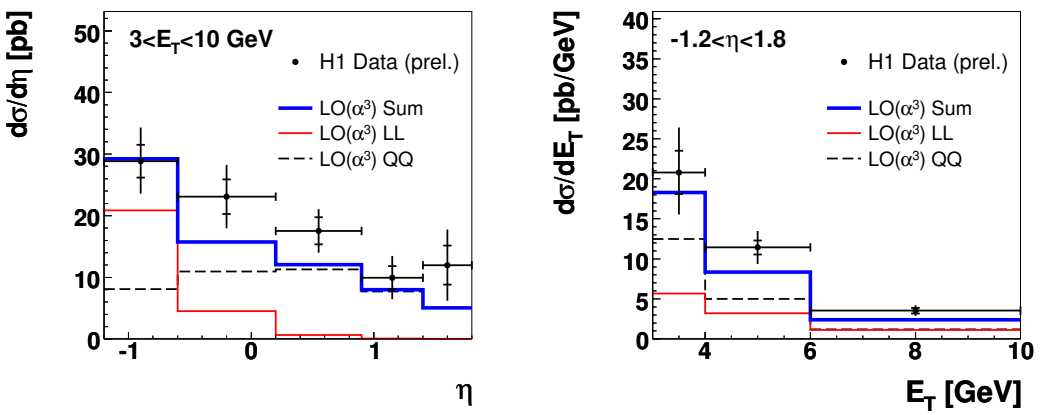

Figure 5.10: Prompt photon differential cross sections $d\sigma/dE_t^\gamma$ for $-1.2 < \eta^\gamma < 1.8$ (a) and $d\sigma/d\eta^\gamma$ (b) for $3 < E_t^\gamma < 10$ GeV, for photon virtualities Q^2 >4 GeV^2 and $y_e > 0.05$ compared to the LO calculation[49; 50]. LL and QQ show the contribution of radiation off the electron and the quark line, respectively. As the interference of these two contributions is very small it is not shown, but included in the sum.

Differential cross sections for the production of isolated photons in deep inelastic scattering are shown for Q_e^2 >4 GeV^2, $y_e > 0.05$ for photons with $3 < E_t^\gamma < 10$ GeV, pseudorapidity $-1.2 < \eta^\gamma < 1.8$ and the isolation $z = E_\gamma / E_{\gamma Jet} > 0.9$. The errors in the figures contain the statistical error and the systematic errors added in quadrature. Figure 5.10 shows the cross section as a function of transverse energy and the pseudorapidity compared to the new LO (α^3) calculation(49; 50) which gives a good description of the data. At large pseudorapidities the dominant contribution comes from radiation off the quark line (QQ), whereas in the backward region the radiation off the electron line (LL) dominates the cross section. The calculation gives a nice description of the data both in shape and in scale in contrast to the Monte Carlo predictions from PYTHIA and HERWIG which are low by a factor 2.3 and 2.6 to describe the data.

The analysis was carried out in close collaboration with the theory group at the University of Zürich. All cuts were carefully adjusted both in the analysis and the LO calculation. It is planned to extend this fruitful collaboration to further measurements with photons in the H1 detector (thesis project of K. Nowak).

[1] **Search for Excited Quarks at HERA**, Jan Becker, PhD Thesis, University of Zürich (2005)

[2] **τ-Lepton Production in ep-Collisions at HERA**, H1-Collaboration**, A. Aktas et al., DESY 06 – 029, hep-ex/0604022, submitted to Eur.Phys.J.**C** (2006).

[3] **Measurement of $F_2^{c\bar{c}}$ and $F_2^{b\bar{b}}$ at High Q^2 using the H1 Vertex Detector at HERA**, H1-Collaboration, A. Aktas *et al.*, DESY 04 – 209, hep-ex/0411046, Eur.Phys.J.**C40** (2005), 349 - 359.

[4] **Search for Light Gravitinos in Events with Photons and Missing Transverse Momentum at HERA**, H1-Collaboration, A. Aktas *et al.*, DESY 04 – 227, hep-ex/0501030, Phys.Lett.**B616** (2005), 31 - 42.

[5] **A Direct Search for Magnetic Monopoles Produced in Positron-Proton Collisions at HERA**, H1-Collaboration, A. Aktas *et al.*, DESY 04 – 240, hep-ex/0501039, Eur.Phys.J.**C41** (2005), 133 - 141.

[6] **Measurement of Dijet Cross Sections for Events with a Leading Neutron in ep Interactions at HERA**, H1-Collaboration, A. Aktas *et al.*, DESY 04 – 247, hep-ex/0501074, Eur.Phys.J.**C41** (2005), 273 - 286.

[7] **Measurement of Beauty Production at HERA Using Events with Muons and Jets**, H1-Collaboration, A. Aktas *et al.*, DESY 05 – 004, hep-ex/0502010, Eur.Phys.J.**C41** (2005), 453 - 467.

[8] **Measurement of Charm and Beauty Photoproduction at HERA $D^*\mu$ Correlations**, H1-Collaboration, A. Aktas *et al.*, DESY 05 – 040, hep-ex/05003038, Phys.Lett.**B621** (2005), 56 - 71.

[9] **Measurement of Deeply Virtual Compton Scattering at HERA**, H1-Collaboration, A. Aktas *et al.*, DESY 05 – 065, hep-ex/0505061, Eur.Phys.J. **C45** (2005), 1 - 11.

[10] **Search for Leptoquark Bosons in ep Collisions at HERA**, H1-Collaboration**, A. Aktas et al., DESY 05 – 087, hep-ex/0506044, Phys.Lett.**B629** (2005), 9 - 19.

[11] **A Determination of Electroweak Parameters at HERA**, H1-Collaboration**, A. Aktas et al., DESY 05 – 093, hep-ex/0507080, Phys.Lett.**B632** (2006), 35 - 42.

[12] **Measurement of F_2^{cc} and F_2^{bb} at Low Q^2 Using the H1-vertex Detector at HERA**, H1-Collaboration**, A. Aktas et al., DESY 05 – 110, hep-ex/0507081, Eur.Phys.J.**C45** (2006), 23 -33.

[13] **Measurement of Event Shape Variables in Deep Inelastic Scattering at HERA**, H1-Collaboration**, A. Aktas et al., DESY 05 – 225, hep-ex/0512014, Eur.Phys.J.**C46** (2006), 343 - 356.

[14] **Forward Jet Production in Deep Inelastic Scattering at HERA**, H1-Collaboration**, A. Aktas et al., DESY 05 – 135, hep-ex/0508055, Eur.Phys.J.**C46** (2006), 27 -42.

[15] **Elastic J/ψ Production at HERA**, H1-Collaboration**, A. Aktas et al., DESY 05 – 161, hep-ex/0510016, Eur.Phys.J.**C** (2006), in print.

[16] **Photoproduction of Dijets with High Transverse Momenta at HERA**, H1-Collaboration**, A. Aktas et al., DESY 06 – 020, hep-ex/0603014, submitted to Phys.Lett.**B** (2006).

[17] **Diffractive Photoproduction of ρ Mesons with High Transverse Momenta at HERA**, H1-Collaboration**, A. Aktas et al., DESY 06 – 023, hep-ex/0603038, submitted to Phys.Lett.**B** (2006).

[18] **Search for Doubly-Charged Higgs Boson Production at HERA**, H1-Collaboration**, A. Aktas et al., DESY 06 – 038, hep-ex/0604027, submitted to Phys.Lett.**B** (2006).

[19] Contributed papers by the H1-Collaboration to EPS2005/HEP2005: Int. Europhysics Conf. on High Energy Physics, Lisbon (Portugal), July 21-27, 2005 and to LEPTON-PHOTON 2005, XXII. Int. Symp. on Lepton-Photon Interactions at High-Energy, Uppsala, Sweden, June 30 - July 5, 2005. Only those papers are listed, which have not yet been submitted to journals.

[20] **Measurement of the Polarisation Dependence of the Total e^-p Charged Current Cross Section** [19] (621,388)

[21] **Multi-jet Production in High Q^2 Neutral Current Deep Inelastic Scattering at HERA and Determination of α_s** [19] (625,390)

[22] **Inclusive Jet Production in Deep Inelastic Scattering at High Q^2 at HERA** [19] (629)

[23] **Photoproduction of $D^{*\pm}$ Mesons Associated with a Jet at HERA** [19] (648,406)

[24] **The Charm Fragmentation Function in DIS** [19](649,407)

[25] **The Structure of Charm Jets in DIS** [19] (650,408)

[26] **Study of Jet Shapes in Charm Photoproduction at HERA** [19] (651,409)

[27] **Multi-lepton Events at HERA and a Generic Search for New Phenomena at Large Transverse Momentum** [19] (635,420); an updated analysis of the multilepton channel is available as report H1-prelim-06-063 (http://www-h1.desy.de/publications/H1preliminary.short_list.html)

[28] **Events with an Isolated Lepton and Missing Transverse Momentum at HERA** [19] (637,421); an updated analysis is available as report H1-prelim-05-164_PRC_Nov05 (http://www-h1.desy.de/psfiles/confpap/EPS2005/H1-prelim-05-164_PRC_Nov05.ps)

[29] **Acceptance Corrected Ratios of $D^*p(3100)$ and D^* Yields and Differential Cross Sections of $D^*p(3100)$ production** [19] (643,401)

[30] **H1 Search for a Narrow Baryonic Resonance Decaying to $K_s^0p(\bar{p})$** [19] (644,400)

[31] **Dijets in Photoproduction** [19] (680)

[32] **First Measurement of Charged Current Cross Sections at HERA with Longitudinally Polarized Positrons**, H1-Collaboration**, A. Aktas et al., DESY 05 – 249, hep-ex/0512060, Phys.Lett.**B634** (2006), 173 - 179.

[33] **Searches for Leptoquarks and for Lepton Flavor Violation with the H1-Experiment**, L. Lindfeld, Proc. 13. Int. Workshop on Deep Inelastic Scattering, Madison, Wisconsin, USA, April 27 - May 1, 2005, AIP. Conf. Proc. 792 (2005), 631 - 634.

[34] **Search for Leptoquarks and Lepton Flavor Violation at HERA**, S. Schmitt, Proc. EPS Int. Europhysics Conf. on High Energy Physics, Lisbon, Portugal July 21 - 27, 2005, PoS HEPO2005 (2006), 316 - 319.

[35] J. A. M. Vermaseren, Nucl. Phys. B **229** (1983) 347.

[36] U. Baur, J. A. M. Vermaseren and D. Zeppenfeld, Nucl. Phys. B **375** (1992) 3.

[37] T. Ahmed *et al.* [H1 Collaboration], DESY 94-248 (1994).

[38] C. Adloff *et al.* [H1 Collaboration], Eur. Phys. J. C **5** (1998) 575 [hep-ex/9806009].

[39] V. Andreev *et al.* [H1 Collaboration], Phys. Lett. B **561** (2003) 241 [hep-ex/0301030].

[40] J.C. Pati and A. Salam, Phys. Rev. D **81** (1974) 275;
H. Georgi and S.L. Glashow, Phys. Rev. Lett. **32** (1974) 438;
P. Langacker, Phys. Rep. **72** (1981) 185.

[41] H.P. Nilles, Phys. Rep. **110** (1984) 1;
H.E. Haber and G.L. Kane, Phys. Rep. **117** (1985) 75.

[42] B. Schrempp and F. Schrempp, Phys. Lett. B **153** (1985) 101;
J. Wudka, Phys. Lett. B **167** (1986) 337.

[43] S. Dimopoulos and L. Susskind, Nucl. Phys. B **155** (1979) 237; S. Dimopoulos, Nucl. Phys. B **168** (1980) 69; E. Farhi and L. Susskind, Phys. Rev. D **20** (1979) 3404; E. Farhi and L. Susskind, Phys. Rep. **74** (1981) 277.

[44] W. Buchmüller, R. Rückl and D. Wyler, Phys. Lett. B **191** (1987) 442.

[45] A. Aktas *et al.* [H1 Collaboration], Phys. Lett. B **629** (2005) 9 [hep-ex/0506044].

[46] J. Breitweg *et al.* [ZEUS Collaboration], Phys. Lett.**B 472** (2000) 175 [hep-ex/9910045].

[47] A. Aktas *et al.* [H1 Collaboration], Eur. Phys. J.**C38** (2005) 437 [hep-ex/0407018].

[48] S. Chekanov *et al.* [ZEUS Collaboration], Phys. Lett.**B 595** (2004) 86 [hep-ex/0402019].

[49] A. Gehrmann-De Ridder, T. Gehrmann and E. Poulsen, Phys. Rev. Lett. **96** (2006) 132002 [hep-ph/0601073].

[50] A. Gehrmann-De Ridder, T. Gehrmann and E. Poulsen [hep-ph/0604030].

[51] I. Abt *et al.* [H1 Collaboration] Nucl. Instr. and Meth. **A 386** (1997) 310, ibid, 348.

[52] T. Nicholls *et al.* [H1 SPACAL Group], Nucl. Instrum. Meth. A **374** (1996) 149.

[53] B. Andrieu *et al.* [H1 Calorimeter Group Collaboration], Nucl. Instrum. Meth. A**336** (1993) 460.

[54] E. W. N. Glover and A. G. Morgan, Z. Phys. C **62** (1994) 311.

[55] D. Buskulic *et al.* [ALEPH Collaboration], Z. Phys. C **69** (1996) 365.

[56] T. Sjöstrand *et al.*, PYTHIA 6.2 Physics and Manual [hep-ph/0108264].

[57] G. Corcella *et al.*, HERWIG 6.5 Release Note **135** (2001) 128 [hep-ph/0210213].

[58] H. Jung, Comput. Phys. Commun. **86** (1995) 147
(see also http://www.desy.de/ jung/rapgap.html).

[59] Stephen D. Ellis, Davison E. Soper, Phys.Rev. **D48** (1993) 3160 [hep-ph/9305266].

6 The DØ Experiment at the Tevatron $p\bar{p}$ Collider: Search for Rare Decays of the B_s^0-Mesons

Ralf Bernhard, Frank Lehner, Christophe Salzmann and Andreas Wenger

The full DØ collaboration consists of 86 institutes from 19 countries:
Argentina (1), Brazil (3), Canada (4), China (1), Czech Republic (3), Colombia (1), Ecuador (1), France (8), Germany (6), India (3), Ireland (1), Korea (1), Mexico (1), Netherlands (3), Russia (5), Sweden (4), United Kingdom (3), United States of America (36) and Vietnam (1)

(DØ Collaboration)

Until LHC turns on in 2007 the Tevatron collider at the Fermi National Accelerator Laboratory, Batavia, USA, will remain the world's highest-energy accelerator with an available center of mass energy of $\sqrt{s} = 2$ TeV. The accelerator is routinely delivering $p\bar{p}$ collisions with a peak luminosity of 1.7×10^{32} cm^{-2}s^{-1}. The two main detectors, CDF and DØ, are taking continuously collision data and have recorded more than 1 fb^{-1} of collision data up to now. The Tevatron physics program is rich and includes direct and indirect searches for as yet unknown particles and forces, including those that are predicted in the Standard Model (SM) like the Higgs boson and those that would come as a surprise. Moreover, numerous measurements of various B meson decay modes have already allowed the investigation of B meson properties that are not accessible at e^+e^- annihilation machines. One of the most recent results highlighting Tevatron's great potential in B physics is the first direct experimental determination (1) of the oscillation frequency Δm_s in the B_s^0 meson system albeit with large uncertainties. The precise value of the oscillation frequency Δm_s is of large importance for the fundamental parameters of the CKM matrix and will be later accurately measured at LHCb. A participation in the Tevatron B physics program is therefore one of the best preparations of a successful contribution in the physics activities at LHCb.

The main physics topic of the DØ group at the Physik Institut is the investigation of flavor-changing neutral current (FCNC) B meson decays. FCNC decays are forbidden in the SM at tree level but proceed through higher order diagrams at low rate. Due to interference effects with new particles in the loops FCNC decays are a good place to probe new physics and to provide severe constraints on several models beyond the SM. For instance, the purely leptonic decay amplitude of $B_s^0 \to \mu^+\mu^-$ suffers from helicity suppression and has therefore a small branching ratio in the SM. However, it can be significantly enhanced in most extensions of the SM: in type-II two-Higgs-doublet models (2HDM) the branching fraction depends only on the charged Higgs mass M_{H^+} and $\tan\beta$, the ratio of the two neutral Higgs field vacuum expectation values, with the branching fraction growing like $(\tan\beta)^4$ (2). In the minimal supersymmetric standard model (MSSM), however, $\mathcal{B}(B_s^0 \to \mu^+\mu^-) \propto (\tan\beta)^6$, leading to an enhancement by up to two orders of magnitude (3) compared to the SM value of $\mathcal{B}(B_s^0 \to \mu^+\mu^-) = 3.5 \times 10^{-9}$, even if the MSSM with minimal flavor violation (MFV) is considered, in which case the CKM matrix is the only source of flavor violation.

Since this decay shows such a strong sensitivity to many new models and its amplitude is theoretically very clean, it allows one of the most sensitive (indirect) searches for new physics with the statistics presently available at the Tevatron. Moreover, in a long-term perspective, the LHCb experiment expects to discover this process being one of the most important prospects in the B-physics program at hadron colliders.

In October 2005 Ralf Bernhard completed his PhD thesis on an analysis of rare B_s^0 decays

using DØ data (4). As one of his main results he conducted a search for $B_s^0 \to \mu^+\mu^-$ events. The result of this analysis using 300 pb^{-1} of data was published in Ref. (5) and allowed to set an upper bound at a 90% C.L. of $\mathcal{B}(B_s^0 \to \mu^+\mu^-) < 3.0 \times 10^{-7}$. This upper limit was then combined (6) with the CDF result taking correlated systematic uncertainties properly into account to obtain the world-best limit on $B_s^0 \to \mu^+\mu^-$. The combined exclusion limit of $\mathcal{B}(B_s^0 \to \mu^+\mu^-) < 1.2 \times 10^{-7}$ at a 90% C.L. is used to constrain supersymmetric models at high $\tan\beta$.

An updated DØ analysis on $B_s^0 \to \mu^+\mu^-$ is presently being performed by Ralf Bernhard and will exploit additional 400 pb^{-1} of DØ data. It is expected to release a new result by summer 2006. The signal region in the analysis is currently kept hidden during the optimization in order to avoid any experimenter's bias. The events next to the region around the B_s^0 invariant mass are used to determine the background and as a normalization mode events from the known decay $B^\pm \to J/\psi(\to \mu^+\mu^-)K^\pm$ are reconstructed. The current sensitivity at a 90% C.L. of the entire DØ data set is given by 1.9×10^{-7}. A new combination with CDF will then allow to further push the branching ratio of this important decay to smaller values.

A second analysis of Ralf Bernhard focused on the search for rare $B_s^0 \to \mu^+\mu^-\phi$ events, which is an exclusive FCNC process mediated by $b \to s l^+ l^-$ quark transitions. Since the decay has a hadronic final state, the SM calculation of the branching ratio has larger theoretical uncertainties than $B_s^0 \to \mu^+\mu^-$. In addition, the decay $B_s^0 \to \mu^+\mu^-\phi$ is not helicity suppressed showing therefore less sensitivity to new physics. The analysis using 450 pb^{-1} of data was just recently concluded and submitted to Phys. Rev. Lett. (7). In the analysis the search for the non-resonant decay is normalized to the known resonant decay $B_s^0 \to J/\psi(\to \mu^+\mu^-)\phi$ since the final event signature is the same and many systematic uncertainties tend to cancel in the ratio. For the search of the rare candidate events we have used discriminating variables to best exploit the properties of the signal decay and the multi-variate technique of a random-grid search to optimize the analysis. After all cuts zero events were found in the signal box with an expected background of 1.6 ± 0.4. The upper limit on the decay $B_s^0 \to \mu^+\mu^-\phi$ is then calculated to be 3.2×10^{-6} at a 90% C.L improving the only existing published limit (8) by CDF by a factor of ten. The new result is only a factor of two above the SM and an updated analysis may well yield to the first observation of a FCNC decay in the B_s^0 meson system. The future refinement of this search using more available data from DØ will be one of the contents of the PhD thesis of Andreas Wenger. Moreover, he will extend the search to $B_d^0 \to K^*\mu^+\mu^-$ events as well.

The anticipated luminosity at Tevatron will accumulate to about 4 fb^{-1} in fall 2007, the time when LHC turns on. In case of no signal, an expected upper limit on the branching fraction of $B_s^0 \to \mu^+\mu^-$ of 2×10^{-8} at a 90% C.L. is possible if both experiments, CDF and DØ are combined. Although such a limit will be sufficient to exclude large regions of very large $\tan\beta$ in the framework of supersymmetric models, the expected sensitivity is still about $10\times$ worse than the SM prediction. Thus, an experimental observation of the decay at a SM rate is clearly out of reach at Tevatron, but will be possible at the LHC. The LHCb experiment, for instance, expects an annual yield of 17 reconstructed $B_s^0 \to \mu^+\mu^-$ decays and is very likely to discover this rare decay at the first time if no significant enhancements due to new physics exist. After all the DØ analysis activities on rare B_s^0 decays represent an important ingredient for the preparation of physics analysis at the upcoming LHCb.

The DØ detector is presently being upgraded in the Tevatron shutdown lasting from March to June 2006 by installing a new silicon detector layer. This additional layer is very close to the beam pipe and its insertion into the existing detector becomes necessary to compensate for the radiation induced damage of the silicon device. We have contributed to

the production of this new layer and developed together with the Swiss based company Dyconex long flexible fine-pitch cables, which transmit the analog signals from the silicon sensors to the front-end electronics situated at the module's end. Christophe Salzmann who has just started his master thesis on the analysis of $B_s^0 \to \psi(2)\phi$ decays has helped to install the detector at Fermilab in March 2006. Andreas Wenger is presently spending a eight-month research period at Fermilab to work on alignment improvement and calibration tasks of the silicon detector. For that reason he will exploit a new detector alignment method that was pioneered (9) by the H1 experiment at DESY.

[1] V. Abazov *et al.*, [DØ Collab.], hep-ex/0603029, submitted to PRL; For CDF result see http://www-cdf.fnal.gov/physics/new/bottom/060406.blessed-Bsmix/

[2] H. E. Logan and U. Nierste, Nucl. Phys. B **586**, 39 (2000).

[3] K. S. Babu and C. F. Kolda, Phys. Rev. Lett. **84**, 228 (2000); A. Dedes *et al.*, FERMILAB-PUB-02-129-T (2002); S. R. Choudhury and N. Gaur, Phys. Lett. B **451**, 86 (1999).

[4] Ralf Bernhard, Search for Rare Decays of the B_s^0 Meson with the DØ Experiment, PhD Thesis U Zurich, 2005.

[5] V. Abazov *et al.* [DØ Collab.], Phys. Rev. Lett. **94**, 071802 (2005); A preliminary result using 300 pb^{-1} is described in DØ note 4733-CONF (2005).

[6] R. Bernhard *et al.*, hep-ex/0508058.

[7] V. Abazov *et al.* [DØ Collab.], hep-ex/0604015, submitted to Phys.Rev.Lett.

[8] T. Affolder *et al.* [CDF Collaboration], Phys. Rev. Lett. **83**, 3378 (1999).

[9] V. Blobel, Software Alignment for Tracking Detectors, invited talk given at the Workshop on Tracking in High Multiplicity Environments, TIME'05, Zurich, October 2005. Submitted to NIM.

7 High-precision CP-violation Physics at LHCb

R. Bernet, R.P. Bernhard, J. Gassner, F. Lehner, M. Needham, M. Regli, T. Sakhelashvili, S. Steiner, O. Steinkamp, U. Straumann, J. van Tilburg, A. Vollhardt, D. Volyanskyy, A. Wenger

in collaboration with: The silicon tracking group of LHCb: University of Lausanne; Max Planck Institute, Heidelberg, Germany; University of Santiago de Compostela, Spain; and Ukrainian Academy of Sciences, Kiev, Ukraine.

The full LHCb collaboration consists of 48 institutes from Brazil, China, France, Germany, Italy, The Netherlands, Poland, Romania, Russia, Spain, Switzerland, Ukraine, the United Kingdom, and the United States of America.

(LHCb)

The LHCb experiment (1; 2) aims to perform high precision measurements of CP violating processes and rare decays in the B meson systems. The comparison of results from many different decay modes will permit to perform consistency tests of the Standard Model explanation of CP violation. In the Standard-Model picture, CP violating asymmetries are generated through processes involving internal loops of virtual particles and are therefore very sensitive to contributions from possible new particles, as they are predicted by almost all extentions of the Standard Model. Precision measurements of CP violating processes therefore provide a powerful tool to search for physics beyond the Standard Model, which is complementary to direct searches at the high energy frontier. Our group concentrates on the development, construction, operation and data analysis of the LHCb Silicon Tracker as well as on the preparation of physics analyses.

7.1 LHCb experiment

The LHCb experiment is designed to exploit the large $b\bar{b}$ production cross section at the Large Hadron Collider (LHC) at CERN in order to perform a wide range of precision studies of CP violating phenomena and rare decays in the B meson systems. The experiment will operate at a moderate luminosity of $2\times\mathbf{10^{32}}$ cm^{-2}s^{-1} and will be fully operational from the start of LHC operation in 2007.

In particular, the copious production of B_s^0 mesons, combined with the unique particle-identification capabilities of the LHCb detector, will permit the experiment to perform sensitive measurements of CP violating asymmetries in a variety of decay channels that are beyond the reach of the current generation of CP-violation experiments.

A vertical cut through the LHCb detector is shown in Fig. 7.1. Since the production of b quarks in proton-proton collisions at the LHC is strongly peaked towards small polar angles with respect to the beam axis, the detector is layed out as a single-arm forward spectrometer. Its acceptance extends out to 300 mrad in the horizontal bending plane of the 4 Tm dipole magnet and to 250 mrad in the vertical plane. The forward acceptance of the experiment is limited by the LHC beam pipe that passes through the detector and follows a 10 mrad cone pointing back to the proton-proton interaction region.

The precise and efficient reconstruction of the trajectories of charged particles is a key requirement for the experiment. Many of the interesting decay channels require the reconstruction of several decay particles in a high-multiplicity environment. Furthermore, excellent

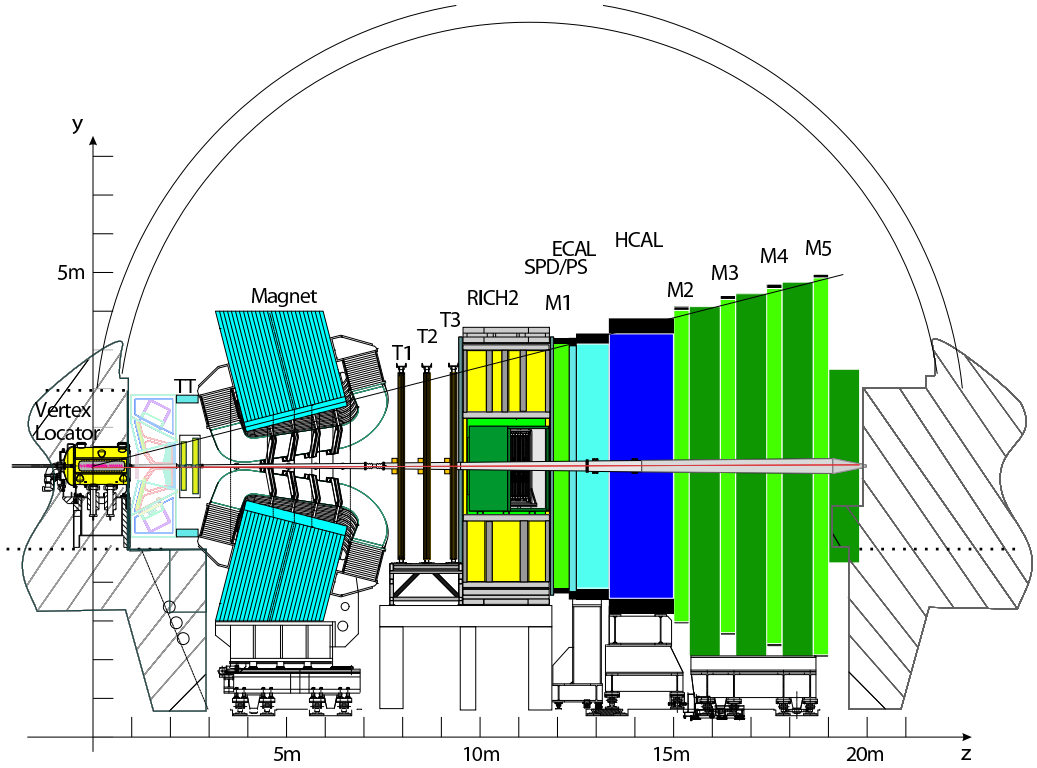

Figure 7.1: Vertical cross section through the LHCb detector.

momentum resolution is mandatory to resolve the fast flavour oscillation of B_s^0 mesons, which is required for time-dependent CP violation analyses. The LHCb tracking system consists of a silicon vertex detector (VELO), the Trigger Tracker (TT) upstream of the dipole magnet and four tracking stations (T1-T3) downstream of the magnet. The Trigger Tracker (2; 4) covers the full acceptance of the experiment with long silicon micro-strip detectors, whereas two detector technologies are employed in the large tracking stations T1-T3. Here, the innermost region around the beam pipe is covered by silicon micro-strips (Inner Tracker (3)) whereas the outer part of these stations is covered by straw drift-tubes (Outer Tracker).

Other components of the LHCb detector are two ring-imaging cherenkov (RICH) detectors, calorimeters (SPD,PS,ECAL,HCAL) and muon chambers (M1-M5).

7.2 Silicon tracker

Our group has taken a leading rôle in the development, production and operation of the LHCb Silicon Tracker, which consists of the Trigger Tracker and the Inner Tracker described above. Both these detectors employ silicon micro-strip technology but differ in important details of the technical design. The Silicon Tracker project is led by O. Steinkamp with U. Straumann as his deputy.

The main responsibility of the group is the design and construction of the Trigger Tracker. A

large fraction of our efforts in 2005 were spent in launching the detector module production and quality assurance (QA) and in designing and preparing the various parts of the detector box and support frames. In addition, our group is responsible for the procurement and quality assurance of the silicon sensors for Inner Tracker and Trigger Tracker, and for design and production of the optical digital readout link for both these detectors. Almost all silicon sensors have been delivered to us and a large fraction of these have passed the QA programme. A full readout system, using the final components, has been set up and is routinely operated as part of the detector module quality assurance programme.

7.3 Trigger tracker

The Trigger Tracker fulfills a two-fold purpose: It will be used in the Level-1 trigger (hence its name) to assign transverse-momentum information to large-impact parameter tracks, and it will be used in higher-level triggers and offline analysis to reconstruct the trajectories of low-momentum particles that are bent out of the acceptance of the experiment before reaching tracking stations T1-T3.

The Trigger Tracker consists of four detection layers (4). Its active area is approximately 160 cm wide and 130 cm high and will be covered entirely by silicon micro-strip detectors with a strip pitch of 183 μm. An isometric drawing of the basic detector module is shown in Fig. 7.2 (5). It consists of seven silicon sensors that are electronically organised into either two or three readout sectors. All readout electronics and associated mechanics are located at one end of the module, outside of the acceptance of the experiment. The inner readout sectors are connected to their readout electronics via approximately 39 cm and 58 cm long Kapton interconnect cables. The layout of a detection layer is illustrated in Fig. 7.3, where the different readout sectors are indicated by different shadings. The areas above and below the beam pipe are each covered by a single detector module, the areas to the left and to the right of the beam pipe are covered by 14-sensor long ladders that are assembled by joining two detector modules together at their ends.

Including 15% spares, a total of 148 detector modules with about 165'000 readout channels has to be produced. A rigorous quality assurance programme has to be carried out in order to ensure that each module fulfills the strict mechanical and electrical acceptance criteria.

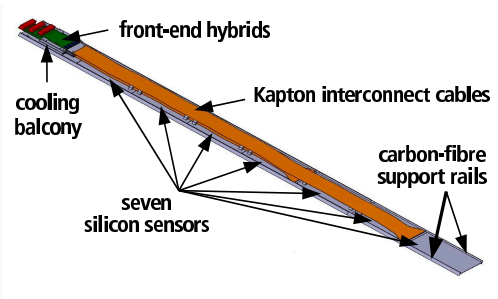

Figure 7.2: Isometric drawing of a detector module for the Trigger Tracker.

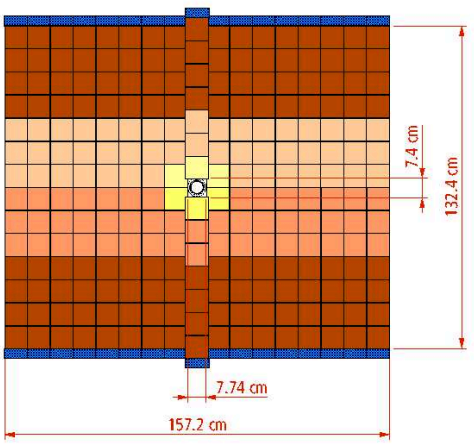

Figure 7.3: Layout of one detection layer of the Trigger Tracker.

7.3.1 Module production

The production of detector modules for the Trigger Tracker is proceeding under the responsibility of F. Lehner and T. Sakhelashvili. A laboratory at the Physik Institut has been converted into a clean room and equipped with the required infrastructure and equipment, such as microscopes for visual inspections and an automatic ultrasonic wire-bonding machine. In a pre-series production, that took place between May and August 2005, seven modules were assembled and thoroughly tested after each production step. This permitted to refine various details of the module assembly procedure (6) and to identify and improve a few weak points in the module design. For instance, the high voltage insulation between the carbon fiber support rails and the backplane of the silicon sensors was significantly improved to prevent sparking. Improvements to the alignment jigs used in the module assembly permitted to achieve an accuracy of the silicon sensor placement well within the tight specifications (Fig. 7.4).

The series production of detector modules was launched in September 2005. The production of a module proceeds in two stages. The first production stage includes the initial alignment of the seven silicon sensors and the lower readout hybrid under the control of an optical metrology machine, the glueing of the two suppport rails onto the edges of the hybrid and the sensors, the attachment of high-voltage and ground connections with silver epoxy glue, the wire bonding of the outer four silicon sensors to the readout hybrid, and the attachment of Kevlar protection caps over the wire bonds. After this first stage, the outer readout sector is fully operational and the module undergoes a first burn-in cycle as described in the quality assurance programme below. After the module has successfully passed the burn-in, it is completed in the second stage of the production. This consists of mounting and bonding the second (and third, where applicable) readout hybrid and Kapton interconnect cable(s) to the inner readout sector(s). The completed module then undergoes a second and final burn-in cycle.

The production of a detector module involves several gluing steps, each of which requires over-night curing of the glue. Several modules are produced in parallel to achieve an average module production rate of five modules per week. By the end of March 2005, about 60 modules were completed after the first production stage and twelve modules were fully completed (see Fig. 7.5 and 7.6).

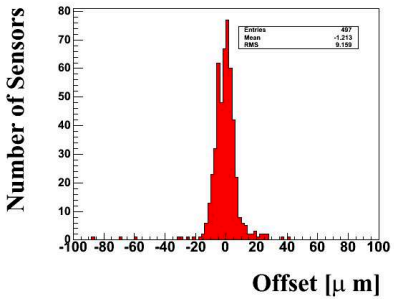

Figure 7.4: Distribution of the measured offsets of silicon sensors. Offsets should be small compared to the expected spatial resolution of 50 μm.

Figure 7.5: Storage of produced detector modules.

Figure 7.6: Two stage-I modules and two completed modules on their way from the production lab to the burn-in test stand.

A bottleneck during the start-up of the module production was caused by the late delivery of the Kapton interconnect cables, which are used to connect the inner readout sectors to their front-end readout hybrids. These cables were produced in industry and their delivery was delayed several times due to unexpectedly low production yields at the company. J. Gassner spent a significant amount of time and effort in discussions and tests with the company in order to overcome this problem. He recently managed to retrieve a sufficiently large number of cables of acceptable quality, so that all necessary components for the TT module production are now in hand. The production schedule foresees the completion of the module production by the end of October 2006.

7.3.2 Module quality assurance

Each module undergoes two extensive burn-in programmes, one after the first production stage and another one when the module is completed. A dedicated test stand that can hold up to four detector modules in parallel has been set up for this purpose by M. Needham and A. Vollhardt, with help from D. Volyanskyy and A. Wenger.

The burn-in programme takes two days and runs fully automatic, controlled by LabView running on a Linux PC. It includes measurements of sensor leakage currents as a function of the applied bias voltage as well as searches for interrupted and shorted readout strips and pinholes. A pulsed infra-red laser system is used to generate charges at well-defined locations on each silicon sensor and permits to measure signal pulse shapes and charge collection efficiency as a function of the applied bias voltage. Each module undergoes several temperature cycles between room temperature and +5°C, the latter being the operating temperature foreseen in LHCb.

As final readout electronics are employed to read out the detector modules, the burn-in test stand also serves as a full system test. Furthermore, the box that holds the modules during the tests uses many components of the final detector box (described below) and therefore serves as a small-scale prototype of that box.

So far, the quality of the tested modules is excellent. The fraction of non-working readout channels is in the sub-permille range and only a small number of modules showed operational problems and had to go through a repair cycle.

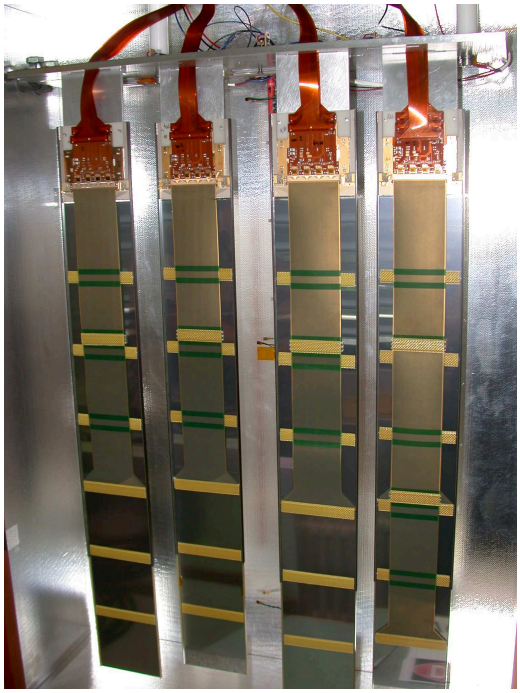

Figure 7.7:
Four completed detector modules installed in the burn-in test stand. The readout-hybrids can be seen at the upper end of the modules.

7.3.3 Station mechanics

All detector modules will be housed in a single light-tight and thermally insulating box, which also provides electrical insulation to the environment (5). Each module will be mounted into one of two C-shaped aluminum frames. These two frames will be mounted onto precision rails and can be retracted from the beam pipe for detector maintenance and for bake-outs of the beam pipe (Fig. 7.8). The frames include a cooling plate through which C_6F_{14} will be circulated as cooling agent to remove the heat generated by the readout hybrids and to create the desired ambient temperature of around 5°C inside the detector box. The design and production of the station mechanics has been the responsibility of S. Steiner. Almost all parts and pieces have been produced and are currently being assembled in a laboratory at our institute. Here, detailed mechanical and thermal studies will be performed on the detector box, before it will be shipped to CERN in autumn 2006.

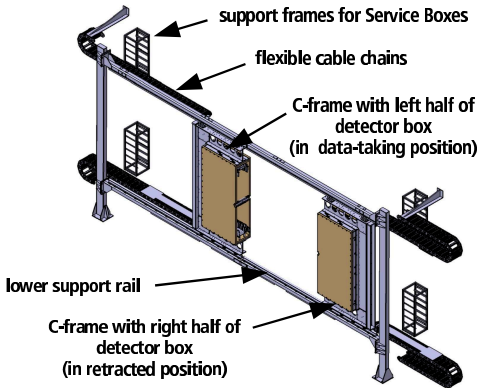

Figure 7.8:
Isometric drawing of the Trigger Tracker support frames and detector box. One half of the detector box is shown in the retracted position that is used for detector installation and maintenance.

7.4 Silicon sensors

The different types of silicon sensors that are used for the Inner Tracker and the Trigger Tracker have been described in earlier reports. The design specifications for the Inner Tracker sensors were defined in our group, whereas an existing design developed for the Outer Barrel of the CMS silicon tracker could be used for the Trigger Tracker. All types of silicon sensors have been produced by Hamamatsu Photonics, Japan. Upon arrival in Zürich, the sensors undergo a detailed quality assurance programme, which includes visual inspection, electrical characterisation and metrology. The largest part of this work has been carried out by students working under the supervision of F. Lehner (7). The last batch of sensors has been delivered recently and their testing is expected to be completed soon. The quality of the sensors is excellent and well within the strict mechanical and electrical specifications.

7.5 Readout system

The detector modules are equipped with Beetle front-end chips, which sample the detector data at the LHC bunch crossing frequency of 40 MHz and store the analog data for the latency of the Level-0 trigger. On reception of a trigger accept, the data are transmitted to a so-called Service Box, which is located close to the detector but outside of the acceptance of the experiment. Here, they are digitised, multiplexed and prepared for optical transmission to the LHCb electronics barrack. The Service Boxes and the optical links have been designed by A. Vollhardt, who is also responsible for the production and commissioning of the readout system. All relevant components have been radiation qualified for the

expected radiation dose of up to 15 kRad for 10 years of operation at the location of the Service Boxes. Digitizer boards from a pre-production run are used to read out the data of the module burn-in stand described above, and in a similar setup used in the Inner Tracker module production at CERN. The series production of the boards is scheduled for summer 2006.

7.6 Detector simulation and reconstruction software

In preparation for data taking, a considerable software effort has been undertaken in our group to provide a detailed description of the Silicon Tracker and its performance in the framework of the LHCb Monte-Carlo and reconstruction programs. As input for the GEANT4-based LHCb detector simulation, a detailed XML description of the geometry of the Trigger Tracker, including sensitive detector elements as well as dead material, has been prepared by D. Volyanskyy and A. Wenger under the guidance of M. Needham. A refined description of the signal generation in the detector has been implemented and tuned to reproduce the detector performance measured in various test beams and laboratory tests. Furthermore, the final detector readout partitioning and data format have been defined and Monte-Carlo generated events are now stored in the same data format in which data will later be provided by the detector. This will permit more precise estimates of the expected data volumes and will significantly simplify the transition of the reconstruction code from Monte-Carlo to "real" data. The development and optimisation of track reconstruction algorithms is continuing.

M. Needham having left our group in November 2005, his responsibilities in these areas have been taken over by J.v. Tilburg, who joined us in February 2006. J.v. Tilburg has also started to participate in the development of alignment algorithms for the LHCb tracking system.

7.6.1 Workshop on tracking in high multiplicity environments

Members of our group organised a workshop on Tracking in High Multiplicity Environments, which took place at our institute in October 2005. The workshop brought together about 50 physicists working on hardware and software aspects of tracking devices, with the aim of transferring experience from running High Energy Physics experiments to those currently under development. Topics covered in the workshop included operational and system aspects, tracking and vertexing algorithms, radiation environments and aging, and detector technologies. Introductions to these topics were given by invited keynote speakers. All presentations are available on the conference web page, the proceedings will be published in a special edition of Nucl. Instr. and Meth. A.

Figure 7.9: Conference poster for the TIME 2005 workshop.

7.7 Physics studies

In parallel to our detector-related activities, work on physics simulation studies has also continued in our group. Such studies are required to understand the physics reach of the experiment, to investigate possible sources of systematic uncertainty and to optimize trigger selection criteria. We have chosen to concentrate our efforts on the decay mode $B_s \to J/\psi\eta'$. A time-dependent measurement of the CP asymmetry can be used to determine the phase of $B_s\overline{B_s}$ oscillations (i.e. the CKM angle χ). Since this phase is predicted to be very small in the Standard Model, a high precision measurement provides a sensitive search for contributions from "new" physics beyond the Standard Model (8).

This work is being undertaken by D. Volyanskyy as part of his Ph.D. thesis, under the guidance of M. Needham and U. Straumann. An initial optimisation of selection cuts has been performed and, for these cuts, a background-to-signal ratio of around one and an annual signal yield of about 5.3 k reconstructed events have been estimated, respectively. Specific background studies have been carried out to test the performance of the selection cuts in suppressing events from b hadron decays with similar event topologies to that of the signal decay. Invariant-mass, primary-vertex and secondary-vertex resolutions have been estimated and a proper-time resolution of (34.8 $\pm$ 1.2) fs has been found. This resolution is sufficient to perform a precise measurement of the time-dependent CP asymmetry. In the near future, an overall re-optimisation of selection cuts will be performed using a random grid search. This will allow to better take into account correlations between the different cuts. Larger samples of Monte-Carlo events will be processed in order to obtain more precise estimates of the expected background-to-signal ratio. Based on the results of these investigations, a study of the sensitivity of LHCb to the CP-violating parameters will finally be performed.

7.8 Summary and outlook

The series production of detector modules for the Trigger Tracker has been launched in 2005 and will be completed in autumn 2006. A detailed testing and quality assurance programme is performed on all modules. For this purpose, a burn-in stand has been set up in our laboratory. The setup uses final readout electronics and also serves as a small-scale prototype for the final detector box. All silicon sensors for the Silicon have been received from industry, the quality assurance programme on these sensors is close to being completed. The Trigger Tracker detector box is being assembled and will soon be commissioned in our institute. The detector will be shipped to CERN and installed in the experiment in autumn 2006. The final readout electronics are routinely used in the module testing, the series production of the electronics boards will start very soon.

Software developments for detector simulation and reconstruction algorithms are ongoing. In preparation for physics analyses, the group continues its work on simulation studies, especially concentrating on a study of the decay mode $B_s \to J/\psi\eta'$ and the sensitivity of LHCb to the phase of $B_s\overline{B_s}$ oscillations in this decay mode.

[1] **LHCb technical proposal**, CERN/LHCC 998-4.

[2] **LHCb Reoptimised Detector Technical Design Report**, CERN/LHCC 2003-030.

[3] **LHCb Inner Tracker Technical Design Report**, CERN/LHCC 2002-029.

[4] **Layout and expected performance of the LHCb TT station**, J. Gassner, M. Needham, O. Steinkamp, LHCb note 2003-140.

[5] **The Mechanical Design of the LHCb Silicon Trigger Tracker**, J. Gassner, F. Lehner, S. Steiner, LHCb note 2004-110.

[6] **The Production, Assembly and Testing of the LHCb Silicon Trigger Tracker**, J. Gassner, F. Lehner, S. Steiner, LHCb note 2004-109.

[7] **Pre-Series Sensor Qualification for the Inner Tracker of LHCb**, G. Baumann et al., LHCb note 2005-037.

[8] J.P. Silva and L. Wolfenstein, Phys. Rev. **D 55** (1997) 5331.

8 Particle Physics with CMS

E. Alagöz, C. Amsler, V. Chiochia, C. Hörmann, K. Prokofiev[5] , H. Pruys[6], C. Regenfus, P. Robmann, J. Rochet, T. Speer, S. Steiner, D. Tsirigkas[7], and L. Wilke

In collaboration with: ETH - Zürich, Paul Scherrer Institut (PSI) and the CMS Collaboration

Physics at the LHC is the main activity of the Zurich group. We are interested in B-physics issues which can be performed during the first 2- 3 years of LHC operation, when the luminosity will still be too low for Higgs searches. In particular, we are preparing with the decay $B_s^0 \rightarrow (J/\psi)\phi \rightarrow \mu^+\mu^- K^+K^-$ a measurement of $B_s^0 - \bar{B}_s^0$ oscillations, of the lifetime of the CP-eigenstates B_s^H and B_s^L, and of CP-violation. Our group is contributing to the CMS reconstruction and simulation software using the pixel vertex detector required to efficiently tag B-decays. T. Speer has been appointed CMS coordinator for B - tagging. We are involved in the design, construction and test of the barrel pixel detector, a three layer cylindrical silicon device built mostly by Swiss institutions. We are responsible for performance measurements on test beams at CERN (such as position resolution, Lorentz angle and efficiency) on highly irradiated prototypes, and are leading the preparation of the online performance monitoring programs. V. Chiochia is coordinating the CMS pixel offline software group. We are also involved in the development of the sensor readout chip at PSI, and of the power distribution to the pixel detector. The mechanical support structure, cooling system and service tubes are built in the workshop of the Physik-Institut. Details on the software and detector performance can be found in the physics technical design report (1).

8.1 B - physics with CMS

The LHC will be commissioned in 2007 with an initial luminosity of about $10^{30} - 10^{33}$ cm^{-2}s^{-1}. An integrated luminosity of 30 fb^{-1} will be collected after three years of data-taking (assuming an overall beam and detector on efficiency of 30%), after which the luminosity will hopefully reach the design value of 10^{34} cm^{-2}s^{-1}. The main motivation for CMS is the search for the Higgs boson and for supersymmetric particles. However, unless the Higgs is heavy, a significant signal will not be observed during the first 2 - 3 years of operation at low luminosity. Meanwhile, our group intends to concentrate on issues related to the B_s-meson, making full use of the pixel vertex detector.

We intend to perform a high statistics study of the channel $B_s^0 \rightarrow (J/\psi)\phi$ with $J/\psi \rightarrow \mu^+\mu^-$ and $\phi \rightarrow K^+K^-$. This is a good channel to study many properties of B_s^0 - mesons, such as CP - violation, $B_s^0 - \bar{B}_s^0$ oscillations, and to measure the lifetimes of the two eigenstates, B_s^H and B_s^L. The pixel detector is an essential component for these studies requiring a precise determination of the mean life of the B_s^0-meson. Its relatively long lifetime (1.46 $\pm$ 0.06 ps) can be used to reject the short-lived background.

B_s^0 - $\bar{B}_s^0$ oscillations have not been observed so far since the oscillation frequency Δm_s is large. The lower limit (95% C.L.) on Δm_s is currently 14.4 ps^{-1} (2). The relative difference between the mean lives of B_s^H and B_s^L is also predicted to be large, in the range 10 - 20%.

CP - violation and particle-antiparticle mixing can also be studied with $B_s^0 \rightarrow (J/\psi)\phi$. This

[5] until September 2005
[6] until August 2005
[7] CERN doctoral student

decay proceeds mainly through the tree spectator diagram (Fig. 8.1a), second order processes (such as penguin diagrams, Fig. 8.1b) being suppressed.

A full reconstruction of the B_s^0 is achieved through the decays $J/\psi \to \mu^+\mu^-$ and $\phi \to K^+K^-$. CP - violation is induced by interference between the decay and particle–antiparticle mixing. One measures the (CP - violating) asymmetry between $B_s^0 \to (J/\psi)\phi$ and $\bar{B}_s^0 \to (J/\psi)\phi$ which requires tagging the flavor of the B_s^0. An alternative method is to measure the angular distributions of the final state kaons and muons. The CP - even and CP - odd components correspond to even, respectively odd, relative angular momenta between the J/ψ and the ϕ, and have therefore different angular distributions (3). This does not require tagging but very large data samples which can be obtained at the LHC. The decay rate asymmetry determines the CP - violating weak phase $\phi_{CKM} = 2\lambda^2\eta$, where $\lambda \equiv V_{us}$ and η is the height of the unitarity triangle, expected to be very small (about 0.03). The measurement of a significantly larger phase would indicate contributions from processes beyond the standard model.

The branching fraction for $B_s^0 \to (J/\psi)\phi$ is about 10^{-3} (2). With the help of simulations we have developed a selection strategy for the final state $K^+K^-\mu^+\mu^-$ relying on the reconstruction of the four charged particles by a high level trigger (HLT) (4). An event of this type is shown in Fig. 8.2. The muon trigger selects two muons of opposite charges from the muon chambers with a transverse momentum above 3 GeV/c. We require two muons tracks of opposite charges with mass within 100 MeV of the J/ψ mass, and two kaon tracks of opposite charges with mass within 100 MeV of the ϕ mass. The four tracks are required to come from a common secondary vertex. The trigger efficiency is about 10% (4).

Considerable progress was made in 2005 in the development of the tracking and vertex software (5). A general kinematic fitting program was developed for CMS (4). The kinematic fit can be applied to $B_s \to (J/\psi)\phi \to K^+K^-\mu^+\mu^-$ during offline reconstruction to increase the experimental resolution on the B_s^0 mass which improves from 34 MeV to 14 MeV (Fig. 8.3).

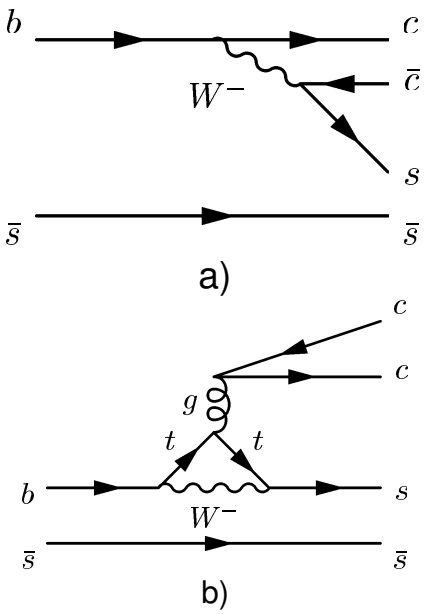

Figure 8.1: Feynman diagram for the $B_s^0 \to (J/\psi)\phi$ decay (a). The penguin diagram (b) is suppressed.

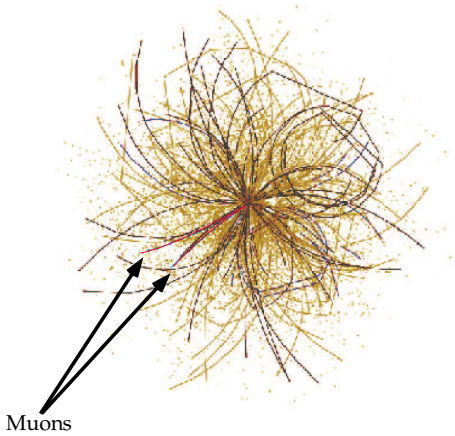

Figure 8.2: A typical simulated event at CMS which contains a decay of the type $B_s^0 \to (J/\psi)\phi \to \mu^+\mu^-K^+K^-$.

Some 250'000 signal events would be reconstructed after 2 years of LHC running with a background of about 40'000 events. For comparison, only a few hundred events have been

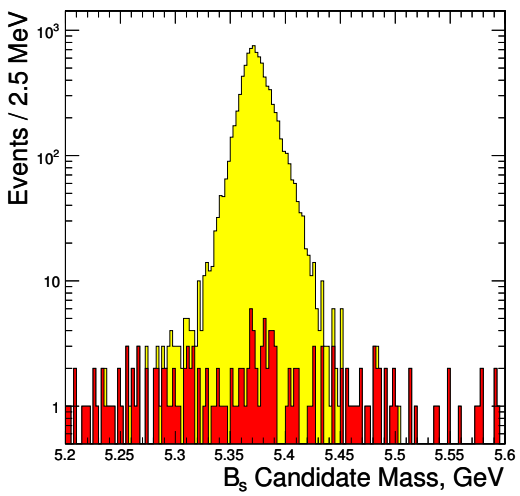

Figure 8.3: Invariant mass distribution of $B_s \rightarrow (J/\psi)\ \phi$ after the kinematics fit (yellow area). The bottom (red) area is the residual combinatorial background.

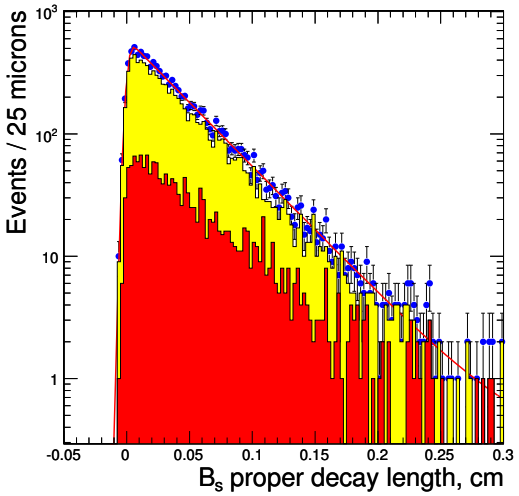

Figure 8.4: Distribution of decay length in the B_s rest frame showing the B_s^L contribution in yellow and the B_s^H contribution in red. The red curve is a two - component exponential fit (from ref. [4]).

observed so far for this decay channel. The resolution on the proper decay length ($c\tau_s$) of the B_s^0 meson is about 30 μm, from which one concludes that the observation of $B_s^0 - \bar{B}_s^0$ oscillations is possible with CMS, provided that the oscillation frequency is close to its present lower limit of 14.4 ps^{-1}.

However, the lifetime difference between the two CP eigenstates B_s^H and B_s^L is too small to be measured directly. Figure 8.4 shows a double exponential fit to the decay length distribution. This task will require an analysis of the angular correlations in the $K^+K^-\mu^+\mu^-$ final state which are different for B_s^H and B_s^L. A corresponding study is in progress. We are investigating in parallel the analogous decay $B_s \rightarrow (J/\psi)\ \phi$ where $J/\psi \rightarrow e^+e^-$. This decay will increase the B_s^0 sample, but the reconstruction of low-momentum electrons is notoriously difficult.

8.2 Silicon pixel sensors

The pixel detector consists of three concentric cylindrical layers, 53 cm long, with radii of 4.4, 7.3 and 10.2 cm, and forward/backward wheels. The pixel sensors are mounted on segmented silicon plates and are connected by indium bump bonds to the readout chips. The analog signals are read out using charge sharing between pixels to determine the coordinates more accurately. Details can be found in previous annual reports.

We have tested prototypes of sensors (pixel size 125$\times$125 μm^2) with 105 - 225 GeV pions in the H2 beam line of the CERN SPS and measured the charge collection, hit detection efficiencies and the Lorentz angle (6; 7; 8; 9). Oxygenated pixel sensors with p-spray isolation (manufactured by CiS, Erfurt) were chosen. The pixel cell size was finally fixed to 100$\times$150 μm^2.

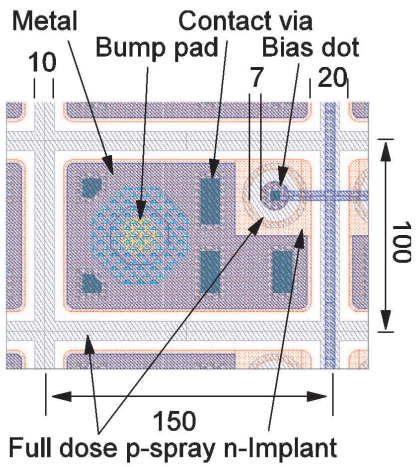

Figure 8.5: Pixel cell layout for the barrel detector.

Figure 8.5 shows a sketch of the final pixel cell layout.

In pixel sensors effects due to irradiation can be investigated with the grazing angle technique (8). As shown in Fig. 8.6 the surface of the sensor is tilted by a small angle (15°) with respect to the pion beam. The charge measured by each pixel along the x direction samples a different depth z in the sensor. The precise entry point is measured with our silicon beam telescope which measures tracks with an r.m.s. position resolution of about 1 μm (10). For un-irradiated sensors the cluster length determines the depth over which charge is collected in the sensor.

The profiles measured with an un-irradiated sensor and with a sensor irradiated to a fluence of 6×10^{14} $\mathrm{n_{eq}/cm^2}$ are shown in Fig. 8.7 as a function of the distance x from the beam entry point. This fluence corresponds to the first four years of LHC operation for the innermost layer. The un-irradiated sensor was operated at a bias voltage of 150 V, well above its depletion voltage of 70 V). The irradiated sensor was operated at bias voltages between 150 V

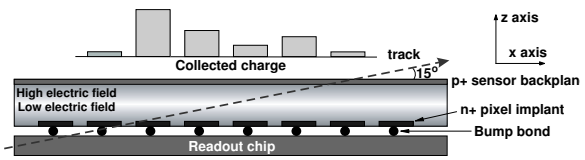

Figure 8.6: Grazing angle method to determine the charge collection profiles.

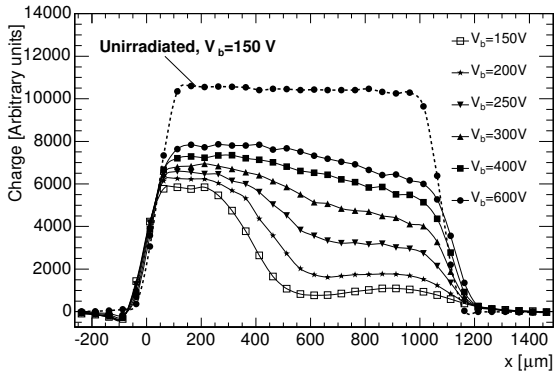

Figure 8.7: Charge collection profiles measured with an un-irradiated (dashed line) sensor and a sensor irradiated to 6×10^{14} $\mathrm{n_{eq}/cm^2}$ (solid lines). The latter is operated at bias voltages V_b between 150 V and 600 V.

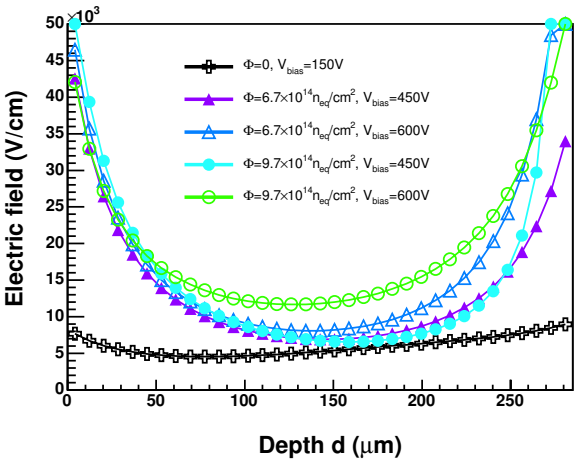

Figure 8.8: Electric field as a function of sensor depth (from ref. [7]). The regions immediately below the surfaces ($\sim$ 20μm) are affected by large systematic uncertainties (not shown).

and 600 V. It appears to be partly depleted at 150 V, but a second peak is observed at large x. By increasing the bias voltage one also increases the amplitude of the second peak, as more charge is collected from the sensor side close to the backplane, while the increase at the n+ side is about 30%. At 600 V charge collection is saturated but the profile is not uniform due to the trapping of carriers produced far from the collecting electrode.

When a magnetic field is applied along the x-direction, the charge is deflected in the y-direction towards the adjacent pixel row. A measurement of the charge distribution among adjacent pixels yields the Lorentz angle θ_L as a function of x, and hence sensor depth. The Lorentz angle appears to depend on depth. A measurement of θ_L as a function of depth determines the behaviour of the electric field. Using a known empirical parameterization of the mobility one can extract the electric field as a function of sensor depth (7). The electric field reaches maxima below both surfaces and a minimum in the bulk center (Fig. 8.8). This behaviour in irradiated sensors does not correspond to the classical picture of a partially depleted sensor, but can be described by a double junction model (11).

A detailed modeling (PIXELAV) of charge collection in heavily irradiated sensors was developed in collaboration with M. Swartz from Johns Hopkins University. This model takes into account e.g. the charge deposition by hadrons, a 3D intrapixel electric field map, the mobility, diffusion and trapping, and a simulation of the electronic noise (12). Simulations were performed and tuned on the tests results described above for the 125×125 μm^2 sensors. The charge collection profiles for a sensor irradiated to a fluence of 2×10^{14} n$_{\rm eq}$/cm^2 and operated at several bias voltages are presented in Fig. 8.9. The measured profiles are compared to the simulated PIXELAV profiles. The simulation describes the measured charge collection profiles rather well, both in shape and normalization. In particular, the wiggle observed at low bias voltages is also described correctly.

Our simulations can now be applied to the final pixel dimensions of 100×150 μm^2. Since charge is shared among several pixels on can improve on the position resolution by applying the so - called η correction (13). The hit position is first calculated with the center of gravity method. The η fraction is defined as the non - integer part of the reconstructed pixel number. Figure 8.10 shows the distribution of η for all events, where $\eta = 0$ corresponds to the

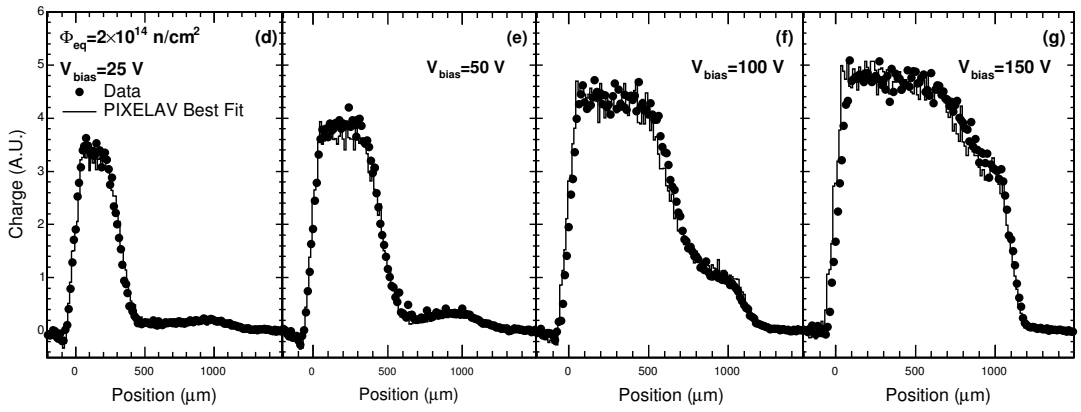

Figure 8.9: Measured (dots) and simulated (histogram) charge collection profiles for a sensor irradiated to a fluence of 2×10^{14} n$_{\rm eq}$/cm^2 and operated at several bias voltages. The simulation was performed with the PIXELAV software (from ref. [11]).

center of the pixel cell and $\eta = \pm 0.5$ to the borders. The measured distribution is almost flat in the pixel regions close to the pixel borders but has a dip at the center. The peak at $\eta = 0$ is due to single pixel clusters. For each η one then associates a corrected value given by the function

$$F(\eta) = \frac{\int_{-0.5}^{\eta} \frac{dN}{d\eta}\, d\eta}{\int_{-0.5}^{0.5} \frac{dN}{d\eta}\, d\eta} - \frac{1}{2}, \qquad (8.12)$$

where η is in pixel units. The $F(\eta)$ function is shown in Fig. 8.11. The corrected position is calculated by adding $F(\eta)$ to the integer part of the pixel number.
Figure 8.12 shows the residual distribution for clusters of two pixels, simulated for a sensor irradiated to 5.9×10^{14} n_{eq}/cm^2, and for tracks with an incident angle of 20° with respect to the normal to the sensor surface. The distribution before correction (left) is not described by a single Gaussian and is affected by large systematic errors which depend on the hit position. Systematic errors can be largely reduced by applying the η-correction (Fig. 8.12, right). This simulation shows that resolutions below 15 μm can be achieved after irradiation. A comparison with beam tests of the final sensors will be performed in 2006.

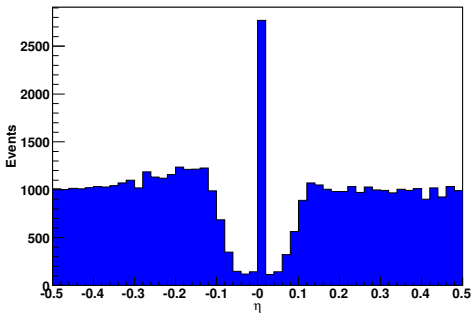

Figure 8.10: Distribution of the reconstructed impact position within a single pixel for perpendicular tracks.

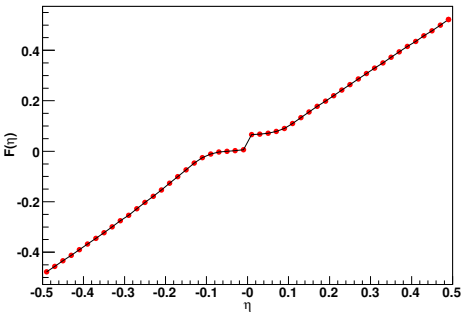

Figure 8.11: Correction function $F(\eta)$ (from ref. [14]).

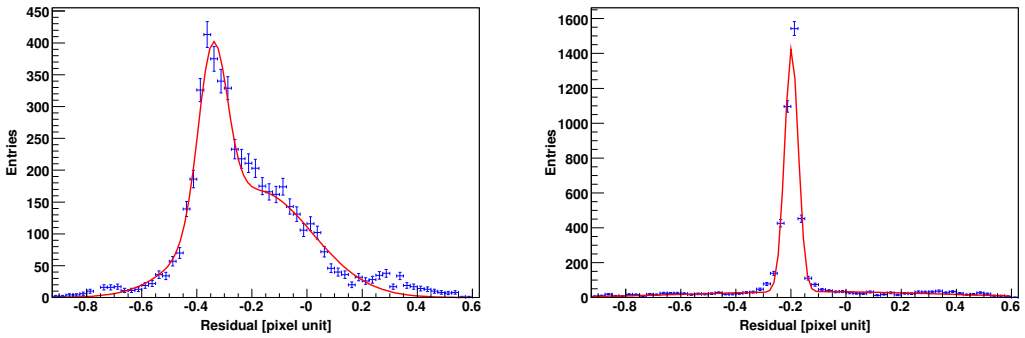

Figure 8.12: Residual (simulated - reconstructed hit) distribution for tracks with an incident angle of 20°. The distributions are calculated without (left) and with η-corrections (right) and are not corrected for the Lorentz shift due to the magnetic field. The simulated data points are represented by markers and the continuous line is a double-Gaussian fit to the distribution (from ref. [14]).

8.3 Readout electronics

We have also contributed to the readout chip (ROC), the design of which is under the direct responsibility of PSI. The ROC, manufactured in CMOS 0.25 μm technology by IBM, has a much higher yield (80%) than our previous prototype in DMILL radiation hard technology (20%). The first complete module (16 ROC chips, each reading 52 $\times$ 80 pixels) were irradiated with 300 MeV/c pions at PSI (Fig. 8.13 and 8.14). The purpose was to measure the efficiency as a function of inclination ϕ and readout threshold, and to check the timing performance. The incoming intensity was typically 40 MHz/cm^2 (corresponding to the rate in the first pixel layer at 4.4 cm in LHC). The trigger was provided by two scintillators of dimensions 2 $\times$ 2 $\times$ 2 mm^3 (which counted at a rate of 1 MHz) in coincidence with an americium radioactive source to simulate the level 1 trigger in CMS. The data analysis is in progress (15).

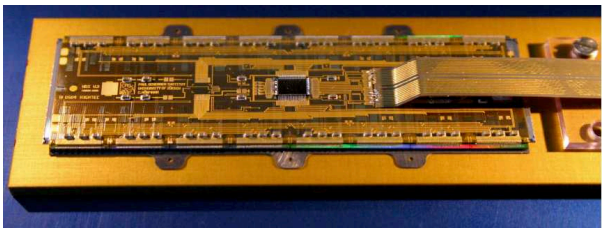

Figure 8.13: First assembled module consisting of 16 PSI46V2 readout chips bump-bonded to a sensor with 66'560 pixels.

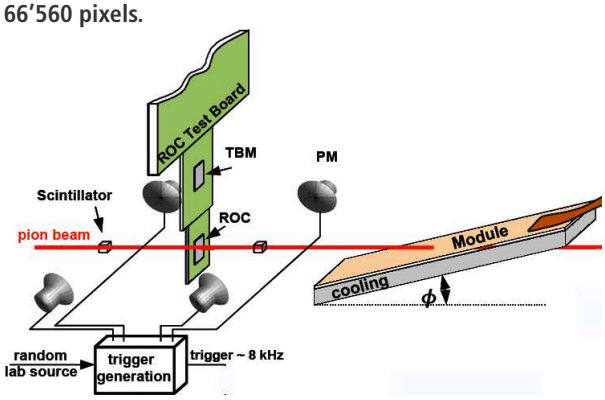

Figure 8.14: Setup for the beam tests at PSI.

8.4 Mechanical support structure

The Institute's workshop is building the support structure for the barrel pixel detector and the service tubes along the beam line. The pixel detector consists of three 57 cm long layers (Fig. 8.15) equipped with silicon pixel modules and two 2.2 m long service tubes. Two vertically separated half shells will be introduced into the CMS detector. The support structure consists of individual ladders built of pure aluminum tubes with trapezoidal cross sections and wall thickness of 300 μm.

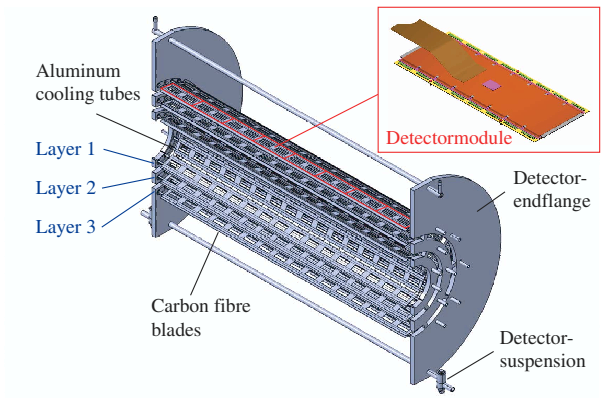

Figure 8.15: Half shell of the support structure with the three detector layers.

Custom made 240 μm thick carbon fiber blades which support the pixel modules are glued to the tubes, forming the detector segments (Fig. 8.16). Four to five of these tubes are then laser welded to an aluminum container which distributes the coolant. The manifold provides the cooling of the detector modules to about -10°C with C_6F_{14}. Support frames on both ends

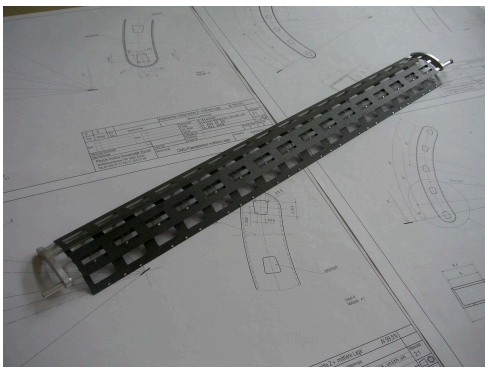

Figure 8.16: Prototype segment. The aluminum tubes are laser welded to the end-flange containers that distribute the cooling fluid.

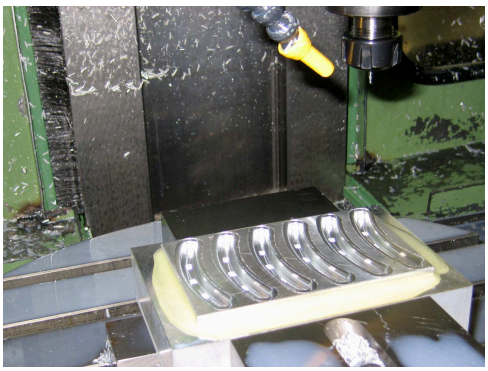

Figure 8.17: Production of the carbon fiber blades (upper picture) and of the cooling containers (lower picture) on the milling machines of the Physik - Institut.

connect the segments and form a detector layer half shell. The flanges consist of thin fiberglass frames (FR4) filled with foam (Airex) covered by carbon fiber blades. This technique guarantees stability and precision for a minimum mass. Mass production of the various components (blades, cooling containers, etc.) is performed in our workshop (Fig. 8.17). The laser welding technique (in collaboration with industry) was strongly improved. We have upgraded the welding equipment to prevent leakage of the coolant and have obtained higher quality welding seams than achieved before.

The electrical power, control and optical signals and the coolant are transferred to the detector through supply tubes. The forward and backward supply tubes are mechanically connected and carry the pixel detector. The structure is made of tubes and is filled with foam. The motherboards (Fig. 8.18) holding the optical hybrids for analog and digital controls, will be installed near the detector. The outer ends contain power regulators and connectors for the electrical and optical lines, and the central region the digital control boards and slow controls, such as voltages, currents, temperatures, pressures and humidity.

The project proceeds according to schedule. The 800 modules required for the three pixel layers will be assembled at PSI. In 2006 our group will perform further beam tests at CERN. Production of the parts for the three layers is proceeding in our workshop. Prototypes of the service tubes will be built in 2006. The pixel detector will be introduced into CMS after the LHC commissioning in 2007, to prevent damage during initial beam tuning. We are preparing a test support structure for the 2007 pilot run, consisting of a half shell partially equipped with detectors.

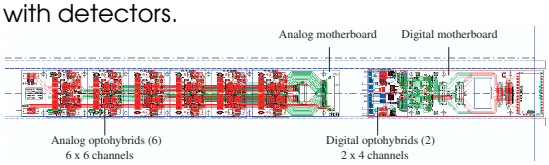

Figure 8.18: Sketch of the readout slot with the analog and digital motherboards holding the optical hybrids.

[1] E. Alagöz *et al.*, CMS TDR I : Software and detector performance, CMS - TDR - 08, CERN-LHCC-2006-001.

[2] S. Eidelman *et al.* (Particle Data Group), Phys. Lett. **B 592** (2004) 1.

[3] A.S. Dighe *et al.*, Phys. Lett. **B 269** (1996) 144; Eur. J. Phys. **C6** (1999) 647.

[4] K. Prokofiev, PhD Thesis, Universität Zürich (2005); K. Prokofiev Proc. 10th Int. Conf. on B-Physics at Hadron Machines (BEAUTY 2005), Assisi, Nucl. Phys. **B** Proc. Suppl. **156** (2006) 109.

[5] T. Speer *et al.*, Proc. of the Workshop on Tracking in High Multiplicity Environments (TIME 2005), Zurich (in print); T. Speer and R. Frühwirth, Comp. Phys. Comm (in print).

[6] R. Kaufmann, PhD Thesis, Universität Zürich (2001).

[7] A. Dorokhov, PhD Thesis, Universität Zürich (2005); A. Dorokhov *et al.*, Proc. Vertex 2004 Conf., Como, 2004, Nucl. Instr. Meth. in Phys. Research **A** (in print), prep. physics/0412036.

[8] A. Dorokhov *et al.*, Nucl. Instr. and Meth. in Phys. Research **A 530** (2004) 71.

[9] T. Rohe *et al.*, Nucl. Instr. and Meth. in Phys. Research **A 552** (2005) 232.

[10] C. Amsler *et al.*, Nucl. Instr. and Meth. in Phys. Research **A 480** (2002) 501.

[11] V. Chiochia *et al.*, Proc. 2004 IEEE Trans. on Nucl. Sc. **52** (2004) 1067; V. Chiochia *et al.*, Proc. 10th Eur. Symp. on Semiconductor Detectors, Wildbad-Kreuth, Nucl. Instr. Meth. in Phys. Research **A** (in print), prep. physics/0506228.

[12] M. Swartz, Nucl. Instr. and Meth. in Phys. Research **A 511** (2003) 88.

[13] E. Belau *et al.*, Nucl. Instr. and Meth. **214** (1983) 253.

[14] E. Alagöz, V. Chiochia, M. Swartz, Proc. of the Workshop on Tracking in High Multiplicity Environments (TIME 2005), Zurich, Nucl. Instr. Meth. in Phys. Research **A** (in print), prep. physics/0512027.

[15] C. Hörmann, PhD Thesis, Universität Zürich, in preparation.

9 Superconductivity and Magnetism

D.G. Eshchenko, H. Keller, R. Khasanov, S. Kohout (till August 2005), I. Landau (October till December 2005), F. La Mattina, A. Maisuradze, T. Paraiso (June 2005 till February 2006), J. Roos, A. Shengelaya (till November 2005), S. Strässle, S. Weyeneth (since October 2005)

Visiting scientists: A. Dooglav, V.A. Ivanshin, B. Kochelaev, I.M. Savić

Emeritus members: Prof. K.A. Müller (Honorarprofessor), Prof. T. Schneider (Titularprofessor), Dr. M. Mali

in collaboration with:
ETH Zürich (K. Conder, J. Karpinski), Paul Scherrer Institute (K. Conder, E. Morenzoni), Max-Planck-Institute for Solid State Research Stuttgart (A. Bussmann-Holder), IBM Rüschlikon Research Laboratory (J.G. Bednorz), University of Birmingham (E.M. Forgan), University of Rome (A. Bianconi, D. Di Castro), Kazan State University (A. Dooglav, M.V. Eremin, V. Ivanshin, B.I. Kochelaev), University of Belgrade (I.M. Savić), University of Tokyo (T. Sasagawa, H. Takagi)

In the last year we continued our research projects on the magnetic and electronic properties of novel superconductors and related materials by means of a combination of various complementary experimental techniques, such as muon-spin rotation (μSR), low-energy μSR (LE-μSR), electron paramagnetic resonance (EPR), nuclear magnetic resonance (NMR), nuclear quadrupole resonance (NQR), as well as SQUID and torque magnetometry. In particular, detailed isotope-effect and pressure-effect studies in novel superconductors were performed. The aim of our research activities is to explore the *macroscopic* and *microscopic* physical properties of cuprate high-temperature superconductors (HTS), other novel superconductors, and related materials in order to understand the basic physics of these systems. In addition, in collaboration with the IBM Rüschlikon Laboratory we continued our investigations of electric-field effects on the electronic structure of Cr-doped strontium titanate by means of EPR.

9.1 Studies of isotope effects in novel superconductors

9.1.1 μSR investigation of the oxygen-isotope effect on the in-plane penetration depth in cuprate high-temperature superconductors close to optimal doping

The observation of unusual oxygen-isotope (^{16}O/^{18}O) effects (OIE's) in cuprate high-temperature superconductors (HTS) on the transition temperature T_c (1; 2; 3; 4) and on the zero-temperature in-plane magnetic penetration depth $\lambda_{ab}(0)$ (3; 4; 5; 6; 7; 8; 9; 10; 11) poses a challenge to the understanding of high-temperature superconductivity. Recently, it was established that for different families of cuprate HTS there is the universal correlation between the isotope shifts of T_c and $\lambda_{ab}(0)$ (4; 7; 10; 11). Namely, in the underdoped region $\Delta T_c/T_c$ and $\Delta\lambda_{ab}(0)/\lambda_{ab}(0)$ scale linearly in respect to each other with $|\Delta T_c/T_c| \simeq |\Delta\lambda_{ab}(0)/\lambda_{ab}(0)|$. However, close to optimal doping the situation is not so clear. Khasanov *et al.* (10) observed that in optimally doped $YBa_2Cu_3O_{7-\delta}$ the small OIE on T_c is associated with a rather big isotope shift of $\lambda_{ab}(0)$ which is even compatible with that in underdoped cuprates. In contrast, Tallon *et al.* (11) found that in slightly overdoped $La_{2-x}Sr_xCu_{1-y}Zn_yO_4$ the OIE on $\lambda_{ab}(0)$ becomes zero, while the OIE on T_c remains still substantial.

In order to clarify this discrepancy the OIE's on T_c and $\lambda_{ab}(0)$ were investigated by means of magnetization and muon-spin rotation (μSR) experiments in optimally doped $YBa_2Cu_3O_{7-\delta}$ and $La_{1.85}Sr_{0.15}CuO_4$, as well as in slightly underdoped $YBa_2Cu_4O_8$ and $Y_{0.8}Pr_{0.2}Ba_2Cu_3O_{7-\delta}$. We observed a small OIE on the transition temperature T_c that is associated with a substantial OIE on the in-plane penetration depth $\lambda_{ab}(0)$ (see Fig. 9.1). The fact that a substantial oxygen-isotope effect on $\lambda_{ab}(0)$ is observed even in cuprates with a rather small OIE on T_c strongly suggests that phonons are *directly* or *indirectly* involved in the pairing. It is worth to note that in colossal magnetoresistance (CMR) manganites similar peculiar OIE on various quantities (e.g.ferromagnetic transition temperature, charge-ordering temperature) were observed (13). This suggests that in both classes of perovskites, HTS and CMR manganites, lattice vibrations play an essential role.

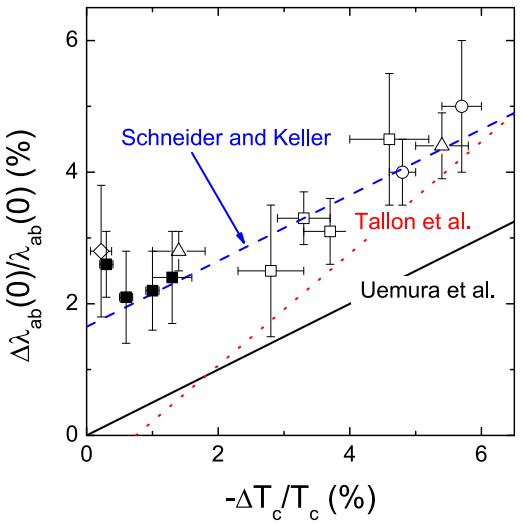

Figure 9.1: Plot of the OIE shift of the zero-temperature magnetic penetration depth $\Delta\lambda_{ab}(0)/\lambda_{ab}$(0) versus the OIE shift of the superconducting transition temperature $-\Delta T_c/T_c$ for $Y_{1-x}Pr_xBa_2Cu_3O_{7-\delta}$, $YBa_2Cu_4O_8$, and $La_{2-x}Sr_xCuO_4$ (closed squares). Open squares are bulk μSR data for $Y_{1-x}Pr_xBa_2Cu_3O_{7-\delta}$ [7; 8]. Diamonds are LE-μSR data for optimally doped $YBa_2Cu_3O_{7-\delta}$ [9]. Open circles are torque magnetization data for $La_{2-x}Sr_xCuO_4$ from [6]. Open triangles are Meissner-fraction data for$La_{2-x}Sr_xCuO_4$ [5]. The solid line corresponds to the "differential Uemura" relation with $\Delta\lambda_{ab}(0)/\lambda_{ab}(0) = 0.5|\Delta T_c/T_c|$. The dotted line corresponds to the "pseudogap" line from [11]. The dashed line indicates the flow to 2D quantum superconductor to insulator criticality as described in [12].

[1] J.P. Franck, in Physical Properties of High Temperature Superconductors IV (ed. D.M Ginsberg), 189-293 (World Scientific, Singapore, 1994).

[2] D. Zech et al., Nature **385**, 681 (1994).

[3] G.-M. Zhao, H. Keller, and K. Conder, J. Phys.: Cond. Mat. **13**, R569 (2001).

[4] H. Keller, in Structure and Bonding, Vol. 114, 143-169 (2005), A. Bussmann-Holder and K.A. Müller, eds., Springer-Verlag Berlin Heidelberg (2005).

[5] G.-M. Zhao, M.B. Hunt, H. Keller, and K.A. Müller, Nature **385**, 236 (1997).

[6] J. Hofer et al., Phys. Rev. Lett. **84**, 4192 (2000).

[7] R. Khasanov et al., J. Phys.: Condens Matter **15**, L17 (2003).

[8] R. Khasanov et al., Phys. Rev. B **68**, 220506 (2003).

[9] R. Khasanov et al., Phys. Rev. Lett. **92**, 057602 (2004).

[10] R. Khasanov et al., J. Phys.: Cond. Mat. **16**, S4439 (2004).

[11] J.L. Tallon et al., Phys. Rev. Lett. **94**, 237002 (2005).

[12] T. Schneider and H. Keller, Phys. Rev. Lett. **86**, 4899 (2001).

[13] G.M. Zhao, H. Keller, R.L. Greene, and K.A. Müller in Physics of manganites, T.A. Kaplan and S.D. Mahanti (eds.), Kluwer Academic/Plenum Publishers, New York, p. 221 (1999).

9.2 Studies of pressure effects in novel superconductors

9.2.1 Anomalous electron-phonon coupling probed on the surface of the superconductor ZrB_{12}

The traditional concept of superconductivity is strictly associated with the electron-phonon interaction. The conventional theory is based on the Migdal-Eliashberg adiabatic approximation (1) that leads to the prediction of many peculiar features which are a direct evidence of phonon-mediated superconductivity. The adiabatic approximation is valid if the parameter ω_0/E_f is small (ω_0 is the relevant phonon frequency and E_f is the Fermi energy). Most conventional superconductors satisfy this criteria with very few exceptions. Zirconium dodecaboride (ZrB_{12}) is a good candidate for anomalous (nonadiabatic) coupling. It stems from the rather small value of the Fermi energy $\sim$1 eV (2) that, together with the Debye temperature $\sim$20 meV (3), leads to a ratio ω_0/E_f $\sim$0.02. One of the key features of nonadiabatic superconductivity is the observation of unconventional isotope and pressure effects on the magnetic field penetration depth λ. Note, that in adiabatic superconductors (or in superconductors where nonadiabatic effects are small) the pressure effect (PE) (4; 5), as well as the isotope effect (IE) (6) on λ were found to be almost zero, in contrast to the substantial PE (7) and IE (8) on λ observed in highly nonadiabatic cuprate HTS.

We performed detailed studies of the PE on T_c and λ in ZrB_{12} (9). A *negative* pressure effect on T_c with $\mathrm{d}T_c/\mathrm{d}p = -0.0225(3)$ K/kbar is observed (see Fig. 9.2(a)). The magnetic field penetration depth λ measured in the Meissner state is largely determined by surface characteristics. The superfluid density $\rho_s(0) \propto \lambda^{-2}(0)$ was found to increase with pressure, with the pressure effect coefficient $\mathrm{d}\ln\lambda^{-2}(0)/\mathrm{d}p = 0.60(23)$ %/kbar (see Fig. 9.2(b)). This coefficient is much larger than that one estimated theoretically within the adiabatic approximation. This can be explained by considering that in ZrB_{12} the coupling of the charge carriers to the lattice close to the surface has a *nonadiabatic* character (9).

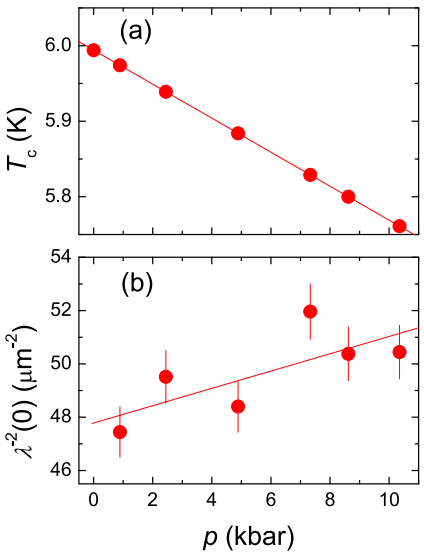

Figure 9.2: Pressure dependences of the transition temperature T_c (a) and the superfluid density $\rho_s(0) \propto \lambda^{-2}(0)$ (b) of ZrB_{12}. The solid lines are linear fits as described in [9].

[1] A.B. Migdal, Sov. Phys. JETP **7**, 996 (1958); G.M. Eliashberg, Sov. Phys. JETP **11**, 696 (1960).

[2] D. Daghero et al., Supercond. Sci. Technol. **17**, S250 (2004).

[3] R. Lortz et al., cond-mat/0502193.

[4] R. Khasanov et al., Phys. Rev. Lett. **93**, 157004 (2004).

[5] D. Di Castro et al., cond-mat/0411719.

[6] D. Di Castro et al., Phys. Rev. B **70**, 014519 (2004).

[7] R. Khasanov, J. Karpinski, and H. Keller, J. Phys.: Condens. Matter **17**, 2453 (2005).

[8] G.M. Zhao, M.B. Hunt, H. Keller, and K.A. Müller, Nature (London) **385**, 236 (1997); J. Hofer et al., Phys. Rev. Lett.

84, 4192 (2000); R. Khasanov et al., Phys. Rev. Lett. **92**, 057602 (2004); R. Khasanov et al., J. Phys.: Cond. Matt. **16**, S4439 (2004).

[9] R. Khasanov et al., Phys. Rev. B **72**, 224509 (2005).

9.2.2 Pressure effects on the superconducting properties of $YBa_2Cu_4O_8$

In the cuprate HTS the critical regime where thermal critical fluctuations dominate is experimentally accessible. It was recently shown that in this regime various critical properties are not independent, but related by universal relations (see *e.g.* (1)). Accordingly, the IE or PE on these quantities are expected to be related as well (2; 3). We performed a scaling analysis of the pressure effect on the magnetization and the in-plane penetration depth in underdoped $YBa_2Cu_4O_8$ (4). It was found that the rise of the transition temperature T_c of underdoped $YBa_2Cu_4O_8$ with increasing pressure p is associated with a decreasing anisotropy parameter γ and volume V. Figure 9.3 reveals that the relative change of the transition temperature $\Delta T_c/T_c$ is seen to mirror essentially that of the anisotropy parameter $\Delta\gamma/\gamma$. Note, that this behavior is consistent with the generic behavior for cuprate HTS, where for a given HTS family T_c increases with reduced anisotropy and thus gives a natural explanation why the PE on T_c becomes very small in optimally and overdoped cuprate HTS (5).

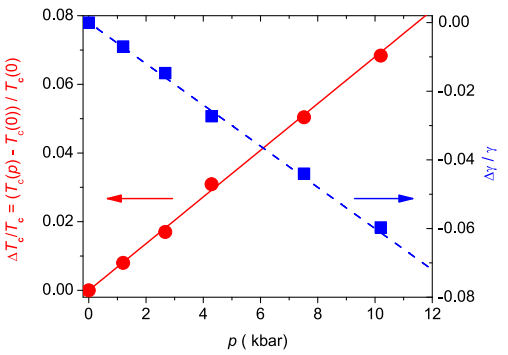

Figure 9.3: $\Delta T_c/T_c$ **and** $\Delta\gamma/\gamma$ **versus** p **of** $YBa_2Cu_4O_8$ **obtained from the scaling analysis [4]. The solid line is** $\Delta T_c/T_c = 0.0068p$ **and the dashed one is** $\Delta\gamma/\gamma = -0.006p$ **with** p **in kbar.**

[1] T. Schneider and J. M. Singer, *Phase Transition Approach To High Temperature Superconductivity*, (Imperial College Press, London, 2000).

[2] T. Schneider, Phys. Rev. B **67**, 134514 (2003).

[3] T. Schneider, Phys. Stat. Sol. B **242**, 58 (2005).

[4] R. Khasanov, T. Schneider, and H. Keller, Phys. Rev. B **72**, 014524 (2005).

[5] R.J. Wijngaarden, D.T. Jover, and R. Griessen, Physica B **265**, 128 (1999).

9.3 Spectroscopic studies of novel superconductors

9.3.1 EPR study of the spin-lattice relaxation of Yb^{3+}-doped $YBa_2Cu_3O_x$

The mechanism of the spin-lattice relaxation of rare-earth ions in HTS cuprates is still under debate (1; 2). Different models have been proposed to explain the experimental data. In

order to clarify this question we performed Electron Paramagnetic Resonance (EPR) measurements of Yb^{3+}-doped $YBa_2Cu_3O_x$ in a wide range of oxygen doping x (from the antiferromagnetic to the optimally doped superconducting state). The temperature dependence of the EPR line width as a function of doping x indicates that there are electronic and phononic contributions to the relaxation process. The electronic contribution increases with increasing hole doping. Figure 9.4 shows the temperature dependence of the relaxation rate for optimally doped $YBa_2Cu_3O_x$ without (T_c = 90 K) and with 3% Zn substitution (T_c = 55 K). In both samples one can see a drop of relaxation rate below T_c. This drop is more pronounced in the sample without Zn doping. However, small Zn doping cannot significantly change the phonon spectrum. Therefore, we conclude that the drop of the relaxation rate is related to a reduction of the electronic (Korringa) relaxation contribution below T_c due to the opening of the superconducting gap and a resulting decrease of the density of states at the Fermi level.

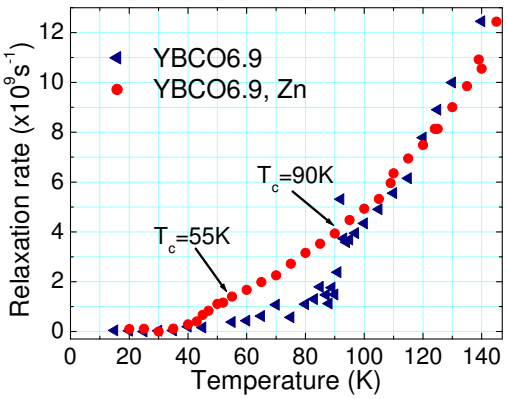

Figure 9.4: Temperature dependence of the relaxation rate for optimally doped $YBa_2Cu_3O_x$ samples with and without Zn doping.

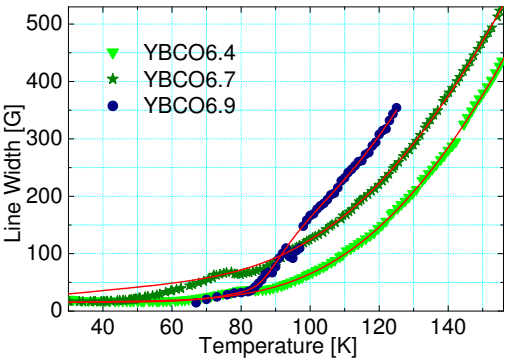

Figure 9.5: Doping dependence of the relaxation rate (line width) for $YBa_2Cu_3O_x$ ($x = 6.4, 6.7, 6.9$).

The remaining contribution to the relaxation is phononic and its temperature dependence follows an exponential function with activation energy of about 600 K. Figure 9.5 shows the temperature dependence of the relaxation rate for samples with different oxygen doping x. With decreasing x the Korringa contribution is decreasing, and for $x = 6.4$ there is practically only a phononic contribution to the relaxation.

Our results clearly show that both electronic and phononic mechanisms contribute to the relaxation of the rare-earth ions in $YBa_2Cu_3O_x$. For an optimally doped sample these contributions are approximately equal at 100 K, but at high temperatures and/or low hole-doping the phonon contribution dominates.

[1] St. W. Lovesey and U. Staub, Phys. Rev. B **64**, 066502 (2001).

[2] A. T. Boothroyd *et al.*, Phys. Rev. B **64**, 066501 (2001).

9.3.2 NMR/NQR investigations of YBCO compounds

In the search for orbital-current effects in cuprates we continued our study of various ^{89}Y NMR parameters in oriented powder samples of normal conducting $Y_2Ba_4Cu_7O_{15}$. The measurements were performed in an external magnetic field B of 9 T in the temperature range from 98 K to 300 K. Static or fluctuating magnetic fields originating from an orbital-current pattern in the CuO_2-planes as predicted (1) would appear perpendicular to the planes (parallel to the c axis) of the compound. Whereas static magnetic fields parallel to B influence the NMR linewidth only, fluctuating fields perpendicular to B alter the spin-lattice relaxation. Hence, orbital-current effects should change this ratio of investigated Y NMR parameters measured perpendicular to and parallel to the c axis, respectively. The measured ^{89}Y linewidth ratio is temperature independent within error bars. This result yields an upper limit of 0.02 mT for a possible static orbital-current field at the Y site. An estimate for the amplitude of fluctuating fields Δh_{orb} generated by the orbital-current pattern can be obtained from ^{89}Y spin-lattice relaxation measurements. The orbital-current contribution to the relaxation rate, $1/^{89}T^{\perp}_{1,tot} = 1/^{89}T^{\perp}_{1} + 1/^{89}T^{\perp}_{1,orb}$, changes the ratio $^{89}T^{||}_1/^{89}T^{\perp}_1$. The experimentally determined ratio, measured with two different NMR pulse schemes is temperature independent as shown in Fig. 9.6.

For the investigated temperature range, within error bars, a relative change of maximal 3% can be estimated. Provided we know the correlation time of fluctuating fields τ_c, we may estimate Δh_{orb} from this value using the relation

$$\frac{1}{^{89}T^{\perp}_{1,orb}} = \overline{\gamma^2 \Delta h^2_{orb}}^{t} \cdot \frac{\tau_c}{1+(\omega_L \tau_c)^2} < 0.03 \cdot \frac{1}{^{89}T^{\perp}_{1}(98K)} = 3.6 \cdot 10^{-4} s^{-1},$$

where γ denotes the gyromagnetic ratio and ω_L the Larmor frequency of ^{89}Y, respectively. τ_c may then be obtained from the underlaying energy scale of the orbital-current effect via Heisenberg's uncertainty principle. As a reasonable value the energy gap of 0.02 eV related to the pseudogap phenomena can be taken, yielding $\tau_c > 2 \cdot 10^{-13}$s. From this we obtain as an upper limit of the of fluctuating field amplitude $\Delta h_{orb} = 4.5$ mT.
A much lower energy scale has recently been observed in the plane ^{63,65}Cu spin-lattice

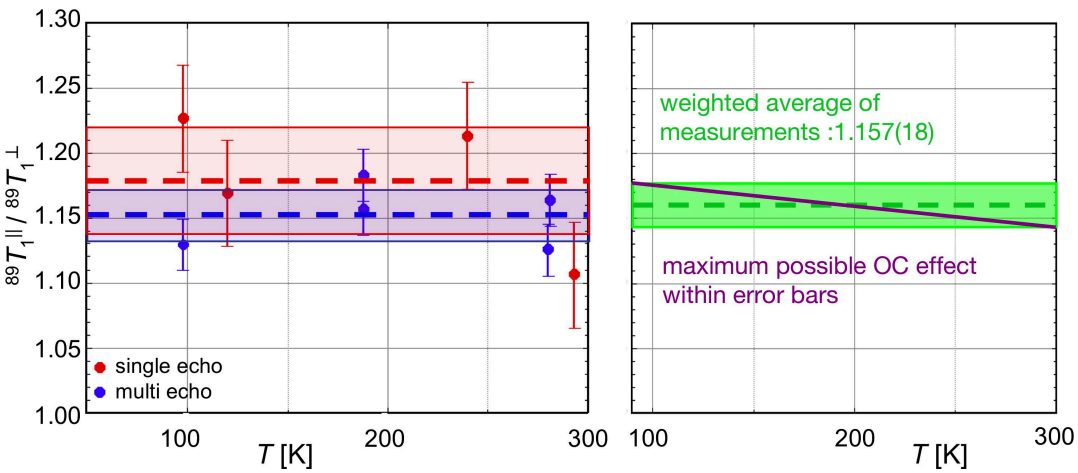

Figure 9.6: Temperature behaviour of the spin-lattice relaxation ratio $\frac{^{89}T^{||}_1}{^{89}T^{\perp}_1}$ in $Y_2Ba_4Cu_7O_{15}$ measured with two different NMR pulse schemes.

relaxation in superconducting $YBa_2Cu_4O_8$ at mK temperatures. In the superconducting phase the magnetic contribution to the Cu spin-lattice relaxation due to spin fluctuations diminishes because of the opening of the superconducting gap (2). At very low temperature this reduced relaxation progressively changes its character from magnetic towards quadrupolar (3). Moreover, it shows an unexpected rate maximum below 1 K, which can be explained by thermally activated charge fluctuations with a frequency of $\sim 10^{-10}$s and a distribution of activation energies centered at 0.09 meV ($\sim$ 1 K). This work was performed in collaboration with the research group of A.V. Dooglav and M. Eremin at the State University of Kazan and completed with ^{63,65}Cu spin-lattice measurements of the related Ca-doped compounds $Y_{1-x}Ba_{2-y}Ca_{x+y}Cu_4O_8$ (x+y = 0.02, 0.05, 0.1). During a visit of A.V. Dooglav in our group a careful reanalysis of the measurements in the Ca-doped samples was performed showing that investigations of samples with lower Ca content are necessary, in order to further clarify this exceptional behaviour of $YBa_2Cu_4O_8$ at lowest temperatures.

[1] P.A. Lee and G. Sha, Solid State Commun. **126**, 71 (2003).
[2] M. Bankay et al., Phys. Rev. B **50**, 6416 (1994).
[3] M. Mali et al., J. Supercond. **15**, 511 (2002).

9.3.3 Muon-spin rotation measurements of the penetration depth in Li_2Pd_3B

The discovery of superconductivity in the ternary boride superconductors Li_2Pd_3B and Li_2Pt_3B has attracted considerable interest in the study of these materials (1; 2; 3; 4; 5; 6). It is believed that superconductivity in both compounds is most likely mediated by phonons. It stems from photoemission (2), nuclear magnetic resonance (NMR) (3), and specific heat (6) experiments. However, experimental results concerning the structure of the superconducting energy gap are still controversal. On the one hand, NMR (3) data of Li_2Pd_3B and specific heat data of Li_2Pd_3B and Li_2Pt_3B (6) can be well explained by assuming the presence of only *one* isotropic energy gap. On the other hand, magnetic field penetration depth λ measurements suggest the presence of *two* isotropic superconducting gaps in Li_3Pd_2B and point to the presence of nodes in the gap in Li_3Pt_2B (4; 5). Systematic studies of the magnetic field and temperature dependence of λ can help to clarify this discrepancy.

Muon-spin rotation studies were performed on the ternary boride superconductor Li_2Pd_3B ($T_c \simeq 7.5$ K) (7). The following results were obtained: (i) over the whole temperature range (from T_c down to 30 mK) the temperature dependence of λ is consistent with what is expected for a single-gap s–wave BCS superconductor (Fig. 9.7), (ii) the shape of $\lambda(T)$ is almost independent of the magnetic field, (iii) at $T = 0$ the magnetic field penetration depth λ is almost field independent (inset in Fig. 9.7), as expected for a superconductor with an isotropic energy gap.

All the above mentioned features suggest that Li_2Pd_3B is *a BCS superconductor with an isotropic energy gap*.

[1] K. Togano et al., Phys. Rev. Lett. **93**, 247004 (2004).
[2] T. Yokoya et al., Phys. Rev. B **71**, 092507 (2005).
[3] M. Nishiyama et al., Phys. Rev. B **71**, 220505(R) (2005).

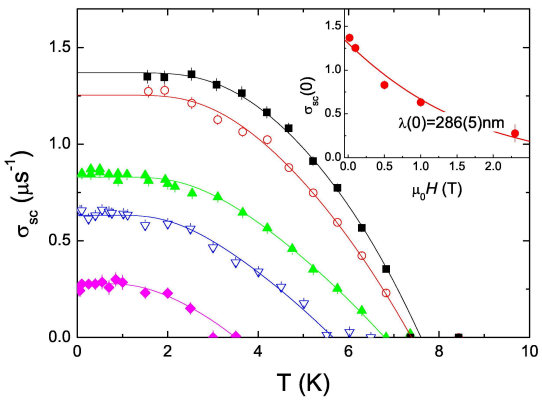

Figure 9.7:
Temperature dependence of the zero-temperature μSR depolarization rate $\sigma_{sc} \propto \lambda^{-2}$ of Li_2Pd_3B measured in various magnetic fields (from top to the bottom: 0.02 T, 0.1 T, 0.5 T, 1.0 T and 2.3 T). Solid lines represent fits with the weak-coupling BCS model [7]. The inset shows the field dependence of $\sigma_{sc}(0)$. The solid line corresponds to a fit with a field independent $\lambda(0) = 286(5)$ nm [7].

[4] H.Q. Yuan et al., cond-mat/0506771.
[5] H.Q. Yuan et al., cond-mat/0512601.
[6] H. Takeya et al., Phys. Rev. B **72**, 104506 (2005).
[7] R. Khasanov et al., cond-mat/0601156.

9.3.4 Low-energy μSR experiments in multilayers and thin superconducting films

Over recent years the μSR technique has demonstrated to be a unique and powerful microscopic tool for investigating fundamental parameters of superconductors. The low-energy μSR technique (LE-μSR) allows to explore local magnetic field profiles in HTS and/or magnetic systems near the surface of thin films and multilayer systems on a nanometer scale (1; 2). In the last year the upgrade of the LE-μSR apparatus at PSI was finished: The rate of good events approaches now 1500 per second, making the technique ready for more detailed experiments. In the first experiment with the improved apparatus a $YBa_2Cu_3O_{7-\delta}$ thin film grown at the University of Geneva was investigated. The thickness of the film was chosen to be about 200 nm which is slightly bigger than the maximum range of the low energy muons in $YBa_2Cu_3O_7$ and, on the other hand, is comparable with the magnetic field penetration depth in this material. These two circumstances made it possible to study for the first time the magnetic field profile inside a superconductor in a Meissner state when the magnetic field penetrates from both sides of a sample. The reconstructed field profile (averaged magnetic field seen by muons versus averaged muon penetration depth) is presented in Fig. 9.8.

The sample was first cooled in zero magnetic field (ZFC) from a temperature well above T_c, then a field of 195 Oe was applied parallel to the sample surface. One can see that the magnetic field penetrates (and is screened due to the supercurrent) form both surfaces of the sample achieving a minimum at the half thickness of the film, as predicted theoretically (but was never confirmed experimentally before). The solid line represents a fit with the magnetic field penetration depth $\lambda(T = 10\ \mathrm{K}) = 187(2)$ nm, which is in agreement with the literature data for nearly optimally doped $YBa_2Cu_3O_{7-\delta}$ bulk samples with T_c~87 K, confirming the good quality of the film. As a next step we are planning experiments in thin $PrBa_2Cu_3O_7$ films and $YBa_2Cu_3O_7$/ $PrBa_2Cu_3O_7$/ $YBa_2Cu_3O_7$ tri-layers with different thickness of individual layers with the goal to test a possible coupling of the superconducting $YBa_2Cu_3O_7$ layers through the antiferromagnetic $PrBa_2Cu_3O_7$ layer.

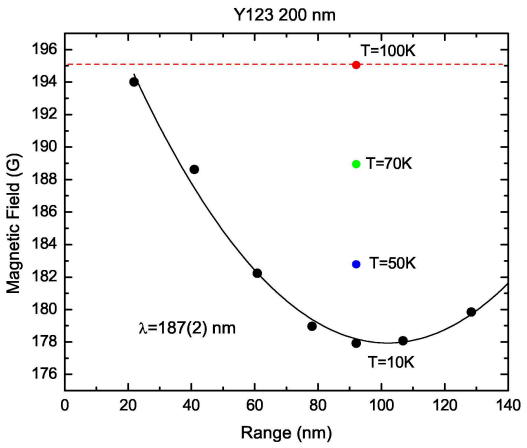

Figure 9.8: Magnetic field profile measured inside a thin (200 nm) $YBa_2Cu_3O_{7-\delta}$ film. The external magnetic field of 195 Oe is parallel to the surface of the film. One can see that the magnetic field penetrates (and is screened due to the supercurrent) from both surfaces of the sample achieving a minimum at the mid thickness of the film, as expected theoretically (but was never confirmed experimentally before). The solid line represents a fit with a magnetic field penetration depth $\lambda(T = 10\,\mathrm{K}) = 187(2)$ nm, which is in agreement with the literature data for nearly optimally doped $YBa_2Cu_3O_{7-\delta}$ bulk samples. Colored points represent a temperature scan at fixed implantation range close to the mid thickness of the sample.

[1] E. Morenzoni et al., J. Appl. Phys. **81**, 3340 (1997).
[2] T Proksch et al., Hyperfine Interactions **159**, 227 (2004).

9.4 Electric field effects in perovskites

9.4.1 Electric field effects on Cr-doped $SrTiO_3$

In collaboration with the IBM Rüschlikon Laboratory, we are investigating resistive and switching effects that were found on thin films of perovskites like (Ba,Sr)TiO_3, $SrZrO_3$, and $SrTiO_3$ (1). These materials exhibit a charge-induced insulator-to-metal transition with a resistive memory effect. Single crystals of Cr-doped $SrTiO_3$ (2) are used as a model system for this class of materials to study the drastic resistivity changes in the bulk under applied electric field, the switching between memory levels and to clarify the role of defects with different valencies. Strontium titanate is a band insulator ($E_{gap} \approx 3.2$ eV), but when exposed to an electric field the resistance of the doped perovskite is reduced by several orders of magnitude. The conducting state is a prerequisite for the memory switching. In order to avoid the crystals to be damaged by high-power load, a typical forming procedure is performed in several steps by limiting the power (Fig. 9.9a).

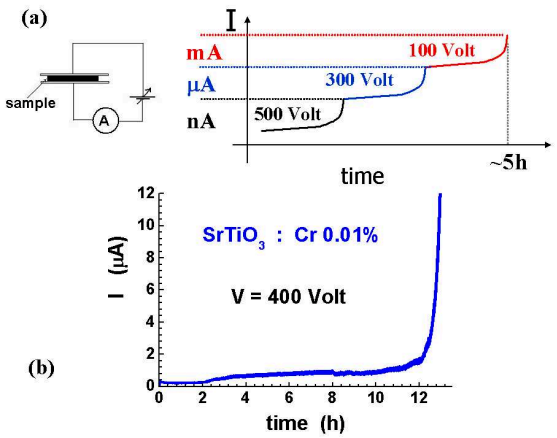

Figure 9.9: (a) Forming procedure on a Cr-doped $SrTiO_3$ single crystal. Once the current reaches the compliance the voltage source is decreased in order to avoid power damage. (b) The increase of the conductivity shows a drastical change after long-time exposure to high voltage.

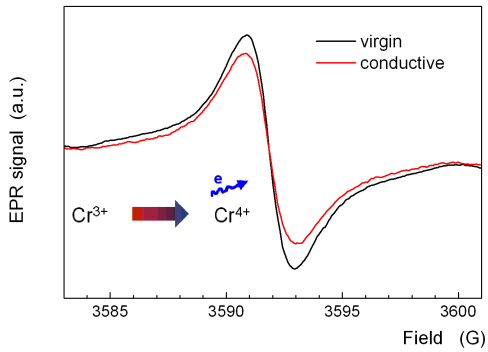

Figure 9.10:
Comparison of the EPR signal of Cr^{3+} in Cr-doped $SrTiO_3$ between a virgin and a conductive sample.

We prepared a series of single crystals to systematically investigate the effects in a wide range of the Cr doping (from 0.001 to 0.2 molar %). A decreasing forming time by increasing the Cr content was observed. Figure 9.9b shows the typical behavior of one forming step in a sample with 0.01 molar % of Cr. Here the conductivity increases by one order of magnitude in 12h. At the higher amount of Cr (0.2 molar %) the full forming procedure takes only a day. Another clear evidence of the Cr influence on the forming procedure is reported in Ref. (4) where changes of the electronic state of the Cr dopant are detected by X-ray absorption spectroscopy on crystals. During electrical stressing they observed the transformation of Cr^{3+} to Cr^{4+} in a volume close to the metal electrode (anode). Because the X-ray absorption collects information restricted to the surface region, we decided to study these materials using electron paramagnetic resonance (EPR) which allows to distinguish different valence states of Cr and probes the entire bulk. In Fig. 9.10 we compare the EPR signal of Cr^{3+} at room temperature in the insulating and the conducting state. The amount of Cr^{3+} decreases in the conductive state.

The simplest process we assume to explain the decreasing of the Cr^{3+} EPR signal is a ionization of the Cr site which increases its valence by one unit (Fig. 9.10). The nature of the free carriers in the conductive state and their precursor centers are still open questions. In order to clarify the role of the electron removed from the Cr site, it is important to understand whether there is a correlation between the conductivity and the amount Cr^{3+} centers. Therefore, a special sample holder will be developed for in-situ experiments which will allow to apply an electric field to the $SrTiO_3$ crystals directly in the resonance cavity. This will allow the study of changes in the electronic state of Cr during the electrical stressing, leading to the insulator-to-metal transition at the different conductive states and possibly will help to clarify its microscopic mechanism.

[1] A. Beck *et al.*, Appl. Phys. Lett. **77**, 139 (2000).
[2] Y. Watanabe *et al.*, Appl. Phys. Lett. **78**, 3738 (2001).
[3] K.A. Müller *et al.*, Solid State Commun. **85**, 381 (1993).
[4] I. Meijer *et al.*, Phys. Rev. B **72**, 155102 (2005).

9.5 New developments in instrumentation

9.5.1 Soft- and hardware upgrade of the 5.5T-MPMS

Due to the ongoing interest in investigating magnetic properties of novel materials in our laboratory we decided to update our 5.5T-MPMS (Magnetic Properties Measurement System) to a more modern measurement platform. The company *Quantum Design* offered us an installation procedure which allows an update to a *Windows* based software called *MultiVu*. This is not simply done by installing the corresponding program files, also the CPU of the MPMS control board, the EPROM drive, and the measuring PC needed to be replaced. This was achieved by using a faster *Pentium* Computer running under *Windows XP*. We have chosen *Windows XP* as operating system, because it is more robust than the earlier *Windows* versions and allows a convenient way to handle GPIB-interfaces. The installation has worked out without any significant problems. A recalibration of the system was not needed; the relevant values and factors for the field calculation and the measurement algorithms were simply copied from the older software. We checked many of the calibration factors after the update by some simple test measurements on $La_{1.85}Sr_{0.15}CuO_4$ single crystals in order to make sure that the system works properly. With the help of the new and much more helpful diagnostics menu of *MultiVu* we now have access to more system parameters during a measurement and we can check any anomaly during a programmed sequence without aborting the current run.

9.5.2 NMR insert device for the 9T-PPMS

A 9T-PPMS (Physical Properties Measurement System) is a very flexible equipment for various types of measurements to be performed at temperatures from 1.8 K to 300 K and in any field from 0 T to 9 T. These features make it very attractive to extend the range of our NMR equipment to temperatures below liquid helium and to use swept field procedures for broad line NMR studies. In the framework of a diploma thesis (1) performed in the research group of Prof. A. Schilling a NMR insert adapted to the specifications of the PPMS was constructed and a new software was designed in order to run the PPMS fully under control of the NMR system. Extensive tests showed that the new NMR-PPMS apparatus is fully operational.

[1] Alexander Gafner, Diploma thesis, Physik-Institut, Universität Zürich (2006).

10 Phase Transitions, New Materials and Superconducting Photon Detectors

M. Reibelt, R. Dell'Amore, H. Bartolf, S. Siegrist (since October 2005), A. Engel and A. Schilling

in collaboration with: Paul Scherrer Institute (Ch. Rüegg, J. Mesot, M. Medarde, K. Pomjakushina, K. Conder), University of Bern (K. Krämer), Bhaba Atomic Research Center (G. Ravikumar), Forschungszentrum Karlsruhe (Th. Wolf, H. Küpfer), Universität Karlsruhe (K. Il'in), ETH Zürich (J. Karpinksi), Deutsches Zentrum für Luft- und Raumfahrt (H.-W. Hübers), CSEM Neuenburg, FIRST Lab ETH Zürich.

Last year we have started our activities at the FIRST Center for Micro- and Nanoscience at the ETH Zürich where we are exploring lift-off techniques as an alternative to electron-beam lithography for producing superconducting thin-film photon detectors (H. Bartolf and A. Engel). Within another new project supported by the NCCR MaNEP (Materials with Novel Electronic Properties) we have also started to synthesize and to study certain nickel oxides with the aim to explain some of their peculiar electronic properties (S. Siegrist). Details in the magnetic phase diagrams of the type-II superconductors V_3Si and $NbSe_2$ have been studied using a differential calorimeter (M. Reibelt), and a novel technique to detect possible resonance phenomena in $TlCuCl_3$ has been significantly improved and successfully tested on a quartz resonator (R. Dell'Amore).

10.1 Physics of superconducting thin-film nanostructures and possible applications as fast single-photon detectors

We investigate the properties of thin film superconductors, which we further structure into narrow bridges or meander lines with typical dimensions less than 10 nm thick and about 100 nm wide. The meander lines are of particular interest. It has been shown (1) that such structures, suitably operated, can be utilized as very fast and sensitive single-photon counters in the visible and near-infrared spectral range. Recently, such superconducting single-photon detectors have attracted increasing interest from such diverse fields as astronomy, spectroscopy or quantum cryptography.

In last year's annual report we have already discussed the principal detection mechanism for single photons in these nanostructured devices. There, we also introduced our refined detection model (2) that gives a much more consistent account of the experimental data. It follows from the detection mechanism that the cross-section of the strip line needs to be comparable in size to the cross-section of the quasi-particle cloud, hence the above mentioned dimensions in the 10 to 100 nm range. Otherwise, stable operation of the detector is hampered by inevitable noise superimposed on the bias current which needs to be closer to the equilibrium critical current of the strip the larger the cross-section is compared to the quasi-particle cloud. Further on, it is obviously also necessary for the strip line to be as homogeneous as possible along its entire length; chemically, morphologically and also geometrically, i.e. width and thickness have to be constant.

These requirements make great demands on lithography processes and device production technology. We have made great efforts to improve our situation in this respect. We have started, for example, to explore lift-off techniques as alternative means to obtain the required nanostructures. In Fig. 10.1 we show a cross-section of an already etched co-polymer

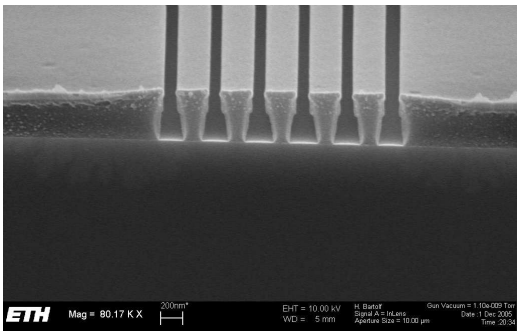

Figure 10.1: SEM-photo of the cross-section of a resist bi-layer. A set of parallel lines was written in the resist using e-beam lithography. The SEM examination was done after the etching process and before deposition of a metal film. The lift-off technique is based on a geometrical shadowing effect. After deposition the resist is removed using an appropriate solvent and the film deposited on top of the resist is washed away with it. The resulting line width would have been about 100 nm.

film before deposition and lift-off. First deposition tests with different metal films are promising and we are confident to be able to optimize the process parameters in order to obtain the necessary high-quality nanostructures. In Fig. 10.2 we show an example of one of the first successfully prepared meander structures. In this case a Ti-film was deposited onto a silicon substrate. The lines' width is about 200 nm and the film thickness is 5 nm. Also visible in this photo are 4 leads allowing for 4-point conductivity measurements. In further processing steps bonding pads overlapping with the leads will be deposited using photolithography.
A big advantage of this lift-off technique is the effortless adaptation to new superconducting materials other than the commonly used NbN. A shift to new materials seems to be necessary to increase the spectral range of these detectors. We have already shown in last year's report that with NbN the sensitivity will be limited to wavelengths below a few μm. The spectral sensitivity of NbN detectors is sufficient for applications using wavelengths near 1.3 and 1.5 μm, wavelengths commonly used in telecommunication. However, for astronomical applications for example, the limit should be pushed to wavelengths longer than 10 μm. This may be achieved with materials having lower T_c or much smaller strip cross-sections. At the other end of the spectral range, these detectors are interesting for x-ray spectroscopy due to their fast response and low jitter. Here, the absorption probability for x-ray photons needs to be increased; this implies the need for a superconductor with high Z-number.
Besides the efforts to increase the spectral range of these devices, it is also important to keep the noise, i.e. voltage pulses caused by effects other than the absorption of a photon, as low as possible. We have found indications that vortices could be a significant source of such dark counts (3). Other effects that could come into play are for example fluctuations in the quasi-particle density and thermal or even quantum phase-slips, depending on the dimensions of the strip line and the superconducting material used. These questions are also of fundamental interest and we have planned future experiments to shed light onto these issues.

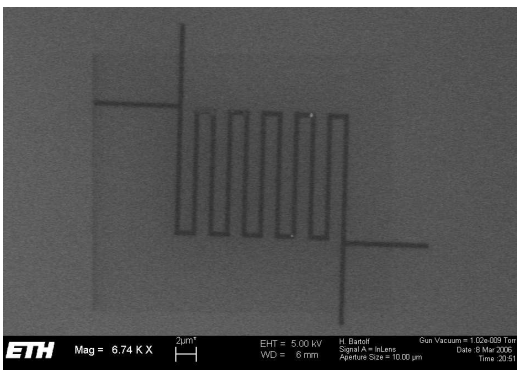

Figure 10.2: One of the first successfully prepared meander structures using the lift-off technique. In this SEM picture the meander appears as the dark structure. For test purposes a 5 nm thick Ti-film was deposited onto a silicon substrate. The linewidth in this case was approx. 200 nm.

In summary, we have developed a refined detection model for superconducting single-photon detectors. This new model gives a much more consistent description of experimental data. It also serves as the basis to describe fluctuation phenomena, which could be the origin of observed dark count rates. In this context we have found evidence that vortices also play a significant role. Within the report period we have also made substantial progress in lithography and device production.

[1] A. D. Semenov *et al.*, Physica C, **351**, (2001) 349.
[2] A. Semenov, *et al.*, submitted to Eur. Phys. J. B, **47**, (2005) 495.
[3] A. Engel, *et al.*, phys. stat. sol. (c), **2**, (2005) 1668.

10.2 Search for resonance phenomena in $TlCuCl_3$

In the last few years, quantum spin systems exhibiting magnetic-field-induced quantum phase transitions have attracted much attention (1; 2; 3). We have focused our work on $TlCuCl_3$, a 3D coupled spin ladder system, in which magnetic quasiparticles (magnons) are supposed to form a Bose-Einstein condensate above $\mu_0 H_c \approx$5.5 T at low temperatures (4). However, this BEC quantum phase transition requires the spin environment to be axially symmetric with respect to the applied magnetic field (5). ESR measurements, on the other hand, revealed a certain deviation from axial symmetry in $TlCuCl_3$ (6). To what extent this asymmetry precisely affects the quantum phase transition is not known.

Last year we have started to build an AC driven Wheatstone-like bridge set-up to detect resonance phenomena that can be expected if standing entropy waves form in a BEC. This work has been continued and significant improvements have been implemented. The bridge set-up is composed of two branches of identical coils and resistors, respectively. The same configuration, with the coils replaced by capacitors, can also be used to detect any kind of electrical or mechanical resonance. The drive signal is frequency modulated by the output signal of a lock-in amplifier. This signal is fed into the two branches of the bridge set-up. The voltage difference between the centers of

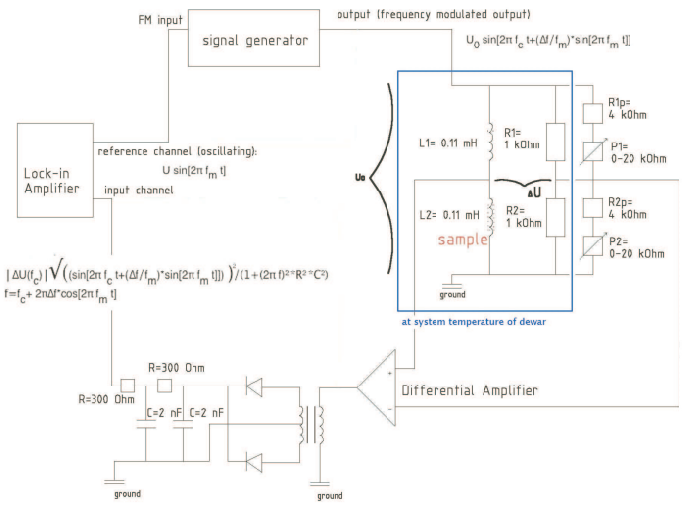

Figure 10.3: Bridge circuit to excite and detect collective modes in $TlCuCl_3$. The carrier wave of varying frequency f_c =0.25-2 MHz is frequency modulated ($f_m \ll f_c$). The voltage difference ΔU across a balanced Wheatstone bridge composed of identical coils and resistors is amplified and rectified, low-pass filtered and analyzed with a lock-in amplifier. Absorption of energy by the sample in one of the coils should drive the bridge out of balance.

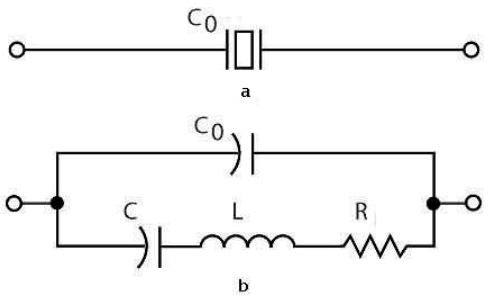

Figure 10.4: A quartz crystal in a shunt capacitance C_0 (a) and its equivalent circuit diagram (b).

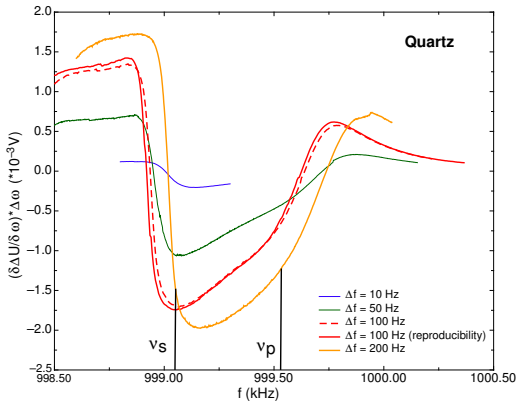

Figure 10.5: The resonances ν_s and ν_p detected on a quartz resonator.

the respective branches is detected differentially by low-capacitance probes. This voltage is then amplified, and the resulting signal is low-pass filtered to obtain a signal ΔU. This signal is measured with a lock-in amplifier, which now only varies with the modulation frequency f_m. By sweeping the carrier frequency f_c of the signal from 250 kHz to 4 MHz (self-resonance of the coil circuit), we can measure frequency dependent changes of the self inductance L or the capacitance C, respectively. The detected signal ΔU represents a measure for the derivative of the resonance curve with respect to frequency, whereas the peak-to-peak value scales with the standard-frequency deviation Δf (parameter of the signal generator) if this value is much smaller then the resonance linewidth $\Delta\nu$ ($\Delta f \ll \Delta\nu$).

As a first test we used a commercially available quartz crystal as a mechanical resonator, with a resonance frequency ν=1 MHz. The bridge set-up for this experiment consisted of two resistors on one branch and a resistor and a capacitance of similar impedance in this frequency range on the other branch. A piece of quartz in a shunt capacitance C_0 (Fig. 10.4a) can be regarded as a simple LCR resonating circuit (Fig. 10.4b), where the resistance R represents a measure for the losses, and C and L are equivalents for the elasticity of the quartz and mass of the vibrating crystal, respectively. Consequently, there are two close resonances $\nu_s = 2\pi\frac{1}{\sqrt{LC}}$ and $\nu_p = 2\pi\frac{1}{\sqrt{LC_0}}$, ($\nu_p > \nu_s$). Figure 10.5 shows the detected resonances using this technique.

Corresponding measurements on $TlCuCl_3$ at T =2 K and $\mu_0 H$ =9 T have not yet revealed the resonances that can be expected in a possible BEC-state, however. A small but irreproducible background signal of unknown origin and the remaining electrical noise may still be too large to detect the expected small signals coming from the sample. Further changes on the set-up have been attempted to reduce the noise and to make a reasonable background subtraction possible. A step motor enables us now to move the sample in and out of the detection coil "in situ" in helium atmosphere. This allows us to perform an immediate background subtraction. Measurements with this new improved set-up are in progress.

[1] B. C. Watson et al., Phys. Rev. Lett. **86**, 5168 (2001).
[2] Ch. Rüegg et al., Nature **423**, 62 (2003).
[3] V. S. Zapf et al., Phys. Rev. Lett. **96**, 077204 (2006).
[4] T. Nikuni et al., Phys. Rev. Lett. **84**, 5868 (2000).
[5] I. Affleck et al., Phys. Rev. B **43**, 3215 (1991).
[6] V. N. Glazkov et al., Phys. Rev. B **69**, 184410 (2004)

10.3 Vortex phases in type-II superconductors

The physics of vortices in high-T_c superconductors has been a matter of active research because of its high relevance for the technical applications of these materials. In weakly pinned superconductors it should be possible to observe a transition of the vortex matter from a quasi-ordered Bragg glass (BG) to a disordered vortex solid or vortex glass (VG) phase (1). Pinning effects can lead to "superheating" or "supercooling" of the disordered phase (DP), and metastable phases of the vortex matter can be formed in the Bragg glass region. These metastable phases may hide first-order like phase transitions of an equilibrium state. In order to get access to the equilibrium state and to the respective phase diagram, one can use repeated quasi-static field cycling with a small amplitude (2) or a dynamic equilibration process involving a small AC field applied transverse to the DC field (vortex-shaking) (3; 4; 5; 6). We built a split-coil arrangement, which creates an AC magnetic field perpendicular to the main magnetic field, and we can also perform field-cycling loops to get access to the equilibrium state. First-order like magnetization steps below the onset of the peak effect (i.e., a sharp increase in the pinning force and critical-current density j_c as a function of field and/or temperature in conventional and high-T_c superconductors) have been recently observed in a single crystalline V_3Si sphere (7), and experiments on $NbSe_2$ also point in the same direction (8). However, no thermodynamic data on the different vortex phases and the respective phase transitions in these systems are available. Currently we are investigating the phase diagram of V_3Si and $NbSe_2$ with a differential-thermal analysis (DTA)-apparatus (9) that is particularly sensitive to phase transitions and allows us to conduct high-resolution specific-heat measurements.

V_3Si is in the clean limit, has a high Ginzburg-Landau parameter and a very small anisotropy. H. Küpfer from the Institut für Festkörperphysik, Forschungszentrum Karlsruhe (Germany) provided us with a spherical V_3Si sample on which first-order like features in the magnetization have been observed (1; 7). Since the orientation of the crystal with respect to the magnetic field is of importance, we let the sphere be oriented by G. Krauss from the Laboratorium für Kristallographie, ETH Zurich. A $NbSe_2$ single crystal was kindly provided to us by G. Ravikumar, Bhabha Atomic Research Centre, Mumbai (India). The $NbSe_2$ single crystal was a large, flat, thin disk ($m \approx 6.6$ mg), that we had to cut into pieces and stack them together using a small amount of *Apiezon* grease. This procedure resulted in a sample which has more surface roughness than a bulk object of equal mass. This circumstance and the lower T_c of $NbSe_2$ ($T_c \approx 7$ K) may make the investigation on $NbSe_2$ somewhat more difficult than on V_3Si.

In our first experiments on V_3Si we oriented the magnetic field away from the high symmetry axes of the crystal. The magnetic field was kept constant while we performed temperature sweeps. Figure 10.6 shows representative measurements on V_3Si for $\mu_0 H = 1$ T. The data exhibit many interesting features, but at the large scale to plot the data in Fig. 10.6 only the most pronounced ones can be seen. Besides the large discontinuity at T_c, the data show a

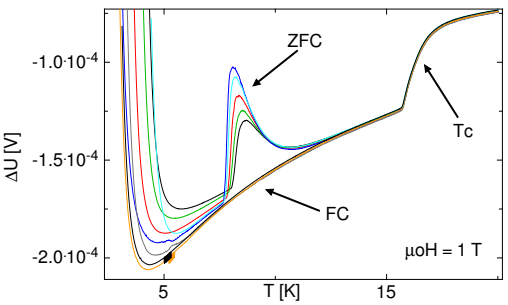

Figure 10.6: Temperature sweep DTA-measurements on V_3Si at $\mu_0 H = 1$ T with different magnetic histories. From ΔU one can calculate the temperature difference between the two thermometers, and, in principle, the specific heat of the sample.

strong self-heating effect around T =9 K, which is history dependent and occurs only for zero-field cooling (ZFC), but not for a field-cooling (FC) history. This and other even more interesting features are currently under investigation. We are studying the influence of several parameters: The magnetic field H, the orientation of the symmetry axis (101) of the V_3Si sphere relative to the magnetic field, the temperature-sweep velocity, the strength of the magnetic AC-shaking field and its frequency, and the history dependence which results, for example, from the difference between zero-field cooling and field-cooling procedures.

[1] H. Küpfer, G. Ravikumar et al., Phys. Rev. B **70**, 144509 (2004).
[2] G. Ravikumar, V. C. Sahin et al., Phys. Rev. B **63**, 24505 (2001).
[3] M. Willemin et al., Phys. Rev. B **58**, R5940 (1998).
[4] M. Willemin et al., Phys. Rev. Lett. **81**, 4236 (1998).
[5] N. Avraham et al., Nature (London) **411**, 451 (2001).
[6] E. H. Brandt and G. P. Mikitik, Phys. Rev. Lett. **89**, 027002 (2002).
[7] G. Ravikumar and H. Küpfer, Phys. Rev. B **72**, 144530 (2005).
[8] S. S. Banerjee, N. G. Patil et al., preprint.
[9] A. Schilling and O. Jeandupeux, Phys. Rev. B **52**, 9714 (1995).

10.4 Synthesis and characterization of $LaBaNiO_{4-\delta}$

The compound $LaBaNiO_{4-\delta}$ is a structural analogue to $LaSrNiO_4$, and in particular to the well-known cuprate La_2CuO_4. While $LaSrNiO_4$ is known to be metallic (1), $LaBaNiO_{4-\delta}$ (at first sight an electronic analogue to $LaSrNiO_4$) is insulating or at least semiconducting (2). To clarify this issue we have prepared polycrystalline samples of $LaBaNiO_{4-\delta}$, and characterized them by X-ray diffraction, neutron diffraction, chemical analysis, resistivity, magnetic-susceptibility, and specific-heat measurements.

The neutron-diffraction data as well as a chemical analysis indicate that the $LaBaNiO_{4-\delta}$ samples are oxygen deficient ($\delta = 0.15$), which might also explain the observed superstructure (here interpreted as an oxygen-vacancy ordering), as well as the poor electrical conductivity as compared to $LaSrNiO_4$ (since also the planar oxygen atoms seem to be affected). We are therefore planning to try to ensure a full oxygenation of the $LaBaNiO_{4-\delta}$ samples by applying approriate oxygen-annealing techniques, and to repeat the various analysis experiments.

[1] R. J. Cava et al., Phys. Rev. B **43**, 1229 (1991).
[2] G. Demazeau et al., Mat. Res. Bull. **17**, 37 (1982).

11 Surface Physics

T. Greber, M. Hengsberger, J. Lobo, R. Schillinger, T. Okuda, S. Berner, C. Galli Marxer, B. Xue, A. Tamai, A. Dolocan, M. Corso, C. Cirelli, M. Morscher, T. Brugger, L. Brandenberger, M. Allan, D. Leuenberger, M. Klöckner, J. Osterwalder

With the growing impact of nanoscience and -technology, surface and interface phenomena have to be understood at the atomic level. The surface physics laboratory is well equipped for the preparation and characterization of clean surfaces, metal and molecular monolayer films, as well as self-assembling nanostructures, all under ultrahigh vacuum (UHV) conditions. Experimental techniques available to us include x-ray photoelectron spectroscopy (XPS) and diffraction (XPD), angle-resolved photoemission spectroscopy (ARPES), two-photon photoemission (2PPE) using femtosecond laser pulses, low-energy electron diffraction (LEED) and scanning tunneling microscopy (STM). At the nearby Swiss Light Source we have built up two more photoemission spectrometers, one for spin-resolved Fermi surface mapping and one for near-node photoelectron holography. A growing network of national and international collaborations expands this set of experimental techniques and provides us also with the necessary theoretical support.

The research carried out during the report period can be grouped into four topics:

- **Electronic states at metal surfaces**
  On the close-packed (111) surface of nickel two types of surface states, with wave functions that decay exponentially both into the vacuum and into the bulk of the crystal, are found: a so-called *Shockley state* that propagates almost freely within the surface plane and a *Tamm state* that is derived from the more localized *d* states of the outermost atomic layer. With regards to the surface magnetism of Ni(111) the question arises at to how much these surface states are exchange split and whether their relative majority-versus-minority spin occupation gives rise to a substantial change in the magnetic moments in the surface layer. We have addressed this issue by means of spin-polarized ARPES (Section 11.1). Furthermore, the investigation of reciprocal-space spin structures in the Shockley state on vicinal Au(111), induced by the Rashba effect, was continued (Annual Report 04/05). It became apparent that these subtle effects could not be studied reliably and reproducibly with the present COPHEE (COmplete PHotoEmission Experiment) instrument due to insufficient magnetic shielding. The identification and the solution of this problem have caused considerable delays in the project; a major construction effort, encasing the complete analyzer-polarimeter unit in a double-layer μ-metal shield, is currently underway. At the same time a toroidal-grating monochromator has been added to the high-flux ultraviolet source of the spectrometer, permitting us to take data also during the long periods where we have no access to the synchrotron beam. We expect the instrument to be fully upgraded and commissioned in summer 2006.

- **Monolayer films of hexagonal boron nitride on metal surfaces**
  The discovery, two years ago, of a highly intriguing nanostructure in hexagonal boron nitride (*h*-BN) layers on Rh(111), the *nanomesh*, has provided the group with a non-trivial model system for nanostructure self-assembly. It forms upon high-temperature decomposition of borazine $(HBNH)_3$. The lattice mismatch, the high intralayer stiffness of the *h*-BN layer, resulting from the strong sp^2 bonds, and the *lock-in* energy associated with the affinity of the nitrogen atoms to atop bonding sites (*i.e.* on top of metal atoms), appear to be important ingredients in the self-assembly mechanism. This insight results mainly from comparative studies for *h*-BN layers on other transition metal surfaces, such

as Pd(111) or Ru(0001), where, depending on a subtle balance between these parameters, a well-ordered two-layer nanomesh forms or a single-layer Moiré pattern (Section 11.2). On Mo(110), a substrate with a quasi-hexagonal surface lattice, a superstructure with a small unit cell forms, leading to a one-dimensional Moiré type structure (Section 11.3). At even higher preparation temperatures, formation of a boron-only structure is observed, with nitrogen presumably being released into the gas phase. This phase consists of a dense agglomerate of straight, parallel nanowires with widths of 5 to 20 nm and lengths of up to several micrometers.

In April 2005 we have launched the European STREP (Specific Targeted Research Project) *NanoMesh* with the aim to explore potential applications of this type of nanostructure while furthering the understanding of its formation. One important aspect for any application is the stability and chemical inertness. As is shown in Section 11.4, the structure easily survives full immersion in water. This represents not only a surface scientist's dream of creating a very robust monolayer-defined nanostructure, but it opens a pathway to molecular functionalization of the mesh through aqueous solutions. In Section 11.5 a 2PPE study of the nanomesh on Rh(111) is presented. This technique can help to determine the dispersion of the unoccupied conduction band states in the insulating nanomesh layer. However, from the photon-energy dependence of the 2PPE spectra we have to conclude that, unlike in the case of *h*-BN/Ni(111) (Annual Report 04/05), the dominant peak is coming from an occupied state. Finally, our earlier 2PPE study of the *h*-BN/Ni(111) system has ended in a proposal for a spin-polarized electron source with superior stability as compared to existing devices. Spin-polarized currents have been demonstrated (Section 11.6), and a provisional patent has been filed.

- **Adsorbed molecules**

Organic chemists can provide identical nanometer-sized units with desired functionalities in large quantities. By adsorbing these molecules in well-defined geometries on surfaces, physicists can play with these functionalities and try to make them useful for specific applications. One interesting issue is the controlled motion of molecules triggered by some external parameter. In Section 11.7, the adsorption of corannulene on a *h*-BN monolayer is discussed. This is a bowl-shaped carbon molecule with hydrogen-saturated edges. In order to study its response to the presence of magnetic fields (or more generally of local spin density), the boron nitride layer has been prepared on the (110) surface of a picture-frame nickel sample that can easily be magnetized parallel to the surface layer. First results, obtained in the diploma thesis of Louis Brandenberger, show that the molecules preserve their properties upon adsorption to the boron nitride layer, while they partly dissociate on the bare nickel surface.

Another important issue is trying to understand the electronic properties of supramolecular assemblies. For this purpose, monolayers of C_{60} have proven to be a fruitful system. On vicinal Cu(111) surfaces, long linear chains of molecules can be prepared. The positions and the orientations of the molecules have been well characterized. The electronic structure measured by ARPES shows clearly one-dimensional dispersion of the highest occupied molecular orbital (HOMO) peak. Due to charge transfer from the substrate the lowest unoccupied molecular orbital (LUMO) is partly occupied. It does not show significant dispersion but a rather intriguing line shape near the Fermi level, reminiscent of the one-dimensional physics of a Luttinger liquid (Section 11.8).

The adsorption of chiral molecules to a surface with chiral centers provides direct insight in chiral recognition, which is a fundamental concept in nature. Au(17 11 9) is a gold surface vicinal to Au(111) with a dense array of kink sites of defined chirality. XPD experiments show directly that the L and D forms of the amino acid cysteine adsorb at these sites with

entirely different bonding geometries. In Section 11.9 it is now shown that this difference reflects itself also in the N 1s core-level binding energy.

- **Time–resolved electron diffraction**
  The time-resolved LEED experiment has progressed by an important step in this last year: for the first time clear and reproducible temporal correlation was observed in a pump-probe experiment overlapping an intense laser pulse and a delay-controlled low-energy electron pulse in a scattering geometry on a Cu(111) surface (Section 11.10). The energy analysis of the scattered beam shows small but consistent shifts to higher energies near zero delay, *i.e.* when pump and probe hit the surface at the same time. This energy gain is explained by electron acceleration in the nascent space charge cloud generated by the laser pulse. While our main interest lies in the structural dynamics of the surface induced by the pump pulse, such space-charge effects will always present in these experiments and have to be understood accordingly.

11.1 Spin polarization and exchange splitting of the surface states on Ni(111)

in collaboration with: Peter Blaha, Institut für Materialchemie, Technische Universität Wien, Austria; Markus Roos, Departement Technik, Informatik und Naturwissenschaften, Zürcher Hochschule Winterthur; and Vladimir N. Petrov, St. Petersburg Technical University, Russia.

The breaking of the translational symmetry provoked by the surface creates new electronic states called surface states. In the case of Ni(111) there are two types of surface states: Tamm- and Shockley states. The Tamm states have predominant d-character and follow the Λ_3 bands, while the Shockley states mainly have sp-character. Below the Curie temperature (631 K), each of the surface states should split into two spin components. Up to date, only three surface states have been observed experimentally (1; 2; 3; 4), while density functional theory (DFT) calculations (5) indicate the existence of four surface states, i.e. two exchange-split Tamm- and Shockley states.
We measured the spin polarization and the exchange splitting of the surface states on Ni(111) by means of spin- and angle-resolved photoelectron spectroscopy (SARPES) with an energy and angle resolution of 85 meV and 0.5°, respectively. This experiment is quite challenging for mainly two reasons: First, the Ni(111) surface is very reactive to residual hydrogen gas (surface lifetime was less than 1 hour) and, second, with this technique the acquisition times are very long (10^{-3} times lower efficiency than spin-integrated ARPES). Acquiring data sets with sufficient statistical accuracy thus required the accumulation of spectra from many surface preparations. We used linearly p-polarized light from the SIS beamline at the Swiss Light Source with a photon energy of $h\nu = 21.2$ eV. Figure 11.1 shows the experimental geometry. Normal emission spectra were obtained at room temperature after magnetizing the sample along the second easy magnetization direction. From the independently determined remanent magnetization of ≈30% and the Sherman function of the Mott detectors (13%)

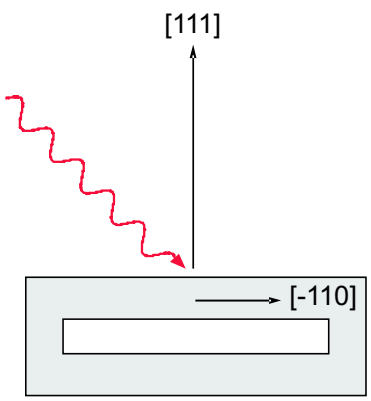

Figure 11.1: Experimental geometry.

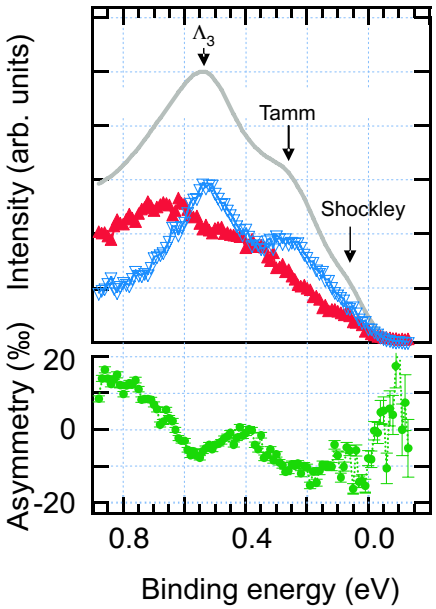

Figure 11.2: SARPES ($h\nu$=21.2 eV) normal emission data from Ni(111) at room temperature. In the top panel the spin-integrated spectrum (full gray line) clearly shows the Λ_3 bulk band, the Tamm and the Shockley states. The spin resolved spectra depict minority and majority spin components with red up triangles and blue down triangles for majority and minority spins, respectively. The bottom panel shows the experimentally observed Mott-scattering asymmetry along the bulk magnetization direction.

we derive the spin resolved spectra along the magnetization axis as shown in Fig. 11.2. The exchange splitting for the Λ_3 bulk d-band is ΔE_x=160±10 meV, in excellent agreement with the work of Ref.(6). The Tamm state shows an energy splitting which is also found in DFT (5). The main difference is the magnitude of the splitting which is, like for the bulk bands, smaller in the experiment (ΔE_x=120±10 meV) due to correlation effects in the photoemission final state (7). The exchange splitting of the Shockley surface state is consistent with the upper limit proposed in the work of Ref. (3).

[1] F. J. Himpsel, D. E. Eastman, Phys. Rev. Lett. **41**, 507 (1978).
[2] M. Donath, F. Passek, V. Dose, Phys. Rev. Lett. **70**, 2802 (1993).
[3] J. Kutzner, R. Paucksch, C. Jabs, H. Zacharias, J. Braun, Phys. Rev. B **56**, 16003 (1997).
[4] W. Auwärter, PhD. Thesis, University of Zurich (2003).
[5] G. B. Grad, P. Blaha, Internal communication (2003).
[6] K. P. Kämper, W. Schmitt, G. Güntherodt, Phys. Rev. B, **42**, 10696 (1990).
[7] F. Manghi, V. Bellini, J. Osterwalder, T.J. Kreutz, P. Aebi, and C. Arcangeli, Phys. Rev. B **59**, R10409 (1999).

11.2 Boron nitride nanomeshes on different substrates

in collaboration with: Andrii Goryachko and Herbert Over, Physikalisch-Chemisches Institut, Justus-Liebig-Universität Giessen; Hermann Sachdev, Anorganische Chemie, Universität des Saarlandes; Peter Blaha, Robert Laskowski, Thomas Gallauner, Institut für Materialchemie, Technische Universität Wien, Austria.

Recently our group discovered a peculiar, highly ordered nanostructure: a *nanomesh* of hexagonal boron nitride (*h*–BN) self-assembles on a hot (1070 K) Rh(111) surface upon exposure to 40 L (1 Langmuir=10^{-6} torr×s) of borazine $(HBNH)_3$ (Fig. 11.3a) (1). *h*–BN units

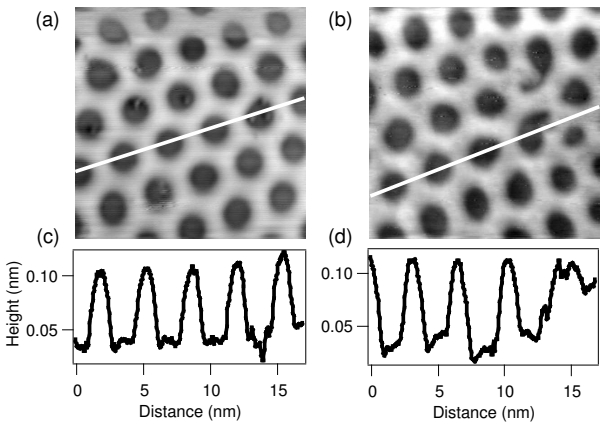

Figure 11.3:
a) and b): Constant–current STM images (-2 V and 1.0 nA, 13×13 nm^2) of the h–BN nanomesh on Rh(111) and Ru(0001), respectively.
c) and d): Cross–sectional profiles along the white lines in images a) and b), respectively.

aggregate to form this double-layer honeycombed network of 3 nm periodicity and 2 nm hole size. The two layers are offset so that nearly the entire underlying metal surface is covered. One of the driving forces for its formation is the large lattice mismatch of -6.8 % between the *h*–BN film and the Rh substrate. In the case of *h*–BN on Ni(111), where the lattice mismatch is only +0.4%, complete and flat monolayers form. The growth of nanomeshes on different substrates is now investigated, with the purpose to control hole size and shape. A nanomesh can be grown also on the Ru(0001) surface (Fig. 11.3b). The lattice mismatch is here -7.3 %, a value similar to the one on rhodium, since the two metals have almost equal in-plane lattice constants (0.269 nm for Rh and 0.270 nm for Ru (2)). A difference between the two substrates arises in the stacking of the third layer below the surface since rhodium has a face–centred cubic (*fcc*) bulk structure while ruthenium is hexagonal close-packed (*hcp*). STM images show that the nanomeshes grown on these surfaces have similar periodicity, hole size, wire thickness and corrugation (Fig. 11.3c and d). Also the number of electronic bands assigned to the *h*–BN overstructure is the same in both cases, as was measured with ARPES (not shown).

Nevertheless, intriguing differences arise in the regularity and the ordering of the mesh units. In the nanomesh grown on Ru(0001) the density of defects such as asymmetric holes or mesh dislocations is significantly higher than in the Rh(111) nanomesh (Figs. 2a and 2b). In the latter case deviations from a perfect hexagonal pattern of perfectly circular holes are mainly observed in close vicinity to brighter patches. These patches have been tentatively identified as being induced by the Ar^+ ion sputtering for cleaning the substrate prior to nanomesh formation. Argon bubbles form in the subsurface region and induce local strain in the surface layer (3). Far from these regions the nanomesh is very regular. In the Ru(0001) nanomesh on the other hand, defects are abundant and occur without obvious correlation to surface defects on the substrate.

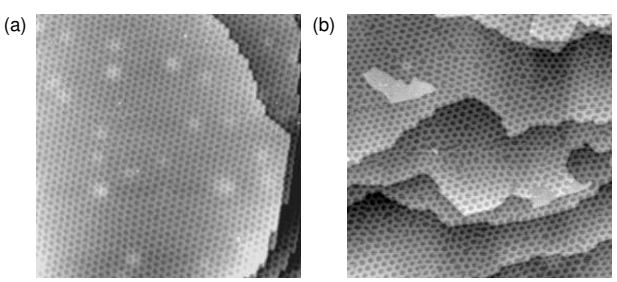

Figure 11.4:
Constant–current STM images (-2 V and 0.5 nA, 100×100 nm^2) of the h–BN nanomesh on Rh(111) (a) and Ru(0001) (b).
These images illustrate the different degree of order observed for the two structures.

Total energy calculations indicate that the strongest bonding of *h*–BN adsorbed on various noble and transition metal surfaces, with the N atoms sitting atop and B on fcc sites, occurs for the *4d* series. The bonding is stronger the more holes are present in the *d*-band (Pd, Rh, Ru in increasing order).

On Ru(0001) the N atoms are thus particularly strongly bound to the underlying metal atoms, providing a high *lock-in* energy with regard to lateral shifts of the *h*–BN units. It is also found that the energy cost for pseudomorphic *h*–BN growth, where the boron nitride adopts the lattice constant of the substrate, would be too large on these surfaces (0.6 eV per *h*–BN unit for Rh). Therefore, the *h*–BN layer conserves its own lattice constant. On Pd(111), this has been shown to lead to Moiré patterns with various orientations of the *h*–BN layer (4). It seems that the formation of a *h*–BN nanomesh is not only dependent on the lattice mismatch, but also on the ability of the *h*–BN units to lock onto the substrate atoms. A subtle balance of these two features may also be crucial for the degree of order in the mesh.

[1] M. Corso, W. Auwärter, M. Muntwiler, A. Tamai, T. Greber, J. Osterwalder, Science 303 (2004) 217.
[2] N.W. Ashcroft, N.D. Mermin, Solid State Physics, Saundres College Publishing, New York 1976.
[3] M. Gsell, P. Jakob, D. Menzel, Science 280 (1998) 717.
[4] M. Morscher, M. Corso, T. Greber, J. Osterwalder, Surf. Sci., submitted.

11.3 h-BN and boron nanowires on Mo(110)

High temperature decomposition of borazine $(HBNH)_3$ is a convenient method to grow monolayers of hexagonal boron nitride (*h*-BN) on transition metal surfaces, leading to a variety of interesting superperiodicities and nanostructures including the recently discovered *nanomesh* (1). In the diploma thesis of Milan Allan the same method was applied to the molybdenum (110) surface. Two new and interesting structures were observed.
At very high preparation temperatures (about 1170 K) ultra-narrow (2 to 30 nm) boron nanowires form (Fig. 11.5a). They are very long (up to some μm), leading to aspect ratios between 10 and 500. The wires are straight and well arranged along the (001) direction of the Mo(110) surface. In the direction along the wires, the crystal structure matches the periodicity of the underlying Mo surface, as revealed by LEED. No periodicity is seen perpendicular to them.

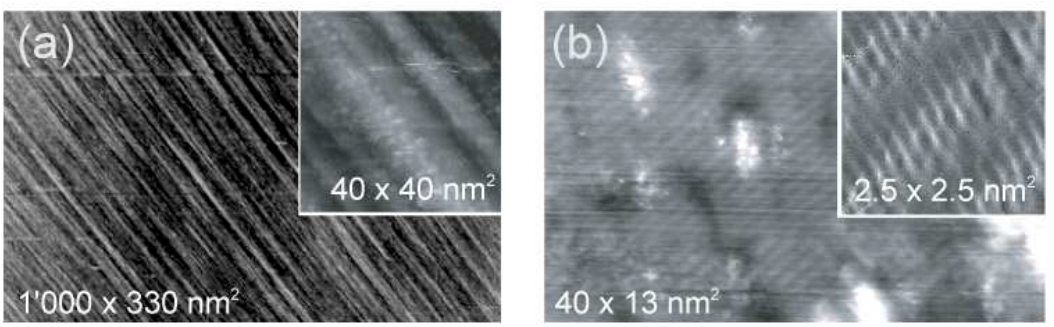

Figure 11.5: STM images of a) boron nanowires obtained by borazine exposure of Mo(110) at 1112 K, and b) the h-BN structure prepared at 944 K. The insets show small area scans.

At lower preparation temperatures (about 950 K), a *h*-BN monolayer is formed, with a superlattice structure similar to the one recently observed on Ni(110) (2). The *h*-BN layer and the Mo(110) surface form a coincidence lattice along the (001) direction. Four Mo(110) lattice spacings match five *h*-BN lattice spacings (mismatch -0.8%). This is indeed confirmed by LEED which shows a (4×1) superstructure. ARPES shows clearly back-folded boron nitride bands shifted by a wave vector that corresponds to a five-fold overstructure in the *h*-BN layer. Stripes along the $(1\bar{1}0)$ direction are observed on STM images (Fig. 11.5b). It is still unclear whether they arise from a new kind of nanostructure or simply from a Moiré pattern. The boron 1s core level XPS reveals a chemical shift of 2.3 eV between the *h*-BN structure and the boron nanowire structure. This shows the different chemical bonding of the boron in the two phases.

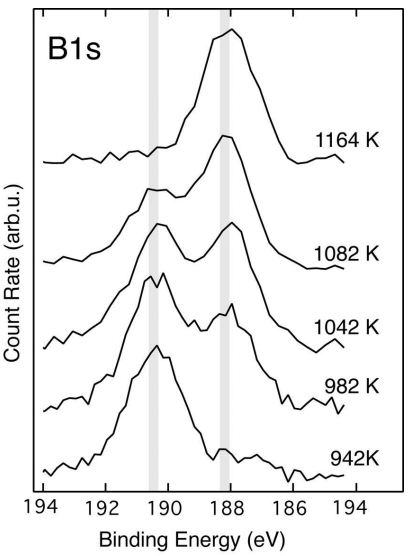

Figure 11.6: XPS spectra of the B1s core level. Each curve is labeled with the Mo(110) temperature at which the structure was prepared.

At intermediate preparation temperatures, a mixture of the two structures (*h*-BN and boron nanowires) is observed. The coexisting phases conserve their characteristic properties. This is evidenced by XPD, LEED and XPS. The relative abundance of the two phases on the surface can be measured using the relative weight of the integrals of the corresponding B1s peaks. These measurements reveal that the phase ratio is easily tunable by varying the temperature (Fig. 11.6). It is also possible to first prepare the lower-temperature phase (*h*-BN) and anneal it to obtain the high temperature phase (boron nanowires).

[1] M. Corso, W. Auwärter, M. Muntwiler, A. Tamai, T. Greber and J. Osterwalder, Science 300 (2004) 217.
[2] T. Greber, L. Brandenberger, M. Corso, A. Tamai and J. Osterwalder, e-J. Surf. Sci. Nanotech., in press.

11.4 Stability of the h–BN nanomesh on Rh(111) in aqueous environment

in collaboration with:
Matthias Schreck, Stefan Gsell, Experimentalphysik, Universität Augsburg.

The stability of the nanomesh in various environments is important for possible applications as a template for regular nanostructures or as a functional surface for chemistry or biology applications. Therefore, the stability of the nanomesh has been further tested in aqueous conditions by immersion of the sample into liquid water.

A nanomesh layer was prepared on a Rh(111) thin film that had been grown by MBE on a sapphire (0001) substrate at the University of Augsburg. The sample was then removed from the UHV system through the fast-entry air lock. The sample was then immersed for 30 minutes

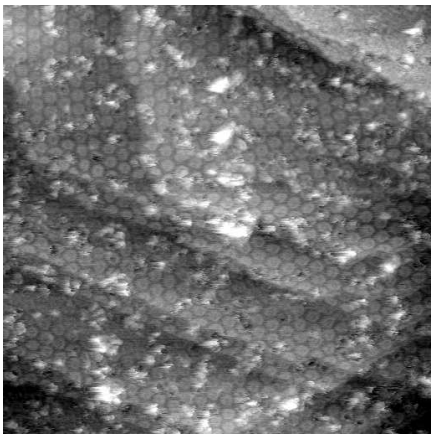

Figure 11.7:
Constant–current STM image of a nanomesh sample immersed in water and reintroduced in UHV for analysis (80×80 nm^2, 80 pA, -1V).

in ultra pure water and subsequently blow-dried in He. The dry sample was immediately reintroduced into the entry lock. A slow annealing up to 750°C in UHV followed for outgassing. After this procedure, the nanomesh is clearly visible in STM images (Fig. 11.7), although there is some contamination present on the surface. UPS and LEED confirmed the presence of the nanomesh.

11.5 Two-photon photoemission from the h-BN nanomesh

The boron nitride nanomesh on Rh(111) (1) has two hexagonal mesh layers with 2 nm diameter holes and 3.2 nm periodicity, which are offset such as to cover most of the metallic substrate. Due to its very high thermal stability this regular nanostructure represents an interesting template for ordered supramolecular architectures. For applications of this kind, it is necessary to investigate the conduction bands of this insulating bilayer. The unoccupied electronic band structure was therefore mapped by means of pump-probe two-photon photoemission (2PPE). Briefly, by photon absorption from a first light pulse (pump) electrons are promoted from occupied initial states into unoccupied intermediate states, where they are probed after a defined time delay by the second light pulse (probe) via the photoelectric effect. Therefore, beside spectroscopic information, 2PPE gives access to both, lifetimes of intermediate states, and coherent excitation dynamics (2).

Our femtosecond laser system has been set up for two-color 2PPE experiments where pump and probe pulses have different quantum energies: the fundamental of a Coherent MIRA oscillator, with 790-840 nm wavelength, 76 MHz repetition rate and 60 fs time duration (red pulse), and its second harmonic (blue pulse), generated with a 0.5 mm thick $\beta-$bariumborate (BBO) crystal. The initial red beam is split into two identical beams by a 50% beam splitter. One of the two beams is used to produce the blue beam while the second is going over an in-house built delay stage in order to vary the pump-probe time delay on the sample. The blue pulses were pre-compressed in a prism compressor stage in order to compensate for the chirp acquired during their propagation.

For blue laser pulses only (one-color 2PPE), the normal emission spectrum from the *h*-BN nanomesh exhibits generally low intensities (Fig. 11.8, blue spectrum). When red and blue pulses arrive in coincidence on the sample (zero delay), a peak at 4.57 $\pm$ 0.02 eV as well as the secondary peak near the low-energy cutoff are greatly enhanced (Fig. 11.8, red spectrum). This would suggest the presence of an intermediate state, the occupation of

which is pumped efficiently by blue (red) light and probed by red (blue) light. The energy of this unoccupied state should be either 1.47 eV or 3.02 eV depending on whether the red light or the blue light is responsible for the pumping.

The interpretation of 2PPE spectra is complicated by the involvement of three states (initial, intermediate and final states) and the difficulty of identifying the origin of a peak as due to one of the three. In order to correctly attribute peaks in the spectra to initial or intermediate state energies, the peak position can be traced as a function of exciting photon energy. For initial states, the peak moves with the sum of pump and probe photon energies (here three times the fundamental), while for intermediate states it moves with the probe photon energy only. In our case the fundamental wavelength was varied between 790 and 840 nm (corresponding to photon energies of the red light between 1.57 and 1.47 eV). The peak positions measured at coincidence of red and blue pulses were linearly fitted showing a slope very close to 3 (Fig. 11.9). This means that the peak position moves with three times the fundamental photon energy, *i.e.* it can be assigned to an initial state. On the *h*-BN nanomesh on Rh(111) we thus observe an initial state at a binding energy of 80 $\pm$ 20 meV. By comparison, the spectra for *h*-BN/Ni(111), where an even stronger intensity enhancement is seen for coincident red and blue pulses, reveal a slope of 1.28 which is likely to be caused by a contribution of two intermediate states. This marked difference between the two systems raises the question as to whether it is due to the different bonding to the substrates or due to the nanostructuring in the nanomesh film.

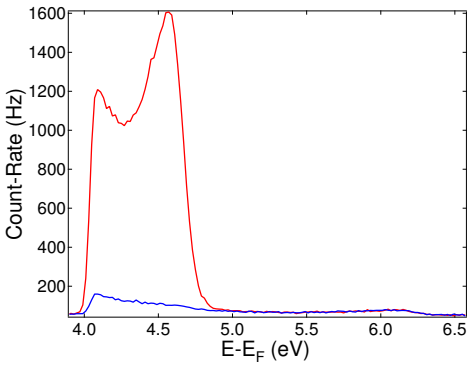

Figure 11.8:
Red curve: 2PPE spectrum measured at coincidence of red ($h\nu$=1.55 eV) plus blue ($h\nu$=3.10 eV) laser pulses.
Blue curve: Spectrum measured far away from coincidence. The same spectrum is produced when using blue light only. The energy scale is referenced to the Fermi energy of the sample.

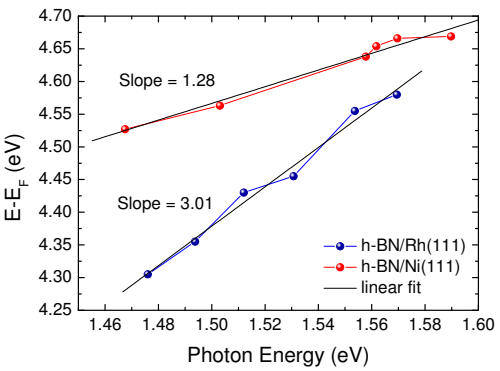

Figure 11.9:
The two-color (red plus blue) 2PPE peak energies (cf. Fig. 11.8, red curve) measured for different photon energies on the h-BN/Rh(111) nanomesh, and, for comparison, on h-BN/Ni(111). The latter data have been taken from Ref. [3].

[1] M. Corso, W. Auwärter, M. Muntwiler, A. Tamai, T. Greber and J. Osterwalder, Science **303**, 217 (2004).
[2] T. Hertel, E. Knoesel, M. Wolf and G. Ertl, Phys. Rev. Lett. **76**, 535 (1996).
[3] M. Hengsberger, M. Muntwiler et al., to be published.

11.6 A source of spin-polarized electrons: h-BN/Ni(111)

in collaboration with: W. Schüsslbauer and T. Ruchti, Time-Bandwidth Products AG, Technopark, 8005 Zürich, Switzerland.

Electron sources are used in all domains ranging from technical devices of daily life like cathode-ray tubes to large-scale scientific experiments like electron accelerators. While the energy distribution and the average kinetic energy of the electrons can easily be controlled by fine tuning of the electron emission parameters (like e.g. bias potential and temperature of the source), the control over the spin polarization of the electron beam is difficult. The latter is of great interest for particle physics experiments and for studies of magnetic systems in condensed matter physics, including the burgeoning field of *spintronics*.

In recent two-photon-photoemission (2PPE) experiments, we found that a high electron current can be obtained within a very small solid angle of about 5° opening from a Ni(111) surface covered with a monolayer of hexagonal boron nitride (1). Briefly, using the resonant superposition of two excitation pathways for photons of an energy of 1.55 eV and 3.1 eV (or 800 nm and 400 nm, respectively), electrons are excited out of initial states close to the Fermi level via two different intermediate states into the very same final state with very high efficiency (see Annual Report 2004/05). The nickel bands exhibit a strong exchange splitting in the ferromagnetic ground state with only minority d-bands and both exchange-split sp-bands crossing the Fermi level (2). Since the electron spin is preserved during the excitation process it may be expected that this photoelectron current be spin polarized. Moreover, due to the small emission cone, the brilliance of such a source would be high making it an ideal candidate for applications where good focusing of the electron beam is required. The *h*-BN layer is chemically inert, and only slight degradation of the surface has been observed in a moderate vacuum of 10^{-9} mbar over periods of several days.

In order to test the hypothesis of a spin-polarized electron current, a small experimental 2PPE setup was mounted at the COPHEE endstation of the Swiss Light Source (3), which is equipped with a 3D Mott spin polarimeter. It consisted of a small turn-key mode-locked laser oscillator (Pallas test system, Time-Bandwidth Products) which generates 3 nJ pulses of 800 nm light at 100 MHz repetition rate. Part of the output was frequency-doubled in a 1 mm thick β-barium borate crystal. The other part was slightly delayed in time such that both pulses arrived at the same time on the sample and both beams were tightly focused onto the sample, resulting in a count rate of a few Hertz in the Mott channels. The data were taken from a picture-frame like sample in remanent magnetization.

A typical data set is shown in Fig. 11.10 together with the spin analysis. An integral spin polarization of about 5% is observed in these measurements, assuming a resolving power of the Mott detectors (Sherman function) of 0.15. From the known remanent magnetization of the sample, which was only 20%, we conclude that a source with a fully magnetized substrate could yield a spin polarization of the order of 25%. An even higher spin polarization may be expected if light of larger wavelength is used, but this could not be verified with the current setup. On a medium time scale, a fully megnatizable source will be developed utilizing thin nickel films on suitable substrates. Due to its superior stability and high brightness, this device might be an interesting alternative to the currently used cesiated GaAs spin-polarized electron sources (4). A provisional patent has successfully been submitted (5).

[1] M. Muntwiler, M. Hengsberger et al., to be published.

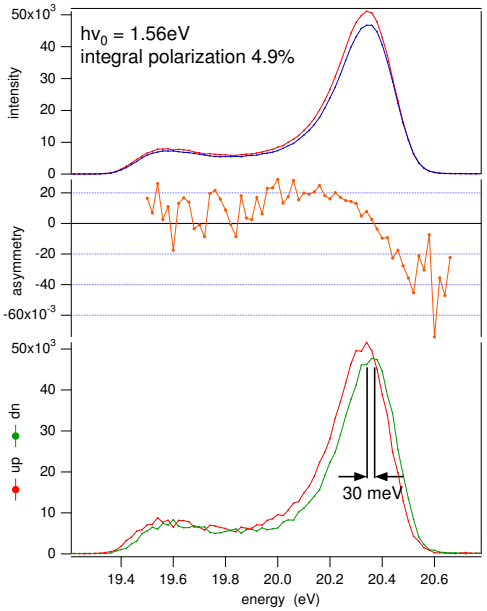

Figure 11.10: Spin-resolved two-colour 2PPE experiments on *h*-BN/Ni(1 1 1). Top panel: raw data from the Mott channels analysing the in-plane component of the spin polarization along the magnetization axis. Center panel: asymmetry obtained from the raw data. Bottom panel: spin-resolved spectra recovered from the raw data using the asymmetry scaled with the Sherman function of the Mott detector.

[2] G.B. Grad, P. Blaha, K. Schwarz, W. Auwärter, and T. Greber, Phys. Rev. B **68**, 085404 (2003).

[3] M. Hoesch, T. Greber, V.N. Petrov, M. Muntwiler, M. Hengsberger, W. Auwärter, and J. Osterwalder, J. El. Spec. Rel. Phen. **124**, 263 (2002).

[4] D.T. Pierce and F.A. Meier, Phys. Rev. B **13**, 5484 (1976).

[5] M. Hengsberger, M. Muntwiler, J. Lobo-Checa, and T. Greber, Source for spin-polarized electrons, US-provisional patent (filed July 13, 2005).

11.7 Corannulene adsorption on h-BN/Ni(110)

in collaboration with: Jay S. Siegel and Yao-Ting Wu, Organisch-chemisches Institut der Universität Zürich, and Ari P. Seitsonen, Institut de Minéralogie et de Physique des Milieux Condensés, Université Pierre et Marie Curie Paris-VI, France.

Corannulene ($C_{20}H_{10}$) is a bowl-shaped molecule with a five-fold symmetry axis, where three corannulene skeletons may be assembled into C_{60} (see Figure 11.11. On surfaces it is expected to become charged, as does C_{60}. It has a dipole moment and a larger diamagnetic response than C_{60}. Together with its curved but non-spherical geometry, it is thus a candidate molecule for molecular magnetostriction. Along the lines of a recent experiment with C_{60} on h-BN/Ni(111) (1) we prepared one monolayer of corannulene on h-BN/Ni(110), since Ni(110) has in-plane easy magnetization axes. As on Ni(111) closed single-layer hexagonal boron nitride may be formed by exposure of Ni(110) to borazine ($HBNH)_3$, where we find in coexistence a (1×6) and a (5×7) superstructure (2). In Figure 11.12 the He Iα excited photoemission spectrum for h-BN/Ni(110) and for one mono-

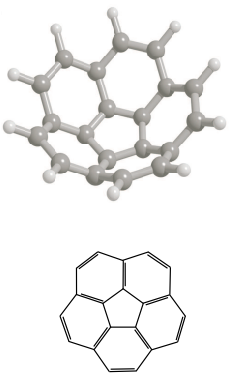

Corannulene $C_{20}H_{10}$

Figure 11.11: Three dimensional view and line bond structural representation of corannulene.

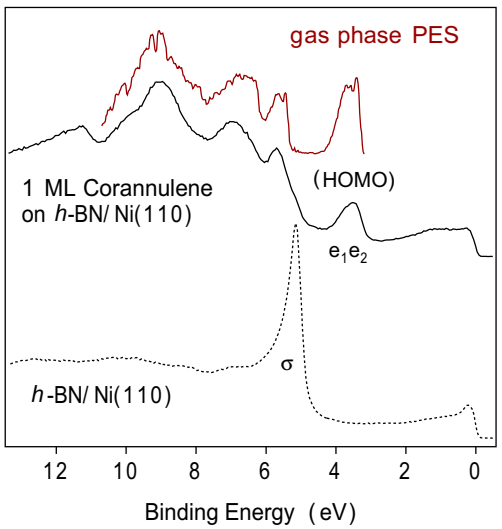

Figure 11.12:
Normal emission photoemission spectrum ($h\nu$ = 21.22 eV) of h-BN/Ni(110) (dashed line) and of one monolayer of corannulene on h-BN/Ni(110) (solid line). The gas phase photoemission spectrum from Ref. [3] serves for identification of the molecular orbitals.

layer of corannulene on top of it is shown. The data demonstrate that one monolayer of corannulene suppresses the subsrate emission, which is most clearly seen by the strong reduction of the h-BN σ band feature. A comparison with corannulene gas phase photoemission data of Seiders et al. (3) shows molecular orbitals which coincide with those of one monolayer of corannulene on h-BN/Ni(110). This is a clear indication that the molecules survive the evaporation and adsorption process intact. The intensity appearing between the highest occupied molecular orbitals (HOMO's) (e_1,e_2) and the Fermi level signals charge transfer into the lowest unoccupied molecular orbital (LUMO) of the molecule.

[1] M. Muntwiler, W. Auwärter, A.P. Seitsonen, J. Osterwalder, and T. Greber, Phys. Rev. B, **71**, 241401 (2005).
[2] T. Greber, L. Brandenberger, M. Corso, A. Tamai and J. Osterwalder, e-J. Surf. Sci. Nanotech., in press.
[3] T.J. Seiders, K.K. Baldridge, J.S. Siegel and R. Gleiter, Tetrahedron Letters, **41**, 4519 (2000).

11.8 LUMO photoemission lineshape in low-dimensional C_{60} arrays

in collaboration with: A. P. Seitsonen, Institut de Minéralogie et de Physique des Milieux Condensés, Université Pierre et Marie Curie Paris-VI; L. Patthey, Swiss Light Source, Paul Scherrer Institut; F. Baumberger and Z.-X Shen, Department of Applied Physics, Stanford University.

The electronic properties of conventional three-dimensional metals are successfully described by the Fermi-liquid theory. When the dimensionality of such a system is reduced to one, the Fermi-liquid state becomes unstable towards any many-body interactions and under certain conditions the conduction electrons may be described like a Luttinger-liquid (1). In photoemission such a state reveals itself through a characteristic exponential decay of the intensity towards the Fermi level and the presence of independent spin and charge excitations in the spectrum.

C_{60} molecular chains grown on a Cu(553) vicinal surfaces are a good system to investigate the properties of electrons in low dimensions (2). Angle resolved photoemission (ARPES) has

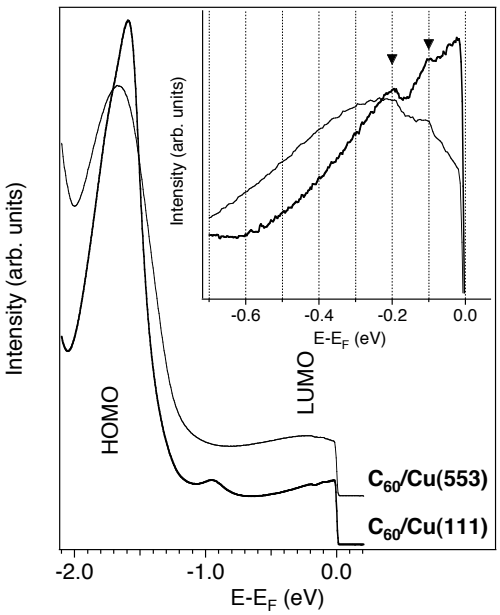

Figure 11.13: Low temperature (T=10 K) He Iα angle integrated photoemission spectra of one monolayer of C_{60} in a 1D and in a 2D molecular arrangement on Cu(553) and Cu(111), respectively. Inset: High-resolution spectra measured near the Fermi level; the thick line corresponds to Cu(111). The triangles mark the position of the satellites due to electron-phonon coupling.

shown a very anisotropic dispersion of the C_{60} HOMO (highest occupied molecular orbital), which indicates that the electronic coupling is predominant along the chains. The electrons in the t_{1u} conduction band, which derives from the lowest unoccupied molecular orbital (LUMO), determine the transport properties of the C_{60} chains. Because of charge transfer from the metal substrate, the LUMO is partially occupied and contributes significantly to the density of states near the Fermi level.

In Fig. 11.13 the angle integrated photoemission spectrum for the C_{60} chains is compared with the one for a C_{60} monolayer on Cu(111), where the molecules form a regular 2D hexagonal pattern. In that case, the spectrum presents a sharp Fermi edge, indicative of the metallic character of the layer. The maximum of the peak is just below the Fermi level position as expected for a partially occupied LUMO band. At higher binding energies we see additional features, in particular a peak at 0.1 eV and a peak-dip structure around 0.2 eV, which resemble those observed in the gas phase C_{60}^-, where the shoulders were interpreted in terms of energy loss processes due to electron-phonon coupling (3).

The spectrum of the LUMO in the one-dimensional chains is remarkably different. The peak is broader than in 2D systems. There is significant LUMO emission up to 0.6 eV below the Fermi level, which is much higher than the non–interacting total bandwidth (0.3 eV) calculated within LDA for the experimental 1D C_{60} structure. Very surprising is the fact that the maximum of the broad hump appears more than 0.2 eV below the Fermi level; moving towards E_F the intensity decreases and no sharp quasi-particle-like peak appears. This behavior has not been encountered before in photoemission from other C_{60} films and we believe it is deeply related to the highly anisotropic band structure of the one-dimensional chains. In particular it would be very tempting to interpret the loss of intensity at E_F as the signature of a Luttinger liquid. However, the spectrum maintains some features of the 2D LUMOs. The phonon satellites appear at the same energies as on Cu(111), and there is a well defined Fermi edge due to emission from the C_{60} layer. A similar lineshape has been observed for potassium intercalated bundles of single-wall carbon nanotubes, where a transition from a Luttinger liquid to a Fermi-liquid behavior has been induced upon K doping (4). For the C_{60}

chains it is possible that scattering of the electrons through the metal substrate reduces the 1D character of the LUMO states developing interchain coherence. The peculiar lineshape we observe could indicate dimensional crossover from one to higher dimensions.

[1] J. Voit, Rep. Prog. Phys. 58 (1995)977.

[2] A. Tamai, W. Auwärter, C. Cepek, F. Baumberger, T. Greber, and J. Osterwalder, Surf. Sci. 566–568 (2004) 633; A. Tamai, A.P. Seitsonen, T. Greber, and J. Osterwalder, Phys. Rev. B, submitted (2005).

[3] O. Gunnarsson, H. Handschuh, P.S. Bechthold, B. Kessler, G. Ganteför and W. Eberhardt, Phys. Rev. Lett. 74 (1995)1875.

[4] H. Rauf, T. Pichler, M. Knupfer, J. Fink and H. Kataura, Phys. Rev. Lett. 93 (2004) 0968051.

11.9 Identifying enantiomers with core level photoelectron spectroscopy: the amino acid cysteine on Au(17 11 9)^S

in collaboration with: Željko Šljivančanin, École Polytechnique Fédérale de Lausanne, and Bjørk Hammer, Department of Physics and Astronomy and iNANO, University of Aarhus, Denmark

Atomic kink sites on a vicinal single crystal surface provide an array of chiral centers as a model system to study processes such as chiral recognition. Chiral heterorecognition of the chiral amino acid cysteine ($HSCH_2 - CHNH_2 - COOH$) by the chiral Au(17 11 9)^S surface has recently been demonstrated by x-ray photoelectron diffraction (XPD) and density functional theory (DFT) calculations (1). On Au(17 11 9) cysteine adsorbs in two distinct, non-mirror symmetric conformations for D- and L-cysteine. From XPD data a well-ordered single orientation adsorption was inferred for each enantiomer. The theoretical predictions and the experimental results for the bonding geometry are in excellent agreement. The calculations find a difference in the total adsorption energies for the two enantiomers of 140 meV, where D-cysteine binds stronger to the S kinks of the surface than L-cysteine. In the structural model from the DFT calculations, the nitrogen atom of D-cysteine binds to the outer kink atom (coordination c=6, see Fig 11.14) and the N atom of L-cysteine binds to the step edge (c=7). This different binding environment should also be reflected in different, enantiospecific N 1s binding energies. Indeed, upon adsorption of slightly less than one molecule per (17 11 9) unit cell, and thus per kink site, we find a difference in the N 1s binding energy between L- and D-cysteine of 204±10 meV in x-ray photoelectron spectroscopy (XPS) (Fig. 11.15). To our knowledge this is the first identification of enantiomers by core level shifts. Moreover, the L-cysteine spectrum shows a second feature at 1.77 eV higher N 1s binding

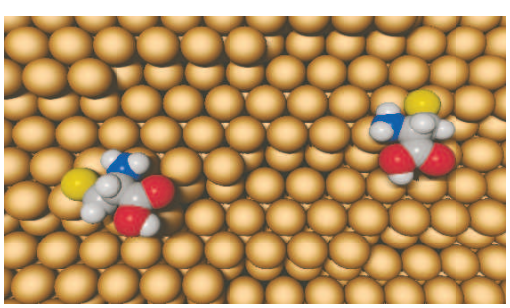

Figure 11.14: Sketch of the Au(17 11 9) surface with L- and D-cysteine. The depicted adsorption structures are those found by DFT calculations [1] and are fully consistent with XPD and XPS data.

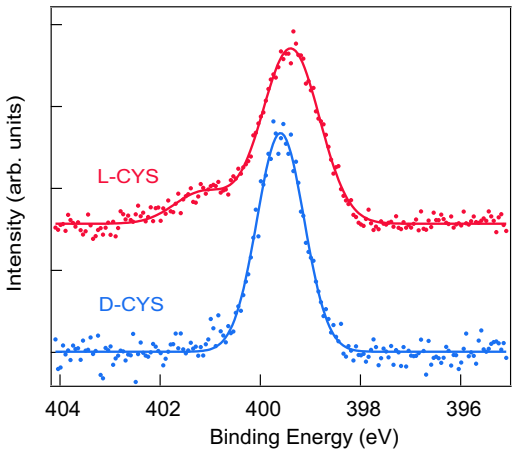

Figure 11.15: XPS spectra of the N1s core level of cysteine adsorbed on Au(17 11 9). The upper (red) spectrum is from L-cysteine (L-CYS) and the lower (blue) from D-cysteine (D-CYS). The solid lines are fits to the spectra with two or one Gaussians, respectively. See text for details.

energy, which indicates the presence of NH_3^+, in accordance with literature (2). Since the D-cysteine/Au(17 11 9) and the L-cysteine/Au(17 11 9) systems were prepared under identical conditions, this also indicates enantio specific adsorption reaction pathways. These experiments were performed at the Swiss Light Source (SLS), at the Paul Scherrer Institut in Villigen.

[1] T. Greber, Z. Sljivancanin, R. Schillinger, J. Wider, and B. Hammer, Phys. Rev. Lett. 96, 056103 (2006).

[2] G. Gonella, S. Terreni, D. Cvetko, A. Cossaro, L. Mattera, O. Cavalleri, R. Rolandi, A. Morgante, L. Floreano, and M. Canepa, J. Phys. Chem. 109, 18003 (2005).

11.10 Time-resolved low-energy electron diffraction

in collaboration with: Herbert Over, Physikalisch-Chemisches Institut, Justus-Liebig-Universität Giessen

Stroboscopic experiments access the motion of objects. In pump-probe experiments the object is first excited and subsequently probed. In order to see dynamics on the molecular scale one needs an experiment with nanometer and picosecond resolution.

This can be realized with x-rays (1) or massive particles (2; 3). The high scattering sensitivity of slow electrons for light elements can be exploited in low-energy electron diffraction (LEED) where the elastic scattering cross section is larger than for high-energy electrons or x-ray photons. This advantage has to be paid for by the difficulty to prepare a sufficient number of electrons with good energy definition ΔE/E. This is, besides the path length differences of various trajectories between electron source and target, the main source for loss of time resolution (4).

The electron source is a gold photocathode, which is excited from the back side with a 400 nm femtosecond laser pulse. Two-photon photoemission processes provide a partly collimated electron pulse. In the present gun design the nominal temporal spread of electrons on the sample is 5 picoseconds at an electron energy of 100 eV and a photocathode to

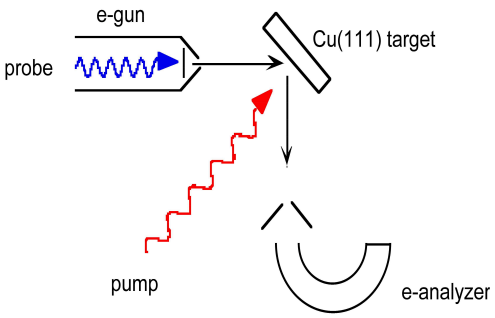

Figure 11.16: Experimental setup for time-resolved low-energy electron scattering: a pump-probe experiment probes space-charge dynamics on a Cu(111) surface with 55 eV electron pulses.

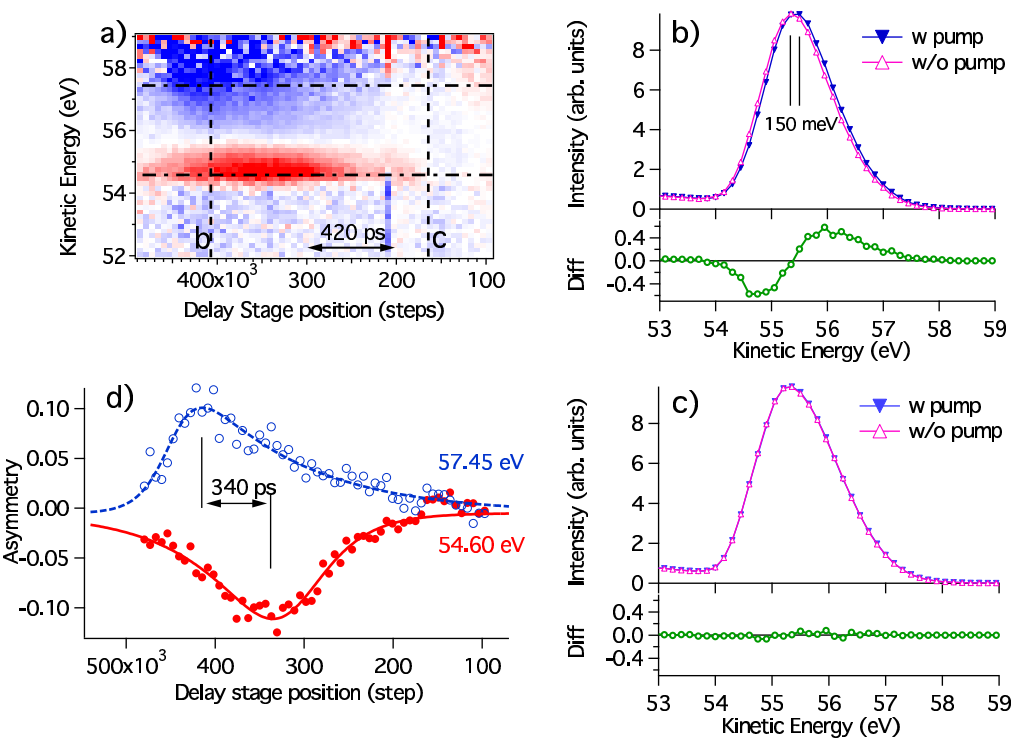

Figure 11.17:
a) Asymmetry of the electron energy distribution after scattering on a Cu(111) as a function of the time delay between pump and probe pulse. On the left hand side of the delay scale the electrons hit the surface before the pump pulse. The asymmetry is $(I_w - I_0)/(I_w + I_0)$, where I_w is the intensity of the scattered electrons with pump and I_0 that without pump beam.
b) Energy spectra with and without pump at coincidence (dashed line in a) labeled 'b'). Note the shift in energy of about 150 meV in the presence of the pump pulse. The bottom panel shows the difference between the two curves.
c) Energy spectra with and without pump off coincidence (around 1 ns after coincidence, dashed line in a) labeled 'c').
d) Asymmetries as a function of delay time at two different energies.

sample distance of 5 mm. At the space-charge limit we detect 0.1 electrons per pulse in the (0,0) LEED reflection. Figure 11.16 shows the actual experimental setup where specularly reflected 55 eV electrons probe structural changes on the target. By varying the delay of the electron arrival relative to the surface excitation by an energetic pump pulse, the evolution of these changes can be monitored in principle. Here we demonstrate that the scattered electrons are also sensitive to the dynamics of the space charge created by the pump pulse.

Fig. 11.17 shows the response of a Cu(111) target upon 100 fs, 800 nm light pulse excitations with an energy of 2.6 μJ/pulse. In order to highlight the transient changes we give in Fig. 11.17a the asymmetry $(I_w - I_0)/(I_w + I_0)$, where I_w is the intensity of the scattered electrons with pump and I_0 that without pump, as a function of the delay stage position. The electron energy spectrum is affected by the pump pulse, which is seen by a delay-dependent energy shift. At a certain delay stage position, which we define as temporal coincidence of pump and probe (delay zero), the electrons which are scattered in the presence of the pump beam gain about 150 meV kinetic energy (see Figs. 11.17b and 11.17c for comparison).

These energy shifts cannot be explained by changes in elastic scattering, nor by inelastic energy losses. More likely, the space charge that is created by the intense pump pulse, with a fluence in the order of 4 mJ/cm^2 and a duration of about 100 fs, affects the electrons. We see space-charge dynamics on the picosecond scale. Electron pulses hitting the sample surface at the same time as the pump pulses (coincidence) feel the repulsive force after the scattering and they are thus accelerated; electron pulses hitting the sample *after* coincidence have to travel twice across the space-charge electron cloud and are thus both accelerated and decelerated. For 55 eV electrons a delay of 340 ps translates in an electron traveling distance of 1.4 mm. From the energy shift of 150 meV and the interaction time of 340 ps we estimate an acceleration field strength in the order of 110 V/m, which corresponds to surface charge densities in the order of 10^{10} electrons/m^2.

[1] K.Sokolowski-Tinten, C. Blome, J. Blums, A. Cavalleri, C. Dietrich, A. Tarasevitch, I. Uschmann, E. Förster, M. Kammler, M. Horn-von-Hoegen and D. von der Linde, Nature 422, 287 (2003).

[2] M. Aeschlimann, E. Hull„ J. Cao, C.A. Schutenmaer, L.G. Jahn, Y. Gao, and H.E. Elsayed-Ali, D. A. Mantell, and M.R. Scheinfein, Rev. Sci. Intrum. 66, 1000 (1995).

[3] J.C. Williamson, J.M. Cao, H. Ihee, H. Frey, A.H. Zewail, Nature 386, 159 (1997).

[4] R. Karrer, H.J. Neff, M. Hengsberger, T. Greber, and J. Osterwalder, Rev. Sci. Intrum. 72, 4404 (2001).

12 Physics of Biological Systems

Cornel Andreoli, Conrad Escher, Hans-Werner Fink, Michael Krüger,
Tatiana Latychevskaia, Hiroshi Okamoto, Gregory Stevens.

in collaboration with:
Jevgeni Ermantraut, Clondiag Chip Technologies (Germany); Pierre Sudraud, Orsay Physics (France); Roger Morin, CNRS Marseille (France); John Miao, University of California at Los Angeles (USA); Dieter Pohl, University of Basel; Andreas Plückthun, Peter Lindner, Biochemistry Institute, University of Zurich; Bettina Böttcher, EMBL-European Institute for Molecular Biology, Heidelberg; Andre Geim, Centre for Mesoscience & Nanotechnology, University of Manchester.

In connection with the structural investigation of biological objects by Low Energy Electron Point Source (LEEPS) microscopy we established a reliable sample preparation technique to be able to investigate single phage molecules. Holograms of single molecules have been recorded and numerically reconstructed. The reconstructed images have been compared with TEM images of the same molecule which was very useful to validate the numerical reconstruction step. A European NEST ADVENTURE grant proposal has been accepted for funding, our group being the leading partner within a European consortium. After significant technical improvements of our low-temperature LEEPS microscope, electron holograms could be recorded from carbon fibers at liquid He temperature. The numerical routine for hologram reconstructions has been improved and allows now the simultaneous retrieval of absorption and phase shifting properties of the holographically recorded object with the consequence that transparent phase objects can be reconstructed from holograms. After the successful development of a new ion source based on the solid electrolyte $(AgI)(AgPO_3)$, which has been reported last year, studies on the conduction mechanism have been performed. Direct experimental evidence for the existence of ion conduction pathways has been found by observing the emission patterns of a sharp solid electrolyte tip in a field ion microscope. A new field emission microscope has been built in the framework of the advanced practical student courses in physics to observe and analyse the motion of Cs atoms on a W (110) surface.

12.1 Structure of individual biological molecules

Gregory Stevens, Michael Krüger and Hans-Werner Fink
in collaboration with: Andreas Plückthun and Peter Lindner of the Biochemistry Institute

The objective of this project is to acquire in-line electron holograms of individual molecules, from which an image of the molecule can be numerically reconstructed. In order to present the molecule to the coherent electron wave, it must be prepared so that electrons are scattered by the molecule, with minimum disturbance from a supporting substrate. One way of doing this is to use a filamentous molecule that has been suspended across a hole in a supporting film. The molecule chosen for these experiments is a mutant of filamentous bacteriophage called f1K. This was chosen because not only can it be placed in the electron beam, but it may also be used as a convenient scaffold to present other molecules to the electrons.

Since April 2005, we have obtained electron holograms of a single f1K using a purpose-built Low Energy Electron Point Source (LEEPS) microscope. This microscope is called the bioLEEPS, and was designed and constructed for imaging biological molecules. From these holograms, numerically reconstructed images of the phage were obtained and compared to a transmission electron microscope (TEM) image of the same phage. Although the resolution of the image does not provide detailed structural information about the phage, it is nevertheless encouraging that the size and shape of the object image obtained by holography is in good agreement with the size and shape of the image obtained with the TEM.

A new development in the preparation of the phage is that the specimen is more quickly frozen than before. This seems to prevent the phage forming bundles of two or more phage particles across the hole in the support film. An understanding of the need to rapidly freeze the specimen, to encourage the formation of amorphous rather than crystalline ice, came about during a visit to the lab of Prof. Kühlbrandt at the Max Planck Institute for Biophysics in Frankfurt (Main).

A TEM micrograph of an individual free-standing phage is shown in Fig. 12.1 (a). The width of the filament, 7.5 nm, indicates that

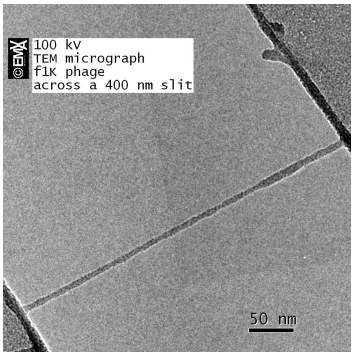

(a): 100 kV TEM micrograph of a single f1K phage suspended across a 400 nm wide slit in a carbon film.

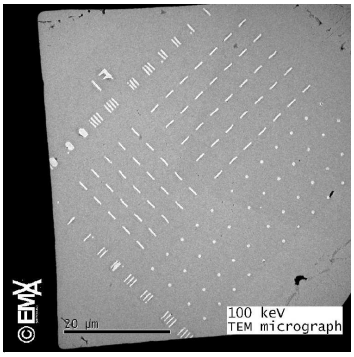

(b): a micro machined carbon support film with an array of addressable slits.

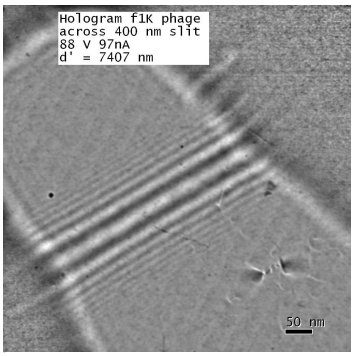

(c): a hologram of the same phage in (a), recorded with an electron energy of 88 eV.

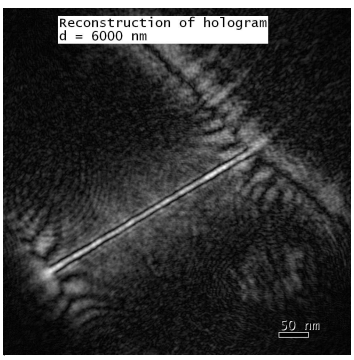

(d): numerically reconstructed image from the hologram in (c) obtained with software developed by Dr.Tatiana Latychevskaia.

Figure 12.1: We gratefully acknowledge the Institute of Veterinary Anatomy and Virology, University of Zurich for the use of their facilities in making the TEM images.

this is an image of a single phage, rather than a bundle of two or more strands. Another new development is the use of a carbon support film with holes and slits that are addressable, as shown in Fig. 12.1 (b). These special support membranes are prepared in our lab with a state-of-the-art focussed ion beam system. With this kind of support film, it is relatively easy to locate the same molecule so that it can be imaged in both the TEM and the LEEPS microscope.

The phage shown in Fig. 12.1 (a) was placed in the LEEPS microscope at a distance of 7.4 μm from a point source of coherent electrons so that a high contrast in-line electron hologram was cast on a detector screen located 100 mm away. The resulting hologram is shown in Fig. 12.1(c). The phage structure, depicted in Fig. 12.1 (d) as the amplitude of the reconstructed object wave, was obtained numerically, and shows the phage magnified by a factor of about 1.1×10^5.

Images of the phage obtained using the TEM and by numerically reconstructing the hologram are shown in Fig.12.1 (a) and (d). It was possible to compare the two imaging methods because the same molecule was located using the addressing system for the slit. In these images, it can be seen that the ratios of the width to the length of the filament are in good agreement, as are variations in the width of the molecule along its length.

We studied the effect of varying the distance between the electron source and the specimen on the formation of holograms. It is clear from these experiments, together with simulations of electron trajectories near an uncharged filament, that there is a lower limit in the source-specimen distance, beyond which the holograms cannot be reconstructed with the presently available software. This lower limit appears to depend on the experimental conditions, including the diameter of the filament being imaged.

It has been possible to obtain and reconstruct electron holograms of an individual phage. It is now a matter of extending these studies towards structural biology of single molecules. We envision proceeding towards this goal by employing the phage as a scaffold to bind single molecules to its protein shell.

As a first step towards this goal, we have succeeded in binding mono N-Hydroxy Succinimide (NHS) gold nanoparticles to the protein coat of the phage without causing the phage to cross-link and form aggregates. We found that it is necessary to keep the ratio of nanogold particles to phage binding sites to a value of less than one so as not to overload the phage with gold nanoparticles. The next step will be to obtain holograms of the nanogold particles attached to the phage. Once it has been established that the nanogold particles can be imaged on the phage coat by electron holography, we plan to extent this technique to attach biological proteins of interest to the phage. Initial experiments in this direction will focus on binding green fluorescent protein to the phage with NHS cross linker molecules.

Apart from the challenge associated with presenting single molecules to the coherent electron wave, various improvements in the instrumentation and hologram reconstruction routine are needed towards obtaining three-dimensional high resolution data on single biological molecules. We plan to begin this by improving the sensitivity of the data collection system: a fibre optic plate will be employed to couple the detector screen directly to the chip of the CCD camera.

12.2 The SIBMAR project

Hans-Werner Fink, Tatiana Latychevskaia, Gregory Stevens and Michael Krüger
in collaboration with: Andreas Plückthun of the Biochemistry institute, Andre Geim of Manchester University and Bettina Böttcher of EMBL Heidelberg

We formed a consortium with two other European partners: groups headed by Prof. Andre Geim of the University of Manchester and Dr. Bettina Böttcher of the EMBL in Heidelberg, and applied for a European NEST ADVENTURE grant to develop LEEPS microscopy for imaging biological macromolecules at atomic resolution. This proposal was called SIBMAR, and in January 2006 it was awarded funding for up to five postdoctoral positions for three years.

The main objective of this project, to obtain structural information about individual biological macromolecules at atomic resolution, will be accomplished by tackling the following sub objectives:

- An atomically thin carbon support substrate will be developed by Prof. Geim's group.
- The effects of low energy electrons on biological molecules will be studied by Dr. Böttcher's group.
- Prof. Plückthun's group will develop methodologies for preparing individual bio molecules.
- Dr. Latychevskaia, of Prof. Fink's group, will develop numerical reconstruction routines for recovering three-dimensional images from a set of holograms.
- Others in Prof. Fink's group will develop a prototype LEEPS microscope for obtaining high resolution holograms.

We are now in the process of negotiating a contract with the European Commission and expect that the project will begin around the middle of 2006.

12.3 The cryogenic LEEPS project

Hiroshi Okamoto and Hans-Werner Fink

The construction of the cryogenic low energy electron point source microscope (cryo-LEEPS) has come to a successful conclusion during the last year. Although the microscope has been capable of imaging for more than a couple of years, numerous improvements on electro-static environment, magnetic shield, and cooling system among others resulted in high enough reliability of the instrument as well as sufficient image quality at low temperatures that finally allowed for publication of the technical description of the microscope (1). The microscope (Fig.12.2) is one of the only two currently existing helium-temperature LEEPS systems in the world. The other one developed by Dr. B. Cho of Prof. Oshima's group at Waseda University in Japan (2) allows for cooling of the field emitter.

One unique feature of our system is that the whole microscope including the imaging screen is immersed to liquid helium to guarantee sufficient cooling of the specimen. The reason is as follows. Viewed from the specimen-emitter assembly, the imaging screen spans a considerable solid angle. According to Stefan-Bolzmann's law, infrared radiation heat flux is proportional to T^4, and clearly we must cool the screen down to cryogenic temperature to

stop large radiation heat influx to the specimen. Indeed, we have observed a significantly higher degree of charge-up of a lacey carbon specimen at liquid helium temperature (Fig. 12.3 c) but not at room temperature (Fig. 12.3 a) or at liquid nitrogen temperature (Fig. 12.3 b): Such a significant change with temperature had not been reported before. Moreover, it was found that charging was not observed near the metallic grid supporting lacey carbon film at liquid helium temperature. This fact underscores the notion that

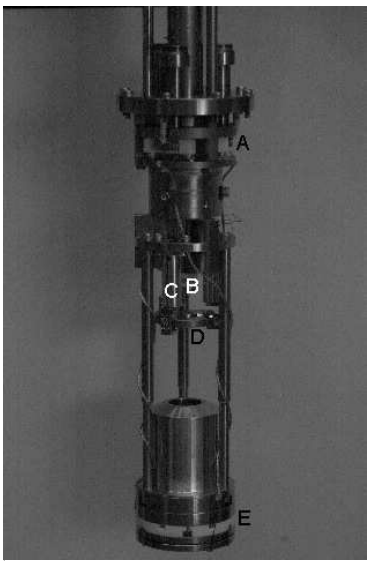

Figure 12.2: The LEEPS microscope unit. (A) The cryogenic connector. (B) The field emitter. (C) The tube piezo as a part of the Besocke stepper, hidden inside the aluminium shield. (D) The Besocke plate, on which specimens are mounted. (E) The screen assembly consisting of a metallic mesh and a phosphor screen. The copper tube above the screen assembly prevents stray electrons from reaching the screen.

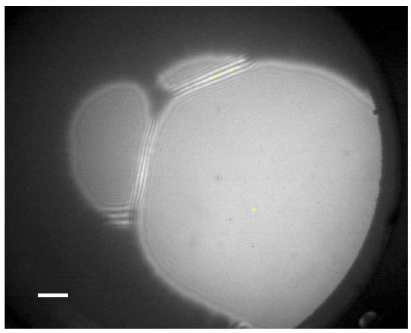

(a)

Carbon fibers at room temperature.

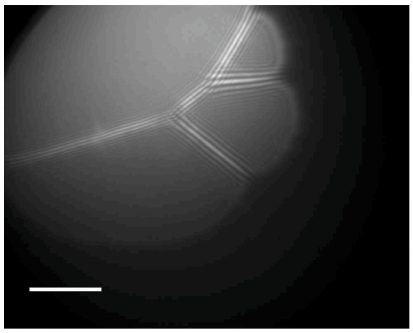

(b)

An image taken at liquid nitrogen temperature.

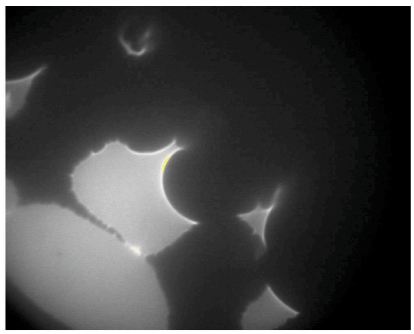

(c)

At liquid helium temperature, carbon film appears to become rather insulating.

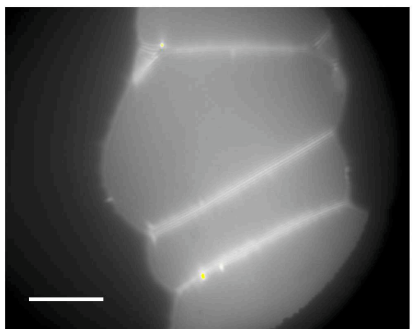

(d)

At places close to the supporting gold 400 mesh grid, interference fringes are still visible.

Figure 12.3:
LEEPS images of a lacey carbon film. The horizontal bars in (a), (b), and (d) indicate estimated 100 nm, 100 nm, and 500 nm scales, respectively, as deduced from the Fresnel fringes seen in these images. The electron energies were 80 eV, 65 eV, 85 eV, and 65 eV for (a)-(d), respectively.

electron conductivity of the specimen and/or substrate is of importance at low temperatures. Additionally, we have introduced a method to estimate scale of images based only on the observed Fresnel fringe spacing and known electron energy. This method is particularly useful for a LEEPS system under variable temperature conditions. Based on the method, the scale of the horizontal bars in Fig. 12.3 were estimated to be 100 nm, 100 nm, and 500 nm, respectively.

In line with the group's interest in visualizing electrical conduction in nanoscale objects, this instrument should be ideal to study, for example, the transition of electrical conduction mechanism from thermal excitation to quantum mechanical hopping.

[1] H. Okamoto and H.-W. Fink, Rev. Sci. Instrum. 77, 043714 (2006).

[2] B. Cho *et al.*, Rev. Sci. Instrum. 75, 3091 (2004).

12.4 Numerical hologram reconstruction

Tatiana Latychevskaia and Hans-Werner Fink

An in-line hologram is recorded as following. A single molecule is placed in a divergent beam of coherent electrons, and a magnified shadow of the molecule appears on a detector screen. The image is a hologram, which is formed by the interference of two electron waves: those which are scattered by the molecule (object wave) and those which are not scattered (reference wave). The hologram can be used to numerically reconstruct the field distribution at different distances from the screen, giving the molecule's shape at various distances. By combining this information, the 3-dimensional shape of the molecule can be rendered. The final goal is to retrieve the three-dimensional shape of a biological molecule at a few $\mathring{A}$ resolution.

In the previous year, the numerical routine for hologram reconstructions was developed. In the last year this routine was improved so that phase objects, which are transparent for the electron beam, could be reconstructed from holograms. The present reconstruction routine allows simultaneous retrieval of absorption and phase properties of the holographically recorded object.

To validate our phase reconstruction method experimentally, we recorded optical holograms of a microscopic glass sample with engraved psi-letters in it. For both, pure amplitude and pure phase objects, a 10 nm thin layer of ITO was deposited onto a round glass cover slide (thickness of about 0.15 mm) by e-beam evaporation. For the pure amplitude object, additional layers of titanium (1.5 nm) and then gold (20.5 nm) were deposited onto the ITO layer. The psi-letter was then formed by removing parts of titanium and gold with a focussed ion beam machine (FIB). For the pure phase object, a psi-letter was engraved in the ITO layer and the under laying glass.

Fig. 12.4 a) shows a hologram of an area of the glass piece where both objects, amplitude and phase psis are engraved. Fig. 12.4 b) shows the reconstructed absorption distribution and Fig. 12.4 c) shows the reconstructed phase distribution. While the *amplitude psi-letter* appears sharp on the reconstructed absorption distribution, it appears out of focus on the reconstructed phase distribution, and the *phase psi-letter* is only visible in the reconstructed phase distribution.

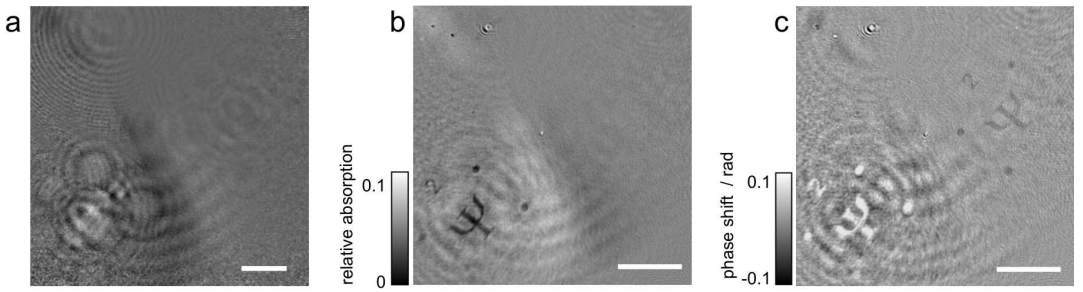

Figure 12.4:
a) Hologram of a glass area with two psis engraved , one is a pure amplitude and the other one is a pure phase object; the size of the area is about 300$\times$300 mm^2. The scale bar is about 50 mm.
b) Reconstructed absorption distribution.
c) Reconstructed phase distribution. The size of the reconstructed area is about 435$\times$435μm^2.
The scale bars in b) and c) are about 100 μm.

The developed numerical routine is especially important for reconstruction of holograms of biological objects, as biological objects demonstrate both, absorption and phase shifting properties when recorded with low energy electrons (100-200 eV).

12.5 Studies on the Conduction Mechanism in a Solid Electrolyte

Conrad Escher, Cornel Andreoli, Tatiana Latychevskaia and Hans-Werner Fink

in collaboration with: Dieter Pohl, Physics Institute, University of Basel

Having developed a solid electrolyte ion source for focused ion beam applications, the source is eventually used as a tool to study the conduction mechanism in solid electrolytes.

In a good solid-electrolyte, the mobile ions can move almost as freely as in a liquid. The resulting DC and AC conduction in solid state devices of the type shown in Fig. 12.5 (a) has been studied extensively (1; 2). However, details about the microscopic conduction mechanism in solid electrolyte conductors are experimentally not directly accessible. If, on the other hand, the solid electrolyte is given the shape of a sharp tip, set on high potential with respect to some counter electrode, ions of the mobile species may be field emitted and detected on a screen of a field ion microscope (3). This opens up the possibility to measure the emission current (4) and to observe the emission dynamics. In this way, direct insight into the conduction mechanism can be obtained. Here we report on such an experiment with a source made of amorphous $(AgI)_{0.5}(AgPO_3)_{0.5}$.

The fabrication of this solid electrolyte is fairly easy and it can readily be shaped into a sharp tip. Furthermore, its conductivity at room temperature is one of the largest known ($\sigma \approx 10^{-2}$ S/cm at 25^{o}C) (5; 6) . Contacting the tip to a silver wire or fixing it with silver paste to the source holder provides a silver reservoir, which is required for continuous operation. The solid electrolyte tip is incorporated into a field ion microscope (Fig. 12.5 (b)). When a high voltage is applied between tip and detector, Ag^+ ions are field emitted from the solid electrolyte and accelerated onto the detector. The ion emission signal is finally transferred into a light signal on a fluorescent screen as shown in Fig. 12.5 (c). A highly magnified image

of the emission sites at the tip apex is observed and the dynamics of the emission patterns on the screen are recorded by a video camera. With this technique, we address the question of the conduction mechanism in amorphous electrolytes.

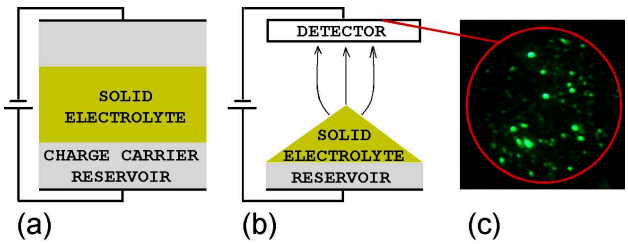

Figure 12.5: Schematic setups to measure ion conduction properties. (a) Electrolytic cell, allows time-resolved measurements, but on a macroscopic scale. (b) Field ion microscope with a solid electrolyte as source allows time- and spatially resolved measurements of a microscopic area. (c) The ion emission signal from an $(AgI)_{0.5}(AgPO_3)_{0.5}$ tip, recorded with a video camera at a frequency of 25 Hz.

Theory predicts that the mobile ions move in conduction *pathways* (6)-(15) but experimental evidence has been indirect only. In amorphous $(AgI)_x(AgPO_3)_{1-x}$ (5,6) with x≈ 0.5, chosen for our investigation, it is believed that the pathways are made up of the highly conductive AgI respectively its Ag^+ ions which squeeze between the glass-forming, less conductive $AgPO_3$ chains. This expands the glass network which might explain the existence of a *first sharp diffraction peak* in the neutron diffraction spectrum at unusually small momentum transfer (12)- (16). Above concentrations x≈0.3, cluster-like regions percolate into extended channels (5)- (7). This allows hopping of Ag^+ through the whole solid-electrolyte. Extended numerical simulations of the atomic arrangement in the ionic glass structure confirm this picture (9; 10). They lead to a refined model where the conduction pathways are created by the dynamic response of the $AgPO_3$ network to the occupation of mobile cation sites by Ag^+. The relaxation of the network is slow compared to the hopping attempt frequency; the network structure thus persists for some time after an ion has hopped to the next site. This leaves a trace for more ions to follow its path.

We shall first describe experimental observations consistent with the model outlined above. Thereafter, we present quantitative data that provide direct experimental evidence for the existence of ion conduction pathways. As apparent from Fig. 12.5 (c), the emission does not originate from a single, large spot as one might have expected for a tip surface that appears completely smooth in the electron microscope (4). Instead it consists of a number of bright spots as small as 3 nm in diameter. As evident from the sequence in Fig. 12.6, cooling the tip with liquid nitrogen decreases the number of spots and the emission current to almost zero. This demonstrates that a thermally activated process is responsible for the rate of ion emission - in agreement with theory predicting a temperature-dependent mobility of ions being the important rate-limiting factor (8). Upon cooling, the number of emission sites decreases while the intensities of the remaining sites stabilize. In view of the conduction pathway model, it ap-

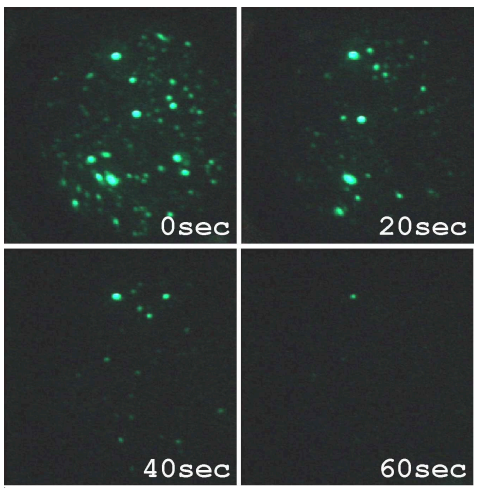

Figure 12.6: Qualitative observation of the temperature dependence of the ion conductivity. The sequence shows the decay of the emission spot intensities at constant voltage upon cooling down by liquid nitrogen to an estimated final temperature of about 100 K.

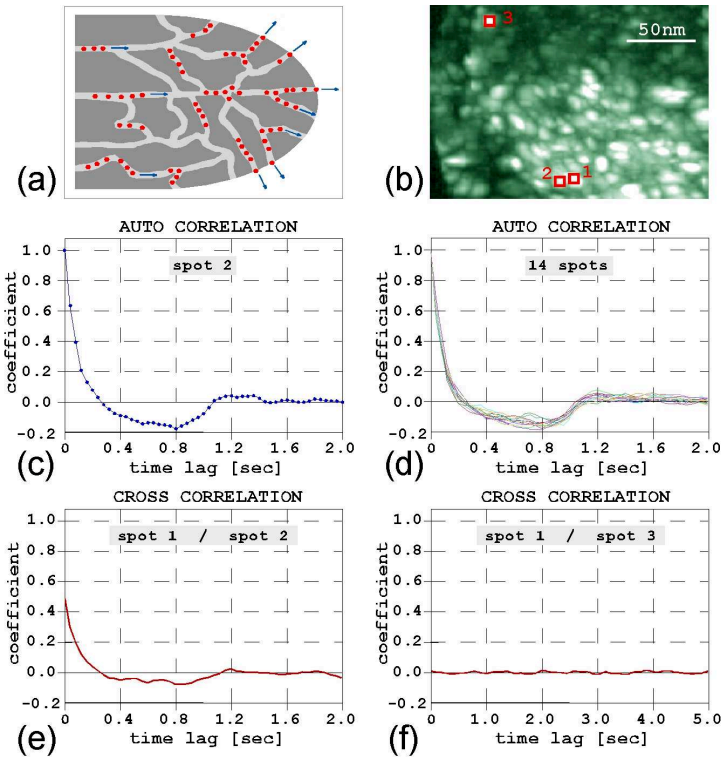

Figure 12.7: Quantitative evaluation of the silver ion emission patterns. (a) Schematic cut through an ion emitter tip exhibiting a network of ion channels. (b) The superposition of 3000 video frames clearly shows the existence of distinct emission spots at the tip apex. Three out of a total of 14 spots for further analysis of their intensities as a function of time have been marked by red squares. (c) The intensity auto-correlation function for spot 2 with a temporal resolution of 40 ms. (d) The auto-correlation functions for 14 individual spots. (e) Cross-correlation between two neighboring spots (1 and 2) 10 nm apart. (f) Cross-correlation between two spots (1 and 3) separated by a distance of 130 nm.

pears plausible that not only the mean hopping attempt frequency is reduced when the electrolyte is cooled down but also the relaxation time of the surrounding network structure is prolonged. As a consequence, only the most pronounced pathways remain active and lead to stabilized currents for the reduced overall flux of Ag^+ ions.

It is interesting to note that the emission current of a $(AgI)_{0.5}(AgPO_3)_{0.5}$ tip needs a few minutes to build up, and hysteresis in the I/V-characteristics was observed (4). This, again in view of the pathway model, indicates that the development of conduction pathways to the apex is not instantaneous.

However, the most direct indication for ion emission from individual end points of conduction pathways, as sketched in Fig. 12.7 (a), is the fact that the emission patterns consist of a number of distinct spots with smallest diameters and separations of the order of 3 nm. Even after a superposition of 3000 consecutive emission patterns, equivalent to an integration over 2 minutes, the discrete nature of the emission is preserved (Fig. 12.7 (b)). Given this distinct spatial distribution of emission sites, the observed fluctuations in the overall ion signal must be due to fluctuations within individual sites.

The analysis of the time dependence of these microscopic currents shall provide insight into the dynamics of charge transport within individual pathways. To explore this, we measured the intensity auto-correlation function for 14 individual spots. The current versus time signal has been evaluated by monitoring the relative detector intensities of individual spots. For each spot the auto-correlation function f has been computed according to:

$$f(\Delta t) = \frac{1}{N-\Delta t} \sum_{t=0}^{N-\Delta t} \frac{(I(t)-\overline{I})(I(t+\Delta t)-\overline{I})}{(I(t)-\overline{I})^2} \qquad (12.13)$$

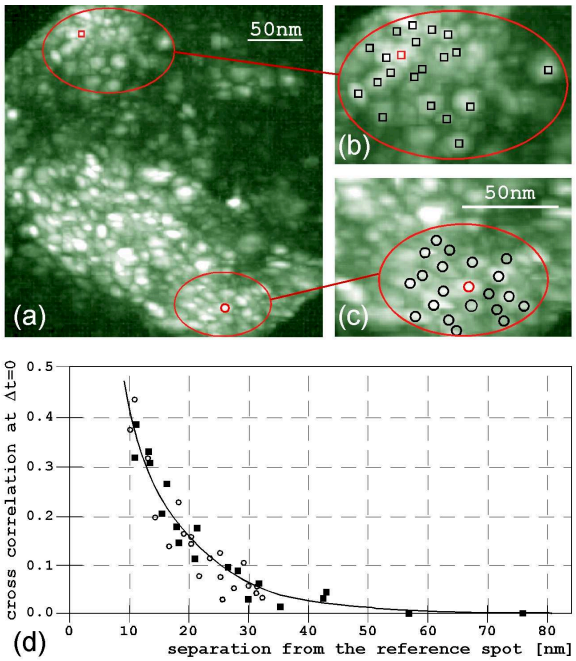

Figure 12.8: Distance dependence of the cross correlation. (a) Emission pattern from which two different regions have been arbitrarily chosen for further analysis. (b,c) In these two regions, the cross correlation function at δt=0 has been evaluated for several spots at different distances in respect to a reference spot, marked in red. (d) The two data sets (circles and squares) represent the decay of the cross-correlation for the two regions on the apex of the solid electrolyte ion source.

where I(t) is the intensity at time t, $\overline{I}$ represents the mean intensity, N+1 is the number of data points t =0,$\cdots$,N and Δt is the time lag. All auto-correlation functions displayed in Fig. 12.7 (c,d) show a characteristic decay time of about 200 ms up to which a positive correlation persists. Once this characteristic time has elapsed, a channel that did emit above the average current is exhausted for some time which is reflected in a negative correlation, maintained for about one second. It is followed by a correlation function that is zero for all longer times, as expected. As a consistency check for the picture drawn above, we also investigated the cross-correlation between different ion emission spots. Neighbouring spots separated by only 10 nm experience the same local over- respectively under-supply. This signifies that they are supplied by joined pathways in the bulk. In fact, the build-up respectively decay of this supply is associated with a characteristic time during which a positive cross-correlation is maintained (Fig. 12.7 (e)). This decay time again amounts to 200 ms, consistent with the results of the auto-correlation experiments. However, spots that are separated by more than 100 nm show no correlation for any time (Fig. 12.7 (f)).

To obtain information about the lateral extent of the ion pathway network, we have finally investigated the distance dependence of the cross-correlation coefficient for Δt=0 as a function of the separation of two spots. The results are shown in Fig. 12.8. In accordance with the model, as sketched in Fig. 12.7 (a), the cross correlation gradually decays with increasing distance between two emission sites. A measure for the density of the network is given by the lateral distance over which a positive correlation between spatially separated ion channels is maintained. It turns out, as apparent from the distance decay of the cross correlation function for Δt=0 (Fig. 12.8 (d)), that individual ion pathways of the network *communicate* over distances up to about 60 nm.

[1] High brightness solid state ion generator, its use, and method for making such generator, Patent filed in March 2005. Invented by: C. Escher, S. Thomann, C. Andreoli and H.-W. Fink (University of Zurich), J. Toquant and D. Pohl (University of Basel)

[2] Vacuum Ion Emission from Solid Electrolytes: A novel source for Focused Ion Beams, C. Escher, S. Thomann, C. Andreoli and H.-W. Fink (University of Zurich), J. Toquant and D. Pohl (University of Basel), submitted to Appl.Phys.Lett.
[3] Direct Evidence for Conduction Pathways in a Solid Electrolyte, C. Escher, T. Latychevskaia and H.-W. Fink (University of Zurich), D. Pohl (University of Basel), submitted to Phys.Rev.Lett.
[4] .C. A. Angell, Annu. Rev. Phys. Chem. 43, 693 (1992).
[5] R. C. Agrawal, R. K. Gupta, J. Mat. Sci. 34, 1131 (1999).
[6] E.W. Mueller and T.T. Tsong, Field Ion Microscopy: Principles and Applications (New York: American Elsevier, 1969).
[7] C. Escher, S. Thomann, C. Andreoli, H.-W. Fink, J. Toquant and D.W. Pohl (submitted)
[8] J.P. Malugani, A. Wasniewski, M. Doreau, G. Robert and A. Al Rikabi, Mat. Res. Bull. 13, 427 (1978).
[9] M. Mangion and G.P. Johari, Phys.Rev. B39, 8845 (1987).
[10] J.D. Wicks, L. Börjesson, G. Bushnell-Wye, W.S. Howells and R.L. McGreevy, Phys. Rev. Lett. 74, 726 (1995).
[11] P. Mustarelli, C. Tomasi and A. Magistris, Phys. Rev. B 63, 144203 (2001).
[12] A. Bunde, K. Funke and M.D. Ingram, Solid State Ionics 86-88, 1311 (1996).
[13] J. Swenson, R.L. McGreevy, L. Börjesson and J.D. Wicks, Solid State Ionics 105, 55 (1998).
[14] J.E. Shelby and D.E. Day, J. Amer. Ceram. Soc. 52, 169 (1969).
[15] C.A. Angell, Chem. Rev. 90, 523 (1990).
[16] A.P. Sokolov, A. Kisliuk, M. Soltwisch and D. Quitmann, Phys. Rev. Lett. 69, 1540 (1992).
[17] C. Rousselot et al., Solid State Ionics 78, 211 (1995).
[18] J.H. Lee and S.R. Elliott, Phys. Rev. B 54, 12109 (1996).
[19] E. Kartini et al., Phys. Rev. B 61, 1036 (2000).

12.6 Teaching

Hiroshi Okamoto, Cornel Andreoli and Hans-Werner Fink

In connection with the new lecture *Physics on the nanometer scale* a new field emission microscope has been set-up in the framework of the advanced practical student courses in physics where the motion of Cs atoms on a W (110) surface can be observed and analyzed by field emission microscopy. The students observe field emission in an ultra high vacuum environment and learn how to measure the work function as well as to extract the tip radius of the field emitter from a Fowler-Nordheim plot. A change of the workfunction after Cs deposition onto the W-tip will be observed and the noise fluctuation of the field emission process is recorded with a spectrum analyzer to determine the diffusion constant of Cs on the W surface at different temperatures.

In addition 3 physical laboratory assistant apprentices spent part of their practical education course within our lab and were guided and advised by Cornel Andreoli.

13 Mechanical Workshop

K. Bösiger, B. Lussi, R. Maier, M. Schaffner, S.Scherr (since April 2005),
P. Treier (retired September 2005), O. Fardin (apprentice since August 2005) and
R. Reichen (apprentice)

The mechanical workshop of the institute is equipped with al large variety of special tooling and machines needed to solve all kinds of mechanical tasks in relation with the research projects of the different groups at the institute. It contributes also to the education of young people which is clearly of vital importance. Presently two apprentices are being educated and in addition the workshop gives the basic courses in mechanical treatment, such as drilling, milling, welding, etc. for the students in physics. These courses were accomplished in autumn 2005 and in spring 2006. Four courses with 35 working hours each were organized. Also in this reporting periode a fraction of the activities was devoted to special designs, modifications and small series for other institutes of the university and outside companies. These tasks provide also some income to the workshop. The workshop maintains in addition the metal and technical material supply store, which was again used by more than 30 institutes [8]. The modern infrastructure of the workshop was again complemented with a new modern mill. The machine was delivered in December 2005 and installed in January 2006. It combines the flexibility of a modern universal milling machine with the performance potential of a vertical machining centre. The machine achieves maximum productivity and flexibility with such innovative features as a linear drive in the X-axis and a tool magazine with double gripper. The NC-rotary table with a large swivel-range permits machining angles of up to -18 degrees. Capabilities ranging from 5-sided machining with 5-axis positioning to 5-axis simultaneous contour machining expand the spectrum of applications. This means bundled performance, both for complete machining of single workpieces and for serial production with high precision and flexibility.

Figure 13.1:
The new mill installed in the workshop.

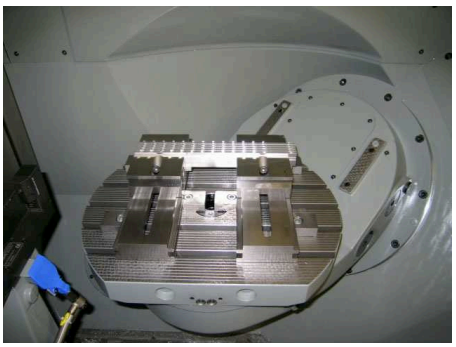

Figure 13.2:
The NC-rotary table of the new mill.

After the training courses in operating the machine for the members of the workshop and the adaptation of the CAD Software we will be prepared to produce also more complex mechanical parts in the in-house. A selection of projects is listed and illustrated below:

[1] For a catalogue see http://www.physik.unizh.ch/groups/werkstatt/dienstleistung.html

- **LHCb inner tracking detector**
  Group Straumann, Sec. 7
  Different prototype parts for tests were manufactured. The production of the final detectors and the support structures started and is an ongoing main job. The pictures show single parts during the production and the completed frames for the electronic racks and the detector frame.

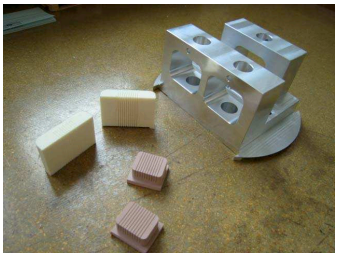
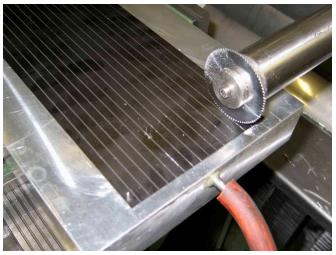

- **Solid State Physics**
  Groups Keller, Sec. 9 and Schilling, Sec. 10
  For these groups we designed and constructed different specimen holders. The picture on the right shows one complete workpiece.

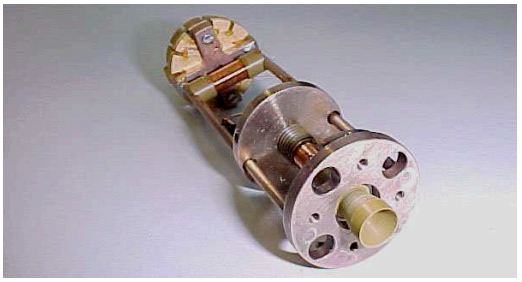

- **Surface Physics**
  Group Osterwalder, Sec. 11
  Here the main focus was maintenance and repair work. We also built a series of Borazon cooler units which are shown in the figures to the right and below.

- **CMS pixel detector**
  Group Amsler, Sec. 8
  All the necessary tooling and the parts for the detector support structure were manufactured. The pictures were taken during the production of the different parts.

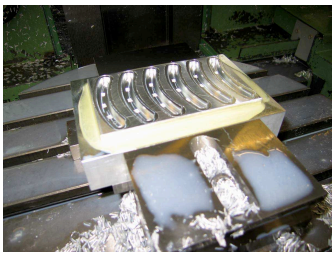
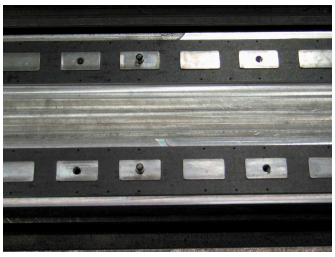

- **H1 Experiment at DESY**
  Groups Straumann and Truöl, Sec. 5
  In November and December 2005 we were involved in the repair of the H1 Detector at DESY in Hamburg. We partly had to replace the front end electronics of a detector which was built at our institute.

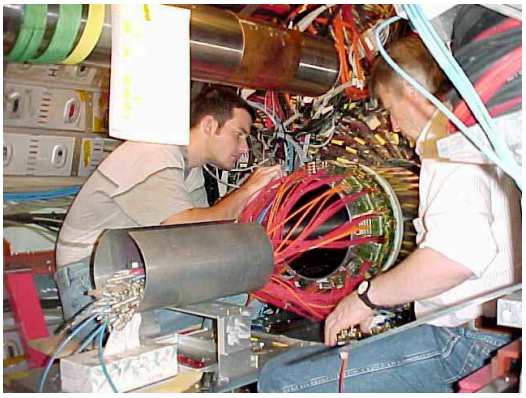

- **Physics of Biological Systems**
  Group Fink, Sec. 12
  Different mechanical infrastructure was manufactured and some test setups were built.

14 Electronics Workshop

W. Fässler, Hp. Meyer, P. Soland and K. Szeker

In the reporting period a lot of repair and maintenance work was done for the different research groups at the institute. Almost all components of an ESR spectrometer had to be fixed. Triggered by a damaged power supply the whole electronic chain was finally affected and several devices had to be replaced. In this particular case it was very difficult to find suppliers for some older components. Despite of this we developed and built different components used in the laboratories at the physics institute, for other institutes of the university and for experiments at outside labs where members from our institute do there research work. For the demonstration experiments in the lecturer halls again different devices and experimental setups were improved and supplemented in collaboration with L. Pauli and J. Seiler, who are responsible for the preparation of the experiments. Different seminars and courses were attended to keep track of the latest developments. The main focus was on the application of micro controllers and the lead-free soldering process. In the future all assemblies will be produced with lead-free components and lead-free alloys used for the soldering so we acquainted ourselves with this technology. The electronic workshop maintains also a small supply store with the most necessary items, which we upgrade and adapt continuously. In this period we renewed and unified the cable stock. We supplemented also the electronic equipment in the laboratory with a modern spectrum analyzer. It is an extremely lightweight and compact spectrum analyzer that is ideal for a large number of applications in development, service and production. Despite its compact size, it offers a wealth of functions. The instrument features a tracking generator up to 3 GHz and can demodulate signals with a bandwidth of 20 MHz. The main functions of the spectrum analyzer are directly accessible by fixed-assignment function keys, with additional functions accessed using softkeys and tables. This shortens the learning curve for new users as well as for users who operate the instrument only rarely. The spectrum analyzer is ideal for fast, easy measurements during production.

In collaboration with members of the institute of physiology (Research group Prof. N.G. Greef) we developed and built the control electronics for an optical shutter (Fig. 14.1) which is used in a fluorescence microscope with laser illumination. To investigate the operation of ion channels they detect the fluorescence light of a fluorophore, a component of a molecule which causes a molecule to be fluorescent with a CCD camera. These fluorophores suffer damages from the intense illumination. To minimise the exposure time the shutter interrupts the laser beam synchronized to the camera control and hence maximises the lifetime of the fluorophore. Ion channels are membrane proteins, found in virtually all cells, that are of crucial physiological importance.

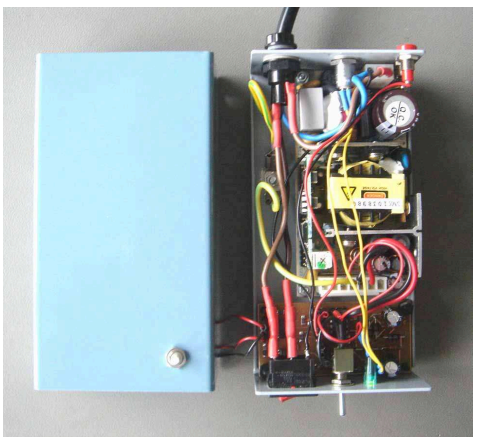

Figure 14.1: Shutter control electronics for the fluorescence microscope.

We also supported a group of high school students from the Kantonsschule Wettingen in performing their "Maturitätsarbeit", which is required as a part of the exam they have to pass. With the help of Kurt Bösiger, Peter Robmann and Stefan Steiner they constructed, built and programmed a robot which can make drawings on a standard blackboard used in class

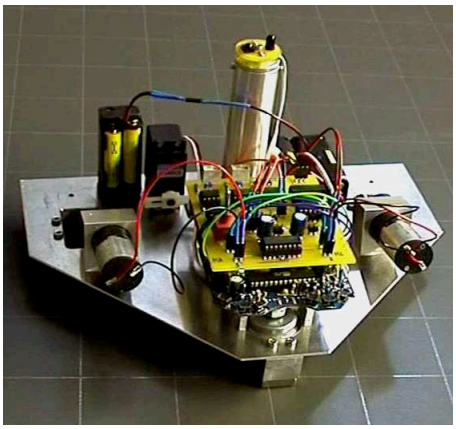

Figure 14.2:
The "Ghostwriter" on the blackboard.

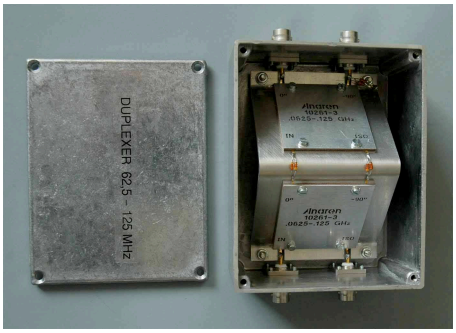

Figure 14.3: Duplexer built for the SCOPES NMR-spectrometers.

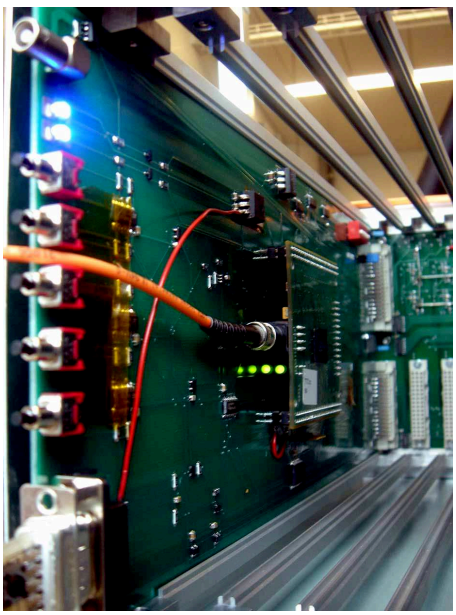

Figure 14.4: Controller card simulator.

rooms. To start with the project a tiny mobile robot developed for educational purposes by DLR, the german aerospace centre was used and adapted to the corresponding needs. The device is very flexible and completely programmable in C. Except for the printed circuit boards only standard parts are utilized and freeware tools can be used for programming. Therefore it is exceptionally suitable as an introduction into processor-controlled electronics, for projects in schools and universities. Special tools, which are freeware for private users, have been used for all electronic development phases and software design, proving that robots can be designed without expensive tools or machines. The robot is equipped with a RISC-processor and an IR-Interface for programming and remote controlling by a PC (Fig. 14.2).

A selection of projects for the different groups is listed below:

- **Physics of Biological Systems (Group Fink, Sec. 12)**
  A high voltage heating power supply transformer was modified and improved. The maximum voltage rating was increased from 3.5 kV to 4.5 kV.

- **Superconductivity and Magnetism (Group Keller, Sec. 9)**
  Several spectrometers, like the already mentioned ESR spectrometer, had to be repaired. Additional devices for the SCOPES NMR spectrometer were designed and built (Fig.14.3).

- **Particle Physics at DESY/HERA (H1) (Group Straumann and Truöl, Sec. 5)**
  The workshop was again involved in the repair and maintenance of the CIP readout electronics for the H1 experiment at DESY in Hamburg.

- **High-precision CP-violation Physics at LHCb (Group Straumann, Sec. 7)**
  Several new layouts of printed circuit boards were made and existing ones were adapted. A control card simulator board with a built on micro-controller was developed and built. (Fig. 14.4).

15 Publications

15.1 Research group of Prof. C. Amsler

Articles

- **Final results on the neutrino magnetic moment from the MUNU experiment**
  Z. Daraktchieva et al. (MUNU Collaboration), Phys. Lett. **B 615** (2005) 153.

- **Vertex reconstruction in CMS**
  E. Chabanat et al., Nucl. Instr. Meth. in Phys. Research **A 549** (2005) 188.

- **The effect of highly ionising particles on the CMS silicon strip tracker**
  W. Adam et al., Nucl. Instr. Meth. in Phys. Research **A 543** (2005) 463.

- **Simulation of Heavily Irradiated Silicon Pixel Sensors and Comparison With Test Beam Measurements**
  V. Chiochia et al., IEEE Trans. Nucl. Sci. **52** (2005) 1067.

- **Fluence dependence of charge collection of irradiated pixel sensors**
  T. Rohe et al., Nucl. Instr. Meth. in Phys. Research **A 552** (2005) 232.

- **Results from Athena**
  A. Rotondi et al. (ATHENA Collaboration), AIP Conference Proceedings **796** (2005) 285.

- **Cold - Antimatter Physics**
  M. Amoretti et al. (ATHENA Collaboration), XLIII Int. Meeting on Nuclear Physics, Bormio, 2005, Ric. Sci. **124** (2005) 25, prep. hep-ex/0503034.

- **Detection of Antihydrogen Annihilations with a Si-Micro-Strip and pure CsI Detector**
  I. Johnson et al. (ATHENA Collaboration), Proc. of the 8th ICATPP Conf. on Astroparticle, Particle, Space Physics, Detectors and Medical Physics Applications, World Scientific (2004) 473, prep. physics/0401034.

- **ATHENA - First Production of Cold Antihydrogen and Beyond**
  A. Kellerbauer et al. (ATHENA Collaboration), Proc. of the Third Meeting on CPT and Lorentz Symmetry, Bloomington, USA, World Scientific (2005) 38, prep. hep-ex/0409045.

- **Production of Cold Antihydrogen with ATHENA for Fundamental Studies**
  A. Kellerbauer et al. (ATHENA Collaboration), Proc. of the XXXIXth Rencontres de Moriond 2004, Gioi Publishers (Hanoi, Ed. J. Tran Thanh Van 2005) 385, prep. hep-ex/0406074.

- **A Gaussian-sum filter for vertex reconstruction**
  T. Speer and R. Frühwirth, Proc. of the 2004 Conf. for Computing in High-Energy and Nuclear Physics (CHEP 04), Interlaken, 2004, CERN Yellow Report 2005-002.

- **A kinematic fit and a decay chain reconstruction library**
  K. Prokofiev and T. Speer, Proc. of the 2004 Conf. for Computing in High-Energy and Nuclear Physics (CHEP 04), Interlaken, 2004, CERN Yellow Report 2005-002.

- **Design and performance of the CMS Pixel Detector Barrel Modules**
  C. Hörmann, Proc. 11 Workshop on Electronics for LHC and future Experiments, Heidelberg, CERN-LHCC 2005-038 (2005).

PhD thesis

- **Study of the $B_s^0 \to (J/\psi)\phi \to \mu^+\mu^- K^+ K^-$ Decay with the CMS Detector at LHC**
  K. Prokofiev, PhD Thesis, Universität Zürich, 2005.

Articles in press

- **Study of $K\bar{K}$ resonances in $\bar{p}p \to K^+K^-\pi^0$ at 900 and 1640 MeV/c**
  C. Amsler et al. (CRYSTAL BARREL Collaboration), Phys. Lett. **B**.

- **CMS Physics technical design report volume I : Software and detector performance**
  E. Alagöz et al., CMS - TDR - 08, CERN-LHCC-2006-001.

- **A Gaussian sum - Filter for the Vertex Reconstruction**
  T. Speer and R. Frühwirth, Comp. Phys. Comm.

- **A double junction model of irradiated silicon pixel sensors for LHC**
  V. Chiochia et al., Proc. 10th Eur. Symp. on Semiconductor Detectors: New Developments in Radiation Detectors, Wildbad Kreuth, Germany, 2005, Prep. physics/0506228, Nucl. Instr. Meth. in Phys. Research **A**.

- **Track reconstruction at the CMS experiment**
  T. Speer et al., Proc. of the X Int. Workshop on Advanced Computing and Analysis Techniques in Physics Research (ACAT 05), DESY Zeuthen, Germany, 2005, Nucl. Instr. Meth. in Phys. Research **A**.

- **Simulation and hit reconstruction of irradiated pixel sensors for the CMS experiment**
  E. Alagöz, V. Chiochia, M. Swartz, Proc. of the Workshop on Tracking in High Multiplicity Environments (TIME 2005), Zurich, Prep. physics/0512027,
  Nucl. Instr. Meth. in Phys. Research **A**.

- **Sensor simulation and position calibration for the CMS pixel detector**
  V. Chiochia, Proc. of Vertex 2005 - 14th Int. Workshop on Vertex detectors, Chuzenji Lake, Nikko, Japan, 2005, Prep. physics/0603192, Nucl. Instr. Meth. in Phys. Research **A**.

- **Extraction of electric field in heavily irradiated silicon pixel sensors**
  A. Dorokhov et al., Proc. Vertex 2004 Conf., Como, 2004, Prep. physics/0412036, Nucl. Instr. Meth. in Phys. Research **A**.

- **Study of the $B_s \to J/\psi\,\phi$ Channel with CMS**
  V. Ciulli et al., Proc. of the X Int. Conf. on B - Physics at Hadron Machines, Assisi, Italy, 2005, Nucl. Phys. **B**.

- **Robust Vertex Fitters**
  T. Speer et al., Proc. of the Workshop on Tracking in High Multiplicity Environments (TIME 2005), Zurich, Nucl. Instr. Meth. in Phys. Research **A**.

- **Observation, modeling and temperature dependence of doubly peaked electric fields in irradiated silicon pixel sensors**
  M. Swartz et al., Proc. at the Pixel 2005 Conf., Bonn, 2005, Prep. physics/0510040,
  Nucl. Instr. Meth. in Phys. Research **A**.

- **The Control and Readout Systems of the CMS Pixel Barrel Detector**
  D. Kotlinski et al., Proc. at the Pixel 2005 Conf., Bonn, 2005,
  Nucl. Instr. Meth. in Phys. Research **A**.

- **Assembly of the CMS Pixel Barrel Modules**
  S. König et al., Proc. at the Pixel 2005 Conf., Bonn, 2005,
  Nucl. Instr. Meth. in Phys. Research **A**.

- **Design and Performance of the CMS Pixel Detector Readout Chip**
  H. Chr. Kästli et al., Proc. at the Pixel 2005 Conf., Bonn, 2005,
  Nucl. Instr. Meth. in Phys. Research **A**.

- **Progress with Cold Antihydrogen**
  M. Amoretti et al. (ATHENA Collaboration), Proc. of XIII Int. Workshop on Positron and Positronium Physics (POS05), Nucl. Instr. Meth. in Phys. Research **B**.

Invited lectures

- E. Alagöz: **Hit reconstruction at CMS from irradiated silicon pixels**
  Contributed paper, Jahrestagung der SPG, Lausanne, 14 February 2006.

- Y. Allkofer: **The lifetime measurement of $\pi^{\pm}K^{\mp}$ atoms with DIRAC**
  Seminar, Budker Institute of Nuclear Physics, Novosibirsk, 14 September 2005.

- Y. Allkofer: **Large area Čerenkov counter for kaon - proton separation between 4 and 8 GeV/c**
  Contributed paper, Jahrestagung der SPG, Lausanne, 14 February 2006.

- C. Amsler: **$K\pi$ atoms with DIRAC**
  Contributed talk, CHIPP plenary meeting, Paul Scherrer Institute, 28 September 2005.

- C. Amsler: **Report of NuPECC activities**
  Invited talk, CHIPP plenary meeting, Paul Scherrer Institute, 28 September 2005.

- V. Chiochia: **Charge collection in irradiated pixel sensors : beam test measurements and simulation**
  Invited talk, ESSD - 10th Eur. Symp. on semiconductor detectors, Wildbald, Kreuth, Germany, 12 June 2005.

- V. Chiochia: **The compact muon solenoid : Status of preparation**
  Invited talk, CHIPP plenary meeting, Paul Scherrer Institute, 28 September 2005.

- V. Chiochia: **Charge collection in irradiated pixel sensors : beam test and simulation**
  Invited talk, Workshop on Tracking in High Multiplicity Environments (TIME 05), Zurich, 7 October 2005.

- V. Chiochia: **CMS pixel simulation**
  14th Int. Workshop on Vertex Detectors (VERTEX 2005), Nikko, Japan, 9 November 2005.

- V. Chiochia: **Silicon tracking detectors for the LHC experiments**
  Seminar, DESY - Hamburg, 7 March 2006.

- V. Chiochia: **Silicon tracking detectors for the LHC experiments**
  Seminar, DESY - Zeuthen, 8 March 2006.

- C. Hörmann: **Performance of CMS pixel detector barrel modules**
  Invited talk,11th Workshop on Electronics for LHC and Future Experiments, Heidelberg, 15 September 2005.

- K. Prokofiev: **Study of the $B_s \to J/\psi\,\phi$ Channel with CMS**
  Invited talk to the X Int. Conf. on B-Physics at Hadron Machines, Assisi, 22 June 2005.

- T. Speer: **Track reconstruction in the CMS tracker**
  Invited talk to the X International Workshop on Advanced Computing and Analysis Techniques in Physics Research, Berlin, Germany, 25 May 2005.

- T. Speer: **Adaptative filter and gaussian sum filter for vertex reconstruction**
  Invited talk, Workshop on Tracking in High Multiplicity Environments (TIME 05), Zurich, 5 October 2005.

- T. Speer: **Search for the decay B_s to $\mu^+\mu^-$ at CMS**
  Invited talk, Workshop Flavour in the Era of the LHC, CERN, 9 November 2005.

- L. Wilke: **Extracting $\Delta\Gamma$ in the B_s system from angular distributions of the $B_s \to J/\psi\phi$ decay with the CMS detector**
  Contributed talk, DPG - Tagung, Dortmund, 28 March 2006.

ATHENA Collaboration:

M. Amoretti, C. Amsler, G. Bonomi, P. Bowe, C. Canali, C. Carraro, C. L. Cesar, M. Charlton, M. Doser, A. Fontana, M. C. Fujiwara,R. Funakoshi, P. Genova, J. S. Hangst, R. S. Hayano, A. Kellerbauer, L. V. Joergensen, I. Johnson, V. Lagomarsino, R. Landua, E. Lodi Rizzini, M. Macri, N. Madsen, G. Manuzio, D. Mitchard, P. Montagna, H. Pruys, C. Regenfus, J. Rochet, A. Rotondi, G. Testera, A. Variola, D. P. van der Werf, Y. Yamazaki, N. Zurlo

MUNU Collaboration:

C. Amsler, M. Avenier, C. Broggini, J. Busto, C. Cerna, Z. Daraktchieva, F. Juget, D.H. Koang, J. Lamblin, D. Lebrun, O. Link, G. Puglierin, A. Stutz, A. Tadsen, J.-L. Vuilleumier, V. Zacek

CRYSTAL BARREL Collaboration:

C. Amsler, C. A. Baker, B. M. Barnett, C. J. Batty, M. Benayoun, P. Blüm, K. Braune, V. Credé, K. M. Crowe, M. Doser, W. Dünnweber, D. Engelhardt, M.A. Faessler, R. P. Haddock, F. H. Heinsius, N. P. Hessey, P. Hidas, D. Jamnik, H. Kalinowsky, P. Kammel, J. Kisiel, E. Klempt, H. Koch, M. Kunze, U. Kurilla, R. Landua, H. Matthäy, C. A. Meyer, F. Meyer-Wildhagen, R. Ouared, K. Peters, B. Pick, M. Ratajczak, C. Regenfus, U. Strohbusch, M. Suffert, U. Thoma, I. Uman, S. Wallis-Plachner, D. Walther, U. Wiedner, B. S. Zou, Č. Zupančič

DIRAC Collaboration:

B. Adeva, L. Afanas'ev, Y. Allkofer, C. Amsler, D. Bartos, A. Benelli, V. Brekhovskikh, A. Caragheorgheopol, T. Cechak, M. Chiba, S. Constantinescu, C.O. Curceanu, C. Detraz, D. Dreossi, D. Drijard, A. Dudarev, I. Evangelou, J. L. Fungueirino Pazos, J. Gerndt, P. Gianotti, G. Giolu, O. Gorchakov, K. Gritsay, C. Guaraldo, M. Hansroul, S. Horikawa, M. Iliescu, V. Karpukhin, J. Kluson, M. Kobayashi, P. Kokkas, V. Komarov, L. Kruglova,

V. Kruglov, A. Kulikov, A. Kuptsov, K. I. Kuroda, A. Lamberto, A. Lanaro, V. Lapchine, R. Lednicky, P. Levi Sandri, L. Lopez Aguera, V. Lucherini, N. Manthos, C. Marinas Pardo, L. Nemenov, M. Nikitin, K. Okada, V. Ol'shevskiy, M. Pentia, A. Penzo, M. Plo, T.C. Ponta, Z. Pustylnik, G.F. Rappazzo, J. Rochet, A. Romero Vidal, J. J. Saborido Silva, J. Schacher, F. Takeutchi, A. Tarasov, L. Tauscher, F. A. Triantis, T. Trojek, S. Trusov, J. Smolik, S. Sugimoto, A. Ryazantsev, V. Rykalin, O. Vazquez Doce, T. Vrba, V. Yaz'kov, M. Zhabitskiy, P. Zrelov

15.2 Research group of Prof. H.-W. Fink

Articles

- **Time-resolved spectroscopic fluorescence imaging, transient absorption and vibrational spectroscopy of intact and photo-inhibited photosynthetic tissue**
  P.B. Lukins, S. Rehman, G.B. Stevens, D. George, Luminescence, 20 (2005), p. 143-151.

- **Synthesis and Characterization of PbSe Nanocrystal Assemblies**
  M. Bashouti, A. Sashchiuk, L. Amirav, S. Berger, M. Eisen, M. Krueger, U. Sivan, E. Lifshitzin, in *Nanoparticle Assemblies and Superstructures* (Ed. N. Kotov), CRC Press Taylor Francis Group, 2005, p. 207-224.

- **Axisymmetric Liquid Hanging Drops**
  E. Meister and T. Yu. Latychevskaia, Journal of Chemical Education 83(1), 2006, p.117-126.

- **Resorcin[4]arene Cavitand-Based Molecular Switches**
  V.A. Azov, A. Beeby, M. Cacciarini, A. G. Cheetham, F. Diederich, M. Frei, J. K. Gimzewski, V. Gramlich, B. Hecht, B. Jaun, T. Latychevskaia, A. Lieb, Y. Lill, F. Marotti, A. Schlegel, R. R. Schlittler, P. J. Skinner, P. Seiler, Y. Yamakoshi, Advanced Functional Materials 16(2), 2006, p. 147-156.

- **A Quantum Mechanical Scheme to reduce Radiation Damage in Electron Microscopy**
  H. Okamoto, T. Latychevskaia and H.-W. Fink, Appl. Phys. Lett. 88, 164103 (2006).

- **A Cryogenic Low Energy Electron Point Source Microscope**
  H. Okamoto and H.-W. Fink, Rev. Sci. Instrum. 77, 043714 (2006).

Diploma thesis

- **Erste Festkörper-Elektrolyt-Ionenquelle**
  Sandra Thomann, Diplomarbeit, Universität Zürich, 2005.

Conference reports

- **Energetics of Single DNA Molecules**
  H.-W. Fink and C. Escher, Extended Abstract, Proceedings of the Symposium on Surface Science, O41, Les Arcs France, 2005.

- **Vacuum Ion Emission from Solid Electrolytes**
  C. Escher, Swiss Physical Society Meeting, EPF Lausanne, 13.2.06.

- **Electron Holography of Individual Filamentous Phage (Poster)**
  G.B. Stevens, M. Krüger, T. Latyschevskaia, A. Plückthun, H.-W. Fink, Swiss Physical Society Meeting, EPF Lausanne, 13-14.2.06.

15.3 Research group of Prof. H. Keller

Articles

- **Essential heterogeneities in hole-doped cuprate superconductors**
  K.A. Müller, in *Structure and Bonding Vol. 114, 1-11 (2005)*, A. Bussmann-Holder and K.A. Müller, eds., Springer-Verlag Berlin Heidelberg (2005).

- **Unconventional isotope effects in cuprate superconductors**
  H. Keller, in *Structure and Bonding Vol. 114, 143-169 (2005)*, A. Bussmann-Holder and K.A. Müller, eds., Springer-Verlag Berlin Heidelberg (2005).

- **Evidences for polaron formation in cuprates**
  A. Bussmann-Holder, H. Keller, and K.A. Müller, in *Structure and Bonding Vol. 114, 365-384 (2005)*, A. Bussmann-Holder and K.A. Müller, eds., Springer-Verlag Berlin Heidelberg (2005).

- **Polaron formation as origin of unconventional isotope effects in cuprate superconductors**
  A. Bussmann-Holder and H. Keller, Eur. Phys. J. B **44**, 487-429 (2005).

- **Unconventional isotope effects as evidence for polaron formation in cuprates**
  A. Bussmann-Holder, H. Keller, A.R. Bishop, A. Simon, R. Micnas, and K.A. Müller, Europhys. Lett. **72**, 423-429 (2005).

- **Magnetic freezeout of electrons into muonium atoms in GaAs**
  V.G. Storchak, D.G. Eshchenko, J.H. Brewer, B. Hitti, R.L. Lichti, and B.A. Aronzon, Phys. Rev. B **71**, 113202-1-4 (2005).

- **Clean and dirty superconductivity in pure, Al-doped, and neutron irradiated MgB_2: A far-infrared study**
  M. Ortolani, D. Di Castro, P. Postorino, I. Pallecchi, M. Monni, M. Putti, and P. Dore, Phys. Rev. B **71**, 172508-1-4 (2005).

- **Automated operation of a homemade torque magnetometer using LabVIEW**
  S. Kohout, J. Roos, and H. Keller, Meas. Sci. Technol. **16**, 2240-2246 (2005).

- **Anisotropy of the antiferromagnetic spin correlations in the superconducting state of $YBa_2Cu_3O_7$ and $YBa_2Cu_4O_8$**
  A. Uldry, M. Mali, J. Roos and P.F. Meier, J. Phys.: Condens. Matter **17**, L499-L505 (2005).

- **Pressure effect on the in-plane magnetic penetration depth in $YBa_2Cu_4O_8$**
  R. Khasanov, J. Karpinski, and H. Keller, J. Phys.: Condens. Matter **17**, 2453 - 2460 (2005).

- **Pressure effects on the superconducting properties of $YBa_2Cu_4O_8$**
  R. Khasanov, T. Schneider, and H. Keller, Phys. Rev. B **72**, 014524-1-4 (2005).

- **Observation of nonexponential magnetic penetration profiles in the Meissner state - A manifestation of nonlocal effects in superconductors**
  A. Suter, E. Morenzoni, N. Garifianov, R. Khasanov, E. Kirk, H. Luetkens, T. Prokscha, and M. Horisberger, Phys. Rev. B **72**, 024506-1-12 (2005).

- **Pressure effect on the magnetic penetration depth in MgB_2**
  D. Di Castro, R. Khasanov, C. Grimaldi, J. Karpinski, S.M. Kazakov, and H. Keller, Phys. Rev. B **72**, 094504-1-5 (2005).

- **Pressure and isotope effect on the anisotropy of MgB_2**
  T. Schneider and D. Di Castro, Phys. Rev. B **72**, 054501-1-4 (2005).

- **Magnetic penetration depth in $RbOs_2O_6$ studied by muon spin rotation**
  R. Khasanov, D.G. Eshchenko, D.Di Castro, A. Shengelaya, F. La Mattina, A. Maisuradze, C. Baines, H. Luetkens, J. Karpinski, S.M. Kazakov, and H. Keller, Phys. Rev. B **72**, 104504-1-7 (2005).

- **Surface dynamics of a thin polystyrene film probed by low energy muons**
  F.L. Pratt, T. Lancaster, M.L. Brooks, S.L. Blundell, T. Prokscha, E. Morenzoni, A. Suter, H. Luetkens, R. Khasanov, K. Shinotsuka, and H.E. Assender, Phys. Rev. B **72**, 121401-1-4 (2005).

- **Anomalous electron-phonon coupling probed on the surface of ZrB_{12} superconductor**
  R. Khasanov, D. Di Castro, M. Belogolovskii, Yu. Paderno, V. Filippov, R. Bruetsch, and H. Keller, Phys. Rev. B **72**, 224509-1-4 (2005).

- **Coexistence and coupling of superconductivity and magnetism in thin film structures**
  A.J. Drew, S.L. Lee, D. Charlambous, A. Potenza, C. Marrows, H. Luetkens, A. Suter, T. Prokscha, R. Khasanov, E. Morenzoni, D. Ucko, and E.M. Forgan, Phys. Rev. Lett. **95**, 197201-1-4 (2005).

- **Muon-spin-rotation measurements of the penetration depth of the infinite-layer electron-doped $Sr_{0.9}La_{0.1}CuO_2$ cuprate superconductor**
  A. Shengelaya, R. Khasanov, D.G. Eshchenko, D. Di Castro, I.M. Savić, M.S. Park, K.H. Kim, Sung-Ik Lee, K.A. Müller, and H. Keller, Phys. Rev. Lett. **94**, 127001-1-4 (2005).

- **Thin Film, Near-Surface and Multi-Layer Investigations by Low-Energy μ^+SR**
  T. Prokscha, E. Morenzoni, A. Suter, R. Khasanov, H. Luetkens, D. Eshchenko, N. Garifianov, E. M. Forgan, H. Keller, J. Litterst, C. Niedermayer, and G. Nieuwenhuis, Hyperfine Interactions **DOI 10.1007/s10751-005-9104-5**, 1-8 (2005).

- **Microscopic phase separation and two type of quasiparticles in lightly doped $La_{2-x}Sr_xCuO_4$ observed by electron paramagnetic resonance**
  A. Shengelaya, M. Bruun, B.I. Kochelaev, A. Safina, K. Conder, and K.A. Müller, in *Symmetry and Heterogeneity in High Temperature Superconductors*, ed. A. Bianconi (Spinger, 2006) (pp. 105-116).

- **The search for new high temperature superconductors**
  K.A. Müller, Supercond. Sci. Technol. **19**, S1-S3 (2006).

Conference reports

- **Insulator to metal transition and resistive memory effect in perovskites induced by electric field.**
  F. La Mattina, A. Shengelaya, J.G. Bednorz, and H. Keller, Annual meeting of the Swiss Physical Society, Bern, 14-15 July, 2005.
- **Oxygen Isotope effect on electronic phase separation in lightly-doped $La_{2-x}Sr_xCuO_4$**
  A. Maisuradze, A. Shengelaya, K. Conder, H. Keller, K. A. Müller, Annual meeting of the Swiss Physical Society, Bern, 14-15 July, 2005.
- **Search for orbital current effects in cuprates by ^{89}Y NMR**
  S. Strässle, M. Mali, J. Roos, J. Karpinski, and H. Keller, Annual meeting of the Swiss Physical Society, Bern, 14-15 July, 2005.
- **Insulator to metal transition and resistive memory effect in Cr-doped $SrTiO_3$ induced by electric field.**
  F. La Mattina, A. Shengelaya, J.G. Bednorz, H. Keller, Swiss Workshop on Materials with Novel Electronic Properties, Les Diablerets, 26-28 September, 2005.
- **EPR study of the spin-lattice relaxation of Yb^{3+}-doped $YBa_2Cu_3O_{7-x}$**
  A. Maisuradze, A. Shengelaya, K. Pomjakushina, K. Conder, K. A. Müller and H. Keller, Swiss Workshop on Materials with Novel Electronic Properties,Les Diablerets, 26-28 September, 2005.
- **Orbital current effects in cuprates: A ^{89}Y NMR study**
  S. Strässle, M. Mali, J. Roos, J. Karpinski, and H. Keller, Swiss Workshop on Materials with Novel Electronic Properties, Les Diablerets, 26-28 September, 2005.
- **Orbital current effects in cuprates: A ^{89}Y NMR study in $Y_2Ba_4Cu_7O_{15}$**
  J. Roos, S. Strässle, M. Mali, T. Ohno, and H. Keller, International ICAM Workshop NMR/EPR of Correlated Electron Superconductors, 15-21 October, 2005.
- **NMR investigation of the vortex-lattice melting in $YBa_2Cu_3O_7$**
  S. Strässle, J. Roos, M. Mali, A. Schilling, and H. Keller, Annual meeting of the Swiss Physical Society, Lausanne, 13-14 February, 2006.
- **EPR study of the spin-lattice relaxation of Yb^{3+}-doped $YBa_2Cu_3O_{7-x}$**
  A. Maisuradze, A. Shengelaya, K. Pomjakushina, K. Conder, K. A. Müller and H. Keller, Annual meeting of the Swiss Physical Society, Lausanne, 13-14 February, 2006.
- **Effect of Cr doping on the voltage-induced insulator-to-metal transition and resistive memory behaviour of $SrTiO_3$**
  F. La Mattina, A. Shengelaya, J.G. Bednorz, and H. Keller, Annual meeting of the Swiss Physical Society, Lausanne, 13-14 February, 2006.

Invited lectures/talks

- D.G. Eshchenko: **Muon spin rotation studies of novel diluted magnetic semiconductors**
  Swiss Workshop on Materials with Novel Electronic Properties, Les Diablerets, 26-28 September, 2005.

- H. Keller: **Luft und Wasser**
  Kinderuniversität, Universität Zürich, Zürich, Switzerland, June 8, 2005.
- H. Keller: **Unconventional isotope effects in cuprate high-temperature superconductors - what can we learn from them?**
  Second Joint Taiwanese-Swiss Workshop on Nanotechnology: towards novel materials, Taipei, Taiwan, June 20-25, 2005.
- H. Keller: **Controlling mesoscopic phase separation: muon-spin rotation investigations**
  COMEPHS Kick-off Meeting, Athens, Greece, June 30 - July 1, 2005.
- H. Keller: **Unconventional isotope effects in cuprate superconductors - what can we learn from them?**
  Conference on *Electron State and Lattice Effects in Cuprate High Temperature Superconductors*, AIST Tsukuba, Japan, October 27-28, 2005.
- H. Keller: **Unconventional isotope effects in high T_c cuprates superconductors - what can we learn from them?**
  Max-Planck Institute for Solid State Research, Stuttgart, Germany, November 23, 2006.
- R. Khasanov: **Study of the magnetic penetration depth in $RbOs_2O_6$**
  SR User's Meeting BVRA , PSI, VIlligen, 19-20 January, 2005.
- R. Khasanov: **Unconventional isotope and pressure effects on the magnetic penetration depth in cuprate superconductors**
  PSI, Villigen, May 19, 2005.
- R. Khasanov: **Unconventional isotope effect on the magnetic penetration depth in cuprate superconductors**
  Ames Lab, Iowa State university, USA, December 6, 2005.
- J. Roos: **Orbital current effects in cuprates: A ^{89}Y NMR study in $Y_2Ba_4Cu_7O_{15}$**
  International ICAM Workshop NMR/EPR of Correlated Electron Superconductors, Dresden, Germany, October 15 - 21, 2005.

15.4 Research group of Prof. J. Osterwalder

Articles

- **Growth of Cr-doped TiO_2 films in the rutile and anatase structure by oxygen-plasma assisted molecular beam epitaxy**
  J. Osterwalder, T. Droubay, T. Kaspar, J. Williams, C. M. Wang, S. A. Chambers,
  Thin Solid Films 484, 289-298 (2005).
- **Doping-induced reorientation of C_{60} molecules on Ag(111)**
  A. Tamai, A. P. Seitsonen, R. Fasel, Z.-X. Shen, J. Osterwalder, T. Greber,
  Phys. Rev. B 72, 085421-1-5 (2005).
- **Electron-photon pulse correlator based on space-charge effects in a metal pinhole**
  A. Dolocan, M. Hengsberger, H. J. Neff, M. Barry, C. Cirelli, T. Greber, J. Osterwalder, Japan. J. Appl. Phys. 45, 285-291 (2006).
- **Chiral recognition of organic molecules by atomic kinks on surfaces**
  T. Greber, Z. Sljivancanin, R. Schillinger, J. Wider, B. Hammer,
  Physical Review Letters 96, 056103-1-4 (2006).

Articles in press

- **Single layer hexagonal boron nitride films on Ni(110)**
  T. Greber, L. Brandenberger, M. Corso, A. Tamai, J. Osterwalder, e-J. Surf. Sci. Nanotech.
- **Spin-polarized photoemission**
  J. Osterwalder, in *Magnetism: Synchrotron Radiation Approach*, E. Beaurepaire, H. Bulou, F. Scheurer, J.-P. Kappler, eds., (Springer, Berlin, Heidelberg, New York 2006) 27 p.

Diploma and PhD theses

- **Molecular arrangement and electronic properties of low-dimensional C_{60} systems**
  Anna Tamai, Ph. D. Thesis, Physik-Institut, Universität Zürich, 2005.
- **Boron nitride and boron nanostructures on the (110) surface of molybdenum**
  Milan Allan, Diploma Thesis, Physik-Departement, ETH Zürich, 2006.

Contributed conference presentations

- **A study of the spin structure in the surface state of a kinked-vicinal Au(111) surface (Poster)**
  J. Lobo, 13th European Physical Society Meeting, Bern, 12.7.05.
- **Structural and electronic properties of C_{60} chains (Poster)**
  A. Tamai, 13th European Physical Society Meeting, Bern, 12.7.05.
- **Towards time-resolved LEED from large molecules on surfaces**
  C. Cirelli, Swiss Physical Society Meeting, Bern, 14.7.05.
- **Hexagonal boron nitride on Pd(111): formation of Moiré patterns**
  M. Morscher, Swiss Physical Society Meeting, Bern, 14.7.05.
- **Giant resonance in two-photon-photoemission spectra from an insulating monolayer**
  M. Hengsberger, 13th European Physical Society Meeting, Bern, 14.7.05.
- **h-BN on Pd(110): a tunable system for self-assembled nanostructures ? (Poster)**
  M. Corso, 8th International Conference on the Structure of Surfaces, München, 18.7.05.
- **Time-resolved low-energy electron diffraction with pump-probe experiments**
  A. Dolocan, 8th International Conference on the Structure of Surfaces, München, 18.7.05.
- **Chiral heterorecognition: cysteine on Au(17 11 9) (Poster)**
  R. Schillinger, 4th PSI Summer School on Condensed Matter Research, Zuoz, 14.8.05.
- **Rashba effect and spin structure of the Shockley surface state on vicinal-kinked Au(111)**
  J. Lobo, 23rd European Conference on Surface Science (ECOSS), Berlin, 5.9.05.
- **Unusually large HOMO dispersion in C_{60} chains**
  A. Tamai, 23rd European Conference on Surface Science (ECOSS), Berlin, 5.9.05.

- **Conformation related changes of molecular ionicity: C_{60} on h-BN/Ni(111)**
  T. Greber, Conference *From Molecular Switches to Molecular Motors*, Monte Veritá, Ascona, 23.9.05.

- **Progress on the nanomesh**
  M. Corso, 1st EMPA Ph. D. Symposium, EMPA Dübendorf, 20.10.05.

- **Two-photon photoemission: an ideal tool for studying lifetimes and excitation dynamics (Poster)**
  M. Hengsberger, 1st optETH Meeting, ETH Zürich, 28.10.05.

- **Magnetisation induced changes in the photoemission current from corannulene on h-BN/Ni(110)**
  L. Brandenberger, Swiss Physical Society Meeting, EPF Lausanne, 14.2.06.

- **Time-resolved low-energy electron scattering**
  T. Greber, Symposium on Surface Science (3S), St. Christoph, Austria, 10.3.06.

- **Chiral heterorecognition of organic molecules and inorganic surfaces**
  T. Greber, APS March Meeting, Baltimore, USA, 14.3.06.

- **Picosecond real-time observation of low-energy electron scattering from large molecules on surfaces**
  C. Cirelli, APS March Meeting, Baltimore, USA, 14.3.06.

- **Boron nitride nanostructures: complete layers and nanomeshes**
  M. Corso, APS March Meeting, Baltimore, USA, 15.3.06.

- **Toward direct structure determination of adsorbed molecules: D and L cysteine on Cu(17 11 9)**
  R. Schillinger, DPG Frühjahrstagung, Dresden, 30.3.06.

Invited lectures

- J. Osterwalder: **Spin-resolved Fermi surface mapping**
  International Workshop on Strong Correlations and ARPES, Dresden, 4.4.05.

- T. Greber: **Formation of boron nitride layers on transition metals with and without holes**
  Nanoscience on Surfaces (NSOS) Workshop , Obergurgl, Austria, 28.4.05.

- J. Osterwalder: **Non-trivial orientations of C_{60} molecules in fullerene monolayers**
  207th Meeting of the Electrochemical Society, Québec, Canada, 19.5.05.

- J. Osterwalder: **Von Einsteins Photoeffect zur hochauflösenden Festkörpersonde**
  Vortrag, Physikalische Gesellschaft Zürich, 2.6.05.

- J. Osterwalder: **Nanotemplates: vicinal surfaces and nanostructured boron nitride films**
  Festkörperphysik-Seminar, Universität Basel, 13.6.05.

- J. Osterwalder: **Nanotemplate surfaces**
  2nd Joint Taiwanese-Swiss Workshop on Nanotechnology: Towards Novel Materials, Academia Sinica, Taipei, Taiwan, 20.6.05.

- T. Greber: **Hexagonal boron nitride layers on transition metal surfaces: templates for building nanostructures**
  13th International Congress on Thin Films (ICTF) / 8th International Conference on Atomically Controlled Surfaces, Interfaces and Nanostructures (ACSIN), Stockholm, Sweden, 22.6.05.

- T. Greber: **The conformation matters: from molecular chains and switches to chiral heterorecognition**
  Physik-Kolloquium, Universität Bielefeld, 27.6.05.

- T. Greber: **X-ray photoelectron diffraction (XPD): probing atom positions and molecular orientations at surfaces**
  4th PSI Summer School on Condensed Matter Research, Zuoz, 14.8.05.

- T. Greber: **Boron nitride layers on metals: a lot for building nanostructures**
  23rd European Conference on Surface Science (ECOSS), Berlin, 5.9.05.

- M. Hengsberger: **Tracking ultrafast changes in solid surfaces: electron diffraction and photoelectron spectroscopy**
  SLS Seminar, PSI, 21.9.05.

- T. Greber: **Monolayers of hexagonal boron nitride with and without small holes: what are they good for ?**
  Abteilungsseminar, EMPA Thun, 13.10.05.

- J. Osterwalder: **Spin-polarized angle-resolved photoemission**
  Workshop on X-ray Spectroscopy in Magnetic Solids, PSI, 18.10.05.

- J. Osterwalder: **About photoemission and electrons in nanostructures**
  Physikalisches Kolloquium, ETH und Universität Zürich, 2.11.05.

- J. Osterwalder: **Photoemission spectroscopy on nanostructures**
  Physikalisches Kolloquium, Universität Regensburg, 28.11.05.

- T. Greber: **Molecular conformation and electronic structure: from molecular switches to chiral heterorecognition**
  ALS Seminar, Lawrence Berkeley Laboratory, Berkeley Ca., 30.11.05.

- M. Hengsberger: **Ultrafast dynamics on surfaces: development of a time-resolved structural probe**
  Seminar Oberflächenmagnetismus, Universität Münster, 2.12.05.

- T. Greber: **Boron nitride layers on transition metal surfaces and their spontaneous nanostructuring**
  5th International Conference on Atomic-Level Characterisation of New Materials and Devices (ALC), Kona, Hawaii, 5.12.05.

- M. Hengsberger: **Stepping towards real-time observation of molecular motion on surfaces: time-resolved electron diffraction**
  Seminar SFB *Energiedissipation an Grenzflächen*, Universität Duisburg-Essen, 10.1.06.

- M. Hengsberger: **Magnetism and angle-resolved photoemission**
  Colloque *Magnétisme à Soleil*, Gif sur Yvette, France, 17.1.06.

- J. Osterwalder: **Electronic structure of nanostructured surfaces and interfaces**
  IFF Kolloquium, Forschungszentrum Jülich, 20.1.06.

- J. Osterwalder: **Nanostructuring of hexagonal boron nitride films on transition metal surfaces**
  Seminar iNANO, University of Aarhus, Denmark, 16.3.06.

15.5 Research group of Prof. A. Schilling

Articles

- **Spectral cut-off in the efficiency of the resistive state formation caused by absorption of a single-photon in current-carrying superconducting nano-strips**
  A. Semenov, A. Engel, H.-W. Hübers, K. Il'in, M. Siegel The European Phys. Journal B, **47**, (2005) 495-501.
- **Noise of a superconducting photon detector**
  A. Semenov, A. Engel, K. Il'in, M. Siegel, H.-W. Hübers IEEE Transactions on Applied Superconductivity, **15**, (2005) 518- 521.

Articles in press

- **Superconducting detector using microwave current-noise**
  A. Semenov, H.-W. Hübers, K. Il'in, M. Siegel, and A. Engel, Supercond. Sci. Technol.
- **Electric noise and local photon-induced nonequilibrium states in a current-carrying nanostructured superconductor**
  A. Engel, A. Semenov, H.-W. Hübers, K. Il'in and M. Siegel, New Frontiers in Superconductivity Research (B.P. Martins, ed.), Nova Science Publishers.

Bachelor thesis

- **Messung der Richtungsabhängigkeit der spezifischen Wärme von $YBa_2Cu_3O_{7-\delta}$: Ein Indikator für $s-$ oder $d-$Wellen Supraleitung?**
  Stefan Menzi, Bachelorarbeit, Physik-Institut, Universität Zürich, 2005.

Contributed conference presentations

- **Superconducting nanostructures: fluctuations and photon detectors (Poster)**
  A. Engel, H. Bartolf, A. Schilling, A. Semenov, H.-W. Hübers, K. Il'in and M. Siegel, Manep workshop 2005, Les Diablerets, Switzerland, 26.-28.9.2005.
- **Spectral performance of a single-photon detector (Poster)**
  A. Semenov, A. Engel, H.-W. Hübers, K. Il'in and M. Siegel, Kryoelektronische Bauelemente KRYO2005, Bad Herrenalb, Germany, 9.-11.10.2005.
- **Superconducting Nanostructures and Single Photon Detectors (Poster)**
  A. Engel, H. Bartolf, A. Schilling, A. Semenov, H.-W. Hübers, K. Il'in and M. Siegel, SPG Jahrestagung 2006, Lausanne, Switzerland, 13.-14.2.2006.
- **Design and realization of a sensitive technique to detect resonance phenomena in the range of 250 kHz to 2 MHz (Poster)**
  R. Dell'Amore, J. Roos and A. Schilling, SPG Jahrestagung 2006, Lausanne, Switzerland, 13.-14.2.2006.

Invited lectures

- A. Schilling: **Materials of Atoms, Matter of Vortices**
  Anorganisch-Chemisches Institut der Universität Zürich, 9.12.2005.
- A. Engel: **Physics of Superconducting Thin-Film Nanostructures – Applications as Single-Photon Detector**
  Manep Project 5 Internal Workshop 2006, Neuchâtel, Switzerland, 8.2.2006.

15.6 Research group of Prof. U. Straumann

PhD theses

- **Losses and Depolarization of Stored Ultracold Neutrons on Diamond-like Carbon**
  Peter Fierlinger, PhD thesis, Universität Zürich, March 2005.
- **An optical readout system for the LHCb silicon tracker**
  Achim Vollhardt, PhD thesis, Universität Zürich, March 2005.
- **A search for excited quarks with the H1 detector at HERA**
  Jan Becker, PhD thesis, Universität Zürich, May 2005.
- **Search for Rare Decays of the B_s Meson with the D0 Experiment**
  Ralf Bernhard, PhD thesis, Universität Zürich, October 2005.
- **Large Area Silicon Tracking Detectors with Fast Signal Readout for the Large Hadron Collider (LHC) at CERN**
  Stephan Köstner, PhD thesis, Universität Zürich and TU Wien, October 2005.

Conference contributions and invited seminars

HERA:

- **Prompt Photons in DIS**
  Carsten Schmitz, Frühjahrstagung 2006 der Deutschen Physikalischen Gesellschaft e.V. - Fachverband Teilchenphysik, Dortmund, Deutschland, 28. - 31. March 2006.
- **Single top production in ep collisions at HERA**
  Stefania Xella Hansen, TOP 2006, International workshop on Top Quark Physics, Jan 12-15, 2006, University of Coimbra, Portugal.
- **Search for leptoquarks and lepton flavor violation at the H1 experiment**
  Linus Lindfeld, 13th International Workshop on Deep Inelastic Scattering (DIS 05), Madison, Wisconsin, 27 Apr - 1 May 2005.

B physics:

- **Flavor-changing neutral current charm and bottom decays at the Tevatron**
  Frank Lehner, International Workshop on Discoveries in Flavour Physics At e^+e^- Colliders, February 28 - March 03, 2006, Frascati, Italy.
- **New Results from Rare B Decays at Hadron Colliders**
  Frank Lehner, 20th International Workshop on Weak Interactions and Neutrinos (WIN '05), June 06-11, 2005, Delphi, Greece.
- **Heavy Flavor Rare Decays at DØ**
  Ralf Bernhard, Frontiers in Contemporary Physics III, 23-28 May 2005, Nashville, USA.
- **Search for rare flavor-changing and penguin decays of the B_s^0 meson with the DØ detector**
  Ralf Bernhard, APS Spring Meeting in Tampa, April 16-49, 2005.

experimental techniques:

- **The LHCb Silicon Tracker**
  D. Volyanskyy, Annual Swiss Physical Society meeting 2006, Feb. 14, 2006, Lausanne, Switzerland.
- **Silicon Detectors for the CMS and LHCb Experiment**
  T. Sakhelashvili, invited seminar, Institute for High Energy Physics, Tbilisi State University, Dec. 21, 2005 and Physic Faculty of Tbilisi State University, Jan. 16, 2006
- **Heavy flavour tagging at the ILC: where are we?**
  Stefania Xella, ECFA study on Physics and Detectors for the International Linear Collider: 3rd workshop. Park Hotel Schönbrunn, Nov 14-17, 2005, Vienna, Austria.
- **Long Ladder Performance**
  O. Steinkamp, 14th International Workshop on Vertex Detectors, Chuzenji Lake, Nikko, Japan, November 7-11, 2005.
- **The Status of the LHCb Silicon Tracker**
  Frank Lehner, 9th ICATPP Conference on Astroparticle, Particle, Space Physics, Detectors and Medical Physics Applications, October 14-17, 2005, Como, Italy.
- **Hybrid Design, Procurement and Testing for the LHCb Silicon Tracker**
  Frank Lehner, 11th Workshop on Electronics for LHC and future Experiments, September 12-16, 2005, Heidelberg, Germany.
- **Production of the LHCb Silicon Tracker Readout Electronics**
  Achim Vollhardt, 11th Workshop on Electronics for LHC and future Experiments, 12.-16. September 2005, Heidelberg, Germany.
- **A radiation tolerant fibre optic readout system for the LHCb Silicon Tracker**
  Achim Vollhardt, 10th European Symposium on Semiconductor Detectors, 12.-16. Juni 2005, Wildbad Kreuth, Germany.
- **Status and prospects of the LHCb experiment**
  U. Straumann, Seminar at Geneva University, 13. April 2005.
- **Diamond-Like Carbon for Ultracold Neutrons**
  P. Fierlinger et al., PANIC05, Santa Fe, NM, USA, Oktober 2005.

- **Deuterium for Ultracold Neutron Sources**
  P. Fierlinger et al., PANIC05, Santa Fe, NM, USA, Oktober 2005.

- **Diamond-like carbon coatings for Ultracold Neutron applications**
  S. Heule et al., Diamond 2005, Toulouse, France, 16.-21. September 2005.

- **Diamond-like carbon for Ultracold Neutron applications'**
  S. Heule et al., Annual Meeting of the Swiss Physics Society SPG, Bern, 14. July 2005.

- **Loss and Depolarisation Studies of Ultracold Neutrons on Diamond Surfaces**
  P. Fierlinger, et al., Annual Meeting of the Swiss Physics Society SPG, Bern, 14. July 2005.

- **Loss and Depolarization Studies of Ultra-cold Neutrons**
  P. Fierlinger, et al., Frühjahrstagung der DPG, FV Hadronen und Kerne, Berlin, March 2005.

- **Diamond-like carbon for Ultracold Neutron applications**
  S. Heule, et al., Frühjahrstagung der DPG, FV Hadronen und Kerne, Berlin, March 2005.

- **Measurement of the Loss and Depolarization Probability of UCN on Beryllium and Diamond Like Carbon Films**
  P. Fierlinger, S. Heule, U. Straumann et al., Int. Conf. on Precision Measurements with Slow Neutrons, NIST, USA, 2004, J. Res. Natl. Inst. Stand. Technol. 110 (2005) 279.

- **Magnetic Field Stabilization for Magnetically Shielded Volumes by External Field Coils**
  P. Fierlinger et al., Int. Conf. on Precision Measurements with Slow Neutrons, NIST, USA, 2004, J. Res. Natl. Inst. Stand. Technol. 110 (2005) 173.

Collaboration notes for DØ and LHCb [9]

- **Performance Studies of the Silicon Strip Detectors of the LHCb Silicon Tracker**
  Proceedings IWORID 2005, Glasgow, Jul 25-29, 2005 S.Köstner et al., LHCb-2005-080

- **Design and Performance of the LHCb Silicon Tracker**
  Proceedings TIME 2005, Zürich, Oct 4-7, 2005, K.Vervink et al., LHCb-2005-102

- **Performance of Long Ladders for the LHCb Silicon Tracker**
  Proceedings VERTEX 2005, Chuzenji Lake, Nikko, Nov 7-11, 2005 O.Steinkamp et al., LHCb-2005-103.

- **Production of the LHCb Silicon Tracker Readout Electronics**
  Proceedings LECC 2005, Heidelberg, Sep 12-16, 2005 A.Vollhardt et al., LHCb-2005-064.

- **Hybrid Design, Procurement and Testing for the LHCb Silicon Tracker**
  Proceedings LECC 2005, Heidelberg, Sep 12-16, 2005 A.Bay et al., LHCb-2005-061.

- **Pre-Series Sensor Qualification for the Inner Tracker of LHCb**
  G. Baumann et al., LHCb-2005-037.

- **Silicon Sensor Probing and Radiation Studies for the LHCb Silicon Tracker**
  Proceedings European Symposium on Semiconductor Detectors, Wildbad Kreuth, Jun 12-16, 2005, C. Lois et al., LHCb-2005-033.

[9] LHCb notes can be accessed through the CERN document server on http://cdsweb.cern.ch/

- **A radiation tolerant fiber-optic readout system for the LHCb Silicon Tracker**
  Proceedings European Symposium on Semiconductor Detectors, Wildbad Kreuth, Jun 12-16, 2005, A. Vollhardt et al., LHCb-2005-032.
- **Noise Considerations for the Beetle Amplifier Used With Long Silicon Strip Detectors**
  S.Koestner and U.Straumann, LHCb-2005-029.
- **Material Budget Calculation for the LHCb TT Station**
  M. Needham, A. Wenger, LHCb-2005-020.
- **Mechanical Characterization of a TT Half-Module Prototype**
  G. Baumann et al., LHCb-2005-007.
- **Updated Occupancies for the LHCb Inner Tracker**
  M. Needham, LHCb-2005-006.
- **Update on the upper limit for the rare decay $B_s^0 \to \mu^+\mu^+$with the D0 detector**
  R. Bernhard and F. Lehner, D0-note 4696, January 2005.
- **Sensitivity Analysis of the rare decay $B_s^0 \to \mu^+\mu^-\phi$ with the D0 detector**
  R. Bernhard and F. Lehner, D0-note 4695, January 2005.

Articles

Ultra-cold neutrons:

- **Measured total cross sections of slow neutrons scattered by solid deuterium and implications for ultracold neutron sources**
  S. Heule, P. Fierlinger et al., Phys. Rev. Lett. 95, 182502 (2005).
- **First storage of ultracold neutrons in a volume formed of foils coated with diamond-like Carbon**
  P. Fierlinger, S. Heule, U. Straumann et al. Phys. Lett. B 625, 19 (2005).
- **Measured total cross section of slow neutrons scattered by gaseous and liquid 2H2**
  P. Fierlinger et al., Phys. Rev. Lett.94, 212502 (2005).
- **Production of ultra-cold neutrons from a cold neutron beam on a 2H2 target**
  P. Fierlinger, S. Heule et al., Phys. Rev. C 71, 054601 (2005).
- **The simulation of ultracold neutron experiments using GEANT4**
  P. Fierlinger et al., Nucl. Instr. Meth. A 552 (2005) 513-521.
- **Magnetron-sputtered Be coatings as reflectors for ultracold neutrons**
  P. Fierlinger et al., Nucl. Instr. Meth. A 551 (2005) 429-447.
- **Magnetic Field Stabilization by a Helmholtz-like Coil Configuration**
  P. Fierlinger et al., Nucl. Instr. Meth. A 554 (2005) 527-539.
- **A novel apparatus for the investigation of material properties for the storage of ultracold neutrons**
  P. Fierlinger, U. Straumann et al., Nucl. Instr. Meth. A 550, 637 (2005).
- **On the use of lead/tin alloys as target material for the production of spallation neutrons**
  P. Fierlinger et al., Nucl. Instr. Meth. A, 539, 3, 1, 646-653 (2005).

DØ:

- **Search for pair production of second generation scalar leptoquarks in $p\overline{p}$ collisions at $\sqrt{s}$ = 1.96 TeV**
  V. M. Abazov *et al.* (DØ Collaboration),
  (arXiv:hep-ex/0601047).

- **Measurement of the isolated photon cross section in $p\overline{p}$ collisions at $\sqrt{s}$ = 1.96 TeV**
  V. M. Abazov *et al.* (DØ Collaboration),
  (arXiv:hep-ex/0511054).

- **A Combination of CDF and DØ Limits on the Branching Ratio of $B^0_{s(d)} \to \mu^+\mu^-$ Decays**
  R. Bernhard *et al.* ,
  (arXiv:hep-ex/0508058).

- **Search for the Higgs boson in $H \to WW(*)$ decays in $p\overline{p}$ collisions at $\sqrt{s}$ = 1.96 TeV**
  V. M. Abazov *et al.* (DØ Collaboration), Phys. Rev. Lett. 96, 011801 (2006),
  (arXiv:hep-ex/0508054).

- **The upgraded DØ detector**
  V. M. Abazov *et al.* (DØ Collaboration), arXiv:physics/0507191.

- **Measurement of the lifetime difference in the B^0_s system**
  V. M. Abazov *et al.* (DØ Collaboration), Phys. Rev. Lett. 95, 171801 (2005),
  (arXiv:hep-ex/0507084).

- **Measurement of semileptonic branching fractions of B mesons to narrow D** states**
  V. M. Abazov *et al.* (DØ Collaboration), Phys. Rev. Lett. 95, 171803 (2005),
  (arXiv:hep-ex/0507046).

- **Search for large extra spatial dimensions in dimuon production at DØ**
  V. M. Abazov *et al.* (DØ Collaboration), Phys. Rev. Lett. 95, 161602 (2005),
  (arXiv:hep-ex/0506063).

- **Measurement of the $t\overline{t}$ production cross section in $p\overline{p}$ collisions at $\sqrt{s}$ = 1.96 TeV in dilepton final states**
  V. M. Abazov *et al.* (DØ Collaboration) Phys. Lett. B 626, 55 (2005),
  (arXiv:hep-ex/0505082).

- **Search for single top quark production in $p\overline{p}$ collisions at $\sqrt{s}$ = 1.96 TeV**
  V. M. Abazov *et al.* (DØ Collaboration), Phys. Lett. B 622, 265 (2005),
  (arXiv:hep-ex/0505063).

- **Measurement of the W boson helicity in top quark decays**
  V. M. Abazov *et al.* (DØ Collaboration), Phys. Rev. D 72, 011104 (2005),
  (arXiv:hep-ex/0505031).

- **Search for Randall-Sundrum gravitons in dilepton and diphoton final states**
  V. M. Abazov *et al.* (DØ Collaboration), Phys. Rev. Lett. 95, 091801 (2005),
  (arXiv:hep-ex/0505018).

- **Measurement of the $t\overline{t}$ production cross section in $p\overline{p}$ collisions at $\sqrt{s}$ = 1.96 TeV using lepton + jets events with lifetime b-tagging**
  V. M. Abazov *et al.* (DØ Collaboration), Phys. Lett. B 626, 35 (2005),
  (arXiv:hep-ex/0504058).

- **Measurement of the $t\bar{t}$ production cross section in $p\overline{p}$ collisions at $\sqrt{s}$ = 1.96 TeV using kinematic characteristics of lepton + jets events**
  V. M. Abazov *et al.* (DØ Collaboration), Phys. Lett. B 626, 45 (2005), (arXiv:hep-ex/0504043).

- **Search for supersymmetry via associated production of charginos and neutralinos in final states with three leptons**
  V. M. Abazov *et al.* (DØ Collaboration), Phys. Rev. Lett. 95, 151805 (2005), (arXiv:hep-ex/0504032).

- **Production of W Z events in $p\overline{p}$ collisions at $\sqrt{s}$ = 1.96 TeV and limits on anomalous W W Z couplings**
  V. M. Abazov *et al.* (DØ Collaboration), Phys. Rev. Lett. 95, 141802 (2005), (arXiv:hep-ex/0504019).

- **Search for neutral supersymmetric Higgs bosons in multijet events at $\sqrt{s}$ = 1.96 TeV**
  V. M. Abazov *et al.* (DØ Collaboration), Phys. Rev. Lett. 95, 151801 (2005), (arXiv:hep-ex/0504018).

- **Measurement of the $p\overline{p} \rightarrow W\gamma + X$ cross section at $\sqrt{s}$ = 1.96 TeV and W W gamma anomalous coupling limits**
  V. M. Abazov *et al.* (DØ Collaboration), Phys. Rev. D 71, 091108 (2005) (arXiv:hep-ex/0503048).

- **Study of $Z\gamma$ events and limits on anomalous $ZZ\gamma$ and $Z\gamma\gamma$ couplings in $p\overline{p}$ collisions at $\sqrt{s}$ = 1.96 TeV**
  V. M. Abazov *et al.* (DØ Collaboration), Phys. Rev. Lett. 95, 051802 (2005), (arXiv:hep-ex/0502036).

- **Measurement of inclusive differential cross sections for Upsilon(1S) production in $p\overline{p}$ collisions at $\sqrt{s}$ = 1.96 TeV**
  V. M. Abazov *et al.* (DØ Collaboration), Phys. Rev. Lett. 94, 232001 (2005), (arXiv:hep-ex/0502030).

- **Search for first-generation scalar leptoquarks in $p\overline{p}$ collisions at $\sqrt{s}$ = 1.96 TeV**
  V. M. Abazov *et al.* (DØ Collaboration), Phys. Rev. D 71, 071104 (2005), (arXiv:hep-ex/0412029).

- **First measurement of $\sigma(p\overline{p} \rightarrow$ Z) x Br(Z $\rightarrow \tau\tau$) at $\sqrt{s}$ = 1.96 TeV**
  V. M. Abazov *et al.* (DØ Collaboration), Phys. Rev. D 71, 072004 (2005), (arXiv:hep-ex/0412020).

- **A search for anomalous heavy-flavor quark production in association with W bosons**
  V. M. Abazov *et al.* (DØ Collaboration), Phys. Rev. Lett. 94, 152002 (2005), (arXiv:hep-ex/0411084).

- **A measurement of the ratio of inclusive cross sections σ(p p $\rightarrow$ Z + b-jet)/σ(p p $\rightarrow$ Z + jet) at $\sqrt{s}$ = 1.96 TeV**
  V. M. Abazov *et al.* (DØ Collaboration), Phys. Rev. Lett. 94, 161801 (2005), (arXiv:hep-ex/0410078).

- **Measurement of the W W production cross section in $p\overline{p}$ collisions at $\sqrt{s}$ = 1.96 TeV**
  V. M. Abazov *et al.* (DØCollaboration), Phys. Rev. Lett. 94, 151801 (2005), (arXiv:hep-ex/0410066).

- **A search for $Wp\overline{p}$ and WH production in $p\overline{p}$ collisions at $\sqrt{s}$ = 1.96 TeV**
  V. M. Abazov *et al.* (DØCollaboration), Phys. Rev. Lett. 94, 091802 (2005)
  (arXiv:hep-ex/0410062).

- **Measurement of the Λ/B^0 lifetime in the decay $\Lambda/B^0 \rightarrow J/\psi\Lambda^0$ with the DØ detector**
  V. M. Abazov *et al.* (DØ Collaboration), Phys. Rev. Lett. 94, 102001 (2005)
  (arXiv:hep-ex/0410054).

- **Measurement of the ratio of B^+ and B^0 meson lifetimes**
  V. M. Abazov *et al.* (DØ Collaboration), Phys. Rev. Lett. 94, 182001 (2005)
  (arXiv:hep-ex/0410052).

- **A search for the flavor-changing neutral current decay $B_s^0 \rightarrow \mu^+\mu^-$ in $p\overline{p}$ collisions at $\sqrt{s}$ = 1.96 TeV with the DØdetector**
  V. M. Abazov *et al.* (DØ Collaboration), Phys. Rev. Lett. 94, 071802 (2005)
  (arXiv:hep-ex/0410039).

- **Measurement of the B_s^0 lifetime in the exclusive decay channel $B_0^s \rightarrow J/\psi\phi$**
  V. M. Abazov *et al.* (DØ Collaboration), Phys. Rev. Lett. 94, 042001 (2005),
  (arXiv:hep-ex/0409043).

- **Measurement of dijet azimuthal decorrelations at central rapidities in $p\overline{p}$ collisions at $\sqrt{s}$ = 1.96 TeV**
  V. M. Abazov *et al.* (DØ Collaboration), Phys. Rev. Lett. 94, 221801 (2005)
  (arXiv:hep-ex/0409040).

- **Search for supersymmetry with gauge-mediated breaking in diphoton events at DØ**
  V. M. Abazov *et al.* (DØ Collaboration), Phys. Rev. Lett. 94, 041801 (2005),
  (arXiv:hep-ex/0408146).

15.7 H1 Publications by the groups of Straumann and Truöl

Articles

- **A Direct Search for Magnetic Monopoles Produced in Positron-Proton Collisions at HERA**
  H1-Collaboration*, A. Aktas *et al.*
  DESY 04 – 240, hep-ex/0501039, Eur.Phys.J.**C41** (2005), 133 - 141.

- **Search for Light Gravitinos in Events with Photons and Missing Transverse Momentum at HERA**
  H1-Collaboration*, A. Aktas *et al.*
  DESY 04 – 227, hep-ex/0501030, Phys.Lett.**B616** (2005), 31 - 42.

- **Measurement of Dijet Cross Sections in ep Interactions with a Leading Neutron at HERA**
  H1-Collaboration*, A. Aktas *et al.*
  DESY 04 – 247, hep-ex/050174, Eur.Phys.J.**C41** (2005), 273 - 286.

- **Measurement of Beauty Production at HERA Using Events with Muons and Jets**
  H1-Collaboration*, A. Aktas *et al.*
  DESY 05 – 004, hep-ex/050201, Eur.Phys.J.**C41** (2005), 453 - 467.

- **Measurement of Charm and Beauty Photoproduction at HERA Using $D^*\mu$ Correlations**
  H1-Collaboration*, A. Aktas *et al.*
  DESY 05 – 040, hep-ex/0503038, Phys.Lett.**B621** (2005), 56 - 71.

- **Measurement of Deeply Virtual Compton Scattering**
  H1-Collaboration*, A. Aktas *et al.*
  DESY 05 – 065, hep-ex/0505061, Eur.Phys.J.**C44** (2005), 1 - 11.

- **Search for Leptoquark Bosons in ep Collisions at HERA**
  H1-Collaboration*, A. Aktas *et al.*
  DESY 05 – 087, hep-ex/0506044
  Phys.Lett.**B629** (2005), 9 - 19.

- **A Determination of Electroweak Parameters at HERA**
  H1-Collaboration*, A. Aktas *et al.*
  DESY 05 – 093, hep-ex/0507080, Phys.Lett.**B632** (2006), 35 - 42.

- **Measurement of F_2^{cc} and F_2^{bb} at Low Q^2 Using the H1-vertex Detector at HERA**
  H1-Collaboration*, A. Aktas *et al.*
  DESY 05 – 110, hep-ex/0507081, Eur.Phys.J.**C45** (2006), 23 -33.

- **First Measurement of Charged Current Cross Sections at HERA with Longitudinally Polarized Positrons**
  H1-Collaboration*, A. Aktas *et al.*
  DESY 05 – 249, hep-ex/0512060, Phys.Lett.**B634** (2006), 173 - 179.

Articles in print

- **Forward Jet Production in Deep Inelastic Scattering at HERA**
  H1-Collaboration*, A. Aktas *et al.*
  DESY 05 – 135, hep-ex/0508055, Eur.Phys.J.**C** (2006), in print.

- **Elastic J/ψ Production at HERA**
  H1-Collaboration*, A. Aktas *et al.*
  DESY 05 – 161, hep-ex/0510016, Eur.Phys.J.**C** (2006), in print.

- **Measurement of Event Shape Variables in Deep Inelastic Scattering at HERA**
  H1-Collaboration*, A. Aktas *et al.*
  DESY 05 – 225, hep-ex/0512014, Eur.Phys.J.**C** (2006), in print.

* H1-collaboration (2005)

A. Aktas, V. Andreev, T. Anthonis, S. Aplin, A. Asmone, A. Astvatsatourov, A. Babaev, S. Backovic, J. Bähr, A. Baghdasaryan, P. Baranov, E. Barrelet, W. Bartel, S. Baudrand, S. Baumgartner, J. Becker, M. Beckingham, O. Behnke, O. Behrendt, A. Belousov, Ch. Berger, N. Berger, J.C. Bizot, M.-O. Boenig, V. Boudry, J. Bracinik, G. Brandt, V. Brisson, D.P. Brown, D. Bruncko, F.W. Büsser, A. Bunyatyan, G. Buschhorn, L. Bystritskaya, A.J. Campbell, S. Caron, F. Cassol-Brunner, K. Cerny, V. Chekelian, J.G. Contreras, J.A. Coughlan, B.E. Cox, G. Cozzika, J. Cvach, J.B. Dainton, W.D. Dau, K. Daum, B. Delcourt, R. Demirchyan, A. De Roeck, K. Desch, E.A. De Wolf, C. Diaconu, V. Dodonov, A. Dubak, G. Eckerlin, V. Efremenko, S. Egli, R. Eichler, F. Eisele, M. Ellerbrock, E. Elsen, W. Erdmann, S. Essenov, P.J.W. Faulkner, L. Favart, A. Fedotov, R. Felst, J. Ferencei, L. Finke, M. Fleischer, P. Fleischmann, Y.H. Fleming, G. Flucke, A. Fomenko, I. Foresti, G. Franke, T. Frisson, E. Gabathuler, E. Garutti, J. Gayler, C. Gerlich, S. Ghazaryan, S. Ginzburgskaya, A. Glazov, I. Glushkov, L. Goerlich, M. Goettlich,

N. Gogitidze, S. Gorbounov, C. Goyon, C. Grab, T. Greenshaw, M. Gregori, G. Grindhammer, C. Gwilliam, D. Haidt, L. Hajduk, J. Haller, M. Hansson, G. Heinzelmann, R.C.W. Henderson, H. Henschel, O. Henshaw, G. Herrera, M. Hildebrandt, K.H. Hiller, D. Hoffmann, R. Horisberger, A. Hovhannisyan, M. Ibbotson, M. Ismail, M. Jacquet, L. Janauschek, X. Janssen, V. Jemanov, L. Jönsson, D.P. Johnson, H. Jung, M. Kapichine, J. Katzy, N. Keller, I.R. Kenyon, C. Kiesling, M. Klein, C. Kleinwort, T. Klimkovich, T. Kluge, G. Knies, A. Knutsson, V. Korbel, P. Kostka, R. Koutouev, K. Krastev, J. Kretzschmar, A. Kropivnitskaya, K. Krüger, J. Kückens, M.P.J. Landon, W. Lange, T. Laštovička, G. Laštovička-Medin, P. Laycock, A. Lebedev, B. Leißner, V. Lendermann, S. Levonian, L. Lindfeld, K. Lipka, B. List, E. Lobodzinska, N. Loktionova, R. Lopez-Fernandez, V. Lubimov, H. Lueders, D. Lüke, T. Lux, L. Lytkin, A. Makankine, N. Malden, E. Malinovski, S. Mangano, P. Marage, R. Marshall, M. Martisikova, H.-U. Martyn, S.J. Maxfield, D. Meer, A. Mehta, K. Meier, A.B. Meyer, H. Meyer, J. Meyer, S. Mikocki, I. Milcewicz-Mika, D. Milstead, A. Mohamed, F. Moreau, A. Morozov, J.V. Morris, M.U. Mozer, K. Müller, P. Murín, K. Nankov, B. Naroska, Th. Naumann, P.R. Newman, C. Niebuhr, A. Nikiforov, D. Nikitin, G. Nowak, M. Nozicka, R. Oganezov, B. Olivier, J.E. Olsson, D. Ozerov, V. Palichik, C. Pascaud, I. Panagoulias, T. Papadopolou, G.D. Patel, M. Peez, E. Perez, D. Perez-Astudillo, A. Perieanu, A. Petrukhin, D. Pitzl, R. Plačakytė, B. Portheault, B. Povh, P. Prideaux, N. Raicevic, P. Reimer, B. Reisert, A. Rimmer, C. Risler, E. Rizvi, P. Robmann, B. Roland, R. Roosen, A. Rostovtsev, Z. Rurikova, S. Rusakov, F. Salvaire, D.P.C. Sankey, E. Sauvan, S. Schätzel, F.-P. Schilling, S. Schmidt, S. Schmitt, C. Schmitz, L. Schoeffel, A. Schöning, V. Schröder, H.-C. Schultz-Coulon, K. Sedlák, F. Sefkow, I. Sheviakov, L.N. Shtarkov, Y. Sirois, T. Sloan, P. Smirnov, Y. Soloviev, D. South, V. Spaskov, A. Specka, B. Stella, J. Stiewe, I. Strauch, U. Straumann, V. Tchoulakov, G. Thompson, P.D. Thompson, F. Tomasz, D. Traynor, P. Truöl, I. Tsakov, G. Tsipolitis, I. Tsurin, J. Turnau, E. Tzamariudaki, M. Urban, A. Usik, D. Utkin, S. Valkár, A. Valkárová, C. Vallée, P. Van Mechelen, N. Van Remortel, A. Vargas Trevino, Y. Vazdik, C. Veelken, A. Vest, S. Vinokurova, V. Volchinski, B. Vujicic, K. Wacker, J. Wagner, G. Weber, R. Weber, D. Wegener, C. Werner, N. Werner, M. Wessels, B. Wessling, C. Wigmore, Ch. Wissing, R. Wolf, E. Wünsch, S. Xella, W. Yan, V. Yeganov, J. Žáček, J. Zálešák, Z. Zhang, A. Zhelezov, A. Zhokin, J. Zimmermann, H. Zohrabyan, and F. Zomer

15.8 Research group of Prof. P. Truöl [10]

Articles

- **An Improved Upper Limit on the Decay $K^+ \to \pi^+\mu^+e^-$**
  E865-Collaboration†, Aleksey Sher *et al.*
  hep-ex/0502020, Phys.Rev.**D72** (2005), 012005-1 - 012005-13.

- **First Observation of the Decay $K^+ \to e^+\nu_e\mu^+\mu^-$**
  E865-Collaboration†, H. Ma *et al.*
  hep-ex/0505011, Phys.Rev.**D73** (2006), 037101-1 - 037101-4.

- **Charm, Beauty and Charmonium Production at HERA-B**
  HERA-B-Collaboration, A. Zoccoli *et al.*
  Int. Conf. on Hard and Electromagnetic Probes of High Energy Nuclear Collisions (HP 2004), Ericeira, Portugal, 4-10 Nov 2004; Eur.Phys.J.**C43** (2005), 179-186.

[10] for H1 publications see Sec.15.7

- **Improved Measurement of the $b\bar{b}$ Production Cross Section in 920 GeV fixed-target Proton-Nucleus Interactions**
  HERA-B-Collaboration, I. Abt *et al.*
  DESY-05-233, hep-ex/0512030, Phys.Rev.**D73** (2006), 052005-1 - 052005-17.

- **High Intensity K experiments**
  A. van der Schaaf, Nucl. Phys. B (Proc. Suppl.) 154 (2006) 12-19.

Articles in print

- **A search for $\mu - e$ conversion in muonic gold**
  SINDRUM II Collaboration, W. Bertl, R. Engfer, E.A. Hermes, G. Kurz, T. Kozlowski, J. Kuth, G. Otter, F. Rosenbaum, N.M. Ryskulov, A. van der Schaaf, P. Wintz, I. Zychor,
  Eur. Phys. J. C (2006).

- **Measurement of the J/Ψ Production Cross Section in 920 GeV/c Fixed-Target Proton-Mucleus Interactions**
  HERA-B-Collaboration, I. Abt *et al.*, DESY-05-232, hep-ex/0512029, Phys.Lett.**B** (2006).

Invited lectures

- A. van der Schaaf: **KOPIO charged particle vetos**
  K-RARE DECAYS meeting, Frascati National Laboratories, Frascati, Italy, 26 - 27 May, 2005.

- A. van der Schaaf: **High Intensity K experiments**
  High Intensity Frontier Workshop, La Biodola, Isola d'Elba, Italy, May 28 - June 1, 2005.

Conference presentation

- S. Scheu: **Studies on wrapping materials and light collection geometries in plastic scintillators (poster)**
  4th International Conference on New Developments in Photodetection, Beaune, France, June 19-24, 2005, to appear in Nucl. Inst. Meth. A, number 5211.

E865-Collaboration

R. Appel, G.S. Atoyan, B. Bassaleck, D.R. Bergman, N. Cheung, S. Dhawan, H. Do, J. Egger, S. Eilerts, W.D. Herold, V.V. Issakov, H. Kaspar, D. Kraus, D. Lazarus, P. Lichard, J. Lowe, J. Lozano, H. Ma, W. Majid, S. Pislak, A.A. Poblaguev, A. Sher, Aleksey Sher, P. Rehak, J.A. Thompson, P. Truöl, and M.E. Zeller

HERA-B Collaboration

I. Abt, M. Adams, H. Albrecht, A. Aleksandrov, V. Amaral, A. Amorim, S.J. Aplin, V. Aushev, Y. Bagaturia, V. Balagura, M. Bargiotti, O. Barsukova, J. Bastos, J. Batista, C. Bauer, Th.S. Bauer, A. Belkov, Ar. Belkov, A. Bertin, B. Bobchenko, M. Bocker, A. Bogatyrev, G. Bohm, M. Brauer, M. Bruinsma, M. Bruschi, P. Buchholz, M. Buchler, T. Buran, J. Carvalho, P. Conde, C. Cruse, M. Dam, K.M. Danielsen, M. Danilov, S. De Castro, H. Deppe, X. Dong, H.B. Dreis, V. Egorytchev, K. Ehret, F. Eisele, D. Emeliyanov, S. Essenov, L. Fabbri, P. Faccioli, M. Feuerstack-Raible, J. Flammer, B. Fominykh, M. Funcke, Ll. Garrido, B. Giacobbe, J. Glass, D. Goloubkov, Y. Golubkov, A. Golutvin, I. Golutvin, I. Gorbounov, A. Gorisek, O. Gouchtchine, D.C. Goulart, S. Gradl, W. Gradl, F. Grimaldi, Yu. Guilitsky, J.D. Hansen, R. Harr, J.M. Hernandez, W. Hofmann, T. Hott, W. Hulsbergen, U. Husemann, O. Igonkina, M. Ispiryan, T. Jagla, C. Jiang, H. Kapitza, S. Karabekyan, P. Karchin, N. Karpenko, S. Keller, J. Kessler, F. Khasanov, Yu. Kiryushin, K.T. Knopfle, H. Kolanoski, S. Korpar, C. Krauss, P. Kreuzer, P. Krizan, D. Krucker, S. Kupper, T. Kvaratskheliia, A. Lanyov, K. Lau, B. Lewendel, T. Lohse, B. Lomonosov, R. Manner, S. Masciocchi, I. Massa, I. Matchikhilian, G. Medin, M. Medinnis, M. Mevius, A. Michetti, Yu. Mikhailov, R. Mizuk, R. Muresan, S. Nam, M. zur Nedden, M. Negodaev, M. Norenberg, S. Nowak, M.T. Nunez Pardo de Vera, M. Ouchrif, F. Ould-Saada, C. Padilla, D. Peralta, R. Pernack, R. Pestotnik, M. Piccinini, M.-A. Pleier, M. Poli, V. Popov, A. Pose, D. Pose, S. Prystupa, V.M. Pugatch, Y. Pylypchenko, J. Pyrlik, K. Reeves, D. Ressing, H. Rick, I. Riu, P. Robmann, V. Rybnikov, F. Sanchez, A. Sbrizzi, M. Schmelling, B. Schmidt, A. Schreiner, H. Schroder, A.-J. Schwartz, A.-S. Schwarz, B. Schwenninger, B. Schwingenheuer, F. Sciacca, N. Semprini-Cesari, J. Shiu, S. Shuvalov, L. Silva, K. Smirnov, L. Sozuer, S. Solunin, A. Somov, S. Somov, J. Spengler, R. Spighi, A. Spiridonov, A. Stanovnik, M. Staric, C. Stegmann, H.S. Subramania, M. Symalla, I. Tikhomirov, M. Titov, I. Tsakov, U. Uwer, C. van Eldik, Yu. Vassiliev, M. Villa, A. Vitale, I. Vukotic, H. Wahlberg, A.H. Walenta, M. Walter, J.J. Wang, D. Wegener, U. Werthenbach, H. Wolters, R. Wurth, A. Wurz, Yu. Zaitsev, M. Zavertyaev, T. Zeuner, A. Zhelezov, Z. Zheng, R. Zimmermann, T. Zivko